

**Critical thicknesses in Nb-H thin films:  
coherent and incoherent phase transitions, change of  
precipitation and growth modes and ultrahigh mechanical  
stress**

Dissertation

zur Erlangung des mathematisch-naturwissenschaftlichen Doktorgrades

"Doctor rerum naturalium"

der Georg-August-Universität Göttingen

im Promotionsprogramm ProPhys

der Georg-August University School of Science (GAUSS)

vorgelegt von

**Vladimir Burlaka**

aus Sankt Petersburg, Russland

Göttingen, 2015

### **Betreuungsausschuss**

Prof. Dr. Astrid Pundt  
Institut für Materialphysik, Georg-August-Universität Göttingen

Prof. Dr. Hans Christian Hofsäss  
II. Physikalisches Institut, Georg-August-Universität Göttingen

### **Mitglieder der Prüfungskommission**

Referentin: Prof. Dr. Astrid Pundt  
Institut für Materialphysik, Georg-August-Universität Göttingen

Korreferent: Prof. Dr. Hans Christian Hofsäss  
II. Physikalisches Institut, Georg-August-Universität Göttingen

### **Weitere Mitglieder der Prüfungskommission**

Prof. Dr. Hans-Ulrich Krebs  
Institut für Materialphysik, Georg-August-Universität Göttingen

Prof. Dr. Michael Seibt  
IV. Physikalisches Institut, Georg-August-Universität Göttingen

Prof. Dr. Vasily Moshnyaga  
I. Physikalisches Institut, Georg-August-Universität Göttingen

PD Dr. -Ing. Helmut Klein  
Abteilung Kristallographie, Geowissenschaftliches Zentrum,  
Georg-August-Universität Göttingen

Tag der mündlichen Prüfung: 09.12.2015

## Abstract

For nanoscale systems such as Me-H thin films, changes of physical properties have been suggested to appear below certain critical sizes. The probable existence of these critical sizes and the related changes of thermodynamical and mechanical properties are the central topics of this thesis, using the model system of Nb-H thin epitaxial films adhered on Al<sub>2</sub>O<sub>3</sub> (11-20) sapphire substrate. Since all the effects and, especially, the efficiency of stress release depends on the film thickness ( $d$ ),  $d$  was considered in this study as a tunable size parameter that was varied from 105 nm to 5 nm. Particularly, this work addresses the suggested occurrence of coherent phase transformations and the appearance of hydrogen-induced ultrahigh mechanical stress in the GPa range, as predicted by calculations.

These topics were experimentally studied by scanning tunneling microscopy (STM), X-ray diffraction (XRD) and electrical resistance measurements as applied *in-situ* during hydrogen gas loading experiments. The main goal was to derive the critical film thickness for coherent phase transformations and to investigate the pre-existing theoretical model. Further, this research was accompanied by a systematic study on the stress development arising within the Nb-H films upon hydrogen loading. This was also studied in dependence on the film thickness. The related data were obtained by use of substrate curvature measurements performed *in-situ* during electrochemical hydrogen loading. Hereby, the regime of linear elastic film expansion and the development of an ultra-high stress state was of interest.

The experimental results suggest an existence of three different regimes in dependence on the film thickness. For  $d \leq d_1 = 37 - 40 \text{ nm}$ , coherent phase transformation appears in Nb-H thin film system. Here, preferential nucleation of hydrides instead of their growth is found. For  $d > d_1$ , semi-coherent phase transformation and preferential growth of hydride precipitates is detected. For  $d \leq d_2 \approx 8 \text{ nm} - 15 \text{ nm}$  no trace of phase separation in the Nb-H thin film system is found at room temperature ( $T_{RT}$ ). This shows that the critical temperature  $T_c$  of the miscibility gap of the Nb-H thin film system drops below  $T_{RT}$ , for  $d \leq d_2$ . The related destabilization of the hydride phase is attributed to a decrease of the H-H interaction energy  $E_{HH}$  and an increasing contribution of mechanical stress in ultrathin films. Besides, the regime of linear elastic film expansion and reproducible ultra-high mechanical stresses is realized for film thicknesses  $d \leq d_3 = 5 \text{ nm}$ . Hydrogen-induced mechanical stress of up to -10 GPa are measured for 5 nm to 10 nm thin Nb films.

Because of the fundamental research character, this study gives insights into the physics of decomposition in thin alloy films when crossing the critical  $d_c$  - values. The general concept can be transferred to other nano-sized systems fixed to stabilizers and offers the possibility to tune the stress state and to affect the stabilities of phases by crossing critical system sizes, particularly in Me-H thin film systems.



## Contents

<b>1</b>	<b>Introduction .....</b>	<b>1</b>
<b>2</b>	<b>Hydrogen in metals .....</b>	<b>6</b>
2.1	Nb-H Bulk system .....	6
2.1.1	Interstitial sites .....	6
2.1.2	Nb-H binary phase diagram .....	7
2.1.3	Hydrogen induced lattice expansion.....	8
2.2	Epitaxial Nb (110) films grown on Al <sub>2</sub> O <sub>3</sub> (11-20) sapphire substrate.....	9
2.3	Me-H thin film system: general findings.....	11
2.3.1	Difference between “bulk” and “thin film” Me-H system .....	11
2.3.2	Intrinsic stress in films.....	11
2.3.3	Interstitials-induced mechanical stress.....	11
2.4	Nb-H thin film system .....	12
2.4.1	Linear elastic theory on hydrogen-loaded thin Nb films clamped to a rigid substrate.....	12
2.4.2	Hydrogen induced lattice expansion in thin Nb-H films.....	17
2.4.3	Plastic deformation at the film/substrate interface upon H-absorption .....	19
2.4.4	Mechanical stress release in M-H films upon hydride formation .....	21
2.4.5	Phase transformation in Nb-H films studied by STM.....	24
2.4.6	Calculation on the critical size: coherent and semi-coherent phase transformation .....	26
2.4.7	Phase boundaries of Nb-H thin films .....	28
2.4.8	Plateau pressure.....	29
2.4.9	Critical point for phase separation (critical temperature $T_c$ ).....	30
<b>3</b>	<b>Experimental methods.....</b>	<b>33</b>
3.1	Sample preparation.....	33
3.2	Hydrogen gas-phase loading .....	35
3.3	Scanning tunneling microscopy (STM).....	36
3.3.1	Introduction of the STM method .....	36
3.3.2	In-situ hydrogen loading STM measurements.....	38
3.3.3	Ex-situ STM data evaluation: drift correction and difference images .....	40
3.4	In-situ resistance measurements during hydrogen loading.....	40
3.5	X-ray diffraction (XRD) and X-ray reflectivity (XRR).....	42
3.5.1	XRD .....	42
3.5.2	XRR.....	43

3.5.3	<i>In-situ XRD during hydrogen loading</i> .....	45
3.6	<i>Electrochemical hydrogen loading</i> .....	48
3.6.1	<i>Electromotive Force (EMF) measurements</i> .....	48
3.6.2	<i>In-situ stress measurements during electrochemical hydrogen loading</i> .....	50
<b>4</b>	<b><i>Optimization of the initial film surface topography and microstructure</i></b> .....	<b>52</b>
4.1	<i>Optimization of the initial surface topography</i> .....	52
4.2	<i>Initial film texture</i> .....	57
4.3	<i>Initial film stress</i> .....	58
4.4	<i>Pd islands on the Nb film surface</i> .....	59
<b>5</b>	<b><i>Results and individual discussion on hydrogen loaded films</i></b> .....	<b>61</b>
5.1	<i>STM results on hydrogen loaded films</i> .....	61
5.1.1	<i>55 nm Nb-H film</i> .....	61
5.1.1.1	<i>Morphology change upon hydrogen loading of a 55 nm Nb-H film</i> .....	61
5.1.1.2	<i>Morphology change upon hydrogen unloading of a 55 nm Nb-H film</i> .....	65
5.1.2	<i>40 nm Nb-H film</i> .....	67
5.1.2.1	<i>Morphology change upon hydrogen loading of a 40 nm Nb-H film</i> .....	67
5.1.3	<i>25 nm Nb-H film</i> .....	70
5.1.3.1	<i>Morphology change upon hydrogen loading of a 25 nm Nb-H film</i> .....	70
5.1.3.2	<i>Morphology change upon hydrogen unloading of a 25 nm Nb-H film</i> .....	73
5.1.4	<i>15 nm Nb-H film</i> .....	76
5.1.4.1	<i>Morphology change upon hydrogen loading of a 15 nm Nb-H film</i> .....	76
5.1.5	<i>8 nm Nb-H film</i> .....	83
5.1.5.1	<i>Morphology change upon hydrogen loading of a 8 nm Nb-H film</i> .....	83
5.1.5.2	<i>Morphology change upon hydrogen unloading of a 8 nm Nb-H film</i> .....	89
5.1.6	<i>Summary of STM measurements</i> .....	92
5.2	<i>XRD results upon hydrogen loading</i> .....	95
5.2.1	<i>Different XRD patterns below and above the critical thickness: refinement of the critical value</i> .....	95
5.2.1.1	<i>Thick Nb film: studies on films with <math>d &gt; 43</math> nm</i> .....	95
5.2.1.2	<i>Intermediate film thickness: studies on 15 nm – 37 nm Nb films</i> .....	97
5.2.1.3	<i>Thin films: studies on films with <math>d &lt; 15</math> nm</i> .....	100
5.2.2	<i>Cyclic hydrogen loading: reversibility test</i> .....	102
5.2.3	<i>Suppression of phase transformation in the 8 nm thin film</i> .....	104
5.2.4	<i>Reversible changes in the 5 nm Nb-H film</i> .....	106

5.2.5	Summary of XRD measurements .....	111
5.3	Mechanical stress measurements upon hydrogen loading .....	113
5.3.1	Stress-strain curve for the 40 nm thick film .....	113
5.3.2	Stress-strain curve for the 25 nm thick film .....	115
5.3.3	Combined stress-strain curves for films of different thickness.....	117
5.3.4	Reaching the elastic limit in stress-strain curves: elastic and quasi-elastic behavior.....	119
5.3.5	Change of phase boundaries.....	121
5.3.6	Summary of stress measurements.....	122
<b>6</b>	<b>Global discussion .....</b>	<b>124</b>
6.1	Precipitation and growth of hydride phase: different modes (based on STM and XRD results) ...	124
6.2	Irreversible changes in thin Nb-H films (based on STM, XRD and stress measurements results) .	130
6.3	Quasi-elastic behavior detected by using stress measurements.....	131
6.4	Evidence of pure elastic one-dimensional film expansion: reversibility test based on XRD, resistance, EMF, stress and XRR measurements .....	132
6.5	Suppression of phase transformation in ultrathin films .....	134
6.6	Stress contribution and change of solubility limits visible in EMF curves .....	137
6.7	Critical film thickness for coherent phase transformation: model validation (STM, XRD, EMF and stress measurements) .....	138
<b>7</b>	<b>Summary and outlook.....</b>	<b>141</b>
	<b>Bibliography.....</b>	<b>145</b>
	<b>Acknowledgments.....</b>	<b>153</b>
	<b>Curriculum vitae.....</b>	<b>155</b>

## 1 Introduction

During the last fifty years, researchers have been working a lot on the creation and the development of new sources of energy and new renewable fuel. This type of research becomes more and more important in our days, when people are starting to think about the needs of future generations and about the prospective of our planet in a whole. Thus, the limitations of the fossil fuels with regard to the continuing growth of energy demand and the growing impact of CO<sub>2</sub> emissions attract an increasing attention. In this context, hydrogen (H) is regarded as one of the carbon-free renewable energy carriers. As a fuel, hydrogen can be fabricated (e.g. via electrolysis), stored (e.g. metal hydrides) and consumed in a cyclic process, only producing water or steam as a combustion product [1].

In general, hydrogen is the most abundant, the smallest and the lightest element in the universe. Thanks to its small dimensions, it can be easily absorbed in the interstitial sites of a metal lattice. The small size of hydrogen atoms permits dense hydrogen packing in metal hosts that have a high affinity to hydrogen, i.e., a large negative heat of solution for hydrogen. It is surprising, but in metal hydrides, the hydrogen density can be even larger than in liquid hydrogen [2], [3]. This has led to the application of metal hydrides for energy storage [4]. However, for transport applications the volume as well as the weight of the host are of major concern [5], [6]. This has resulted in the exclusion of many metals from the use in applications. Nowadays the main research activity on development and application of Me-H storage systems focuses on the improvement of the gravimetric hydrogen density and the reaction kinetics [7], [8].

In relation to this issue, nano-sized systems have been studied since the early 90's to expand the fundamental knowledge about the physical properties of Me-H systems and their dependency on the different contributing factors, e.g. microstructure, size of the grain boundaries, mechanical stress, reduced system dimensions. Pundt and Kirchheim reviewed in detail many fundamental results concerning the difference occurring between bulk and nano-sized Me-H systems [9], [10].

In general, nano-materials show physical properties that differ from their bulk counterparts. To study these differences especially for binary alloys, metal-hydrogen (M-H) systems are of interest. In this material class the alloying content can be controlled just via an external chemical potential, which is further facilitated by the extremely high hydrogen mobility in metals, even at 294 K [4], [9]. This fact allows kinetic and thermodynamic studies at room temperature (RT) within suitable time spans. Because of the hydrogen's interstitial solution, the alloying content can be changed from zero to high concentrations by using one and the same nano-sample. Special microstructures of nano-sized systems can be adjusted beforehand and their influences on the M-H system properties can be studied. Because of the low temperature required for the experiments, defect annihilation commonly triggered by enhanced temperatures, is inhibited.

M-H nano-materials are interesting from fundamental and practical points of view. Fundamental studies can be performed addressing differences and similarities between the physical properties of bulk systems and those with reduced dimensions. Since physical properties of M-H nano-systems are strongly affected by micro-structural contributions [9], [11], [12], [13], [14], microstructure can, vice versa, be used to tune the materials properties. From the practical point of view, nowadays, M-H nano-materials are suggested also as promising candidates for hydrogen energy storage applications because of the fast loading and unloading times due to the intrinsically small diffusion lengths [7], [15].

Usually, by studying the fundamental properties of nano-systems, it is more convenient to work with relatively simple model systems, in which the number of contributing factors (e.g. microstructure, composition etc.) can be adjusted and segregated more accurately as compared to the complex alloys or multilayers films. Besides, well-investigated metals like Nb, V or Pd can be chosen, since their properties are well investigated on the bulk scale and, hence, repeatedly verified reference data are available for comparison and discussion [4], [16]. Further, by consideration of a thin film system fixed on the rigid substrate, the change of elastic properties and an occurrence of mechanical stress caused by lattice dilatation can be often detected. Hereby, dislocation formation and film delamination from the substrate are very common mechanism of stress release [17]. Specifically, for M-H thin film system, dislocation formation can occur at the hydride/ $\alpha$ -matrix interface [9], [18], [19] as well as at the hydride/substrate interface [20], [21], [22], [23] and in both cases causes irreversible lattice distortion [9], [23] and surface roughening [19], [24]. Besides, the efficiency of stress release depends critically of the film microstructure [9], [14], [25] and the film thickness itself [9], [14], [19].

Thin film properties are easy accessible by in-situ experiments that combine information about kinetics and thermodynamics: mechanical stress can be directly measured via substrate curvature and microstructural changes can be determined by many different experimental techniques such as, for example, in-situ X-ray diffraction measurements (in-situ XRD) at Synchrotron sources [23], or in-situ resistance measurements [26]. As recently shown, phase transformation details in thin films such as the coherency condition, the local spreading of the hydrides and the film expansion can be investigated by surface sensitive in-situ scanning tunneling microscopy (in-situ STM) [19], [24].

In the present work, Nb-H thin epitaxial films (Nb (110) // Al<sub>2</sub>O<sub>3</sub> (11-20)) are adopted as a model system. Epitaxial Nb films are well studied [27], [28]. They offer a good lattice matching between both materials [29], allows for good stability during thermal cycling and is known for the strong adhesion that excludes film delamination from the stabilizer as a side mechanism for stress release [30]. Strong adhesion is especially important when additional interstitials-induced mechanical stress arises in the film. Thus, the choice of this model system, on the one hand, allows producing films with a well-defined microstructure and, on the other hand, to perform the hydrogen loading / unloading experiment on the mechanically

stable Me-H system that can reach an ultrahigh mechanical stress state. Furthermore, the hydride phase in Nb-H system is rather stable possessing a suitable hydride-formation pressure of about  $p_H = 10^{-7}$  mbar -  $10^{-6}$  mbar at 294 K. This allows for in-situ STM measurements in the required pressure range without need to use any protective layer [31].

Even though also the thin film system of Nb-H is often studied [32], [33], [34], the measurements performed in other research groups are mainly performed at elevated temperatures above the critical temperature ( $T_c$ ) and, hence, do not consider the region of phase separation in the Nb-H phase diagram, targeted in this study. Furthermore, related literature results, e.g. “finite size effect” [32] appear often conflicting and nowadays seem to be overestimated. This already demonstrates the diversity of parameters (microstructure, stress state, surface morphology, local adhesion) needed to address, understand and attribute the nano-materials properties. The change of stress conditions by varying the size of thin films, as suggested in the actual work, should not be confused with the early studies on coherency stress and coherent phase transitions in bulk systems performed at elevated temperatures above  $T_c$ . The results on thin films differ significantly from the bulk, specifically due to the different type of nucleation (homogeneous  $\leftrightarrow$  surface controlled and strongly dependent on local changes), the different precipitate morphology (spheres  $\leftrightarrow$  cylinders [19]) as well as the different external stress state (zero  $\leftrightarrow$  expected up to -10 GPa, biaxial).

In general, this study is motivated by the need to clarify and investigate systematically the occurrence of coherent phase transformations and the accumulation of high stress in Me-H thin film systems. Hereby, in the past, by studying Nb-H as a model system authors demonstrated relatively high mechanical stress in the GPa range arising in the film upon hydrogen loading [13], [25], [35] and also predicted an existence of critical film thickness ( $d_c = 26$  nm) below which only coherent phase transformation is possible [19], [24].

Thus, the goal of this PhD work is to verify whether the suggested critical thicknesses in Nb-H thin films is present, to substantiate its value, and to investigate the thermodynamic and mechanical changes related to the critical size. This includes the study of the suggested drop of  $T_c$  to less than  $T_{RT} = 294$  K, the suggested occurrence of ultrahigh stresses and the suggested presence of pure linear elasticity for films below critical sizes.

This was done experimentally by STM, XRD and electrical resistance measurements applied to derive the critical film thickness for coherent phase transformations and testing the model of Nörthemann et al. [19]. Further, this was accompanied by a systematic study on the stress development within the Nb-H films upon hydrogen loading depending on the film thickness. Hereby, a regime of the pure elastic one-dimensional film expansion and high stress state predicted by the linear elastic theory [13], [25] is of interest. On top of this, changes that occur in the precipitation and growth of hydride phase are studied

by STM and XRD methods. Finally, the absence of any precipitation of hydride  $\beta$ -phase was addressed when the film thickness reaches certain “critical” values. Furthermore, different aspects of stress release, coherency conservation at different possible interfaces, visibility of phase transformation via different techniques, an occurrence of (ir-)reversible microstructural change, and, finally, the finding of proper boundary conditions for the realization of the pure elastic one-dimensional film expansion model are targeted.

Since all the effects and, especially, the efficiency of stress release depends on the film thickness ( $d$ ),  $d$  is considered in this study as a tunable size parameter that is varied from 105 nm to 5 nm. To avoid the influence of grain boundaries on the hydrogen absorption and the phase transformation and to minimize the number of pre-existing defects in the as-prepared samples, epitaxially grown Nb films with flat surfaces are targeted.

In total, this thesis consist of 7 chapters. In chapter 1, short introduction and motivation of this study are proposed. Chapter 2 contains the theoretical background of metal-hydrogen systems including many aspects of state of the art in the related topic. In chapter 3, experimental methods are shortly introduced. In chapter 4, the results of characterization of surface topographies in dependence on the film thickness and the deposition temperature  $T_d$  are given. Based on these results, an optimization of film deposition temperature  $T_d$  required to avoid a formation of meander-like “open” surface topographies [36], [37] is suggested. Furthermore, the microstructure of the as-prepared samples prepared at the suggested optimum  $T_d$  is analyzed by XRD and texture measurements. Chapter 5 presents the results on in-situ hydrogen loading studies on Nb films of different thickness. Here, due to the large number of different aspects addressed by the variety of experimental techniques (STM, XRD, EMF, stress measurements and electrical resistance measurements), sub/discussion and method related data interpretation are individually given. To guide the reader, this chapter is divided into three sub-chapters introducing separately results obtained by three different techniques: 5.1 – STM, 5.2 - XRD and 5.3 – stress measurements. After each sub-chapter, presented results are shortly summarized. STM results presented in the sub-chapter 5.1 are focused on the measurements of the surface topography changes caused by the phase transformation and plastic deformation processes. Herewith, the regimes of hydride phase precipitation and growth as well as the dislocation related surface corrugations are analyzed. XRD results given in the sub-chapter 5.2 mainly address the problem of reversible/irreversible microstructural changes and the visibility / invisibility of phase transformation in thin Nb-H films upon the hydrogen loading. The result of stress measurements given in the sub-chapter 5.3 are concentrated on the stress development and stress release observed in films of different thickness. In chapter 6, all the results are globally discussed in the combined way, especially focusing on the evidence of coherent phase

transformation, reversible and irreversible microstructural changes, ultrahigh mechanical stress state and the suppression of phase separation in Nb-H thin films. Chapter 7 summarizes this thesis.

## 2 Hydrogen in metals

This chapter is supposed to provide a short theoretical introduction to the Nb-H system. In sub-chapter 2.1, it will be given a brief review about Nb-H bulk system including the description of interstitial sites occupied by hydrogen, the Nb-H bulk phase diagram and the lattice / volume expansion of the Nb host material. In sub-chapter 2.2, it will be briefly presented typical epitaxy conditions of epitaxial Nb (110) films grown on  $\text{Al}_2\text{O}_3$  (11-20) sapphire substrates. In sub-chapter 2.3, the general differences between a “bulk” and a “thin film” Me-H system will be described. Finally, in sub-chapter 2.4 the Nb-H thin film system will be reviewed. Thereby, the theory of linear elasticity is introduced for describing the development of stress and strain in thin Nb films upon H-uptake. Besides, the results of related studies addressing the task of phase transformation, the mechanisms of stress release, the prediction of critical film thickness for coherent phase transformation and contribution of mechanical stress to the thermodynamics of Nb-H thin film system will be summarized.

### 2.1 Nb-H Bulk system

#### 2.1.1 Interstitial sites

Hydrogen atoms introduced in metal host lattice occupy typically two different interstitial sites, known as tetrahedral sites (T-sites) and octahedral sites (O-sites). Depending on the metal-lattice structure, different interstitial sites can be preferentially occupied. In case of Nb that has the bcc crystal structure, the hydrogen atom has three possible octahedral and six tetrahedral sites available per metal atom (see Fig. 2.1). In Nb, hydrogen is preferentially dissolved on tetrahedral lattice sites. T-sites of a bcc lattice are divided according to their symmetry axis and are denoted  $T_x$ ,  $T_y$  or  $T_z$  [16]. Hereby, H atoms at low concentrations occupy T-sites randomly, but at high concentrations, they tend to occupy certain sub-lattices of interstitial sites at low temperatures, causing a small overall distortion of the lattice. This lattice distortion removes the degeneracy of the site energy in the original cubic lattice, allowing the occupancy of a certain interstitial sub-lattice among others [16].

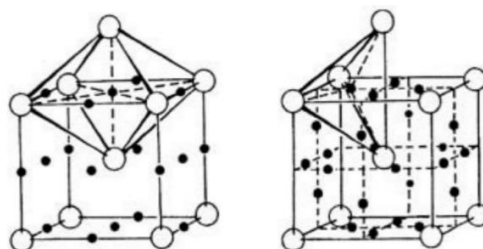


**Fig. 2.1** Interstitial octahedral O-sites (left) and tetrahedral T-sites (right) in a bcc lattice available for the accommodation of hydrogen atoms [16]. Filled circles show all possible interstitial sites that can be theoretically occupied by hydrogen atoms and unfilled circles correspond to positions of metal atoms in the unit-cell of a bcc crystal structure. Reprinted from *The Metal-Hydrogen system, Chapter 2.4.1, 2005, p. 31, Y. Fukai, Copyright 2005, with permission from Springer. (original image is cropped)*

### 2.1.2 Nb-H binary phase diagram

The Nb-H bulk system is a well-studied model system that was deeply investigated in the 70<sup>th</sup> years of the last century [38], [39], [40], [41], [42], [43]. Thus, different graphical variations of phase diagram of Nb-H system can be easily found in any textbooks on the metal-hydrogen systems and are, therefore, supposed to be presented here very briefly.

The phase diagram of Nb-H system is shown in Fig. 2.2 [43], [44]. Here,  $c_H = [H] / [Nb]$  is the hydrogen concentration ( $0 \text{ H/Nb} < c < 0.8 \text{ H/Nb}$ ) and  $T$  is the temperature of the system ( $0^\circ \text{C} < T < 200^\circ \text{C}$ ). Depending on the composition and the temperature, there are three different phases, namely  $\alpha$ ,  $\alpha'$  and  $\beta$  can be visible in the discussed part of the phase diagram. In details:

- 1)  $\alpha$  - phase ("lattice gas phase" for small concentrations [45]) is a disordered interstitial alloy, in which hydrogen atoms randomly occupy tetrahedral interstitial sites in the bcc Nb structure.
- 2)  $\alpha'$  - phase ("lattice liquid phase" [45]) – disordered interstitial alloy of high hydrogen concentration, in which hydrogen atoms are randomly distributed in the host lattice and the Nb crystal retains its cubic symmetry. In  $\alpha$ - and  $\alpha'$ - phases, the lattice parameter increases linearly with the hydrogen concentration. The only difference is the higher hydrogen concentration in  $\alpha'$ -phase. Because of the similarity to gas and liquid phase transition,  $\alpha$ - and the  $\alpha'$ - phases are called, respectively, lattice gas and lattice liquid phase.
- 3)  $\beta$  - phase ("lattice crystal" / ordered hydride phase) – has an orthorhombic distorted face-centered structure. The bcc symmetry is broken due to the formation of H-super-lattice, where the hydrogen is restricted to four ordered tetrahedral sites [46].

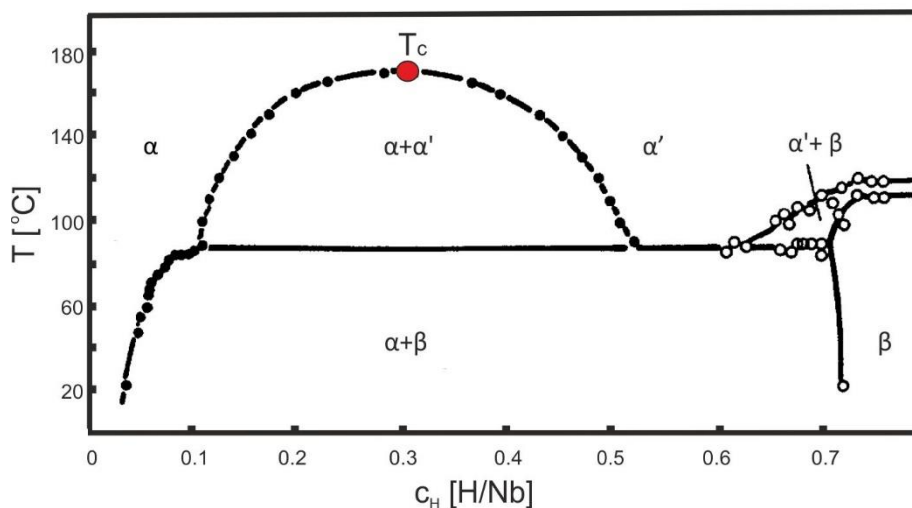


**Fig. 2.2** The phase diagram of hydrogen in a bulk Nb crystal [43]. Areas of phases diagram labeled as  $\alpha$ -,  $\alpha'$ - and  $\beta$ - regions corresponds to different phases.  $T_c$  is the critical temperature. Reprinted from *J. Phys. F: Met. Phys.* 9, 1461-1476, H. Zabel & J. Peisl, *The incoherent phase transitions of hydrogen and deuterium in niobium*, Copyright 1979, with permission from IOP Publishing. (original image is modified)

For hydrogen in the bulk Nb crystal, the critical temperature  $T_c$  separating homogeneous and inhomogeneous phases is about 171 °C and the related critical hydrogen concentration is  $c_c = 0.31$  H/Nb [44]. Further, in this phase diagram, there exists a region labeled  $\alpha + \alpha'$ , where solid solutions of two different concentrations may coexist. Besides, there is region labeled  $\alpha + \beta$ , where phase transformation from the  $\alpha$  - to the  $\beta$  - phase occurs. The concentration range, where two of these phases may coexist (so-called “width of miscibility gap”) at RT lies close to the magnitude of about  $\Delta c = 0.7$  H/Nb and tends to decrease by increasing the temperature. This trend can be understood in terms of increasing entropy contribution to the free energy of the system.

All the other phases appear only for high hydrogen concentration or low temperature and are not shown in Fig. 2.2.

### 2.1.3 Hydrogen induced lattice expansion

Introducing hydrogen into the isotropic crystal that can freely expand in all the spatial directions induces an isotropic volume change  $\Delta V$ . If it is assumed that the number of hydrogen atoms solved in the crystal is  $n$  and the volume occupied by one hydrogen atom is  $\Delta v$ , then the volume change caused by hydrogen atoms in the system is  $\Delta V = \Delta v \cdot n$ . At the same time, initial volume  $V$  of the crystal without hydrogen can be roughly calculated as  $V = N \cdot \Omega$ , where  $N$  is a number of metal atoms and  $\Omega$  is their volume. Thus, relative volume change caused by hydrogen absorption is  $\frac{\Delta V}{V} = c_H \cdot \frac{\Delta v}{\Omega}$ , where  $c_H = \frac{n}{N}$ . Besides, the relative volume change can be approximately expressed via the lattice parameter  $a$ , when a cubic crystal with randomly distributed interstitial hydrogen atoms is considered:

$$\frac{\Delta V}{V} = c_H \cdot \frac{\Delta v}{\Omega} \approx 3 \cdot \frac{\Delta a}{a} \quad (2.1)$$

Thus, in a first approximation, a linear relationship between the hydrogen concentration and the volume change is expected. The linear increase of the lattice parameter is experimentally verified for most metals [47]. In case, when the ratios  $\frac{\Delta v}{\Omega}$  and  $\frac{\Delta a}{a}$  are measured experimentally, the hydrogen concentration causing a known lattice expansion can be roughly estimated from the linear dependency. In case of Nb for low hydrogen concentrations ( $\alpha$ -phase) at RT, the following dependency was experimentally found [48]:

$$\frac{\Delta a}{a} = 0.058 \cdot c_H \quad \text{and} \quad \frac{\Delta V}{V} = 0.174 \cdot c_H \quad (2.2)$$

An example of the linear dependency between the Nb volume change and the hydrogen concentration in the sample measured experimentally [38] is shown in Fig. 2.3.

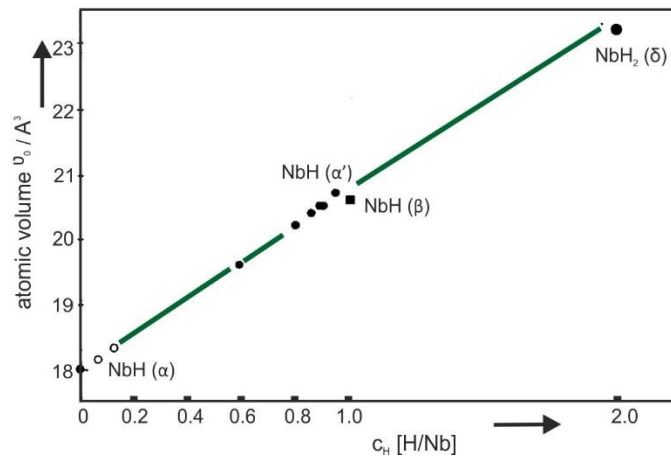


**Fig. 2.3** Volume per Nb atom  $v_0$  at about 300 K measured as a function of hydrogen concentration as determined by X-ray diffraction [38]. Reprinted from *Hydrogen in Metals II*, ed. by G. Alefeld, J. Völkl, Chapter 2, 1978, p. 13, T. Schober & H. Wenzl, Copyright 1978, with permission from Springer.

## 2.2 Epitaxial Nb (110) films grown on Al<sub>2</sub>O<sub>3</sub> (11-20) sapphire substrate

Niobium films can be epitaxially grown on Al<sub>2</sub>O<sub>3</sub> sapphire substrates. To achieve epitaxial films with flat surfaces, elevated temperatures, low deposition rates and a low surface miscut<sup>1</sup> substrate are required. The epitaxial orientation of the Nb lattice with respect to the Al<sub>2</sub>O<sub>3</sub> lattice is unique and three-dimensional. It is controlled by Al<sub>2</sub>O<sub>3</sub> crystal orientation and well defined for different Nb/Al<sub>2</sub>O<sub>3</sub> systems [27], [29], [49]. Figure 2.4 (a) represents the three-dimensional epitaxial relationship between Nb and Al<sub>2</sub>O<sub>3</sub>, shown for the (11-20) substrate orientation [28]. Hereby, the orientation relationship between the epitaxially grown Nb (110) film and the Al<sub>2</sub>O<sub>3</sub> (11-20) substrate is given by the terminating interface planes and two parallel directions in the Nb and Al<sub>2</sub>O<sub>3</sub> lattice, which lie in the Nb/Al<sub>2</sub>O<sub>3</sub> interface plane [29]:

$$\begin{aligned} \text{Nb (110)} // \text{Al}_2\text{O}_3 \text{ (11-20)}, \\ \text{Nb } \langle -11-2 \rangle // \text{Al}_2\text{O}_3 \langle -1100 \rangle, \\ \text{Nb } \langle -111 \rangle // \text{Al}_2\text{O}_3 \langle 0001 \rangle. \end{aligned}$$

Gutekunst et al. developed a model for the atomic structure of the interface [29], shown in Fig. 2.4 (b). In this model, O<sup>2-</sup> anions is approximately positioned on the regular lattice sites of an ideal hcp lattice, Al<sup>3+</sup> occupies two thirds of the octahedral sites within the hcp O<sup>2-</sup> lattice. Thus, during film deposition the Nb atoms of the first layer occupy positions of the Al-sublattice continued across the interface trying to reproduce the substrate lattice structure [28]. This kind of crystal growth resulting from the similarity

<sup>1</sup> The substrate miscut defines the angle between the geometrical surface of the substrate and its crystallographic orientation. By using substrates with a low miscut angle, atomically flat terraces with large area can be obtained

between the Nb bcc lattice and the morphological unit cell of sapphire (hcp). Hereby, according to Gutekunst et al., strong ionic bonding is predicted appearing between the O-sublattice and the Nb-lattice [29].

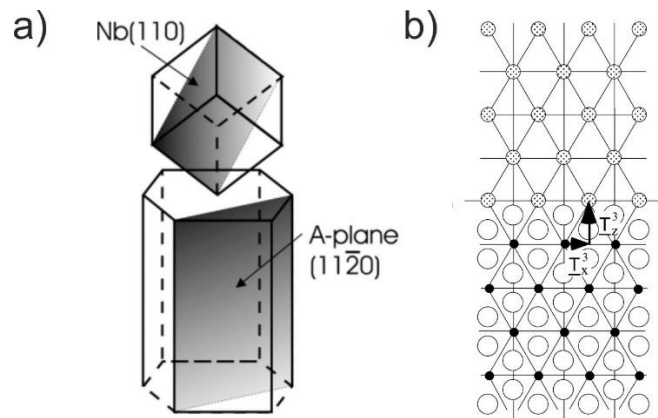


**Fig. 2.4 a)** Three-dimensional epitaxial relationship between Nb and Al<sub>2</sub>O<sub>3</sub>, shown for the (11-20) substrate orientations [28]. **b)** Model describing the atomic structure of the interface (Nb (110) || Al<sub>2</sub>O<sub>3</sub> (11-20)) developed by Gutekunst et al. [29]. The Nb atoms of the first layer exactly occupy positions of the Al-sublattice (●) continued across the interface and form a periodic structure. (○) corresponds to the O-sublattice and (●) - to the Nb-lattice. Reprinted from *Thin Solid Films*, 401, 7-34, A. Wildes, J. Mayer, K. Theis-Bröhl, *The growth and structure of epitaxial niobium on sapphire*, Copyright 2001, with permission from Elsevier. (original image (a) is cropped)

Epitaxial Nb films with the highest quality, large terraces and low surface roughness can grow on the single crystal Al<sub>2</sub>O<sub>3</sub>-substrates with a low surface miscut  $\gamma < 0.1^\circ$ . As Wildes et al. reported a small deposition/sputter rate of less than  $< 1$  nm/min is required to reveal flat surfaces [28]. Hereby, the “optimum” deposition temperature  $T_d$  is usually kept between  $750^\circ\text{C}$  and  $900^\circ\text{C}$  and can be tuned to the specific vacuum system.

For above 50 nm Nb film thickness the influence of the deposition temperature on the surface topography is known to be small when compared to thinner films, as reported by Wildes et al. and Nöthemann et al. [28], [31].  $T_d$  can be varied between  $750^\circ\text{C}$  and  $850^\circ\text{C}$  and the surface remains smooth.

For 20 nm – 50 nm epitaxial Nb films preparation meander-like “open” surface topographies or, in other words, a pitted film surface with deep holes are reported for epitaxial Nb films, under similar conditions [36] or for substrates with higher miscuts [37].

Open surface morphologies are expected to strongly affect the stress relaxation under hydrogen loading [9]. Therefore, to perform experiments on Nb thin films with defined surface conditions, the proper growth temperature has to be determined to exclude the formation of “rough” and “open” surfaces (meander-like surfaces). Thus, the desired 2D “closed” film structure has to consist of large atomically flat terraces and has a relatively smooth and reproducible surface topography. For the film thickness addressed in this thesis, an optimization of film preparation conditions is necessary before any hydrogen-related loading experiments are performed.

## 2.3 Me-H thin film system: general findings

### 2.3.1 Difference between “bulk” and “thin film” Me-H system

Many differences between the physical properties of Me-H bulk systems and Me-H thin film systems of similar composition arise from the different microstructure and the necessity of stabilization [9], [14]. Herewith, a significant role may play the anisotropy of the elastic properties resulting from the boundary conditions, when the system dimension is reduced. Furthermore, high mechanical stresses in the GPa range may arise in the film upon hydrogen loading [9], [13], [30], [50], [51] that might change the system quite a lot.

Mechanical stress is known to affect many materials properties such as the chemical potential [9], [52], or the width of a semiconductor band gap [53]. For binary systems, mechanical stress might influence the thermodynamic properties [75]: it changes the solubility limits [13]; it reduces the critical temperature of a miscibility gap between two adjacent phases [54], [55]; it modifies the hydrogen-hydrogen interaction energy ( $\epsilon_{HH}$ ) [56], [57], [58] or widens the hysteresis area appearing during a phase transition [59]. Besides, high mechanical stress can also destabilize otherwise stable hydrides by about -1.1 kJ / (mole H) per GPa of stress, as shown by Wagner et al. [56].

### 2.3.2 Intrinsic stress in films

In the as-prepared state, many films are typically exposed to intrinsic mechanical stress, which is caused by the presence of rigid substrates and local atomic lattice matching between the film and the support [60], [75]. When high temperature deposition methods are used, additional stress may also result from the different thermal expansion coefficients. Beside, additional stress may arise in the film due to the atom peening or ions forming interstitial defects for high-energy deposition methods (e.g. sputtering techniques or laser deposition methods [61]). Hereby, depending on the kinetic energy of the deposited particles and the working pressure, stress after the film preparation may even change from compressive to tensile [62], [63], [64], [65]. To summarize, this intrinsic mechanical stress resulting from particular preparation conditions, typically ranges from the MPa to the low GPa range [66] and normally should be considered among the other contributing factors affecting the film properties [75].

### 2.3.3 Interstitials-induced mechanical stress

Substantially higher mechanical stresses arise, when the metal films are loaded with interstitial atoms in the presence of strong adhesion between the film and the substrate [75]. The mechanical stress

limit arising from pure elastic behavior of hydrogen-loaded films bonded to rigid substrates can be calculated by using the theory of linear elasticity [9], [13], [75].

## 2.4 Nb-H thin film system

### 2.4.1 Linear elastic theory on hydrogen-loaded thin Nb films clamped to a rigid substrate

Dissolved hydrogen atoms induce volume expansion, as discussed in chapter 2.1.3. Herewith, in case of bulk M-H system isotropic expansion  $\epsilon_o$  appears. In contrast, in case of thin film ideally clamped to the substrate, the expansion becomes anisotropic due to the boundary conditions.

Theory: The biaxial compression model for the expansion of a hydrogen absorbing film is given in Fig. 2.5. Stress and strain of a film in the ideally fixed state can be calculated by doing a Gedanken experiment [13], [67] of compressing a freely expanded metal film onto the size of the rigid substrate layer. This is shown in Fig. 2.5. In Fig. 2.5 (a) the film is separated from the substrate, allowed to freely expand in all the directions ( $\epsilon_{xx} = \epsilon_{yy} = \epsilon_{zz} = \epsilon_o$ ) upon hydrogen loading and assumed to be completely free of stress ( $\sigma_x = \sigma_y = \sigma_z = 0$ ). Then, to satisfy the boundary conditions of the film clamped on the substrate (Fig. 2.5 (b)), the hydrogen loaded film should be compressed to the initial lateral sizes ( $\Delta\epsilon_{xx} = \Delta\epsilon_{yy} = -\epsilon_o$ ). Hereby, the direction oriented normally to the film surface is kept free of stress ( $\sigma_{zz} = 0$ ). The presence of the rigid substrate leads to an appearance of compressive biaxial stress state in lateral directions [13]. Due to the Poisson response it, furthermore, leads to an additional out-of-plane expansion  $\Delta\epsilon_{zz}$  [67], [68], upon hydrogen loading (Fig. 2.5 (c)).

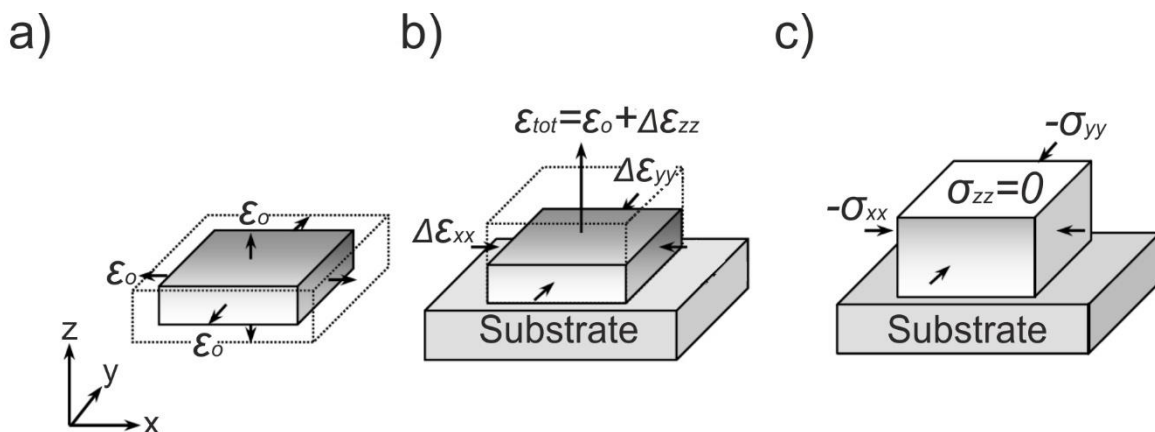


**Fig. 2.5** Sketch on calculation of stress and strain using theory of linear elasticity [67]. **(a)** The free sample expands in all three directions by  $\epsilon_o$  upon hydrogen absorption. **(b)** For the fixed film, in lateral directions this expansion has to be inverted,  $\Delta\epsilon_{xx} = \Delta\epsilon_{yy} = -\epsilon_o$ . Via converse contraction, the lattice additionally expands in vertical direction by  $\Delta\epsilon_{zz}$ . **(c)** Strong out-of-plane expansion and compressive mechanical stress arise upon hydrogen loading in the thin Me-H film fixed on the substrate. Reprinted from *Hydrogen in Metals*, R. Kirchheim & A. Pundt, In D.E. Laughlin, K. Hono (Eds.), *Physical Metallurgy*, 2014, p. 2665, Copyright 2014, with permission from Elsevier.

Hydrogen-induced elastic lattice expansion and mechanical stress can be calculated by using the theory of linear elasticity [69]. Hereby, in the elastic regime, Hooke's law defines the relationship between stress and strain:

$$\sigma_{ij} = C_{ijkl}\varepsilon_{kl} \quad (2.3)$$

with the fourth rank tensor of elasticity  $C_{ijkl}$ , also named elastic stiffness tensor, that generally couples the strain matrix  $\varepsilon_{kl}$  with the stress matrix  $\sigma_{ij}$ . The subscripts  $i, j, k, l$  run from 1 to 3. Usually fourth rank tensors contain  $3^4 = 81$  components, but in case of cubic structure due to the symmetry, only three independent elastic constants  $C_{11}, C_{12}, C_{44}$  are needed to describe the elastic properties of the system. Thus, the number of components in tensor of elasticity can be reduced to 36 ( $6^2=36$  [70]) that significantly simplifies the calculation process. For convenience, we will consider the stress-strain relationship on the crystal directions. Hereby, the presentation of Hooke's law in Voigt notation rather than the matrix notation ( $xx \rightarrow 1; yy \rightarrow 2; zz \rightarrow 3; xy (yx) \rightarrow 4; xz (zx) \rightarrow 5; yz (zy) \rightarrow 6$ ) can be used. It is more practical, specifically, if there is no shear strain assumed to occur in the system ( $\varepsilon_4, \varepsilon_5, \varepsilon_6 = 0$ ):

$$\sigma_{\alpha} = C_{\alpha\beta}\varepsilon_{\beta} \quad (2.4)$$

This representation of Hooke's law includes the six-component stress vectors  $\sigma_{\alpha}$  and  $\varepsilon_{\beta}$  and the quadratic matrix of elasticity  $C_{\alpha\beta}$ . For cubic systems,  $C_{\alpha\beta}$  is given by:

$$C_{\alpha\beta}^{Cub} = \begin{pmatrix} C_{11} & C_{12} & C_{12} & 0 & 0 & 0 \\ C_{12} & C_{11} & C_{12} & 0 & 0 & 0 \\ C_{12} & C_{12} & C_{11} & 0 & 0 & 0 \\ 0 & 0 & 0 & C_{44} & 0 & 0 \\ 0 & 0 & 0 & 0 & C_{44} & 0 \\ 0 & 0 & 0 & 0 & 0 & C_{44} \end{pmatrix} \quad (2.5)$$

Further, for describing the system, the expression for the elastic energy density  $f_{el}$  as a function of the elements of the elastic stiffness tensor  $c_{ijkl}$  and the symmetric strain tensors  $\varepsilon_{ij}$  and  $\varepsilon_{kl}$  are required. In common case it is given by [69]:

$$f_{el} = \frac{1}{2} \cdot C_{ijkl} \cdot \varepsilon_{ij} \cdot \varepsilon_{kl} \quad (2.6)$$

and, in Voigt notation, particularly, for cubic structure is equal to [67]:

$$f_{el} = \frac{1}{2} \cdot C_{11}(\varepsilon_1^2 + \varepsilon_2^2 + \varepsilon_3^2) + C_{12}(\varepsilon_1\varepsilon_2 + \varepsilon_2\varepsilon_3 + \varepsilon_1\varepsilon_3) + \frac{1}{2}C_{44}(\varepsilon_4^2 + \varepsilon_5^2 + \varepsilon_6^2) \quad (2.7)$$

In order to calculate the stress, the (110)-orientation requires that the appropriate tensor transformation is performed, as one of the orthogonal in-plane directions does not coincide with a crystal axis [71]. Therefore, the internal coordinate system of the crystal needs to be correlated to the external coordinate system of the film and the substrate by use the transformation matrix ( $a_{ij}$ ). The strain in the internal coordinate system ( $\varepsilon_{ij}$ ) can be linked with a strain in the external coordinate system ( $\varepsilon'_{mn}$ ) in the following way:

$$\varepsilon_{ij} = a_{mn}^T \cdot \varepsilon'_{mn} \cdot a_{jn} \quad (2.8)$$

Because the bcc-films usually grow (110) oriented, the external z-direction correlates with the [110] internal crystallographic direction. Thus, rotations by  $\phi = -90^\circ$  around the x-axis and afterward by  $\theta = -135^\circ$  around the reoriented z-axis give the new external coordinates  $x', y', z'$  in [1-10], [001] and [110] crystallographic orthogonal directions as it is shown in Fig. 2.6 [67].

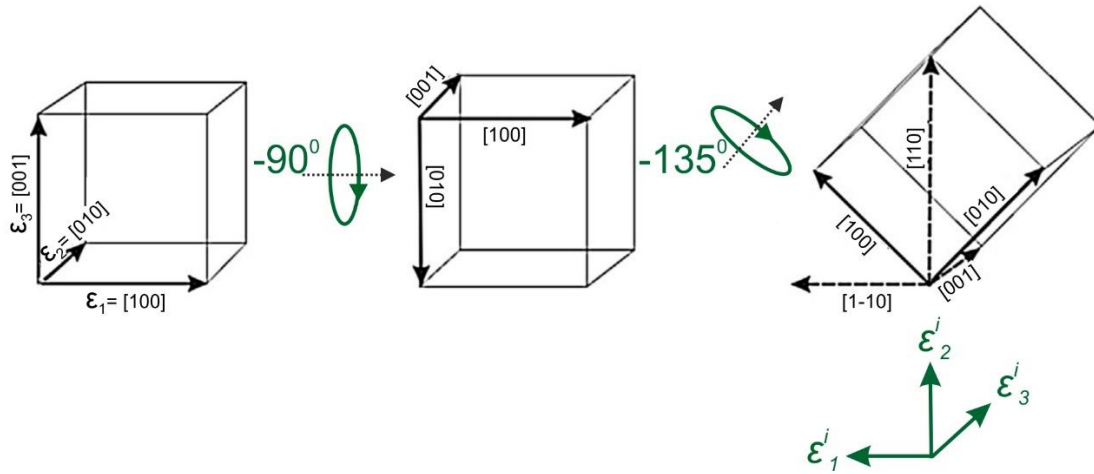


**Fig. 2.6** Sub-rotations required for (110)-oriented films to correlate the internal coordinate system of the crystal to the external coordinate system of the film:  $\phi = -90^\circ$  around the x-axis and afterward by  $\theta = -135^\circ$  around the reoriented z-axis gives the new external coordinates  $x', y', z'$  in [1-10], [001] and [110] crystallographic directions [67].

To obtain the transformation matrix that is required to link the two coordinate systems, multiplication of two rotation matrixes (rotation around the x-axis and z-axis) has to be performed:

$$a_{ij} = \begin{pmatrix} 1 & 0 & 0 \\ 0 & \cos \varphi & -\sin \varphi \\ 0 & \sin \varphi & \cos \varphi \end{pmatrix} \cdot \begin{pmatrix} \cos \theta & -\sin \theta & 0 \\ \sin \theta & \cos \theta & 0 \\ 0 & 0 & 1 \end{pmatrix} \quad (2.9)$$

For  $\phi = -90^\circ$  and  $\theta = -135^\circ$  rotation this gives:

$$\alpha_{ij} = \begin{pmatrix} 1 & 0 & 0 \\ 0 & 0 & 1 \\ 0 & -1 & 0 \end{pmatrix} \cdot \begin{pmatrix} -\frac{1}{\sqrt{2}} & \frac{1}{\sqrt{2}} & 0 \\ \frac{1}{\sqrt{2}} & -\frac{1}{\sqrt{2}} & 0 \\ 0 & 0 & 1 \end{pmatrix} = \begin{pmatrix} -\frac{1}{\sqrt{2}} & \frac{1}{\sqrt{2}} & 0 \\ 0 & 0 & 0 \\ \frac{1}{\sqrt{2}} & \frac{1}{\sqrt{2}} & 0 \end{pmatrix} \quad (2.10)$$

At this state, by substitution the transformation matrix Eq. (2.10) in Eq. (2.8), the tensor transformation for the strain can be performed and therewith, the strain in the internal coordinate system can be expressed via a strain given in the external coordinate system:

$$\varepsilon_{ij} = \begin{pmatrix} \frac{1}{2}\varepsilon'_1 + \frac{1}{2}\varepsilon'_3 & -\frac{1}{2}\varepsilon'_1 + \frac{1}{2}\varepsilon'_3 & 0 \\ -\frac{1}{2}\varepsilon'_1 + \frac{1}{2}\varepsilon'_3 & \frac{1}{2}\varepsilon'_1 + \frac{1}{2}\varepsilon'_3 & 0 \\ 0 & 0 & \varepsilon'_2 \end{pmatrix} \quad (2.11)$$

Thus, the elastic energy density in dependence on the strain, given in the sample (external) coordinate system can be obtained by combining Eq. (2.7) and Eq. (2.11):

$$f_{el} = \frac{1}{4}C_{11}(\varepsilon_1'^2 + 2\varepsilon_2'^2 + 2\varepsilon_1'\varepsilon_3' + \varepsilon_3'^2) + \frac{1}{4}C_{12}(\varepsilon_1'^2 + 2\varepsilon_1'\varepsilon_3' + 4\varepsilon_1'\varepsilon_2' + 4\varepsilon_3'\varepsilon_2') + \frac{1}{2}C_{44}(\varepsilon_3'^2 - 2\varepsilon_3'\varepsilon_1' + \varepsilon_1'^2) \quad (2.12)$$

The stress  $\sigma'_i$  in external coordinates in a certain direction by definition is given by the strain derivative of the free energy density:

$$\sigma'_i = \frac{\partial f_{el}}{\partial \varepsilon'_i} \quad (2.13)$$

For the derivative in z - direction that corresponds to  $\varepsilon'_3$  in the sample coordinate system, by applying the condition of free expansion assumed in Fig. 2.5 ( $\frac{\partial f_{el}}{\partial \varepsilon_3} = \sigma_{zz} = \sigma_3 = 0$ ) we can obtain the expression for the additional vertical strain ( $\Delta\varepsilon_{zz}$ ) suggested in the one-dimensional linear elastic model:

$$\Delta\varepsilon_{zz} = \varepsilon'_3 = -\frac{(C_{11} + C_{12} - 2C_{44})\varepsilon'_1 + 2C_{12}\varepsilon'_2}{(C_{12} + C_{11} + 2C_{44})} \quad (2.14)$$

Further, an assumption of biaxial strain ( $\varepsilon'_1 = \varepsilon'_2 = -\varepsilon_0$ ) allows to calculate the total vertical strain of a Nb (110) film ideally clamped on the rigid substrate. According to the one-dimensional linear elastic model, the total vertical strain  $(\varepsilon_{zz})_{total}$  appearing due to the hydrogen absorption is given by:

$$(\varepsilon_{zz})_{total} = \varepsilon_o + \Delta\varepsilon_{zz} = \varepsilon_o + \frac{C_{11} + 3C_{12} - 2C_{44}}{C_{11} + C_{12} + 2C_{44}} \cdot \varepsilon_o \quad (2.15)$$

Finally, when the  $\varepsilon'_3$  is expressed in terms of  $\varepsilon_o$ , the biaxial in-plane stress  $\sigma_1$  and  $\sigma_2$  arising at the interface between the film and the substrate can be calculated. This stress corresponds to  $[1\bar{1}0]$  and  $[001]$  crystallographic orientation and is given by:

$$\sigma'_{1=[1\bar{1}0]} = \frac{\partial f_{el}}{\partial \varepsilon'_1} = \frac{4(C_{11} + C_{12})C_{44}\varepsilon'_1 + 4C_{12}C_{44}\varepsilon'_2}{C_{11} + C_{12} + 2C_{44}} \quad (2.16)$$

$$\sigma'_{2=[001]} = \frac{\partial f_{el}}{\partial \varepsilon'_2} = \frac{4C_{12}C_{44}\varepsilon'_1 + (C_{11}^2 - 2C_{12}^2 + C_{11}(C_{12} + 2C_{44}))\varepsilon'_2}{C_{11} + C_{12} + 2C_{44}} \quad (2.17)$$

For the same biaxial expansion ( $\varepsilon'_1 = \varepsilon'_2 = -\varepsilon_o$ ), by substituting the known linear dependence

$\varepsilon_o = 0.058 \cdot c_H$  [48] and Nb bulk elastic stiffness constants  $C_{11} = 247.4 \text{ GPa}$ ,  $C_{12} = 133.6 \text{ GPa}$ ,  $C_{44} = 28$  [72] in Eq. (2.16) and Eq. (2.17) the corresponding mechanical stress can be calculated:

$$\sigma'_{1=[1\bar{1}0]} = \frac{\partial f_{el}}{\partial \varepsilon'_1} = -4 \frac{(C_{11} + 2C_{12})C_{44}}{C_{11} + C_{12} + 2C_{44}} \varepsilon_o = -7.6 \cdot c_H \quad (2.18)$$

$$\sigma'_{2=[001]} = \frac{\partial f_{el}}{\partial \varepsilon'_2} = -\frac{2(C_{11} + 2C_{12})C_{44} + C_{11}^2 + C_{11}C_{12} - 2C_{12}^2}{C_{11} + C_{12} + 2C_{44}} \varepsilon_o = -11.6 \cdot c_H \quad (2.19)$$

Thus, in the elastic regime, upon hydrogen loading of Nb thin film, compressive stresses between  $-11.6 \text{ GPa} / c_H$  and  $-7.6 \text{ GPa} / c_H$  are expected. Depending on the crystallographic direction, in that the stress measurements are performed, the obtained stress value may vary, as it is shown in Fig. 2.7. Hereby, the average stress is expected to be about:  $\langle \sigma' \rangle = -9.6 \cdot c_H$  [35].

Figure 2.8 represents the calculation results of elastic modulus and the Poisson's ratio within  $(110)$  – plane of a Nb (bcc) crystal, as given by Nörthemann [73]. It explains the direction-dependent stress development shown in Fig. 2.7.

Thus, for the special case of pure elastic response of a film an extremely high stress state with  $-10 \text{ GPa}$  at  $c_H = 1 \text{ H/Nb}$  can be theoretically achieved. Thus, to summarize, if we find the proper experimental conditions, at that stress release is completely suppressed in thin epitaxial Nb-H film upon hydrogen loading to  $c_H = 1 \text{ H/Nb}$ , ultrahigh stress of about  $-10 \text{ GPa}$  is expected to arise in the linear elastic

regime [74], [75]. Besides, pure one-dimensional vertical film expansion should be observed in this situation.

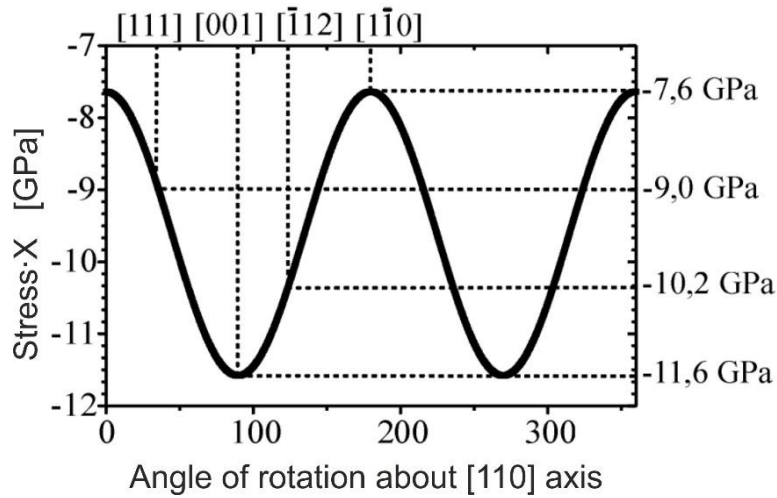


**Fig. 2.7** Dependence between the in-plane stress and crystallographic directions in the Nb film ideally clamped on the rigid substrate. Adapted from M. Dornheim [35].

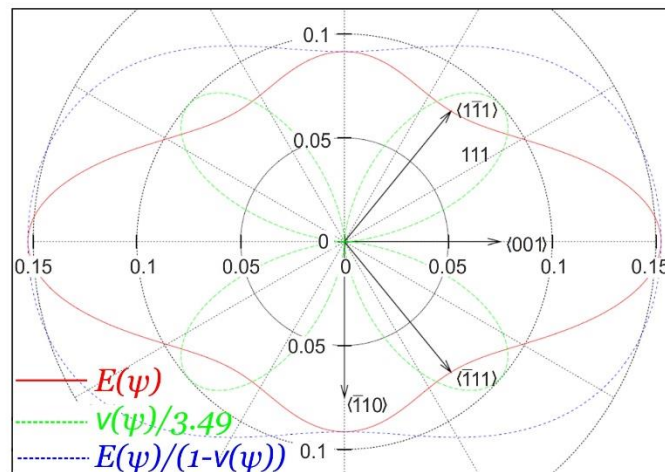


**Fig. 2.8** The calculation results of elastic modulus and the Poisson's ratio in the (110) plane of Nb. Adapted from K. Nörthemann [73] with permission.

### 2.4.2 Hydrogen induced lattice expansion in thin Nb-H films

The total out-of-plane strain contains the bulk strain  $\varepsilon_o$  and the additional term  $\Delta\varepsilon_{zz}$ . It is generated by the imposed transverse contraction and, as it was mathematically derived in the previous section in Eq. 2.15:

$$(\varepsilon_{zz})_{total} = \varepsilon_o + \Delta\varepsilon_{zz} = \varepsilon_o + \frac{C_{11} + 3C_{12} - 2C_{44}}{C_{11} + C_{12} + 2C_{44}} \cdot \varepsilon_o \quad (2.20)$$

where  $C_{ij}$  is the elastic stiffness constants of the bulk material.

By using the model of ideal one-dimensional straining, the expected hydrogen induced vertical expansion, occurring in the thin Nb-H film, can be calculated. As it was already mentioned, for the bulk Nb-H system, the linear relationship between the strain and the hydrogen concentration is given by  $\varepsilon_o = 0.058 \cdot c_H$  [48]. Thus, by substituting the Nb bulk elastic stiffness constants ( $C_{11} = 247.4 \text{ GPa}$ ,  $C_{12} = 133.6 \text{ GPa}$ ,  $C_{44} = 28 \text{ GPa}$  [72]) the total vertical expansion in case of thin Nb-H film clamped on the rigid substrate according to the theory of linear elasticity is assumed to be:

$$(\varepsilon_{zz})_{total} = \frac{\Delta z}{d_o} = 0.136 \cdot c_H \quad (2.21)$$

where  $\Delta z$  is the film expansion in the vertical directing and  $d_o$  is an original film thickness. Thus, in case of a Nb-H thin film, if it is compared to the bulk Nb-H sample, significantly higher vertical expansion is expected. Moreover, if there is a local hydrogen concentration gradient present in the sample (e.g. by phase separation), the amplitude of relative film expansion caused by a difference in the local hydrogen concentration can be estimated by use the following equation:

$$\Delta z_{rel} = 0.136 \cdot \Delta c_H \cdot d_o \quad (2.22)$$

Based on Eq. (2.22), Table 2.1 gives the estimated film expansions  $\Delta z_{rel}$  expected for different  $\Delta c_H$  (ranging from 0.6 H/Nb to 0.1 H/Nb) and different film thickness  $d_o$  (ranging from 100 nm to 5 nm).

**Table 2.1** Nb film expansion  $\Delta z_{rel}$  upon different hydrogen concentrations  $\Delta c_H$ . All expansion values are given in units of nm.

Thickness [nm]	$\Delta c_H$ [H/Nb]					
	0.6	0.5	0.4	0.3	0.2	0.1
100	8.16	6.80	5.44	4.08	2.72	1.36
70	5.71	4.76	3.81	2.86	1.90	0.95
55	4.49	3.74	2.99	2.24	1.50	0.75
40	3.26	2.72	2.18	1.63	1.09	0.54
25	2.04	1.70	1.36	1.02	0.68	0.34
15	1.22	1.02	0.82	0.61	0.41	0.20
8	0.65	0.54	0.44	0.33	0.22	0.11
5	0.41	0.34	0.27	0.20	0.14	0.07

The one-dimensional strong linear film expansion was experimentally confirmed for Nb-H films in initial H-loading stages. In case of a polycrystalline 190 nm Nb film, the predicted linear out-of-plane expansion was found up to  $c_H = 0.08 \text{ H/Nb}$ . In case of an epitaxial Nb film, an almost linear dependency with a slight deviation was confirmed up  $c_H = 0.05 \text{ H/Nb}$  [13], [25]. At higher hydrogen concentrations, the

system tries to reduce the stress arising in the film and, therefore, deforms plastically. At this loading stage, the out-of-plane lattice expansion is non-linearly coupled to the hydrogen concentration and, hence, deviation from the one-dimensional linear behavior can be observed. An example of strain measurements performed by Laudahn et al. [13] is shown in Fig. 2.9 (a, b).  $X_H$  gives the average hydrogen concentration ( $c_H = X_H$ ) achieved in the sample by electrochemical hydrogen loading. In Fig. 2.9 (a), the Nb (110) peak shifts to lower angles and splits up with increasing hydrogen concentration due to the phase separation occurring in the concentration range  $0.06 H/Nb \leq c_H \leq 0.7 H/Nb$ . From the peak position corresponding to the Nb-H  $\alpha$ -phase region ( $2\theta \approx 38.5^\circ$ ), Laudahn et al. calculated the strain as a function of  $c_H$ . [13] (Fig. 2.9 (b)). As it can be seen, a slight deviation from the dashed line predicted by one-dimensional expansion is visible.

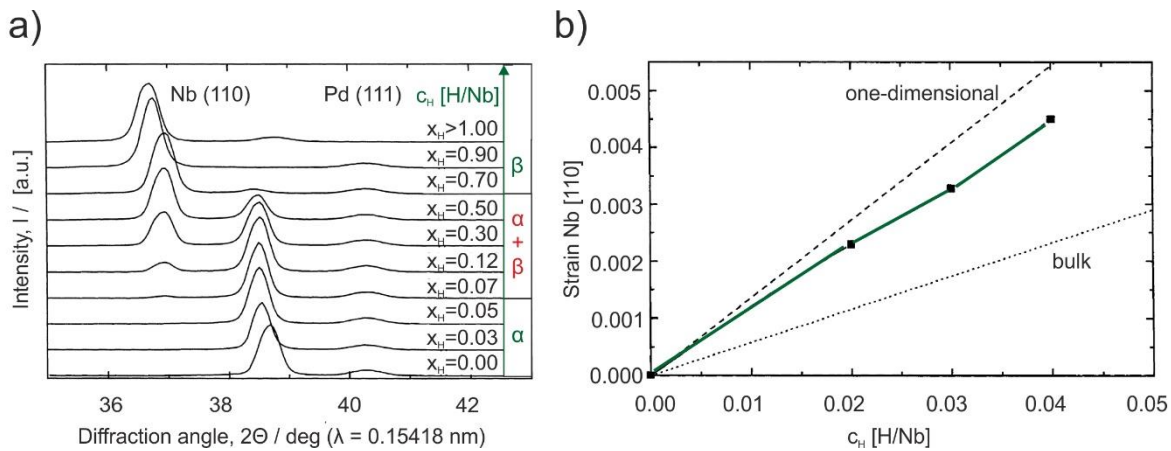


**Fig. 2.9 a)** XRD pattern measured during electrochemical hydrogen loading in the 189 nm epitaxial Nb film ( $\lambda = 0.15418$  nm). [13]  $X_H$  gives the average hydrogen concentration. The Nb (110) peak shifts to lower angles and splits up with increasing hydrogen concentration. Thus, two peaks corresponding to  $\alpha$ -phase and  $\beta$ -phase volume fractions are visible in the concentration range corresponding to the two-phase region ( $\alpha + \beta$ ). The film is protected with a 30 nm Pd top layer **b)** The measured lattice strain initially behaves almost one-dimensional, when only Nb-H  $\alpha$ -phase is present in the system. Reprinted from *J. Alloys. Comp.* 293-295, 490, *Hydrogen induced stresses in Nb single layers*, U. Laudahn, A. Pundt, M. Bicker, U. v. Hülsen, U. Geyer, T. Wagner, R. Kirchheim, Copyright 1999, with permission from Elsevier. (" $\alpha$ ", " $\alpha + \beta$ ", " $\beta$ ", " $c_H$  [H/Nb]" in Fig. 2.9 (a) are added by author of this PhD thesis)

### 2.4.3 Plastic deformation at the film/substrate interface upon H-absorption

For Nb films deposited on  $Al_2O_3$ , Grier et al. determined a critical thickness of 7.2 nm for the formation of intrinsic misfit dislocations between the film and the substrate, immediately after film deposition and without any hydrogen contribution [49], [75]. Above this film thickness, dislocations may occur in the Nb films. For the as prepared 100 nm, epitaxial Nb films grown on  $Al_2O_3$  (11-20) sapphire substrates (miscut  $< 0.1^\circ$ , deposition at  $T_d = 800^\circ C$ ), Nörthemann reported on a dislocation density of about  $7.1(6) \cdot 10^{10} \text{ cm}^{-2}$  which relates to a mean distance  $\approx 38$  nm.

Following the equilibrium theory of misfit dislocation formation of Mathews and Blakeslee [76], [77], [78], van der Merwe [79], [80], or Jain et al. [53], gives a critical yield thickness  $d^*$  for strained epitaxial

film growth above which dislocations are inserted at the film / substrate interface to accommodate for the strain between the film and the substrate. The total energy density of the system  $\xi_{tot}$  mainly contains the elastic energy density  $\xi_{el} = M \cdot d \cdot \varepsilon^2$  that builds up during film growth and the self-energy density of edge dislocations [81]:

$$\xi_{disl} = \frac{Gb^2}{4\pi(1-\nu)} \frac{2}{L} \ln\left(\frac{\beta d}{r_c}\right) \quad (2.23)$$

which are introduced in periodic distances  $L$ .  $G$  is the shear modulus,  $\nu$  is Poisson's ratio,  $b$  is Burgers vector and  $r_c$  is the radius of the dislocation core which is often set to  $r_c = b$ .  $\beta$  is a numerical constant in the order of one. When dislocations with Burgers vector,  $b$ , and spacing,  $L$ , are formed, the remaining homogeneous strain in the film is  $(\varepsilon - b/L)$  and, hence, the corresponding strain energy is reduced. Thereby, the total energy density of thin films containing misfit dislocation can be expressed by adding two these terms [81]:

$$\xi_{tot} = M \cdot d \cdot \left(\varepsilon - \frac{b}{L}\right)^2 + \frac{Gb^2}{4\pi(1-\nu)} \frac{2}{L} \ln\left(\frac{\beta d}{r_c}\right) \quad (2.24)$$

Because the energy associated with a uniform strain depends linearly on the film thickness and the misfit dislocation related term depends logarithmically, only above a critical thickness  $d^*$  the introduction of misfit dislocation leads to a decrease in the energy of the system. Hereby, the equilibrium state of the system will be defined by the condition of energy minimization  $\left(\frac{\partial \xi_{tot}}{\partial \left(\frac{1}{L}\right)} = 0\right)$ . Thus, solving of related equation for the special case of  $\frac{b}{L} = 0$  will give a critical thickness, above which the first dislocation is introduced [81]:

$$d^* = \frac{b}{\varepsilon} \frac{1}{8\pi(1+\nu)} \ln\left(\frac{\beta d^*}{r_c}\right) \quad (2.25)$$

This theory was recently extended to M-H films [68], [75], whereby the lattice is strained by the presence of hydrogen by  $\varepsilon = \alpha_H \cdot c_H$  [47]. Thus, it was shown that the critical  $c_{H,pl}$  allowing stress release depends on the film thickness  $d$  [68], [75]:

$$c_{H,pl} = \frac{b}{\alpha_H \cdot d} \frac{1}{8\pi(1+\nu)} \ln\left(\frac{\beta d}{r_c}\right) = C_1 \cdot \frac{1}{d} \ln(C_2 \cdot d) \quad (2.26)$$

For the Nb-H system, the Burgers vector is of type  $b = 1/2\{111\}$ , and thus, with  $a = 0.330 \text{ nm}$  [82],  $|b| = 0.286 \text{ nm}$ . With  $r_c = 0.286 \text{ nm}$ ,  $\nu = 0.355$  [70] and  $\alpha_H = 0.058$  [48] this theory predicts constants  $C_1 = 1.4 \cdot 10^{-1}$  and  $C_2 = 3.5$ , in equilibrium [75]. Thus, this approach can be used to estimate the thickness dependency of solute-induced stress and the elastic to plastic deformation in thin film metal-hydrogen system. The onset hydrogen concentration for stress release is named the ‘yield concentration’  $c_Y$  (or  $c_{H,pl}$ ).

The ‘yield concentration’  $c_Y$ , was experimentally found to depend on the film thickness, as studied for Nb thin films in the range between 50 nm - 200 nm [22], [25], [35]: Thinner Nb-H films yield higher hydrogen concentrations and higher mechanical stress than thicker Nb-H films, as expected from Eq. 2.26. Reduction of the film thickness, therefore, shifts this critical concentration to high values. By lowering the film thickness, it can be expected that the critical concentration can be even shifted above  $c_H = 1 \text{ H/Nb}$  and, thus, to a value where this type of plastic deformation can be completely excluded.

#### 2.4.4 Mechanical stress release in M-H films upon hydride formation

Specifically, for M-H thin film system, dislocation formation can occur at the hydride / substrate interface [18], [20], [21], [23], [35], but, in the two phase region also at the hydride /  $\alpha$ -matrix interface [9], [19], [22] as schematically depicted in Fig. 2.10 [75].

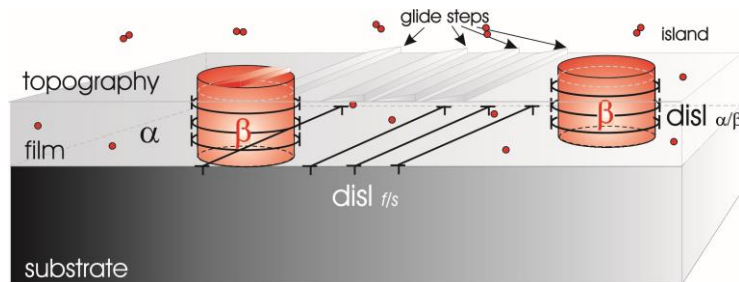


**Fig. 2.10** Schematic drawing of a thin film supported by a rigid substrate. Hydrogen absorption in the film leads to lattice expansion and, as the film is fixed to a rigid substrate, to in-plane mechanical stress. The stress can be released via dislocation formation that allow the metal atoms transfer to the film surface. Two different types of dislocations may arise. One type releases stress between the film and the substrate ( $\text{disl}_{f/s}$ ) transporting material in ramps-shape to the film surface and leaving a glide step [75]. Besides, dislocations occur when hydrides are present in the film. In this case, dislocation loops release stress arising at the interface between the  $\alpha$ -matrix and the  $\beta$ -hydride ( $\text{disl}_{\alpha/\beta}$ ), allowing the hydride to expand vertically and appear like an island elevated from the film surface [75]. Reprinted from *Appl. Phys. Lett.* 106 (2015) 243108, *Achieving reversibility of ultra-high mechanical stress by hydrogen loading of thin films*, M. Hamm, V. Burlaka, S. Wagner, A. Pundt, Copyright 2015, with the permission of AIP Publishing.

Two different types of dislocations are incorporated: 1) straight misfit dislocations elongating close to the film-substrate interface ( $\text{disl}_{f/s}$ ) or 2) extrinsic dislocation loops emitted from hydride precipitates ( $\text{disl}_{\alpha/\beta}$ ). Atomic glide steps, as traces of dislocations, appear upon hydrogen loading.

Linear glide steps were experimentally verified by in-situ STM for 50 nm epitaxial Nb-H films [73] and, recently, for 23 nm epitaxial Pd-H films [23]. Ellipsoidal terraces as traces of dislocation loops were detected for 12 nm Gd-H [18], after hydrogen loading. An example of stress release by forming misfit dislocations near the substrate-film interface visible as glide steps at the film surface reproduced from Nörthemann [73] is shown in Fig. 2.11 (a, b).

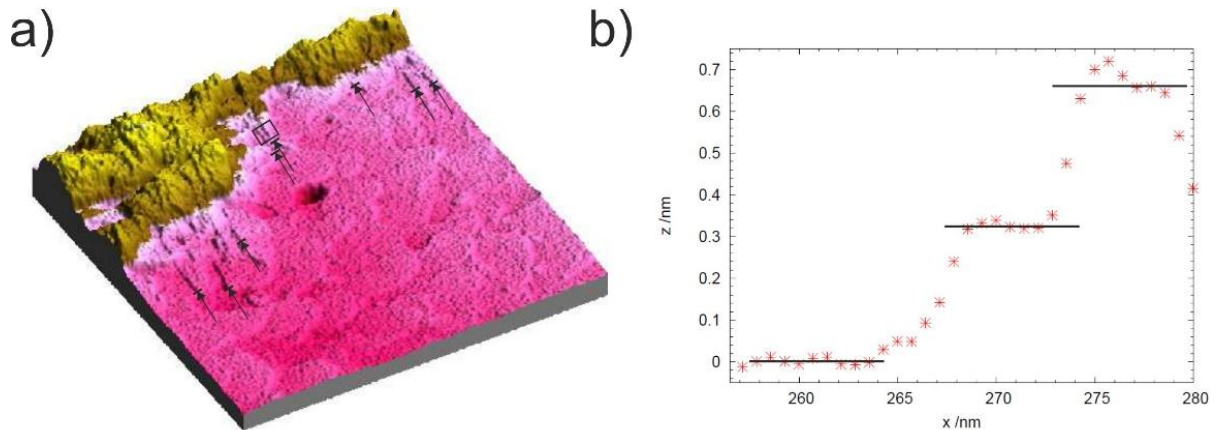


**Fig. 2.11** Emission of dislocations detected upon hydrogen loading in the epitaxial 50 nm Nb-H film. **a)** STM surface-image measured upon hydrogen loading at  $p_H \approx 1 \times 10^{-6}$  mbar (Frame size:  $500 \times 500$  nm<sup>2</sup>). The color scale chosen in the way to identify the transition area between the  $\alpha$ -phase region (pink) and the hydride  $\beta$ -phase region (yellow). Beside of that, the straight lines found near close to the  $\alpha/\beta$  interface are shown (marked with black arrows). The linear profile **(b)** measured from the area marked with a black square shows that these straight lines are the edges of atomic glide steps ( $\Delta h \approx 0.32$  (3) nm) appearing at the surface. Nörthemann interpreted them as an emission of dislocation accommodating the stress appearing upon hydrogen loading at the film/substrate interface ( $\text{disl}_{f/s}$ ). Adapted from K. Nörthemann [73] with permission.

The stress measurements performed in the past showed that above a ‘yield concentration’  $c_Y$ , mechanical stress can be released [13], [25], [83].  $c_Y$  was found to depend on the film microstructure and the film thickness [9], [13]. Noteworthy,  $c_Y$  is not linked to the solubility limit of the solid solution and, potentially, can vary in a rather broad range.

As soon as plastic deformation appears in the system, the mechanical stress build-up deviates from the linear elastic regime. Typical stress build-up for 200 nm thick Nb-H films of different microstructures [9], [84] is presented in Fig. 2.12: For higher concentrations (beyond the arrow), the increase of mechanical stress upon hydrogen uptake is reduced as compared to the theoretical prediction (‘clamped’ state). The reduction strongly depends on the microstructure of the film [9], [84]. For epitaxial films (EV<sub>900°C</sub>), stress release is most efficient and the final stress of  $-1.7$  GPa is comparably small. For nano-crystalline films (LD<sub>20°C</sub>), stress release is less efficient and the final stress reaches about  $-2.6$  GPa.

According to Eq. (2.26) for the thickness range addressed in this thesis,  $c_Y$  is expected to be shifted even stronger to very high hydrogen concentrations.

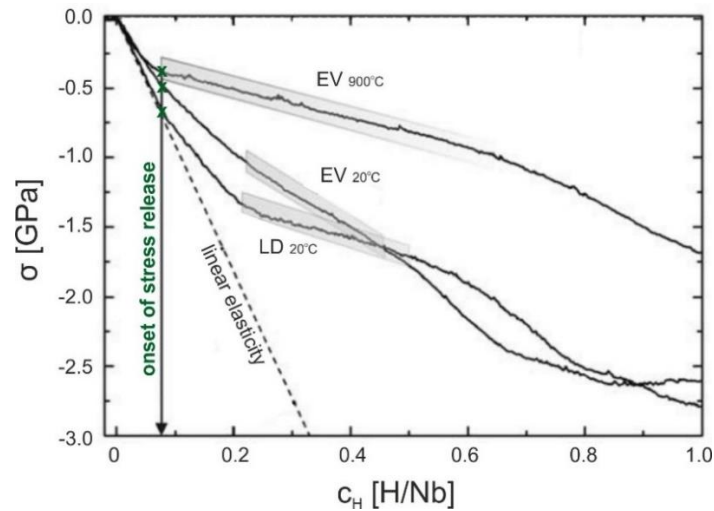


**Fig. 2.12** Mechanical stress evolving during hydrogen absorption in 200 nm Nb-films with different grain sizes  $dG$  (EV900°C: epitaxial film, EV20°C:  $dG \approx 100$  nm; LD20°C:  $dG < 20$  nm). The stress curves of all films deviate from the theory ('linear elasticity') at approximately 0.08 H/Nb (vertical arrow). Shaded areas mark the two-phase regions of the Nb-H films, as determined by additional XRD measurements [9], [84]. Stress release depends on the microstructure. Reprinted from *Annu. Rev. Mater. Res.* 36, 555-608, 2006, A. Pundt & R. Kirchheim, *Hydrogen in Metals: Microstructural Aspects*, Copyright 2006, Annual Reviews. ("linear elasticity" added by author of this thesis)

According to Nix et al., the high efficiency for stress release observed for epitaxial films, in comparison to the low stress release efficiency of nano-crystalline films, can be understood as a Hall-Petch-effect, which is applicable for thin films mechanical properties [85], [86]. In total, thin films with small grains yield higher hydrogen concentrations before plastic deformation occurs.

The next important point that should be briefly mentioned here is related to the stress development. The stress curve shown in Fig. 2.12 shows several slope changes and it was found that, for the studied film thickness, most of them relate to phase boundaries of the individual Nb-H film [84]. A similar result was also observed for Y-H films, in a very detailed study by Dornheim [87].

Besides dislocation formation, slip and formation of twins were reported in the past as a side mechanism of stress release in thinned TEM-samples. Slip upon hydrogen loading was found by Grier et al., performing HREM on Ho-H thin films [88]. For Y-H thin films, Kerssemakers et al. suggested the formation of twins, as based on a HREM study [89]. However, it should be considered that the boundary conditions for experiments on cross-sectional thinned TEM-samples differ from that of a clamped thin film. High stress states are not readily available for such samples since lateral expansion is possible. Further, twin formation might be promoted by the presence of additional surfaces in TEM-samples. Due to these reasons, TEM membranes constitute a different sample system from the clamped film system addressed here and, hence, cannot be directly compared.

Another side mechanism of stress release, namely film delimitation from the stabilizer, can be excluded for the here addressed system [17]. Nb films deposited on  $Al_2O_3$  are known for their strong adhesion [30] that prevents film delimitation, especially for the addressed film thickness.

### 2.4.5 Phase transformation in Nb-H films studied by STM

Because of the strong lattice expansion during hydride formation, hydrides can be spatially identified by their volume expansion [18], [31]. For hydrides in films, this local lattice expansion presumably occurs in out-of-plane direction and, therefore, leads to a local film surface corrugation as schematically shown in Fig. 2.13. Thereby, in films, the spatial arrangement of  $\alpha$ - and  $\beta$ -phases can be monitored by measuring the local surface changes during hydrogen loading, i.e. by in-situ STM [31], [90].

Hydride formation was recently studied by STM and in-situ gas loading for 50 nm – 200 nm thick Nb films. From a shape analysis of the surface corrugations, the hydride morphology inside of the film was deduced. This was done by comparing the experimental results to finite-element calculations performed via the COMSOL MULTIPHYSICS simulation software [91]. Physical modeling showed that the observed surface corrugations in the initial state may result only from hydride precipitates of cylindrical shape ranging through the complete film from the top to the film-substrate interface [19], [73]. This result is in a good agreement with high-resolution electron microscopy results on Nb / Pd multilayers reported by Borchers et al. [92]. Thus, in a first approximation, the fraction of the elevated surface corrugations area can be directly correlated to the volume fraction of the hydride phase. It is assumed that the chosen frame is representative for the complete film.

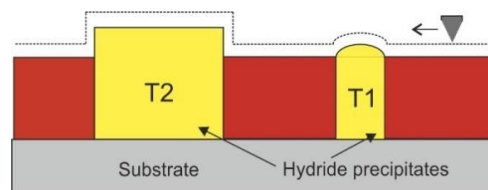


**Fig. 2.13** Sketch of surface corrugations in Nb-H films resulting from internal  $\beta$ -hydride precipitates of different morphology (“Type 1” and “Type 2”, [73]). Local lattice expansion of hydrides leads to surface corrugations that can be detected by STM-methods.

From the evolution of surface topographies measured by in-situ STM for different film thicknesses ( $d$ ) and hydrogen pressures ( $p_H$ ), Nörthemann et al. detected two types of hydride precipitates in their epitaxial Nb-H films, as summarized in Fig. 2.14 [19], [24], [73]:

1) small hydrides of cylindrical shape that are coherently linked to the  $\alpha$ -phase matrix (“Type 1”, T1). These corrugations possess very smooth borders between the  $\alpha$ - and  $\beta$ -phase related surface areas. The slope of the profile in the transition area between the  $\alpha$ -phase and the  $\beta$ -phase was found about  $2.7(0.2)^\circ$ . No glide steps (related to dislocations) are detected on the T1 topographies. From the shape of the surface corrugation it was deduced that these cylindrical hydrides are coherently linked to the  $\alpha$ -phase (see Fig. 2.14 (b)). Coherently matched cylinders were found up to a maximum radius of 30 nm - 40 nm, for a 70 nm film. The size distribution of the hydrides was found to be peaked at this maximum radius.

2) large hydrides of irregular shape with extensions exceeding 36 nm, with elongated morphologies, arranged along the elastically soft  $\{111\}$  lattice directions (“Type 2”, T2). The slope of the profile in the transition area between the  $\alpha$ -phase and the  $\beta$ -phase was found to be roughly  $9(1)^\circ$ ; the height of the upper visible part of hydrides – about 5 nm - 7 nm [73]. Linear profiles measured along hydrides of “Type 2” are exemplary shown in Fig. 2.14 (c). By the height and the shape of the upper visible part of hydride precipitates (for comparison see Fig. 2.14 (b) and Fig. 2.14 (c)) it was deduced that these hydrides are semi-coherently linked to the  $\alpha$ -phase matrix. To remind the reader, as expected from the theory of linear elasticity (see Table 2.1), for 70 nm thick films the maximum relative film expansion  $\Delta z_{rel}$  ( $\approx$  the height of the upper visible part of hydrides) for  $\Delta c_H \sim 0.4 \div 0.5$  should lie between 3.81 nm and 4.76 nm. Thus, according to Fig. 2.14 (c) the experimentally measured value exceeds the theoretical one.

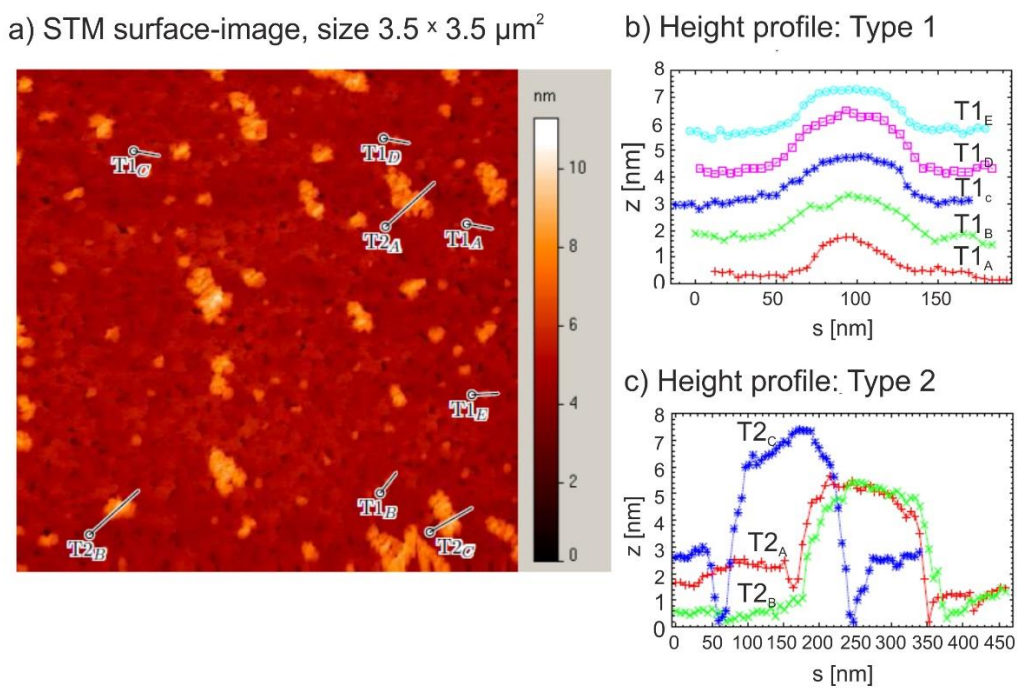


**Fig. 2.14** Different kind of precipitates of hydride phase observed in a 70 nm Nb-H film [73]. In (a) the STM surface-image of a 70 nm Nb-H film obtained during hydrogen loading at  $p_H = 1 \times 10^{-6}$  mbar for  $t_e = 62$  min (Image size:  $3.5 \times 3.5 \mu\text{m}^2$ ). Bright elevated areas corresponds to the locally growing precipitates of the hydride phase. From this topographic image, the line-profiles of different kind of precipitates were measured. The profiles from precipitates of “Type 1” are shown in (b). The slope of the profile in the transition area between the  $\alpha$ -phase and the  $\beta$ -phase was found about  $2.7(0.2)^\circ$ . The profiles from precipitates of “Type 2” are shown in (c). The measured slope in the transition area is  $9(1)^\circ$ . Adapted from K. Nörthemann [73] with permission.

Since semi-coherency implies the presence of dislocations, it was argued that above a certain hydride volume the elastic strain energy of the system exceeds the energy of formation of one dislocation and, therefore, enables dislocation formation. Thus, it was supposed that once a dislocation is generated, the hydride can freely grow [24]. However, before the nucleation barrier for dislocation formation is overcome, the hydrides were found to be “locked-in size” by the arising elastic strain energy [19], [24].

From the detailed analysis of location and growth of different precipitates, it was suggested that T1-related hydrides are precursors of T2-related hydrides [24], [73]. Finally, it was shown that T1 topographies evolve completely differently as compare to T2 topographies: They always show a reduced height compared to the T2 topographies and their surface roughness is similar to that of the original film surface.

## 2.4.6 Calculation on the critical size: coherent and semi-coherent phase transformation

To understand the origin of T1 topographies and confirm the theory about the “locked-in size” coherent precipitates, finite element method (FEM) calculations were performed on hydride precipitates with different lateral sizes and for different film thicknesses of Nb. The focus was set on shapes with circular surface topography. Nörthemann et al. calculated the critical precipitate size separating the coherent and the semi-coherent hydrides (T1→T2), by comparing the elastic energies for a coherent cylindrical hydride in a Nb-film, as calculated by FEM calculations (Fig. 2.15), with the self-energy of a dislocation loop  $E_{loop}(r)$ , in order to determine  $E_{loop}(r)$ , Nörthemann modified [19], [73] the approach of Kroupa et al., who calculated the deformation energy of a circular intrinsic dislocation loop in an unlimited isotropic medium [93]. Further, in the frame of the calculation, it was assumed that the elastic strain energy is accumulated inside the cylindrical precipitate with a radius  $r$  and height  $d$  [19]. The related result is schematically shown in Fig. 2.16 [19].

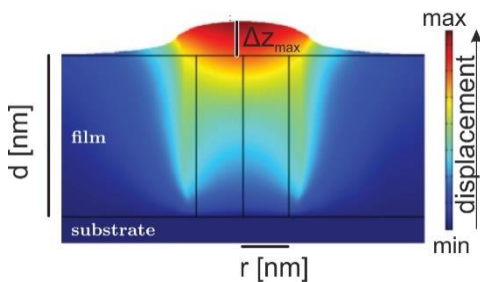


**Fig. 2.15** Example of FEM-calculations on a coherently matched cylindrical Nb-hydride in a Nb-matrix. The film expansion (displacement) is shown in color-scale. Adapted from K. Nörthemann [73] with permission.

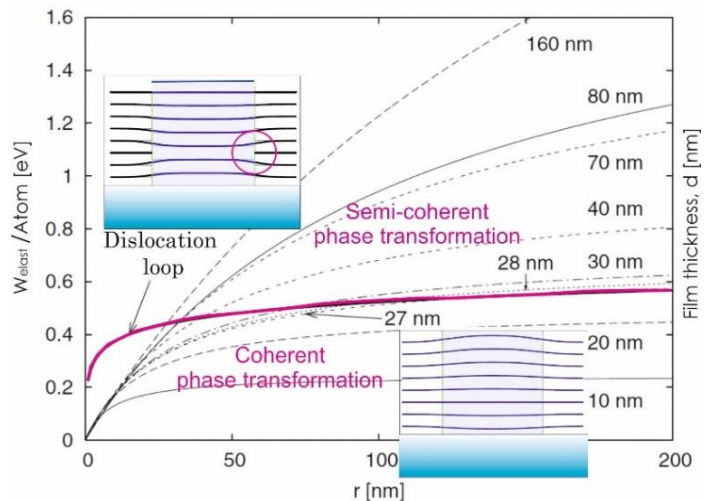


**Fig. 2.16** Elastic energy of coherent cylindrical precipitates in films of different thicknesses, as calculated by FEM. Also implemented is the calculated self-energy of one dislocation loop that crosses the curves at the radius  $r_{crit}$ .  $r_{crit}$  gives the precipitate size above which dislocation implementation is energetically favourable. It depends on the film thickness. For films thinner than  $26.3 \pm 0.2$  nm, the curves do not cross each other. Data originally published by K. Nörthemann et al. [19].

Figure 2.16 gives the elastic strain energy (per interface atom) for different precipitate sizes and for different film thickness ranging from 10 nm to 160 nm. Beside the self-energy of a dislocation loop calculated for different precipitate radii  $r$  is shown. By considering the energy difference between the elastic strain energy and the dislocation loop self-energy shown in Fig. 2.16, Nörthemann et al. made a prediction about a critical film thickness below which the transformation from T1 (coherent) to T2 (semi-coherent) type of precipitates should not appear any more. They calculated the film thickness  $d_{cr} = 26.3 \pm 0.2 \text{ nm}$  for Nb-H, which gives the threshold value where the dislocation loop self-energy curve does never exceed the elastic strain energy curve in Fig. 2.16 [19]. In other words, resulting from these calculations, for Nb thin films below a film thickness  $d_{cr} < 26.3(0.2) \text{ nm}$ , Nörthemann et al. suggested the formation of dislocations at the hydride-matrix interface to be energetically not favorable (see Fig. 2.16) [19], and, for films of about  $d_{cr}$ , the critical precipitate size strives to infinity. Thus, below the critical film thickness no dislocations are expected to form between the  $\alpha$ -matrix and the hydride precipitate within the full concentration range of the two-phase region of the thin film system. This accounts for any precipitate size. It is important to note, that in his simplified model Nörthemann did not implement the effect of stress release at the film / substrate interface as well as the integration of neighboring hydride precipitates at the late stage of sample loading, in the FEM simulation.

Recently, Kumar et al. used similar argumentation in his calculation concerning the problem of coherent precipitation (spherical  $\gamma$ Fe precipitates in Cu-2 wt. % Fe matrix) with respect to the achievement of a critical size [94]. However, the theoretical prediction of Nörthemann et al. derived for Nb-H films has not yet been proven experimentally.

It should be noted that Nb-H thin films of comparable film thickness have been studied at elevated temperatures and in a different decomposition regime in the past [32], [33], [34]. However, the target of the actual study, namely the region of phase separation and coherent hydride precipitates, were not investigated in the related works. In-situ hydrogen gas loading XRD and low-angle neutron reflectivity studies on epitaxial Nb-H thin films of different film thickness performed at the Ludwig - Maximilians University (Munich) [33], [34] focused on the temperature region above the critical temperature (171 °C for Nb-H bulk, compare Fig. 2.2). Edelman [33] and Schmid [34] reported on irreversible structural changes, on the formation of dislocations in Nb-films and on irreversible surface roughening for the film thickness of 22 nm - 26 nm, even in the concentration range of the single-phase region. Contrary to this, for the case of a 26 nm epitaxial Nb-H thin film, Song et al. reported almost full coherency even after cyclic hydrogen loading at 200 - 300 °C, in his measurements of pressure-strain isotherms [95]. These different data interpretations strongly show how sensitive the results depend on the experimental parameters and techniques chosen to address the topic of coherency conservation.

First hints on the absence of dislocation loops around hydrides in thin films were recently found for Pd-H [23] at RT, using in-situ hydrogen gas loading XRD studies on Laue oscillations and, additionally,

by STM. However, it was also reported that dislocations form at the film / substrate interface. Therefore, full coherency was not achieved in these studies.

### 2.4.7 Phase boundaries of Nb-H thin films

Compared to the bulk phase diagram, phase boundaries ( $c_\alpha$  and  $c_\beta$ ) in films are found to be strongly shifted. This was exemplarily shown for Nb-H films in the thickness range between 35 nm and 200 nm in experiments performed at RT, upon electrochemical hydrogen loading [9], [13], [35].

It was also reported that the microstructure of the thin film affects the phase boundaries, because microstructural defects often act as hydrogen traps [9], [96]: Results on different micro-structured Nb films showed different phase boundaries. Pundt suggested estimating the impact of microstructural contributions on the hydrogen solubility as a function of the sample dimension [10], [68]. Contributions of defects, like vacancies, grain boundaries, dislocations, etc. but also surfaces and subsurface regions, can be considered based on the results on defect-rich bulk materials. To summarize these findings, hydrogen trapping in defects leads to changes in the total solubility limits when their volume fraction becomes large. Therefore, microstructure strongly affects the width of the miscibility gap and, thereby, reduces the storage capacity of the metal. To minimize the microstructural impact on solubility limits of films, epitaxial films are required. For epitaxial films, only trapping contributions of surface sites and dislocations pre-existing at the film / substrate interface remain. Thus, epitaxial films can serve as a model system. For ultra-thin films, the ratio between the number of surface sites and the number of volume sites of the sample becomes significant. In total, surface contributions can be minimized by producing atomically flat surfaces.

Nowadays, it is known that mechanical stress has a major impact on the phase boundary shift [14]. Films of similar microstructure, but exposed to different mechanical stress showed completely different phase boundaries. For 100 nm Nb-H films, the  $\alpha$ -phase solubility limit ranges from 0.20 H/Nb for a film deposited on hard Si-substrate, dropping down to about 0.06 H/Nb for the free-standing film [9], [35]. At the same time,  $c_\alpha = 0.06$  H/Nb is also the solubility limit reported for bulk Nb-H system (see Fig. 2.2, [42]).

For epitaxial Nb-films on (11-20) Sapphire, prepared at 800 °C, Dornheim et al. reported on bulk-like phase boundaries for 100 nm Nb ( $c_{\alpha,lim} = 0.06$  H/Nb and  $c_{\beta,lim} = 0.6 - 0.7$  H/Nb) and comparably strong shifts for 35 nm Nb ( $c_{\alpha,lim} = 0.26$  H/Nb and  $c_{\beta,lim} = 0.64 - 0.69$  H/Nb) [35]. From the actual viewpoint, the solubility limits of Dornheim's samples can be explained by a holey or meander-like film morphology, which can be observed in case of very thin epitaxial films [28], [36], [37]. Thus, to use thin epitaxial Nb-H films as a model system, an appearance of a meander – like topography, which contains craters and hills, reported in the past for thin epitaxial Nb films [28], [36], [37] should be avoided and smooth surface

topographies should be targeted. Studies on phase boundaries of such films performed at room temperature so far have not been reported, for the thin film range.

### 2.4.8 Plateau pressure

The chemical potential for phase formation, the analogue of plateau pressure, can be shifted by mechanical stress [59], [97]. Tal-Gutelmacher et al. and Wagner et al. experimentally showed that the substrate induced mechanical stress leads to a shift of the plateau pressure by about 3 orders of magnitude for Ti-H films [97], or by about 1 order of magnitude for Pd-H films [59]. These values can be varied by changing the intrinsic stress conditions in thin films [59], [98], [99], [100], [101]. For thick films, deposition on very soft and thin polymer substrates or complete film detachment from the substrate and, therefore, a quasi-stress-free state, results in a bulk-like plateau pressure [9], [59], [102].

Particularly, in Nb-H thin film system, delamination of the Nb layer from the sapphire substrate does not occur and stress contributions play the dominant role in the plateau pressure shift. For Nb-H films, by hydrogen gas loading performed at room temperature, RT (21 °C / 294 K), first hydride precipitation is found to appear at about  $p_H = 7 \times 10^{-7}$  mbar [31]. Thus, this pressure is about two times larger than that was reported for the bulk Nb-H system, at 23 °C [40].

The chemical potential in the two-phase region for the bulk system is conventionally constant [40]. In opposite, for thin clamped thin films 'sloped plateau' may occur. The slope was suggested to relate to a continuous increase of the strain energy ( $\Delta f_{el} \sim c^2$ ) that adds to the chemical potential, also in the two-phase region [9], [35]. Recently Wagner et al. [14], [103] pointed out that the slope is related to stress non-linearly increasing with H-concentration, whereas a constant stress increment was supposed to simply shift the phase-transition plateau. It was demonstrated that by implementing an additional term  $\vartheta_o \cdot \alpha_H \cdot \sigma_{ii}$  (stress contributing [56], [104], [105]) in the expression of the chemical potential  $\mu_H$  describing the thin film Me-H system adhered to the rigid substrate and by considering this term separately from  $\varepsilon_{HH} \cdot c_H$  term (hydrogen-hydrogen interaction [16]), the experimentally observed chemical potential can be well described [56], [103].

$$\mu_H = E_o + RT \ln \left( \frac{c_H}{r - c_H} \right) - \varepsilon_{HH} \cdot c_H - \vartheta_o \cdot \alpha_H \cdot \sigma_{ii} \quad (2.27)$$

In this expression  $E_o$  is the site energy,  $r$  is the number of available interstitial sites per metal atom,  $\varepsilon_{HH}$  represents the attractive hydrogen-hydrogen interacting energy in the metal,  $\vartheta_o$  is the partial molar volume of sites occupied by an interstitial specie,  $\alpha_H$  is an expansion factor and  $\sigma_{ii}$  is the sum of axial stress present in the system. This description was suggested by implementing the theoretical model for the general case of thin films exposed to stress developed and showed by Cahn and Larché [104], [105].

### 2.4.9 Critical point for phase separation (critical temperature $T_c$ )

As discussed in chapter 2.1.2, in binary M-H systems below  $T_c$  a miscibility gap opens and two phases with two different concentrations are present. Particularly, in the simple miscibility gap of the Nb-H bulk system this happens at a critical temperature  $T_c = 171^\circ$  (see Fig. 2.2). Above this temperature the hydrogen concentration and thus the lattice parameter varies steadily with the applied hydrogen pressure and there is no phase separation.

In case of a thin film, due to the changed boundary conditions, the elastic hydrogen-hydrogen interaction ( $\varepsilon_{HH}$ ), which is attractive in a sample with free surfaces [106], can become more repulsive. Particularly, by using epitaxial multilayers (V/Fe and V/Mo) with a strong modulation of the related hydrogen concentrations, Hjörvarsson and co-authors demonstrated that depending on the film's strain condition, indeed the sign of the H-H interaction can be changed [57], [58], [107]. In their works, the authors demonstrated that hydrogen absorption in the V-H thin film system under different strain conditions, namely compression (V/Fe) or tension (V/Mo), causes an increase or a decrease in the  $\varepsilon_{HH}$ . Because  $T_c$  and  $\varepsilon_{HH}$  are linked [16]:

$$T_c = \frac{r}{4R} \cdot \varepsilon_{HH} \quad (2.28)$$

, the changed  $\varepsilon_{HH}$  should result in a change of the  $T_c$ . Thus, in the thin film Me-H system with an appropriate set of boundary conditions, mechanical stress may change the chemical potential of hydrogen and modify the hydride phase stability with respect to the  $\alpha$ -phase. Furthermore, in some cases, it may even completely suppress the phase separating [58], drastically changing the phase diagram in comparison to bulk-like system.

For 70 nm and 140 nm epitaxial Nb films, Zabel & Weidinger derived a H-H interaction energy of 7.6 kJ/mol [21], which is 50 % lower than the bulk value. The studies of Song and Zabel on epitaxial Nb-films (Nb(110) // Al<sub>2</sub>O<sub>3</sub> (11-20) sapphire substrate) at temperatures of 200 - 300 °C [32], [95], [108] show sloped pressure-expansion isotherms, as obtained for different film thicknesses ( $d$ ) between 32 nm and 527 nm. From these data, the authors calculated critical temperature points, depending on the film thickness. In common, they reported on a reduced  $T_c$  when compared to the bulk system, decreasing with film thickness and claimed that for film thickness  $d \leq 32$  nm,  $T_c$  drops down to about at 21 °C [32]. Thus, at 21 °C, phase separation should not appear at  $d \leq 32$  nm, according to Song's results. In his work Song appealed to the so-called 'Finite size effects' [95], [109], [110] and, at the same time, assumed an effect of elastic boundary condition provided by the rigid substrate. But, the mechanical stress arising in the Nb-H thin film system upon hydrogen uptake was not measured and also, not considered in the data treatment. However, the interpretation of this data can be disputed, because for determination of  $\varepsilon_{HH}$

and the related critical temperature  $T_c$ , Song et al. used the sloped pressure-expansion isotherm that is, nowadays, mainly attributed to mechanical stress arising in thin film [9], [14], [84], [103]. The presence of high mechanical stress and the non-linearly coupled lattice expansion to the hydrogen concentration were not considered in Song's work for the calculation of  $\varepsilon_{HH}$  and the related  $T_c$ . Thus, the determined drop of the critical temperature for the addressed film thickness was clearly overestimated in Song's work.

Recently, Wagner et al. developed a model describing the chemical potential  $\mu_H$  (partly discussed in chapter 2.4.8) and  $T_c$  in a Me-H thin film system [14], [56], [103].

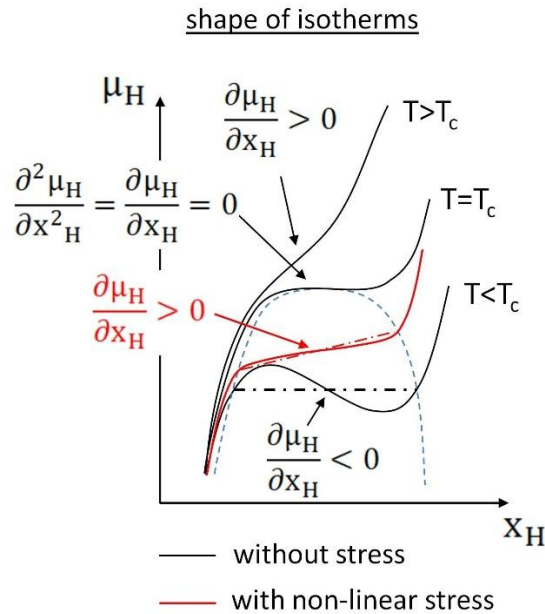


**Fig. 2.17** Determination of the critical temperature  $T_c$  of hydride formation. In a free system, measured isotherms (black dotted line) are flat within the two-phase field. For systems with non-linear stress the isotherms may reveal slopes  $\frac{\partial \mu_H}{\partial x_H} > 0$  already at the presence of phase transition, resulting from plastic processes arising in the film and partial phase transition in relaxed film fractions [103]. Reprinted from *Int. J. Hydrogen Energy* 41, 2727-2738, 2016, S. Wagner & A. Pundt, *Quasi-thermodynamic model on hydride formation in palladium-hydrogen thin films: Impact of elastic and microstructural constraints*, Copyright 2016, with permission from Elsevier.

Wagner suggested that the conventional expression defining the critical temperature  $T_c$  (Fig. 2.17):

$$\left. \frac{\partial^2 \mu_H}{\partial c_H^2} \right|_{T=T_c} = 0 \quad \text{and} \quad \left. \frac{\partial \mu_H}{\partial c_H} \right|_{T=T_c} = 0 \quad (2.29)$$

is not completely applicable in case of in thin films adhered to rigid substrates, because the contribution of H-induced in-plane stress only partially relaxing during H-loading can result in a continuously increasing chemical potential in the two-phase region, even below  $T_c$  (Fig. 2.17):

$$\left. \frac{\partial \mu_H}{\partial c_H} \right|_{\sigma, T < T_c} > 0 \quad (2.30)$$

This fact was experimentally confirmed basing on Pd-H, Nb-H and many other Me-H thin film model systems.

Thus, Wagner et al. supposed that conventional expression of  $T_c$  systematically underestimates the critical temperature [14], [103] in this case. In order to implement the condition of non-linear substrate-induced stress changes and therewith improve the estimation of  $T_c$ , Wagner et al. modified the expression for the  $T_c$  in the following way [14], [103]:

$$\left. \frac{\partial^2 \mu_H}{\partial c_H^2} \right|_{T=T_c} = 0 \text{ and } \left. \frac{\partial \mu_H}{\partial c_H} \right|_{T=T_c} = m > 0 \quad (2.31)$$

Allowing for a constant slope  $m$  within the two-phase region. Assuming a constant stress change in the vicinity of the critical concentration  $c_c = c_H(T_c)$ , Wagner et al. suggested a new general expression for the critical temperature ( $T_c$ ) now containing two additional terms:

$$T_c = \frac{r}{4R} \cdot \varepsilon_{HH} + \frac{r}{2R} \cdot \alpha_H \cdot \vartheta_o \cdot \left. \frac{\partial \sigma}{\partial c_H} \right|_{r/2} + \frac{r}{4R} \cdot \left. \frac{\partial \mu_H}{\partial c_H} \right|_{r/2} \quad (2.32)$$

In this new approach, the first term is the fundamental expression for the  $T_c$  of the bulk metal hydrogen system (see Eq. (2.29) [16]) that was used as well by Song et al. [32], while the other terms are related to non-linear in-plane stress. By applying this methodological approach for Pd-H thin film model system, Wagner et al. addressed films of different thickness and microstructure. To summarize his finding, it was shown that the reduction of the critical temperatures with decreasing film thickness is largest for epitaxial films and smallest for nano-crystalline films. In case of epitaxial Pd-H films ( $d$ : 10 nm - 200 nm) the drop in the  $T_c$  appeared in a low thickness range of  $d < 50$  nm, but even for 10 nm films,  $T_c$  never dropped down below 70( $\pm$ 20) °C. Thus, even in 10 nm thin Pd films phase separation appeared. This was experimentally confirmed via XRD measurements.

To conclude, based on this model, it can be assumed that by choosing a Nb-H thin film system with in-plane stress increasing upon H-loading, in which plastic deformation upon hydrogen uptake will be suppressed, the expected strong contribution of compressive stress may cause a strong reduction of  $T_c$ .

### 3 Experimental methods

In this chapter, the chosen experimental techniques are briefly described. First, chapter 3.1 gives the details regarding the UHV vacuum system used for film preparation. Chapter 3.2 provides a view on the hydrogen gas loading system used for in-situ STM experiments. Chapter 3.3 describes in-situ STM measurements and suggests an example of the data evaluation process. Chapter 3.4 shortly discusses the electrical resistance measurements. Chapter 3.5 shortly introduces the applied XRD and XRR techniques, and, then, gives an idea on the in-situ XRD measurements by considering a particular example. Finally, chapter 3.6 shows the basic principles of electrochemical hydrogen loading and in-situ stress measurements that, for the studies of this thesis, were used in combination.

#### 3.1 Sample preparation

The deposition of the Nb films was performed in an UHV sputter deposition system, as shown in Fig. 3.1. The background pressure inside the chamber is better than  $1.3 \times 10^{-10}$  mbar. For preparing the samples, a RF ion source from Plasma Consult was used [73]. Sputtering was performed in argon at  $p_{Ar} = 2 \times 10^{-4}$  mbar (Ar purity 99.9999 %). High purity niobium (99.99 %) was used as a target material (deposition rate  $0.8 \pm 0.1$  nm/min). (110) oriented epitaxial Nb films of different thicknesses were prepared by  $Ar^+$  ion-beam sputtering on polished  $Al_2O_3(11-20)$  sapphire substrates, as provided by CrysTec GmbH. All substrates had a miscut of less than  $0.1^\circ$ . Two different thicknesses of the substrates, 0.1 mm and 1 mm, were used. To produce epitaxial films, samples were prepared at different deposition temperature:  $T_d = 730 - 850$  °C (for details see chapter 4.1). Before the deposition of the Nb film, the substrates were kept at  $T_d = 800$  °C for at least 20 minutes to clean the surface and to minimize the increase of background pressure arising during heating the sample stage in the sputter chamber. The substrate temperature was adjusted by use of the heating system, consisting of tungsten-wire heaters located directly behind the substrates. An Cr-Al thermocouple fixed to the sample holder was used for controlling the temperature. After Nb film deposition, the samples were cooled down for 1.5 - 2 hours. The details regarding the typical sputtering parameters are summarized in Table 3.1.

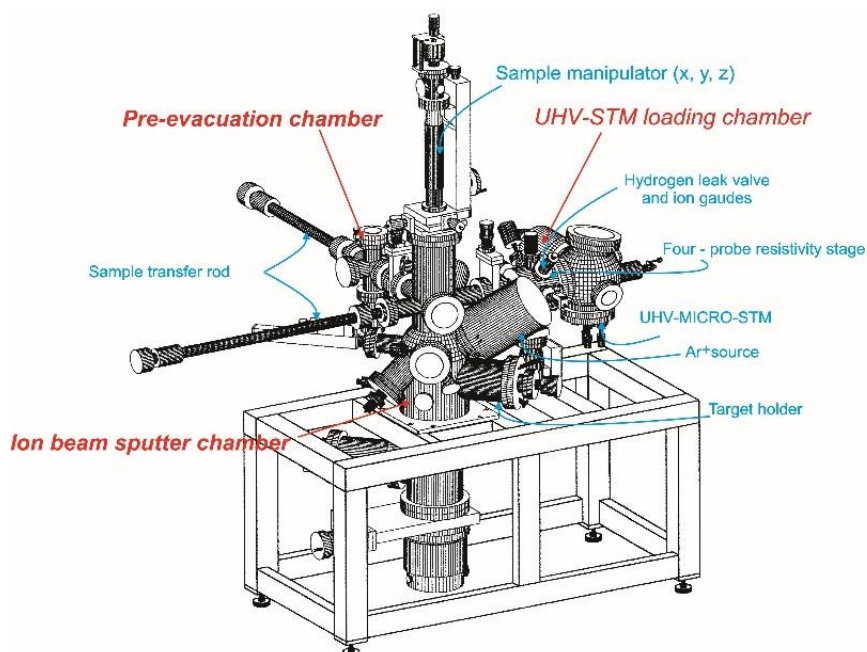


**Fig. 3.1** UHV vacuum system used in this study [73]. The system consists of 3 main parts: Pre-evacuation chamber, Ion beam sputter chamber and UHV-STM loading chamber. To handle and transfer the sample through the vacuum chambers, the system is equipped with two sample transfer rods and the sample manipulator (translational motion in x, y and z directions). The target holder is a cube-shaped Cu block connected with a water cooling system and containing four different sputter targets (Nb, Pd, Mg, V). The UHV-STM loading chamber designed for in-situ hydrogen gas loading STM and electrical resistance measurements. Therefore, UHV Micro-STM (Omicron) and four-probe resistivity stage are available. To perform hydrogen gas experiments at desired background hydrogen pressure, the system is equipped with the hydrogen gas dosing valve, control unit, quadrupole mass spectrometer and set of vacuum gauges.

**Table 3.1** Experimental conditions used for sputter depositions and sample preparations

Background pressure [mbar]	$1.3 \times 10^{-10}$	
Sputtering gas pressure [mbar]	$2 \times 10^{-4}$	
Substrate-target distance [cm]	11	
Sputtering gas	Ar (purity: 99.9999 %)	
Energy of Ar <sup>+</sup> [eV]	880	
RF power [W]	76	
Target purity [%]	Nb:	> 99.95
	Pd:	> 99.9
Substrate size	Al <sub>2</sub> O <sub>3</sub> (11-20) sapphire substrate (miscut < 0.1 °)	
	In-situ STM:	7 mm × 5 mm × 1 mm
	In-situ XRD:	10 mm × 10 mm × 1 mm
	In-situ electrical resistance:	10 mm × 10 mm × 1 mm
	In-situ stress measurements:	30 mm × 7 mm × 0.1 mm
Deposition rate [nm / min]	Nb:	$0.8 \pm 0.1$
	Pd:	$2.1 \pm 0.1$
Substrate temperature [°C]	Nb:	730 - 850
	Pd:	≤ 50

Further, for hydrogen loading experiments performed in the UHV-STM loading chamber (see Fig. 3.1), in order to facilitate hydrogen absorption at RT, a Pd catalyst of less than 0.5 monolayer thickness (0.1 nm) was deposited onto the Nb films [31]. High purity Pd (99.95 %) was used as a target material (deposition rate  $2.1 \pm 0.1$  nm / min). The Pd-deposition was performed at  $T_d \leq 50^\circ\text{C}$ , after about two hours of cooling the Nb-film.

The samples were transferred into the UHV-STM loading chamber directly after film preparation without breaking the vacuum conditions. Thus, rapid oxidation of the Nb surface, occurring in atmosphere already at RT, is prevented.

For samples that were studied outside of the UHV vacuum system, namely by using in-situ XRD and in-situ stress measurements techniques, Nb films were covered alternatively with a 20 nm Pd capping layer. This Pd layer is required to prevent subsequent film oxidation upon air exposure and to facilitate the hydrogen uptake. The solubility ratio between H in Nb and H in Pd in the applied pressure range at RT is about  $3.33 \times 10^4$  [111] and, hence, hydrogen solution in the Pd capping layer can be neglected.

For electrical resistance measurements that were performed in combination with in-situ STM and in-situ XRD measurements for some batches of samples, depending on the particular experimental conditions, a Pd layer of a thickness of either 0.1 nm or 20 nm, respectively, was added.

To optimize the film growth conditions and to characterize the as-prepared samples, pre-studies were performed. Surface topography and microstructure of as-prepared samples were analyzed for different film thicknesses ( $d$ ) and deposition temperatures ( $T_d$ ). The related results are presented in chapter 4.

## 3.2 Hydrogen gas-phase loading

The hydrogen pressure in the UHV-STM loading chamber (Fig. 3.1) can be varied in a range between  $1 \times 10^{-9}$  mbar and 500 mbar. But, for in-situ STM measurements, the pressure range between  $1 \times 10^{-3}$  mbar and 10 mbar must be avoided due to the risk of damaging the electronics of STM by the plasma discharge. Thus, in the STM experiments described in this work, the hydrogen pressure was changed in a range from  $p_H = 1 \times 10^{-9}$  mbar to  $p_H = 4 \times 10^{-5}$  mbar. The purity of the hydrogen gas used for the loading experiment was 5.6. During the experiment the hydrogen pressure was controlled by using a gas dosing valve. It is equipped with a control unit designed for the precise regulation of the gas leak rate. The leak rate was automatically controlled with respect to the actual hydrogen pressure measured by the ionisation manometer. By using this loading system it is possible to keep the hydrogen pressure constant during the long-term STM measurements. It also allows to change relatively fast (within minutes) the hydrogen gas pressure inside the UHV-STM loading chamber. Figure 3.2 shows an example of pressure measurements inside the system. The abscissa gives the relative experimental time. The ordinate shows

the pressure change inside the system. The pressure steps are related to the change of the pre-set point for the control system. The graph demonstrates a good stability and a relatively fast response of the loading system.

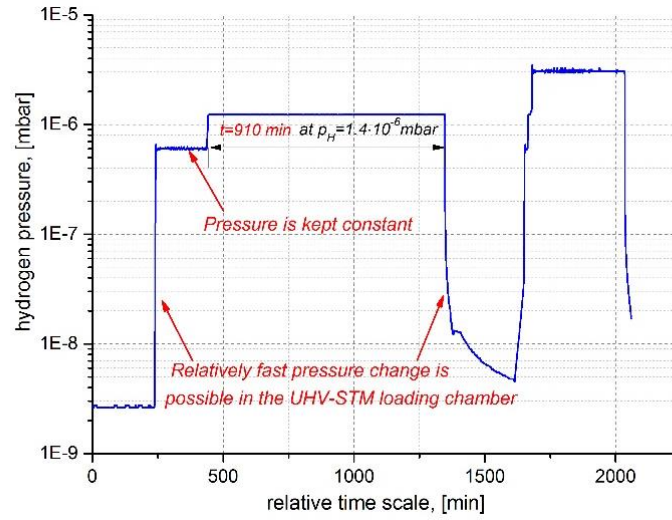


Fig. 3.2 An example of pressure measurements inside the UHV-STM loading chamber.

### 3.3 Scanning tunneling microscopy (STM)

#### 3.3.1 Introduction of the STM method

The scanning tunnelling microscopy (STM) bases on the measurement of the tunneling current that can flow due to the quantum mechanical tunneling effect between the STM - tip and a conductive sample surface (in fact two electrodes). This process can be realized when electrodes are placed close enough to each other (0.1 nm - 1.0 nm) and when a bias voltage is applied [112]. The tunneling current can be used to probe the physical properties locally on the sample surface (e.g. the density of states, DOS) as well as to measure the surface topography. Herewith, the distance control based on the tunneling effect is very sensitive to any change in the separation distance ( $s$ ) between the two electrodes, since the tunneling current depends exponentially on  $s$  [112]:

$$I \sim \sum |\varphi_{surface}|^2 |\varphi_{tip}|^2 e^{-2ks} \quad (3.1)$$

Here,  $\varphi_{surface}$  and  $\varphi_{tip}$ , respectively, are the wave functions of the surface and the tip that are related to the solution of Schrödinger's equation.

Without going into technical details, all STM devices are based on the measurement of the tunneling current that varies depending on the surface topography (height change) and the DOS. During

the measurement, the STM moves the STM tip (scanner) across the sample surface in the x-y plane and measures the change of the tunneling current. The scheme in Fig. 3.3 (a, b) illustrates the principle of STM measurements. The change in a current with respect to position can be measured itself, or the height,  $z$ , of the tip corresponding to a constant current can be measured [113]. Thus, the measurements can be performed in the two different modes that are known, respectively, as constant height mode and constant current mode [112].

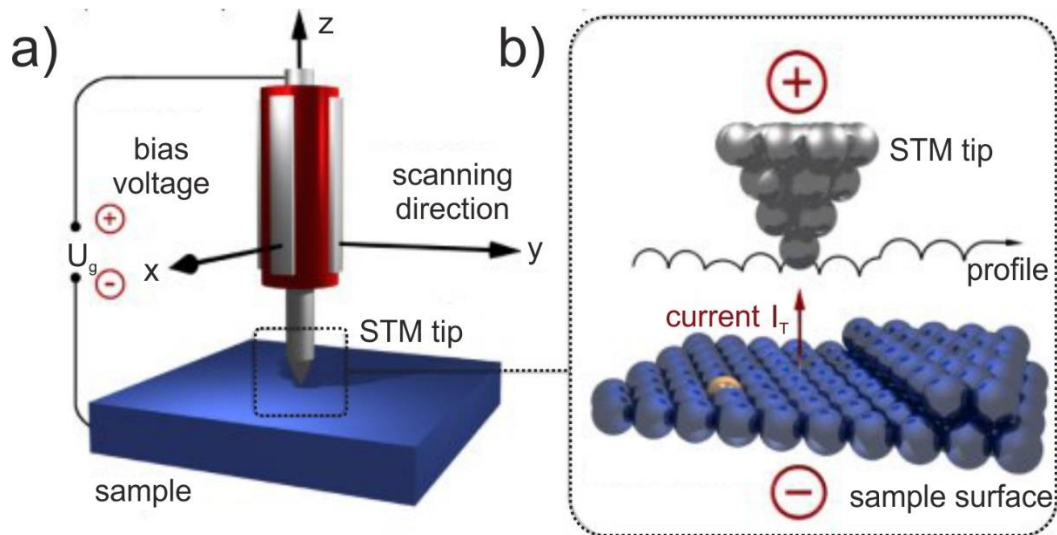


**Fig. 3.3** The basic working principle of STM measurements: **a)** Macroscopic scale: If a small voltage is applied between the sample and the tip, when they are placed close enough to each other (typically 0.1 - 1 nm), the electron tunneling current can start to flow between the electrodes. By scanning the tip over the sample surface while keeping the tunneling current constant by means of the feedback loop (constant current mode), one can follow the surface contour and store the information about the vertical position  $z$  of the tip as a function of the lateral position ( $x, y$ ). **b)** Atomic scale: The direction of the tunneling current is defined by the polarity of the voltage. During the measurement, the experimentally measured current value is compared with a reference value ( $\approx 0.1$  nA - 1 nA) and, then, a corresponding voltage is applied to the  $z$ -piezo to re-adjust the separation distance and, therewith, minimize the difference. Modified after S. Woedtke (*Dissertation, CAU Kiel, 2002* [114]).

The constant current mode is very sensitive to small surface corrugations, but it requires relatively flat surfaces for stable long-term topography measurements. Significant differences of heights on the sample surface may cause an appearance of artifacts during the scan, since the quality of STM measurements depends crucially on the quality of the tip (sharpness, geometry, contamination etc.) and the geometry of the objects presented on the sample surface. In this measuring mode, by scanning the tip over the sample surface while keeping the tunneling current constant by means of the feedback loop, the STM scanner can follow the surface contour. Herewith, the information about the vertical position  $z$  of the tip as a function of the lateral position ( $x, y$ ) can be stored in the file. Based on the stored array of data any SPM software can reconstruct and visualize the surface topography. Thus, STM surface-images can be handled and analyzed.

In this work, all STM measurements were carried out in the constant current mode. The measurements were performed at RT. The typical bias voltage applied between the sample and the tip was about  $U_g = -1$  V, while  $I_{ref} = 0.3$  nA was set as a reference current value. As a tip material, Ir<sub>0.1</sub>Pt<sub>0.9</sub> wire was used. The STM tips were prepared mechanically, by using the simplest procedure based on pulling and cutting [112]. For data evaluation three different SPM softwares, namely WSxM [115], Gwyddion [116] and Scala (Omicron) were used.

It should be mentioned additionally that the positioning of the applied scanners is based on the use of piezo-elements. Thus, even very small temperature variation occurring during the STM measurements carried out at RT, may cause an appearance of the thermal drift directly visible in the STM images. Particularly, by measuring a frame size of 500 x 500 nm<sup>2</sup>, Micro-STM (OMICRON) used in this study demonstrates typically the thermal drift in the range from 1 nm / h to 10 nm / h depending on the hydrogen pressure and the time elapsed from the pressure change within the STM-chamber.

### 3.3.2 In-situ hydrogen loading STM measurements

STM measurements performed in-situ during continuous hydrogen gas loading (*in-situ STM* [31]) were carried out by using an UHV Micro-STM system from OMICRON, as mounted in the UHV-STM loading chamber shown in Fig. 3.1. Most of the experiments were performed immediately after film preparation. The transfer of the sample from the ion-beam sputter chamber to the UHV-STM loading chamber typically didn't exceed 5 minutes. Thus, for this short time span for the used background pressure, topography changes due to the ad- or absorption of background gases are neglected.

The in-situ STM measurement sequence conventionally was performed as follows: during the experiment, a set of STM images measured at different hydrogen pressures and exposure times was stored for subsequent data evaluation. When no topographical changes were detected within several hours or the change occurred too slowly, the hydrogen pressure ( $p_H$ ) was set to a new constant value. Therefore, in this thesis, exposure times  $t_e$  at a newly adjusted pressure are always given relative to the moment of pressure change. Additionally, it has to be noted that because of the presence of the thermal drift (see chapter 3.3.1) and limited lifetime of the STM tip, in some experiments the hydrogen pressure was increased without waiting until thermodynamic equilibrium, since the waiting time would be too large.

The related STM measurements allow detecting the phase transformation occurring in Nb-H thin films and give information about different modes of hydride phase precipitation and growth. Figure 3.4 (a, b) gives an example of in-situ STM experiment on a 25 nm Nb-H film upon hydrogen loading. Figure 3.4 (a) shows the STM surface-image of the film surface in the as-prepared sample state, thus, before the hydrogen loading. Figure 3.4 (b) shows an STM image of the surface measured at the same position, but

after hydrogen loading at  $p_H = 7 \times 10^{-7}$  mbar for  $t_e = 520$  min. Here, the appearance of some elevated (bright) surface regions is visible.

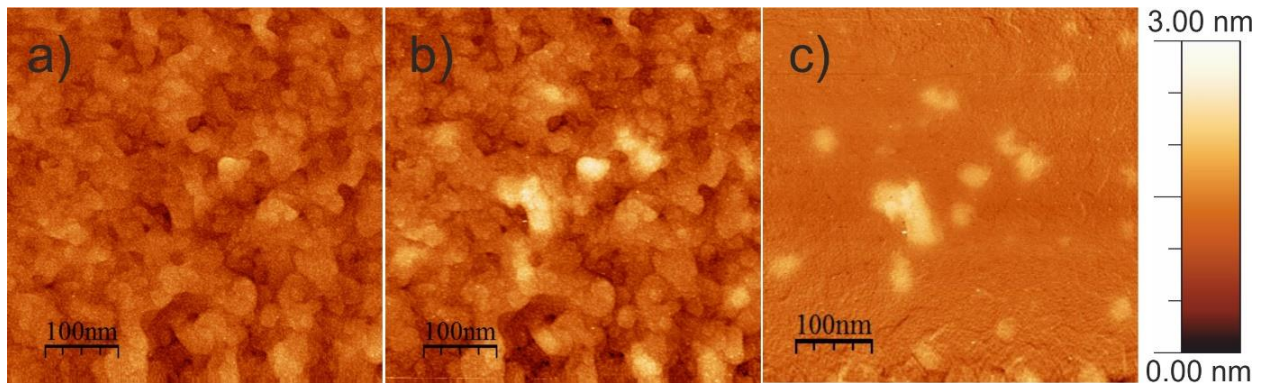


**Fig. 3.4** a) 25 nm Nb film before hydrogen loading b) after 520 min exposure to a hydrogen pressure of  $p_H = 7 \times 10^{-7}$  mbar c) difference image (b-a): bright areas, elevated by about 1.0 nm - 1.5 nm, show hydride precipitates. (Frame size: 500 x 500 nm<sup>2</sup>). Figure created by author from data originally published in Ref. [133]

The observed surface topography changes are related to the precipitation of hydride phase occurring in the system as discussed in chapter 2.4.5. Thereby, they are used to investigate precipitation and growth of hydride phase for different film thicknesses and applied hydrogen pressures. The shape of hydride precipitates as well as their spatial distribution and development during the phase transformation process become visible with this method.

Besides this, *traces of dislocations* can also become visible on the film surface as shown in chapter 2.4.4. Thus, a coherency loss can be detected *in-situ* by the appearance of glide lines or dislocation loops at the film surface. Even the detection of single dislocations is possible by STM.

In order to make the hydrogen induced surface corrugations effectively visible during in-situ STM measurements, stiff sapphire substrates excluding substrate bending are required. Bending can occur due to the high mechanical stress arising between the film and the substrate during hydrogen absorption [13]. It scales with the hydrogen content in the film, and therefore changes with a hydrogen partial pressure. When stress in the film is released, this bending itself also changes. Hence, substrate bending would complicate the data evaluation process. For 1 mm sapphire substrates, Nörthemann reported that substrate bending is negligible in STM measurements [31]. Thus, in this study, for in-situ STM measurements, sapphire substrates of 1 mm thickness were used.

In common, data interpretation, strictly speaking, strongly depends on the image quality and the stability in the position of the measured frame. Sometimes, due to the thermal drift, the position of the frame may leave the analyzed surface region and should be manually re-adjusted. During the STM measurements described in this work typical frame sizes of 250 x 250 nm<sup>2</sup>, 500 x 500 nm<sup>2</sup>, 1000 x 1000 nm<sup>2</sup>, and 2000 x 2000 nm<sup>2</sup> were used. To minimize the effect of thermal drift and exclude the contribution

related to the STM parameters ( $I_{ref}$ ,  $U_g$ , loop gain, scanning speed), the chosen STM parameters were preferentially fixed in the beginning of the experiment.

To summarize, in-situ STM is a highly sensitive and local method to study precipitation and growth of new phases as well as the change of the coherency state in Nb-H thin film systems.

### 3.3.3 Ex-situ STM data evaluation: drift correction and difference images

As shown in chapter 2.4.2, the amplitude of the hydrogen-related surface corrugations becomes smaller with decreasing the film thickness (see Eq. 2.22). As given in Table 2.1, it decreases from about 8 nm for 100 nm films to about 1.5 nm for 25 nm films. Thus, the surface topography change occurring upon hydrogen loading usually becomes poorly visible in the original images, when the film thickness is decreased to 25 nm or even less. Therefore, for very thin films the calculation of difference image between two different states might be required. Difference image highlights the absolute surface corrugation change.

As discussed in chapter 3.3.2, the STM images given in Fig. 3.4 (a) and Fig. 3.4 (b) were measured at the same place, but, correspondingly, before (a) and during (b) hydrogen loading of the 25 nm film. Figure 3.4 (c) gives an example of a typical difference image that was obtained by subtracting two previous images from each other (Fig. 3.4 (b) – Fig. 3.4 (a)). Here, the surface modification that occurs in the time span defined by two STM images gets clearly visible.

For image subtraction, scripts developed by Kai Nörthemann [73] were applied. These scripts help to solve two main challenges accompanying in-situ STM measurements performed in this study: 1) the occurrence of a thermal drift in the STM images and 2) the evaluation of a large amount of graphical data. By utilizing the scripts, plane levelling, background subtraction, drift correction, and, finally, STM image subtraction were performed. By this, even very small surface topography changes of less than 0.3 nm appeared during hydrogen loading were detected and analysed.

### 3.4 In-situ resistance measurements during hydrogen loading

As discussed in chapter 3.3.3, data evaluation of long-term STM measurements was always performed ex-situ, namely, when the experiment was mainly completed. Thus, during STM studies it was vital to use an independent technique to detect the global property of hydrogen ab- and desorption in the Nb-H film in real time.

Therefore, as an alternative method, the electrical resistance measurement was chosen. This choice was caused by simplicity and applicability of resistance measurements under similar experimental conditions as those used for the STM studies. In order to measure the relative resistance change occurring during the hydrogen loading and unloading experiments, a resistivity stage was designed and constructed

in cooperation with the IMP institute's mechanical workshop. Further, it was implemented in the UHV-STM loading chamber that allowed performing combined in-situ STM and resistance measurements. Thus, electrical resistance measurements were done simultaneously with STM measurements during hydrogen loading in the same experimental conditions on similar Nb-films. During hydrogen absorption/desorption, the resistance change was monitored by use of a Keithley 2000-multimeter. The electrical resistance data were automatically plotted and updated on the computer screen during the experiment and additionally saved in the file for later data evaluation.

Figure 3.5 (a) gives the schematic illustration of the electrical contacts in the resistivity stage arranged in the Van der Pauw method style [117]. Here, while a constant current is applied between the electrodes A and B, the resulting potential difference between C and D can be measured and, therewith, the electrical resistance value can be calculated. It should be noted that the specific electrical resistance (resistivity) was not determined and addressed in this work. Only the resistance change and the shape of the resistance curve were considered in this study.

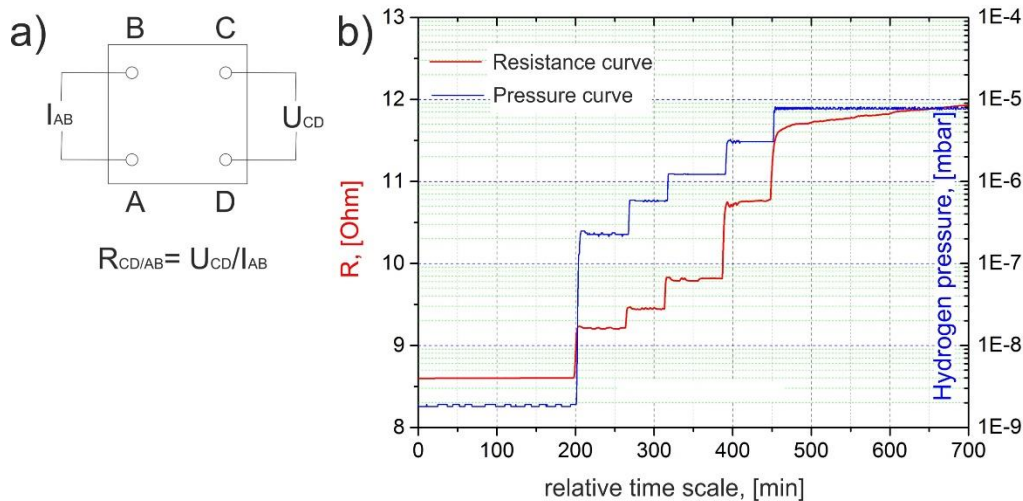


**Fig. 3.5 a)** Schematic illustration of resistance measurements **b)** An example of in-situ resistance measurements (8 nm Nb-H film). On the abscissa axis the relative experiment time is given. On the ordinate axis, on the left side, resistance value and, on the right side, the hydrogen pressure value are given. Blue curve shows the pressure change in the UHV-STM loading chamber, red curve – the change of the resistance value measured during the experiment. Clear resistance changes occurs, when the pressure increases from  $p_H = 2.5 \times 10^{-9}$  mbar to  $p_H = 8 \times 10^{-6}$  mbar.

Figure 3.5 (b) shows an example of the resistance measurements performed during the hydrogen loading of a 8 nm Nb-H film. On the abscissa axis the relative experiment time is given. On the ordinate axis, on the left side, the resistance value and, on the right side, the hydrogen pressure values are given. The blue curve shows the pressure change in the UHV-STM loading chamber, red curve provides the change of the resistance value measured during the experiment. Clear resistance changes are visible, when the hydrogen pressure increases from  $p_H = 2.5 \times 10^{-9}$  mbar to  $p_H = 8 \times 10^{-6}$  mbar.

To summarize, the main benefit of the resistance measurements as compared to STM measurements is that they give a global view on the hydrogenation process directly during the pressure change. The shape of the resistance curve can be used for better understanding of the related physics. It adds on the STM results information. Beside the fact that hydrogen acts as scattering center for electrons, it can produce additional scattering centers when plastic deformation (dislocation) occurs. Thus, the resistance curve contains many different contributions, as e.g. the increased hydrogen concentration, the presence of different phases and the inelastic processes occurring in the sample [118]. If the cyclic loading / unloading experiments are performed, the first two contributions are expected to be reversible, while the third one will irreversibly change the resistance value.

### 3.5 X-ray diffraction (XRD) and X-ray reflectivity (XRR)

#### 3.5.1 XRD

The microstructure, texture and lattice parameter change upon hydrogen loading / unloading were investigated by X-Ray diffraction (XRD). For the samples that were not exposed to hydrogen, the microstructure and texture were analyzed by means of X-ray diffraction in a Phillips X'Pert diffractometer equipped with a Co source ( $\lambda_{\text{Co}} = 0.179026 \text{ nm}$ ).

Details about this method are described for example in reference [119]. In this chapter, only the required information will be briefly given. By Bragg's law, the peak position in  $2\theta$  gives the corresponding interplanar distance  $d$  in the chosen crystallographic direction. Thus, by measuring the XRD patterns and using Bragg's law, one can calculate the interplanar distance  $d$ :

$$2d \sin \theta = n\lambda, \quad (3.2)$$

where  $n$  is a positive integer value and  $\lambda$  is the wavelength. For Nb films that have a cubic crystal structure, the lattice parameter  $a$  and the interplanar distance  $d$  are linked by the following expression:

$$a = d\sqrt{h^2 + k^2 + l^2}, \quad (3.3)$$

where  $(h, k, l)$  are the corresponding *Millers indices*. For epitaxial Nb films, only one lattice reflection, the (110) lattice reflection (and higher orders), is detectable in Bragg condition. This reflex provides information about the interplanar distance  $d_{110}$  in the out-of-plane film direction.

From the shape of the peak, by using the full width at half maximum (FWHM), one can gain information about the domain size ( $D$ ) in the out-of-plane direction of the film. For the determination of

domain size ( $D$ ) Scherrer's formula can be applied [120]:

$$D = \frac{K \cdot \lambda}{\cos\theta \cdot B} \quad (3.4)$$

where  $K = 0.9$ : shape factor,  $\lambda$ : wavelength,  $\vartheta$ : Bragg angle,  $B$ : FWHM and  $D$ : domain size. Hereby, in the case of thin films, the calculated average domain size usually gives the lower limits for the true domain size. Despite the fact that the Scherrer's formula is limited to nano-scale particles and not applicable to grains larger than about  $0.1 \mu\text{m}$ , it can be used, as a first approximation, for estimation of an effect of film expansion on the peak broadening. Hereby, in the case of thin epitaxial films the domain size in a first approximation can be assumed to equal to the film thickness.

### 3.5.2 XRR

To determine film parameters, namely the thickness, the density, the surface- and interface-roughness, X-Ray reflectivity (XRR) measurements were performed [121]. XRR is a surface-sensitive non-destructive and non-contact analytical technique used for characterization of thin films and multilayers systems with a total thickness in a range from 2 nm to 200 nm. Its precision is about 0.1 nm - 0.2 nm that allows a very accurate layer thickness determination. Typically, XRR measurements are carried out in the normal  $\vartheta$ - $2\vartheta$  geometry, but with well-collimated optical conditions at glazing angle. In this thesis, XRR measurements were performed using a Bruker D8 (Bruker) at the IMP and at the Synchrotron facility in Grenoble (ESRF) at beam line BM20. Hereby, the measurements performed at the synchrotron beamline include film characterizations in as-prepared, loaded and unloaded sample stages.

As this method bases on wave reflectivity, the incident electromagnetic wave (X-Ray) can be reflected on the sample surface as well as on the interfaces that separate different layers. The X-Ray penetration into the sample volume and its refraction occurs above the critical incident angle  $\theta_{cr}$  of total reflection. This critical value depends on the density of the surface material and on the used wavelength. Typically, the reflective index  $n$  of material for X-Ray is slightly smaller than 1 ( $n < 1$ ) and can be calculated by using the following expression:

$$n = 1 - \delta - i\beta \quad (3.5)$$

where the reflective index  $n$  is expressed as a complex number. Here,  $\delta$  is related to the dispersion while  $\beta$  is related to the X-Ray absorption. Two these coefficients depend on the material density  $\rho_i$  and are given by [122]:

$$\delta = \left(\frac{r_e}{2\pi}\right) \rho_i N_A \lambda^2 \left(\frac{Z_i + f_i^i}{M_i}\right) \quad (3.6)$$

$$\beta = \left(\frac{r_e}{2\pi}\right) \rho_i N_A \lambda^2 \left(\frac{f_i^{ii}}{M_i}\right) \quad (3.7)$$

Here,  $r_e$  is the classical electron radius,  $N_A$  is Avogadro's number,  $\lambda$  is the wavelength,  $Z_i$  is the number of electrons per atom,  $M_i$  is the atomic weight,  $f_i^i$  and  $f_i^{ii}$  are the atomic scattering factors.

When the optical density of the material varies in vertical direction (e.g. for multilayers or by a substrate), the interference of the refracted X-Rays occur at different interfaces. Hence, a periodic oscillation (Kiessig fringes) related to the thickness of present layers is typically visible in the XRR curve. In common, the shape of the XRR curve strongly depends on the interface morphological roughness (decay of the oscillation), the surface roughness (decay of the XRR curve) and the densities of different interfering layers (critical angle and the amplitude of oscillation). Thus, every specific configuration of thin film layers gives a unique XRR curve. By physical modeling and by fitting the simulated XRR curve to the experimentally measured XRR curve, the physical parameters of the film (e.g.: layers thickness, roughness, density etc.) can be derived.

Figure 3.6 (a) gives an example of a XRR curve (given in red color) and the corresponding simulated XRR curve (given in blue color) obtained for a Pd (18 nm) / Nb (19 nm) double-layer system deposited on  $\text{Al}_2\text{O}_3$ . The nominal thicknesses of Nb and Pd layers are calculated according to the known sputter rate and the deposition time of Nb and Pd (see chapter 3.1). Figure 3.6 (b) gives a table of physical parameters related to the simulated XRR curve shown in Fig. 3.6 (a). As can be seen, besides the intended Nb and the Pd layers, an additional PdO top layer has to be added in the suggested physical model to successfully describe the experimental XRR data. Its presence reflects the difference in the optical properties occurring due to the partial surface oxidation and contamination caused by the interaction with an environment.

The XRR fitting was done by using LAPTOS 7.7 software [123]. Imposing two curves shown in Fig. 3.6 (a) and the evaluation of simulated physical model given in Fig. 3.6 (b) suggest very precise determination of film parameters.

Identical XRR measurements were performed in this study for some exemplary samples in order to determine accurately the thickness of the Nb layers and, in the case of ultra-thin films, to calculate the film expansion upon hydrogen loading. For the fitting of XRR curves, besides the LAPTOS 7.7 software, the IMD 2.2 software was used [124].

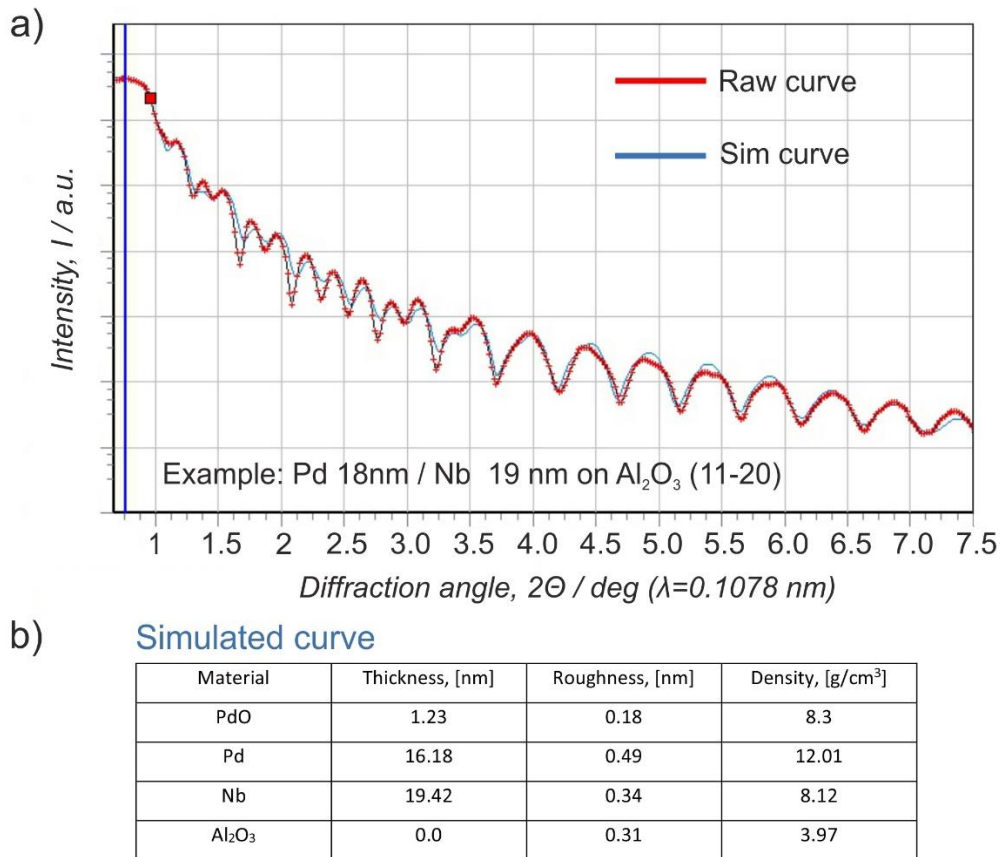


**Fig. 3.6 a)** An example of XRR curve of Pd 18 nm / Nb 19 nm deposited on  $\text{Al}_2\text{O}_3$  (11-20) at  $760^\circ \text{C}$  (given in red color) and the related simulated XRR curve (given in blue color). **b)** The table of physical parameters related to the simulated XRR curve.

### 3.5.3 In-situ XRD during hydrogen loading

In contrast to the STM - technique XRD measurements are more common methods to detect the lattice expansion and phase transformation occurring in thin films. In this work, in-situ hydrogen gas loading XRD measurements were performed in order to study the out-of-plane expansion by observing the shift of the Nb (110) XRD reflection during the hydrogen loading / unloading experiment. The measurements were done at the Synchrotron facility in Grenoble (ESRF) at beam line BM20 ( $\lambda = 0.1078 \text{ nm}$ ) and in Hamburg (Desy / Petra III) at beam line PO8 ( $\lambda = 0.10000 \text{ nm}$ ,  $\lambda = 0.09998 \text{ nm}$ ). Two similar portative vacuum chambers designed for hydrogen loading were used [35]. For XRD measurements both chambers are equipped with kapton windows that are located above the sample. The hydrogen loading was mainly done in the continuous hydrogen gas flow mode. For the corresponding experiments, both chambers were directly mounted in the Euler cradle so that the sample position and spatial orientation could be precisely adjusted ( $x, y, z$  - coordinates and  $\chi, \varphi, \vartheta$  - tilting angles). All the XRD measurements

were additionally accompanied by electrical resistance measurements, available within the loading chambers and performed on the same XRD samples.

Figure 3.7 (a, b) shows the two loading chambers used in this study for in-situ XRD measurements. For the measurements performed at ESRF, the standard BM20 furnace was used, as developed by C. Bächtz and available at the synchrotron facility (see Fig. 3.7 (a)). It is equipped with automatic valves and pressure gauges that allow to precisely control the pressure inside the chamber. Microstructural changes occurring in the sample upon hydrogen exposure can be monitored in-situ. The background vacuum pressure for this setup is  $p_{background} \leq 5 \times 10^{-7}$  mbar. For similar measurements performed at Petra III, a new portable loading chamber was constructed in the frame of this study (see Fig. 3.7 (b)). It contains several valves and pressure gauges that are used to adjust the hydrogen pressure in the system. The background vacuum for this set up is  $p_{background} \leq 5 \times 10^{-6}$  mbar.

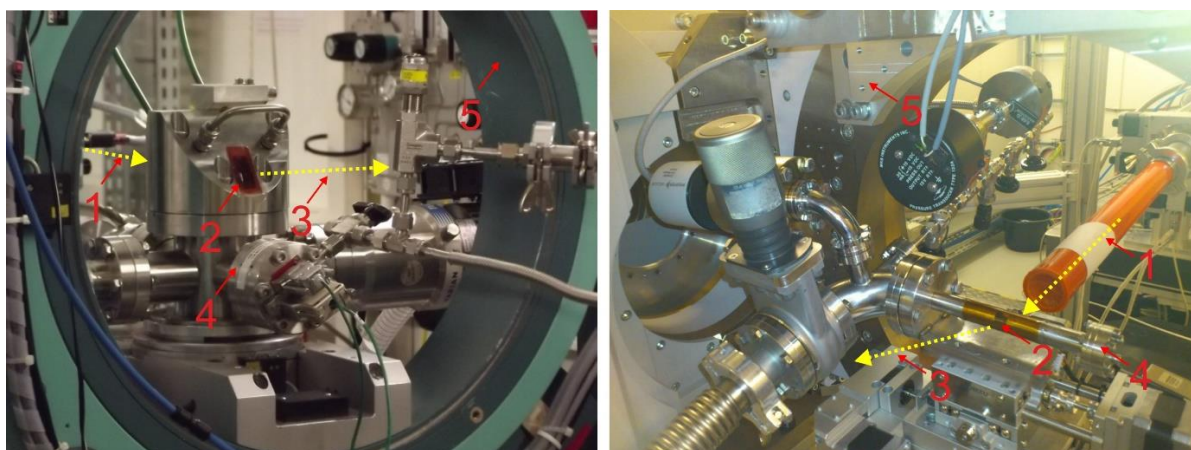


**Fig. 3.7 a)** The standard BM20 furnace was used for in-situ XRD measurements at ESRF at the Beam line BM20 (Grenoble, France). The background vacuum is  $p_{background} \leq 5 \times 10^{-7}$  mbar. **b)** Specially designed portable loading chamber constructed for in-situ XRD measurements performed at Petra III at the Beam line PO8 (Hamburg, Germany). The background vacuum is  $p_{background} \leq 5 \times 10^{-6}$  mbar. (1 - incoming beam, 2 - sample position, 3 - reflected beam, 4 - loading chamber, 5 - Euler cradle)

In a perfectly aligned sample / detector geometry, by observing the shift of the Nb (110) lattice reflection, in the XRD pattern one can see additionally the  $Al_2O_3$  (11-20) peak of the single crystal sapphire substrate with very high intensity. It is placed relatively close to the Nb (110) peak and the Pd (111) peak. A typical intensity difference between the  $Al_2O_3$  (11-20) peak and the Nb (110) peak is about four to five orders of magnitude. Thus, an appearance of the substrate related peak overlapping with the Nb (110) peak complicates the measurements as well as the data evaluation processes. Because of this challenge, directly before the start of every in-situ measurements, all the samples were slightly tilted by a  $\chi$  - offset of about  $0.5^\circ$  to  $1.0^\circ$ . By this, an appearance of the single crystal substrate peak was suppressed, while for the broad Nb (110) and Pd (111) peaks only a slight intensity drop and unchanged peak positions were

found. In this starting experimental condition, hydrogen gas loading at different pressures was carried out.

During in-situ XRD measurements,  $p_H$  was increased stepwise from  $p_H = 1 \times 10^{-6}$  mbar to  $p_H = 1$  mbar. Hereby, first changes in the XRD patterns were typically observed at  $p_H \geq 1 \times 10^{-3}$  mbar. The loading time was varied from 60 min to 300 min depending on the loading pressure and the film thickness.

Figure 3.8 shows an example of change of the XRD pattern observed for a 80 nm Nb film covered with a 20 nm Pd layer, upon hydrogen loading at  $p_H = 1.3 \times 10^{-3}$  mbar. During the hydrogen loading experiment, different XRD patterns including Nb (110) and Pd (111) peaks were measured. The experimental time scale is given in Fig. 3.8. The first curve ( $t = 0$ ) corresponds to the initial stage of the sample before the hydrogen exposure. Here, only two peaks corresponding to Nb (110) and Pd (111) XRD reflections are visible. Further, upon hydrogen gas-pressure increase, the XRD patterns visibly change. The Nb (110) peak first shifts to smaller angles. This result indicates the lattice expansion and the formation of the hydrogen solution within the Nb crystal structure (Nb-H  $\alpha$ -phase). By further increase of the hydrogen concentration, the hydride peak (Nb-H,  $\beta$ -phase) appears; the intensity of the  $\alpha$ -phase peak lowers and the intensity of the hydride-phase peak increases. This behaviour is related to the  $\alpha$ - $\beta$  phase transformation occurring within the Nb-H system. Finally, when the phase transformation is completed, only the hydride-related peak stays visible in the XRD pattern. Hereby, Pd (111) peak doesn't change, its width and the position are not effected by hydrogen. Thus, it shows that hydrogen diffuses through the Pd capping layer into the Nb layer.

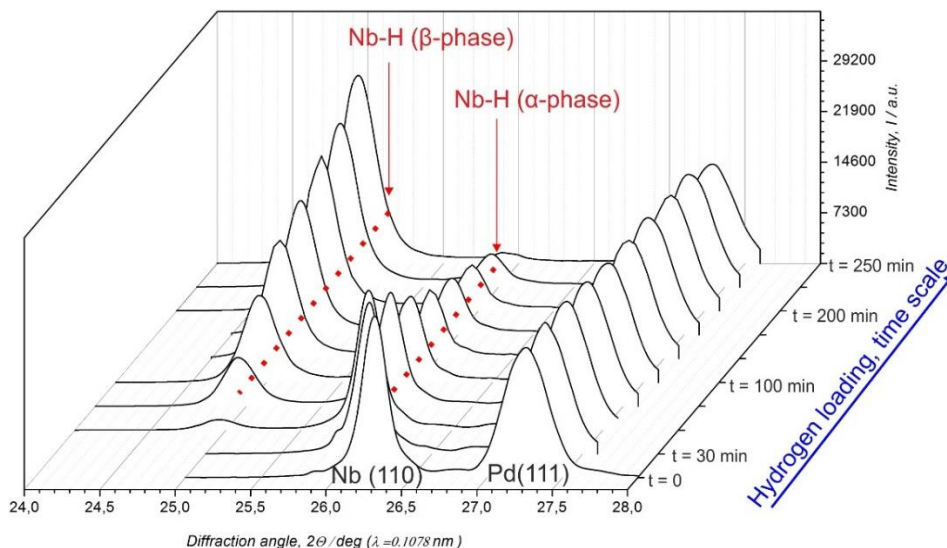


**Fig. 3.8** In-situ XRD measurements upon hydrogen loading at  $p_H = 1.3 \times 10^{-3}$  mbar: 80 nm Nb (110) covered with a 20 nm Pd layer. Initially, two peaks corresponding to the Nb (110) and the Pd (111) XRD reflections are visible. Upon hydrogen loading, Nb (110) peak moves to the lower angle range. Then, due to the phase transformation occurring in the Nb-H system, second peak corresponding to the hydride phase, appears in the graph.

As noted before, for all the samples studied in this work by XRD method, at  $p_H < 1 \times 10^{-3}$  mbar no Nb (110) peak shift was detected. This hydrogen gas-pressure value is significantly higher as compared to the pressure values that were applied in the UHV-STM loading chamber during the STM experiments performed in-situ (see chapter 3.3.2). The related difference is here attributed to the change of sample surface conditions occurring upon atmosphere exposure. The presence of water, different groups of hydrocarbons and other contaminant elements adsorbed on the surface of the Pd layer may drastically change the activation barrier for dissociation of the hydrogen molecule and may slow down the kinetics of hydrogen absorption. Thus, within the measured time span, by applying similar hydrogen pressures to the atmosphere-exposed samples, the observed lattice changes are very small. Furthermore, the still slow kinetic of hydrogen absorption, observed at  $p_H = 1.3 \times 10^{-3}$  mbar (see the time scale in Fig. 3.8) suggests that an applied over-potential of hydrogen pressure at the Pd / vacuum interface does not drastically change the phase transformation process in the related samples (as compared to the in-situ STM experiments). Thus, based on this assumption, STM measurements performed on the very local nano-scale and XRD measurements performed on the much larger macro scale can complement each other, despite the fact that applied hydrogen pressures in these experiments are different.

The unloading of the XRD samples was realized by using an experimental trick. It was found that at the available vacuum conditions ( $p_{background} \leq 1 \times 10^{-5}$  mbar), hydrogen desorption runs very slowly at RT and samples could not be completely unloaded by pumping. Opposite to this, in the presence of oxygen all samples demonstrated relatively fast hydrogen desorption from Nb-H films. Thus, sample exposure to the atmosphere (breaking the vacuum condition in the chamber) or the exposure to oxygen gas in the loading chamber were used to facilitate the unloading. Successful unloading was confirmed by a backward shift of the Nb (110) XRD peak and a simultaneously drop of the resistance. Thereby, the hydrogen release was observed within about 1 - 2 hours, depending on the film thickness and sample loading history.

## 3.6 Electrochemical hydrogen loading

### 3.6.1 Electromotive Force (EMF) measurements

For some measurements, hydrogen was introduced into the films by electrochemical loading. This allows for determination of the hydrogen content in the sample. Electrochemical loading was performed using a 2:1 volume mixture of 85% glycerin and 85% phosphoric acid as an electrolyte [125]. The loading setup consists of a current source, an impedance converter, a counter electrode (Pd), and a reference electrode (Ag/AgCl<sub>sat.</sub>), as described in Kirchheim & Pundt [67].

The number of hydrogen atoms  $\Delta n_H$  per metal atoms  $n_M$ , or equivalently the concentration increase  $\Delta C_H$ , was directly measured via the electrical charge  $Q$ , and Faraday's law:

$$\Delta c_H = \frac{\Delta n_H}{n_M} = \frac{Q}{F} \cdot \frac{V_M}{V_S} \quad (3.8)$$

with  $F$  being the Faraday constant,  $V_S$  - the sample's volume and  $V_M$  - its molar volume. By controlling the loading current  $I$ , and the loading time  $t$ , the hydrogen concentration in the sample can be increased ( $Q = I \cdot t$ ). Hereby, hydrogen atoms produced at the sample surface diffuse in and the process is observed as a change of electromotive force (EMF) curve. In this study, the electromotive force EMF was measured against an Ag/AgCl<sub>sat.</sub> reference electrode (SCHOTT Instruments GmbH) to control the loading / unloading process.

In general, hydrogen can be charged step-by-step (stepwise loading mode) or continuously, by use of a certain fixed ion current (continuous loading), in the sample. If the loading is performed in the stepwise mode, the EMK value is allowed to equilibrate. Because the EMK value is linked to the chemical potential of hydrogen in the system, the corresponding hydrogen partial pressure can be calculated by use the Nernst equation [126]:

$$p_{H_2} = p_0 \cdot \exp\left(\frac{(U - U_0)n_e F}{RT}\right) \quad (3.9)$$

Where,  $U$  is the measured electromotive force (EMF) value,  $U_0$  is the standard potential of reference electrode (0.2223 V for the Ag/AgCl<sub>sat.</sub> electrode at 298 K [127]),  $n_e$  is the number of electrons related to the reaction ( $n = 1$  for hydrogen),  $R$  is the gas constant,  $T$  is the temperature and  $p_0 = 1 \text{ bar}$  is a standard pressure. Hereby, the EMF value  $U$  of a hydrogen - loaded film is linked with a chemical potential  $\mu_H$  via [128]:

$$U = U_0 + \frac{\mu_H}{F} \quad (3.10)$$

In this study, both, stepwise electrochemical loading and continuous electrochemical loading with a constant current were applied depending on the addressed film thickness. Continuous electrochemical loading was especially required for thinner samples to minimize the effect of hydrogen loss. To perform in-situ stress measurements, the electrochemical loading cell was combined with an induction gauge required for the stress measurements arising in the film upon hydrogen loading. The details about this composite set up are given in the next section.

### 3.6.2 In-situ stress measurements during electrochemical hydrogen loading

Mechanical stress and stress release strongly influence the thermodynamics of metal-hydrogen systems. Therefore, stress measurements are required to quantify the in-plane stress arising during hydrogen loading and to study the impact of the film thickness on the mechanical stress arising during the phase transformation. To determine the hydrogen-induced stress and the final stress state, in-situ substrate curvature measurements were carried out in combination with EMF measurements (see chapter 3.6.1). For the stress measurements, the setup shown in Fig. 3.9 was used [17], [127]. The films themselves were deposited on long and thin sapphire substrates of  $30 \times 7 \times 0.1 \text{ mm}^3$ , as required for sufficient substrate bending [35]. For the measurements, the samples were mounted on the sample holder placed inside the loading cell. To facilitate electrochemical hydrogen loading, the loading cell containing the sample was filled with electrolyte (Glycerin+ $\text{H}_3\text{PO}_4$ , see chapter 3.6.1).

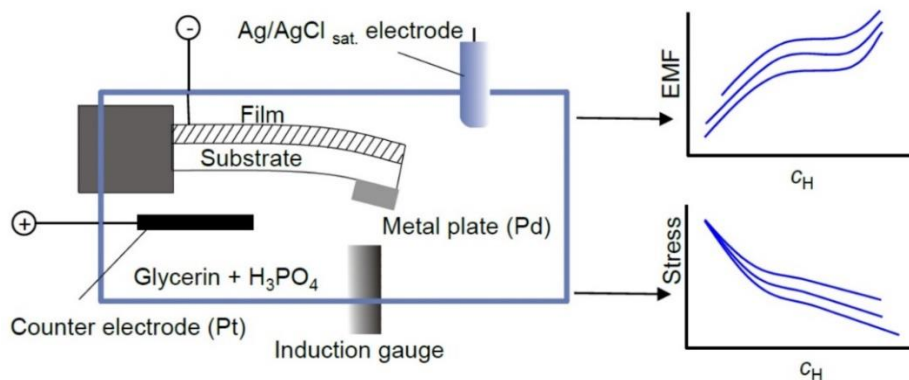


**Fig. 3.9** Schematic illustration of stress measurements set up [127]. From the substrate curvature, the in-plane stress arising in the film upon hydrogen loading can be measured (bottom right corner). Additionally,  $\text{Ag}/\text{AgCl}_{\text{sat}}$  reference electrode can be used to measure change of EMF value (top right corner). Reproduced from R. Gemma, *Hydrogen in V-Fe thin films and Fe/V-Fe multi-layered thin films*, Dissertation, Universität Göttingen 2011, with permission.

The sample was mounted in the way that one side was tightly fixed, while the opposite one stayed freely suspended. For the experiment its position was adjusted so that the backside of the sample connected with a small Pd plate could come close to the induction gauge (Dornier COMPANY) mounted at the bottom of the cell as shown in Fig. 3.9. The basic idea lying behind these measurements is that the distance between the metal plate i.e. the sample and the gauge can be measured by a voltage, in a certain range. Thereby, the voltage has a linear relationship with the distance that can be precisely calibrated for the particular sensor [129]. According to the calibration of the sensor applied in this study, the calibration factor  $\tau$  was  $7.6 \text{ mV}/\mu\text{m}$  (for the Pd plate). Further, when an electromotive force is applied, hydrogen absorption / desorption causes a development of in-plane stress in the film that implies a bending of the  $0.1 \text{ mm}$  thin substrate. Thereby, the radius of curvature varies and can be directly measured. The resulting change of sample-gauge distance  $z$  is detected as change of capacitance  $\Delta U$  [127]. Therefore,

$$z = \frac{\Delta U}{\tau} \quad (3.11)$$

Thereafter, the radius of curvature  $R$  required for the stress calculation can be obtained from  $z$  and length of the sample [17]:

$$R \approx \frac{L^2}{2z} \quad (3.12)$$

Finally, the in-plane stresses, arising in the film upon hydrogen loading / unloading, can be calculated according to Stoney's equation [74], [130]:

$$\sigma = \frac{E_s d_s^2}{6(1 - \nu_s) d_f} \frac{1}{R} \quad (3.13)$$

This equation was first suggested in 1909 and since that time was many times approved and used for stress calculation in the variety of different systems [14], [127], [131]. Here the indexes  $S$  (substrate) and  $F$  (film) indicate on the attitude of parameters used in the equation to the substrate or the film particular features.  $E_s$  is a Young's (elasticity) modulus of the substrate,  $\nu_s$  is a Poisson's ratio of the substrate,  $d_s$  and  $d_f$ , respectively, thicknesses of the substrate and the film.

All the stress calculations performed in this study were done under the assumption that the hydrogen atoms absorb practically only in the Nb layer and, that the Pd capping layer works only as a pathway for hydrogen diffusion from the Pd / electrolyte interface into the Nb-layer. This treatment is supported by the experimental finding in the XRD pattern of a stable Pd peak position upon hydrogen loading as shown in Fig. 3.8. Therefore, hydrogen absorption in the Pd cap layer was neglected.

## 4 Optimization of the initial film surface topography and microstructure

(110) oriented Niobium films can be epitaxially grown on  $\text{Al}_2\text{O}_3$  (11-20) substrates, at elevated temperatures of about  $800^\circ\text{C}$  as shown in chapter 2.2. To allow for in-situ STM-surface studies on hydride precipitation and growth, “closed” surface topographies with low initial roughness and large terrace sizes are targeted. This is of special interest, because rough or even holey surfaces can lead to modified local stress states. Especially for ultra-thin films, holes may even meet the substrate surface leading to complete stress release in some parts of the films. The impact of the stress state on the thermodynamics is of major importance, as demonstrated in chapter 2.4.8.

In order to perform in-situ STM measurements of the desired atomically smooth and “closed” surfaces,  $T_d$  was optimized for our specific vacuum system for different film thicknesses. Therefore, the surface topography of the films of different thickness  $d$  and deposition temperature  $T_d$  was studied by STM. To minimize the number of parameters to be considered, the deposition rate and the substrate miscut were fixed to  $0.8 \pm 0.1 \text{ nm / min}$  and to  $0.1^\circ$ , respectively. To avoid “open” meander-like surface topographies, a lower temperature range  $T_d \leq 820^\circ\text{C}$  was considered.

### 4.1 Optimization of the initial surface topography

To perform experiments on Nb thin films with defined surface conditions, the proper growth temperature has to be determined to exclude the formation of “rough” and “open surfaces” (meander-like surfaces [36], [37]). Hereby, the best desired surface type: “2D surface” should contain large terraces and possess small topography changes within the measured STM frame size.

50 nm Nb film prepared in the UHV vacuum system shown in Fig. 3.1 and deposited at  $T_d$  of about  $800^\circ\text{C}$  appears smooth. A typical STM surface-image of a 50 nm Nb film is shown in Fig. 4.1 (a). As one can see, the film topography consists of atomically flat terraces of 50 nm - 60 nm lateral size and has a relatively small number of local surface corrugations of 2 nm height. This kind of surface topography in the actual study is labeled conditionally as a “2D surface”. The visible surface steps between the neighboring terraces have a height of 0.25 nm - 0.7 nm, as shown in the line profile of Fig. 4.1 (a). As one atomic layer in the  $\langle 110 \rangle$  direction is about 0.233 nm, from the bulk lattice constant, this is about one to three atomic steps in  $\langle 110 \rangle$  directions. The total height difference in Fig. 4.1 (a) is 4 nm over the full  $500 \text{ nm} \times 500 \text{ nm}$  sized area. Additionally, some holes of about 3 nm amplitude are present at the film surface.

A typical STM image of a 30 nm Nb film deposited at  $T_d = 780^\circ\text{C}$  is shown in Fig. 4.1 (b). The film surface consists of atomically flat small terraces of about 30 nm lateral size, distinguishable by atomic steps of about 0.2 nm (Fig. 4.1 (b)). These atomic steps are, most probably, related to dislocations spacing.

Hereby, the observed surface corrugation is of about 5 nm. Thereby, a relatively high topographic roughness of 0.486 nm was detected on a  $250 \times 250 \text{ nm}^2$  sized area.

20 nm Nb-film prepared at  $T_d = 800 \text{ }^\circ\text{C}$  show a strong change in the surface topography [36]. Here, an “open” meander-like surface topography with many pit-holes is found. As shown in a typical STM-image of this film in Fig. 4.1 (c), pit holes of about 4 nm average depths were detected with the STM-tip. These pit holes could be even deeper because of the limited depth resolution of the STM due to the natural radius of curvature of the STM-tip. Hereby, the total height difference in Fig. 4.1 (c) over the full  $1000 \times 1000 \text{ nm}^2$  sized area is about 9 nm that is a big magnitude as compared to the film thickness itself.

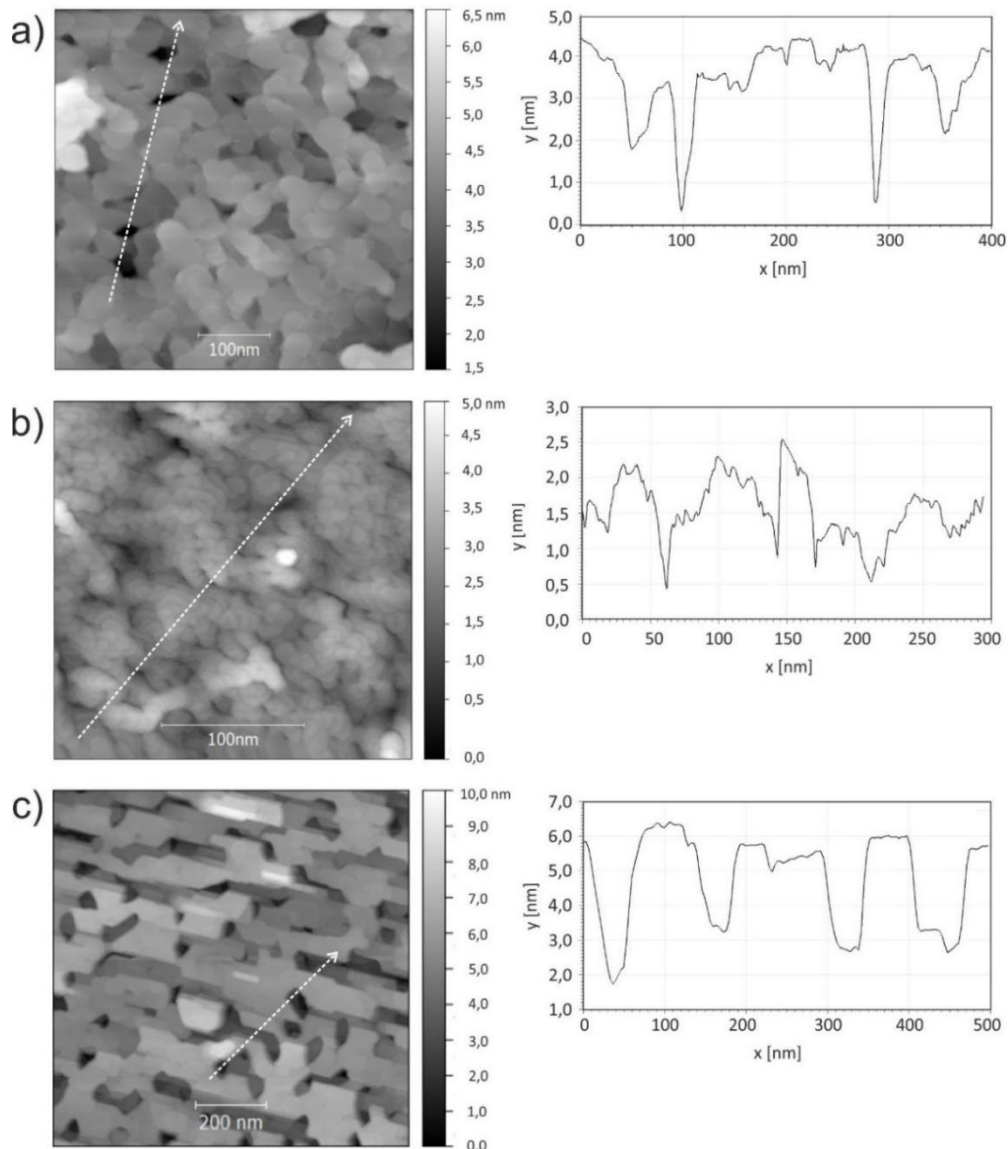


**Fig. 4.1** Influence of the film thickness ( $T_d = 800 \pm 20 \text{ }^\circ\text{C}$ ) **a)** 50 nm Nb film deposited at  $800 \text{ }^\circ\text{C}$  and corresponding linear profile marked with a white dotted line. It shows a smooth surface with large terraces of 50 nm - 60 nm size, no pit-holes are detected; **b)** 30 nm Nb film deposited at  $780 \text{ }^\circ\text{C}$ . The linear profile marked with a white dotted line shows a maximum height difference of 2 nm. The surface is very smooth without any sign of “open” surface topography; **c)** 20 nm Nb film deposited at  $800 \text{ }^\circ\text{C}$  (Figure created by author from data originally published by Pundt et al. [36]). Regular meander-like “open” 2D structure with deep valleys of 4 nm is visible. (Frame size: (a)  $500 \times 500 \text{ nm}^2$ , (b)  $250 \times 250 \text{ nm}^2$  and (c)  $1000 \times 1000 \text{ nm}^2$ )

Reduction of the deposition temperature up to  $T_d \approx 740$  °C leads to a decrease of the absolute surface roughness and reduces the pitted topography. It is exemplary shown in Fig. 4.2 (a) for a 15 nm film. This film possesses a smooth 2D surface topography with a roughness of 0.15 nm. A maximum height difference of 1.5 nm is detected on a  $500 \times 500$  nm<sup>2</sup> sized area. The film surface consists of atomically flat terraces of 50 nm - 60 nm size in diameter and shows traces of dislocations. The visible surface steps have a height of 0.2 nm - 0.4 nm, related to 1 to 2 atomic steps in  $\langle 110 \rangle$  lattice direction, as shown in the linear profile. A similar result was obtained for 25 nm Nb films prepared at  $T_d \approx 730$  °C.

Further reduction of the deposition temperature  $T_d$  leads to a strong change of the surface topography. Fig. 4.2 (b) shows an STM image of a 20 nm Nb film deposited at  $T_d = 670$  °C. Temperature reduction results in decreasing domain sizes and, again, increasing maximum height differences. The surface hillock density gets high. Hillocks are homogeneously distributed over the sample surface. Some prominent hills of 1 nm - 2 nm height and 10 nm - 20 nm diameter appear on the film surface, as shown in the linear profile. This undesired kind of surface topography in the actual study is labeled conditionally as a "3D surface". Because of the large number of hillocks, forming surface topography, the surface roughness increases up to 0.27 nm.

This 3D surface topography is even more pronounced when  $T_d$  is further reduced. Figure 4.2 (c) shows the surface topography of a 10 nm film deposited at 570 °C. It shows that the 3D surface topography dominates. Homogeneously distributed hillocks with an average diameter of about 15 nm are clearly seen on the film surface. A maximum height difference of 2.2 nm and a roughness of 0.26 nm are detected on a  $500 \times 500$  nm<sup>2</sup> sized area.

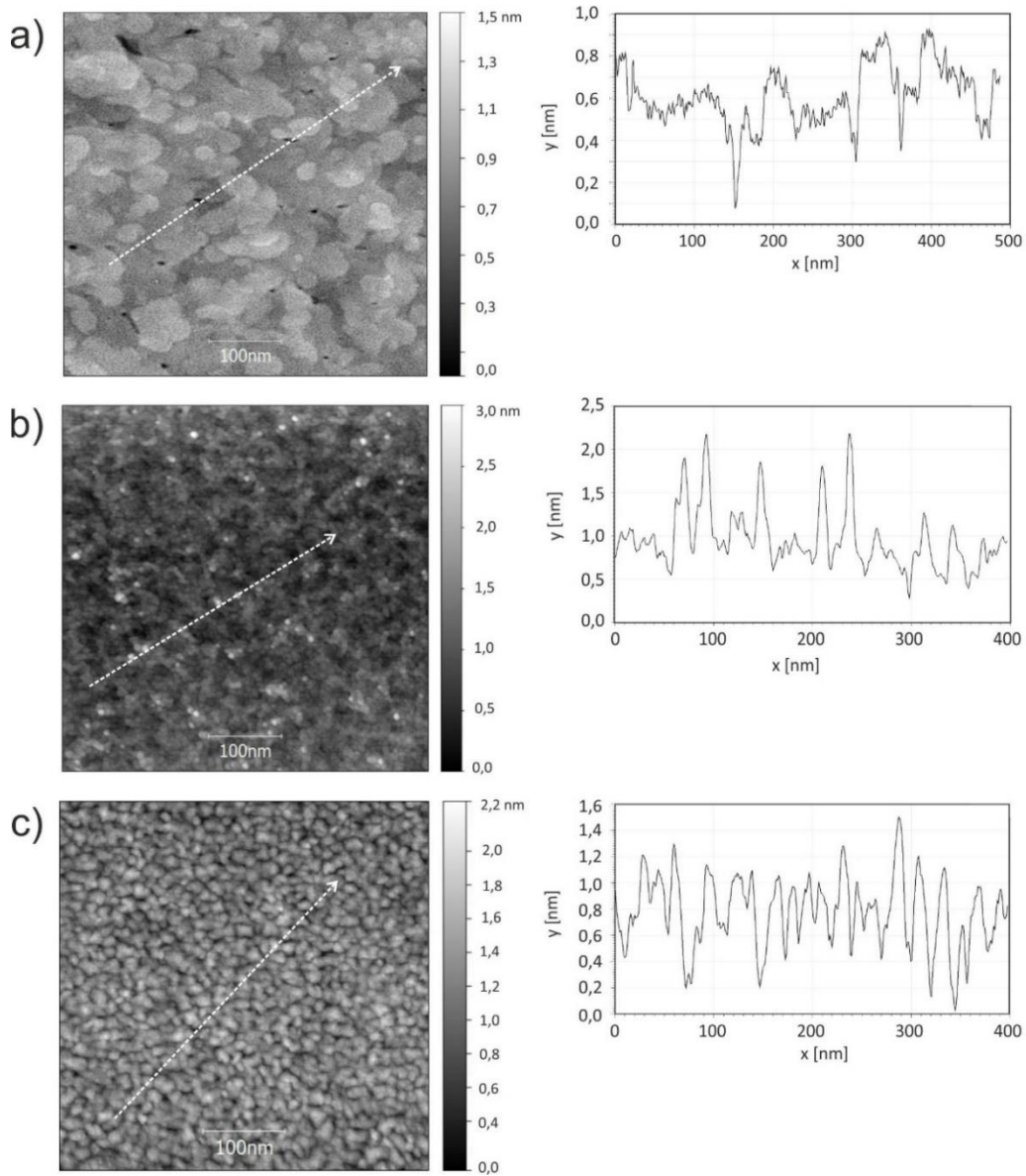


**Fig. 4.2** Influence of deposition temperature ( $d = 15 \pm 5$  nm) **a)** 15 nm Nb film deposited at  $740^\circ\text{C}$ . The linear profile marked with a white dashed line shows a maximum height difference of 1 nm. The surface is very smooth without any sign of “open” surface topography. This kind of surface topography in this study is labeled conditionally as “2D surface”. **b)** 20 nm Nb film deposited at  $670^\circ\text{C}$ . The linear profile shows surface hillocks of 1.0 nm - 1.5 nm in height and 10 nm - 20 nm in diameter. This kind of surface topography in this study is labeled conditionally as “3D surface”. **c)** 10 nm Nb film deposited at  $570^\circ\text{C}$ . Linear profile clearly demonstrates a “3D surface” consisting of homogeneously distributed hillocks with an average diameter of about 15 nm and height of about 1.0 nm - 1.5 nm. (Frame size:  $500 \times 500$  nm<sup>2</sup>)

A schematic overview based on many STM measurements on different films, observed within this study, is shown in Fig. 4.3. Every symbol represents a set of STM measurements performed on a single sample. Hereby, the film topography is characterized for different film thicknesses ( $d$ ) and deposition temperatures ( $T_d$ ). For classification, three different parameters are selected: the lateral size of the terraces / hills, the maximum height difference within the STM surface-image and the topographic roughness (RMS). The analyzed frame sizes used for statistical consideration were:  $500 \times 500$  nm<sup>2</sup> and

1000 × 1000 nm<sup>2</sup>. The surface topographies were conditionally distinguished in i) 2-dimensional (2D) topographies, consisting preferentially of smooth terraces; ii) 3-dimensional (3D) topographies consisting of relatively high hillocks homogeneously distributed and forming a rough surface topography, and iii) those topographies showing a mixture of both (2D-3D). Further, as it was shown in Fig. 4.1 (c), the 2D surface topography can have holes, pits or meander-like features. In this study, it is labeled as “open” surface topography and is undesired. In Fig. 4.3, this kind of surface topography is marked by using half-filled square symbols.

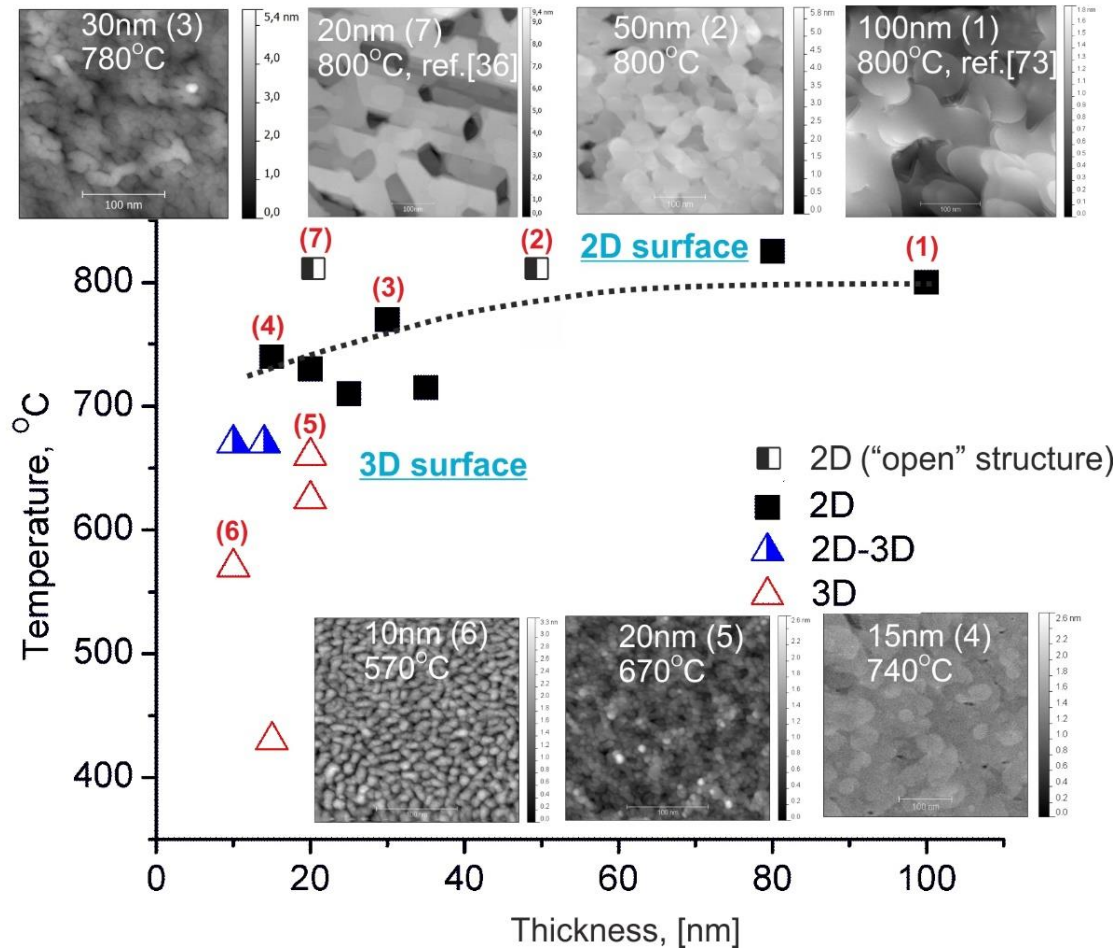


**Fig. 4.3.** Film topography as a function of deposition temperature and film thickness, categorized into 2D “open” (pitted), 2D “closed” and 3D surfaces topographies. The dashed line marks occurrence of 2D “closed” surfaces. Data from Nörthemann et al. are also implemented [36], [73]. Frame sizes are about 500 × 500 nm<sup>2</sup>.

Further, Fig. 4.3 provides a black dotted line carried out by hand. It represents the “optimal” deposition temperature for Nb-films of different thickness in case when an appearance of smooth 2D “closed” surface is desired. In details, Fig. 4.3 shows that “2D surfaces” appear above the dotted line and “3D surfaces” appear below this dotted line. Relatively thick epitaxially grown Nb films ( $d > 50$  nm)

prepared at  $T_d \approx 800^\circ\text{C}$  have mainly closed atomically flat surface topographies. This observation is confirmed as well by Nörthemann's STM data on thicker films [73]. Thinner films may possess "open" meander-like structures, when prepared at the same temperature. When the deposition temperature is slightly decreased to about  $740^\circ\text{C}$  for films with  $d < 50\text{ nm}$ , the meander-like topographies doesn't appear and the surface has the targeted 2D "closed" surface with a low surface roughness ( $\leq 0.25\text{ nm}$ ) and small surface corrugations ( $\leq 2\text{ nm}$ ). Hereby, the temperature should not be reduced too much, since it will affect the microstructure and film quality.

To summarize, Nb films of different thickness, required for the hydrogen loading / unloading experiments can be prepared at "optimal" deposition temperatures that is represented by the black dotted line in Fig. 4.3.

## 4.2 Initial film texture

The films' epitaxy conditions were studied by texture measurements in (110) lattice direction presented in stereographic projection. Figure 4.4 shows a typical pole figure for a 25 nm thick Nb (110) film deposited on  $\text{Al}_2\text{O}_3$  (11-20), as deposited at  $T_d = 740^\circ\text{C}$ . The (110) texture measurements exhibit epitaxial growth of Nb films on the  $\text{Al}_2\text{O}_3$ -substrate. In the pole figure, reflexes typical for the (110) epitaxy are clearly visible and linked with red dotted lines. The main reflex corresponding to the out-of-plane direction is placed in the middle while four other reflexes are detected at the tilting angle  $\psi = 60^\circ$  that corresponds to the theoretically expected value [73]. A random in-plane grain orientation would yield to an appearance of a ring at this tilting angle.

Similar pole figures were obtained for other films (25 nm and 50 nm) prepared in a temperature range from  $710^\circ\text{C}$  to  $820^\circ\text{C}$ , as covers the temperature range used in this study. It is concluded that all films used for this study are epitaxially matched to the  $\text{Al}_2\text{O}_3$  substrate.

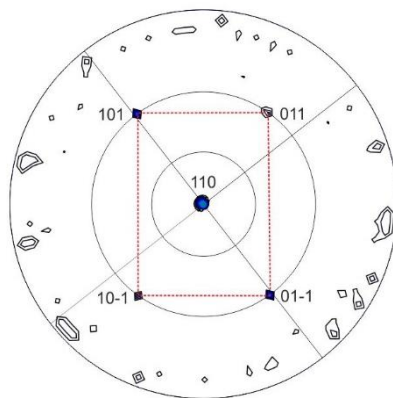


**Fig. 4.4** (110) pole figure of a 25 nm Nb deposited on (11-20) Sapphire substrate at  $T_d = 740^\circ\text{C}$ . The main reflex corresponding to the out-of-plane direction is placed in the middle, while four other are detected at the tilting angle  $\psi = 60^\circ$ .

### 4.3 Initial film stress

As presented in chapter 3.5.1, the films' intrinsic microstructure was studied by means of X-ray diffraction. Figure 4.5 exemplary shows a typical XRD pattern obtained in result of  $\vartheta$ - $2\vartheta$  geometry and measured in the "as-prepared" state before the sample was exposed to hydrogen. This particular example presents a 17 nm Nb (110) film deposited on Al<sub>2</sub>O<sub>3</sub> (11-20) and covered with a 20 nm Pd capping layer. Deposition of the Nb layer was performed at 750 °C. This deposition temperature lies close to the optimal  $T_d$  for this film thickness, as it is given in Fig. 4.3.

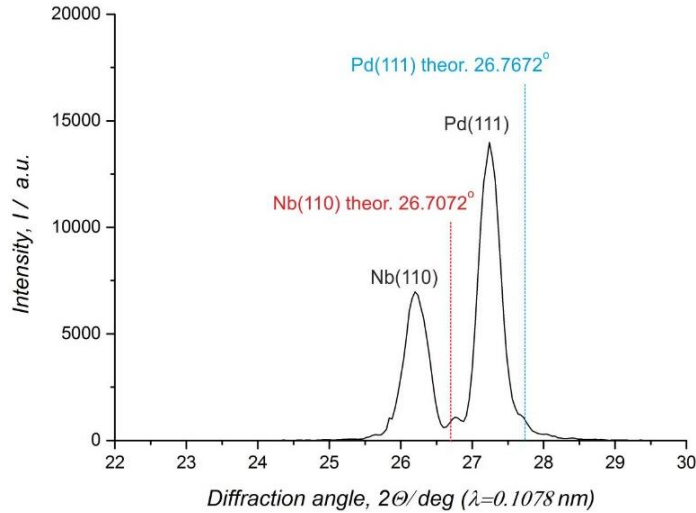


**Fig. 4.5**  $\vartheta$ - $2\vartheta$  XRD scan of Nb (110) film deposited on Al<sub>2</sub>O<sub>3</sub> (11-20) sapphire substrate at  $T_d = 750$  °C and covered with a Pd capping layer. Theoretically expected  $2\vartheta$  positions of Nb and Pd bulk are marked with colored lines. Initially presented in the film out-of-plane expansion is visible. The thicknesses of Nb and Pd layers are 17 nm and 20 nm, correspondently.

The two peaks of Nb (110) and Pd (111) are detected in Fig. 4.5 at about  $2\vartheta = 26.22$  ° and at  $2\vartheta = 27.25$  ° respectively. The Al<sub>2</sub>O<sub>3</sub> (11-20) single crystal peak ( $2\vartheta = 26.84$  °) is not visible since  $\chi = -0.5$  ° offset was applied, as it is discussed in chapter 3.5.3. Additionally, two dashed lines corresponding to the theoretically expected peak positions for bulk Nb and Pd are shown using Bragg's law (Eq. 3.2 with  $a_{Nb} = 0.33004$  nm,  $a_{Pd} = 0.38907$  nm [133] and  $\lambda = 0.1078$  nm). Thus, one can see that the Nb film and the Pd layer are expanded out-of-plane, implying that they are under in-plane compressive stress. This result was common for all samples measured in the "as-prepared" state. However, the state of the initial lattice expansion alters by changing the thickness of the Nb film. By decreasing the film thickness, the initial lattice expansion in the out-of-plane direction was getting stronger and, hence, the in-plane compression was increasing as well. A rough calculation of the initial stress in the Nb films was performed by use of the prediction of the linear elastic model discussed in chapter 2.3.2. For this, Eq. 2.18 was applied.

As a first approximation, the initial strain  $\varepsilon$  was determined from the deviation of  $d_{exp}(110)$  from the theoretically expected value ( $d_o(110) = 0.2333$ ). The lattice expansion and assumed stresses for different film thicknesses are given in Table 4.1.

**Table 4.1** Initial lattice expansion and related in-plane stress for different film thicknesses

Thickness $d$ [nm]	Initial lattice expansion $\left(\frac{d_{exp}(110)-d_o(110)}{d_o(110)}\right)$	Initial in-plane stress $\sigma_o$ [GPa]
105	0.0113	-1.45
60	0.0155	-2.01
30	0.0172	-2.23
17	0.0186	-2.43
8	0.0203	-2.64

The calculated stress lies at about -2 GPa. Because the linear elastic treatment does not allow stress release, the calculated values are most probably overestimated. Nevertheless, high initial stress is clearly present in the system in the “as-prepared” state. Their presence can be attributed to the strong adhesion between the film and the substrate and reduced stress release expected for the addressed film thickness range. Recently, Wagner further pointed out that the presence of peening atoms has to be considered for proper stress determination from XRD peak positions [14]. Any peak shifts should be discussed with respect to the peak of the “alloy”. For Pd films, Wagner determined a factor of 2 overestimation for all stress values. Transferring this to the results on Nb-films, this would mean that the initial in-plane stress values have to be divided by a factor of two.

#### 4.4 Pd islands on the Nb film surface

As it was already mentioned in chapter 3.1, in the case of in-situ hydrogen gas loading STM measurements performed at RT, a Pd catalyst of less than 0.5 monolayer thickness ( $\approx 0.1$  nm - 0.2 nm) was deposited onto the top of Nb layer. An example of the surface topography of a Nb film containing Pd-islands, measured directly after the sample preparation, is given in Fig. 4.6 (a, b). Small Pd islands with a lateral size of about 3 nm - 4 nm and height of less than 0.2 nm are clearly visible in the line profile presented in Fig. 4.6 (b). The islands are homogeneously distributed over the sample surface and can be recognized in the enlarged STM image in Fig. 4.6 (a), right side, as tiny spots. The density of these Pd islands is high, resulting in center-to-center distances between the islands of about 5 nm.

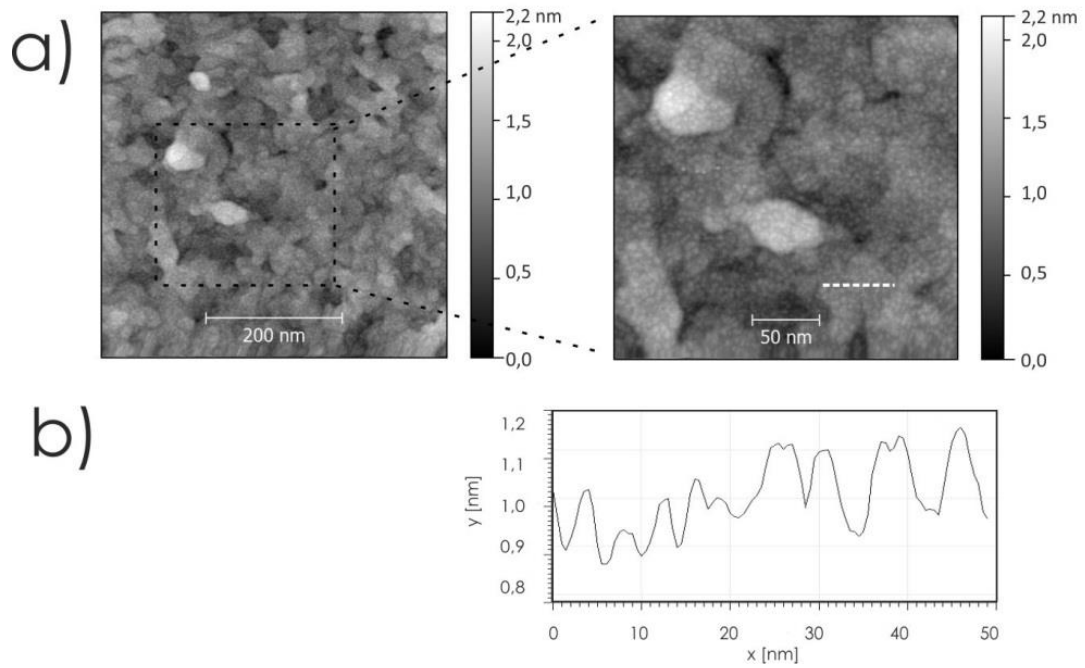


**Fig. 4.6 a)** STM surface-image of Nb film with a tiny Pd island added on the top. They are homogeneously distributed over the sample surface and visible as tiny spots. **b)** Linear profile measured across the surface and marked with a white dotted line in the zoomed in STM surface-image. Small Pd island with a lateral size of about 3 nm - 4 nm and height less, than 0.2 nm are visible.

## 5 Results and individual discussion on hydrogen loaded films

This chapter presents the results on in-situ hydrogen loading studies on Nb films of different thickness. The thickness of the Nb film ( $d$ ) is varied from 105 nm to 5 nm and it is considered as the main experimental parameter. In-situ hydrogen gas loading STM- and XRD- measurements as well as EMF-, stress-measurements and electrical resistance-measurements were carried out. The results are organized by the chosen experimental method and subdivided by the variation of the film thickness.

Due to the large number of different aspects addressed by the variety of experimental techniques (STM, XRD, EMF, stress measurements and electrical resistance measurements), sub/discussion and method related data interpretation will be individually given (when it is required for better intermediate result understanding) already in this chapter.

### 5.1 STM results on hydrogen loaded films

Results on different Nb-H films with a thickness  $d$  ranging from 55 nm to 8 nm are here presented. This thickness range is chosen as it includes the predicted critical thickness of 26 nm suggested by Nörthemann et al. [19], whose occurrence was not yet proven experimentally. Thereby, different samples are considered with thicknesses  $d$ , lying close to the theoretical value, as well as lying well above and well below this value. Hereby, hydride phase precipitation and growth, coherency state and dislocation occurrence will be addressed. The obtained results will be summarized in chapter 5.1.6.

#### 5.1.1 55 nm Nb-H film

##### 5.1.1.1 Morphology change upon hydrogen loading of a 55 nm Nb-H film

To study phase transformation in 55 nm Nb-H films the hydrogenation process was controlled by applying two independent techniques: in-situ STM and in-situ electrical resistance measurements. The Nb film was loaded with hydrogen at hydrogen gas pressures  $p_H$  ranging from  $p_H = 3.3 \times 10^{-9}$  mbar to  $p_H = 4.3 \times 10^{-6}$  mbar. Details regarding  $p_H$  and  $t_e$  for this measurement, are given in Table 5.1.1.

**Table. 5.1.1** Experimental steps for a 55 nm Nb film

Experimental step	$p_H$ [mbar]	$t_e$ [min]
<i>i</i>	$3.3 \times 10^{-9}$	250
<i>ii</i>	$7 \times 10^{-7}$	208
<i>iii</i>	$1.4 \times 10^{-6}$	910
<i>iv</i>	$< 5 \times 10^{-9}$ (Unloading)	300
<i>v</i>	$4.3 \times 10^{-6}$	370
<i>vi</i>	$< 1.1 \times 10^{-9}$ (Unloading)	5370

Surface changes caused by hydrogen loading are presented in Fig. 5.1.1 (a-e) for some representative loading states. The frame size for all the images is  $2000 \times 2000 \text{ nm}^2$ . Figure 5.1.1 (a) shows the STM surface-image before the sample was exposed to hydrogen gas. The initial surface in the area of interest is relatively flat with a topographic roughness of about  $\sigma_{\text{RMS}} = 0.44 \text{ nm}$ .

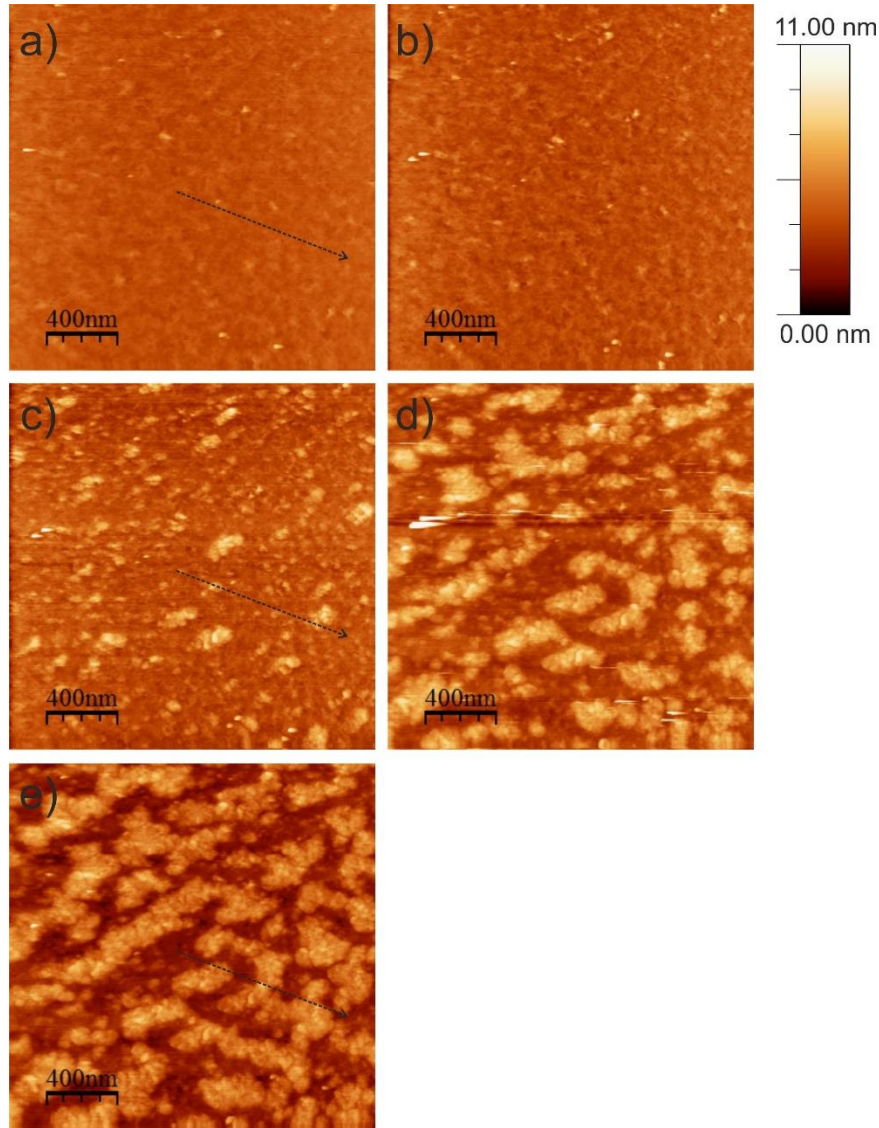


**Fig. 5.1.1** STM surface-image of a 55 nm Nb film: **a)** shortly before applying hydrogen pressure; **b)** during loading the sample at  $p_H = 7 \times 10^{-7} \text{ mbar}$  for  $t_e = 197 \text{ min.}$ ; **c)** during loading the sample at  $p_H = 1.4 \times 10^{-6} \text{ mbar}$  for  $t_e = 285 \text{ min.}$ . Elevated (bright) regions, corresponding to local hydride phase precipitation are detected; **d)** during loading the sample at  $p_H = 1.4 \times 10^{-6} \text{ mbar}$  for  $t_e = 905 \text{ min.}$  Hydride related surface change includes about 42 % of the STM image; **e)** during loading the sample at  $p_H = 4.3 \times 10^{-6} \text{ mbar}$  for 370 min. Hydride related surface change includes about 56 % of the STM image. (Frame sizes:  $2000 \times 2000 \text{ nm}^2$ ).

After the pressure increase to  $p_H = 7 \times 10^{-7} \text{ mbar}$ , the STM surface images do not show any significant change. The STM surface-image in Fig. 5.1.1 (b), for example, was taken after hydrogen loading for about  $t_e = 208 \text{ min}$  at  $p_H = 7 \times 10^{-7} \text{ mbar}$ .

Upon the second pressure increase to  $p_H = 1.4 \times 10^{-6}$  mbar, the sample surface visibly changes, as it is shown in Fig 5.1.1 (c). This particular STM image was taken after loading the sample at  $p_H = 1.4 \times 10^{-6}$  mbar for  $t_e = 285$  min. The observed local surface corrugations reach a typical lateral size in a range of 100 nm – 200 nm as shown in the linear profile in Fig. 5.1.2 (a, green curve). Figure 5.1.2 (a) shows linear profiles measured along the black dotted lines in Fig. 5.1.1 (a, c, e). Further, the presence of new surface corrugations on the film surface produces a quite broad distribution in the height change from 2 nm to 4 nm as visible in the corresponding height distribution histogram in Fig. 5.1.2 (b, green curve). Figure 5.1.2 (b) shows the height distribution histograms of the same area of interest measured for different experimental stages during the hydrogen loading / unloading experiment. During further hydrogen loading, the already modified surface topography areas continued to extend, as visible in Fig 5.1.1 (d) ( $p_H = 1.4 \times 10^{-6}$  mbar,  $t_e = 905$  min), in Fig. 5.1.1 (e) ( $p_H = 4.3 \times 10^{-6}$  mbar,  $t_e = 370$  min) and additionally shown in Fig 5.1.2 (a) (marked by arrows). Furthermore, these hydrogen-induced surface corrugations detected in the area of interest at the late loading stage, demonstrated in Fig. 5.1.1 (e), significantly change also the height distribution histogram, as shown in Fig. 5.1.2 (b, red curve). Here, an additional peak separated from the main peak (mid-plane) by about 2.9 nm appears in the graph. In other words, it means that the new surface topography, in average, has a height change of about of 2.9 nm with respect to the base level. However, the height distribution is relatively broad and shows that some elevated surface regions reach significantly higher values of up to 6 nm, as also visible in Fig. 5.1.2 (a).

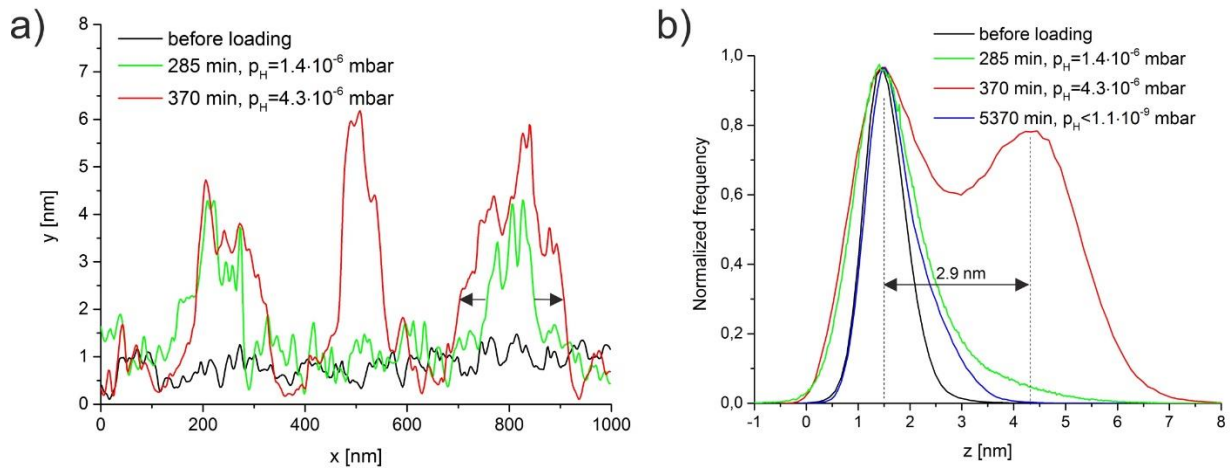


**Fig. 5.1.2 a)** Linear profiles measured along the black dotted lines in Fig. 5.1.1 (a, c, e). Locally growing hydride precipitates have a lateral size of about 200 nm and height variation from 2 nm to 6 nm. **b)** Height distribution histograms describing the STM images in Fig. 5.1.1 (a, c, e): before hydrogen loading (black curve); during hydrogen loading at  $p_H = 1.4 \times 10^{-6}$  mbar,  $t_e = 285$  min (green curve); during hydrogen loading at  $p_H = 4.3 \times 10^{-6}$  mbar,  $t_e = 370$  min (red curve); after sample unloading for  $t_e = 5370$  min at  $p_H < 1.1 \times 10^{-9}$  mbar (blue curve). Red curve has two peaks, separated by 2.9 nm and corresponding, respectively, to Nb-H  $\alpha$ -phase regions (on the left side) and Nb-H  $\beta$ -hydride phase regions (on the right side). Upon hydrogen unloading the second peak disappeared and only small shoulder present on the right side of the main peak shows that hydride related surface corrugation are still present on the sample surface.

Based on the previous results for thicker Nb-H films (see chapter 2.4.5), the magnitude of hydrogen pressures applied in the system (see chapter 2.4.8) and the magnitude of surface corrugations, detected on the surface (see Table 2.1), the observed topography changes were attributed to hydride formation occurring in the film. As already described, hydride precipitates grow through the complete film and, because of the local volume expansion, their upper part and their expansion become visible on the sample surface (see chapter 2.4.2). The amplitude of surface corrugations appearing on the sample surface due to the hydride formation depends on the particular film thickness and the width of the miscibility gap (see chapter 2.4.2), while their shape depends mainly on the elastic properties of the system and the state of the coherency in the underlying hydrides (see chapter 2.4.5). For the 55 nm film a rough estimation of topography change according to the linear elastic approach (see Table 2.1, assumed  $\Delta c = 0.4$ ) gives the expected maximum surface corrugations of about  $\Delta z = 2.99 \text{ nm}$ . This value stays in a good agreement with the experimentally observed average amplitude of surface corrugations shown in Fig. 5.1.2 (b), but it is significantly smaller than the maximum height change detected within the STM frame of Fig. 5.1.1 (e).

Therefore, as the observed surface topographies result from the underlying hydride precipitates in the film, the development of the hydrides precipitates themselves at this point will be included in the description. Herewith, the area fraction of surface corrugations with respect to the total area within the frame, detected by STM, can be approximated with the volume fraction of the hydride phase with respect to the total film volume, as presented in chapter 2.3.3. For instance, the volume fraction of the hydride phase in the loading state shown in Fig. 5.1.1 (d) was about 42 %, while in Fig. 5.1.1 (e) it increased to about 56 %. Thus, according to Fig. 5.1.1 (e) the sample volume was not completely transformed into the hydride phase even after increasing the hydrogen pressure to  $p_H = 4.3 \times 10^{-6} \text{ mbar}$  for  $t_e = 370 \text{ min}$ .

The related resistance curve that was measured simultaneously on a similar sample and at the same experimental hydrogen pressures is shown in Fig. 5.1.3. In details, Fig. 5.1.3 shows how the measured normalized resistance value (red curve) and hydrogen pressure (blue curve) were changing depending on the relative experimental time. The experimental pressure steps, given in the first column in Table 5.1.1, are marked as well in grey color in the lower part of the graph in Fig. 5.1.3. During the first pressure increase to  $p_H = 7 \times 10^{-7} \text{ mbar}$ , the resistance value significantly increased and, within about one hour, reached a new stable state visible as a plateau region in the resistance curve in Fig. 5.1.3 (green line in "range ii"). During the second hydrogen pressure increase to  $p_H = 1.4 \times 10^{-6} \text{ mbar}$ , the resistance curve started to rise permanently as shown Fig. 5.1.3 (green line in "range iii"). Thus, a stable state, as observed for  $p_H = 7 \times 10^{-7} \text{ mbar}$ , was not achieved within the chosen time span. A similar trend was observed by further pressure increase to  $p_H = 4.3 \times 10^{-6} \text{ mbar}$  (green line in "range v"). Hereby, the resistance measurements show that the system did not achieve a stable state. Furthermore, the slope of the resistance curve visibly increases with pressure increase.

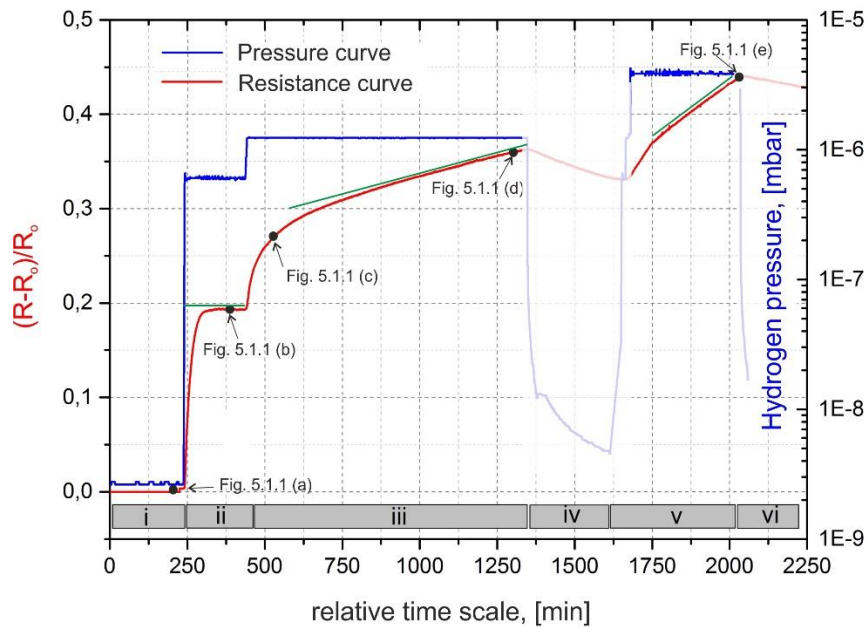


**Fig. 5.1.3** In-situ hydrogen gas loading electrical resistance measurements of a 55 nm Nb film. Blue curve shows the pressure change in the loading chamber, red curve – the change of normalized resistance value during the loading experiment. The experimental steps given in Table 5.1.1 are marked in a gray color. Additionally, the positions where the STM images shown in Fig. 5.1.1 (a, b, c, d, e) was obtained are marked with filled circles (•). The region of the graph, where the hydrogen pressure was decreased are given by transparent curves (range iv and range vi).

Sloping resistance curves, as observed in Fig. 5.1.3 (“range iii” and “range v”) might be attributed to two processes, namely on-going phase transformation (the increase of the volume fraction of the hydride phase) and events of plastic deformation (the formation of dislocations), appearing in the sample during hydrogen loading. Further, the change observed in the slope of the resistance curve in Fig. 5.1.3 (“range ii” and “range iii”) might qualitatively indicate a slower hydrogen absorption kinetics at  $p_H = 1.4 \times 10^{-6}$  mbar. Since the fact of phase transformation occurring in the system at this pressure was clearly confirmed by STM, the observed change of the absorption kinetics can be directly attributed to the onset of phase transformation. At the same time, the resistance curve at  $p_H = 4.3 \times 10^{-6}$  mbar shows, in comparison to hydrogen loading at  $p_H = 1.4 \times 10^{-6}$  mbar, a steeper slope (see Fig. 5.1.3: “range iii” and “range v”). This results hints on the improved kinetics at higher pressure and can be understood in terms of the overpressure (chemical potential) applied to the system.

### 5.1.1.2 Morphology change upon hydrogen unloading of a 55 nm Nb-H film

To promote hydrogen desorption and, therewith, decompose the hydride phase, long sample unloading by pumping of the vacuum chamber was carried out. Thereby, the hydrogen gas pressure was decreased to  $p_H < 1.1 \times 10^{-9}$  mbar. This last experimental step corresponds to “range vi” in Fig. 5.1.3. But, because of the long unloading time ( $t_e = 5370$  min (89.5 hrs)), the pressure curve is only partly shown.

The STM measurements show a significant surface corrugation contraction. However, after relatively long sample unloading for  $t_e = 5370 \text{ min}$  (89.5 hrs), the hydride related surface changes discussed in chapter 5.1.1.1 still could be found on the sample surface. Bright (elevated) regions in Fig. 5.1.4 (a) corresponds to the remaining hydride-related surface corrugations. Hereby, the measured topographic roughness  $\sigma_{\text{RMS}} = 0.64 \text{ nm}$  in the unloaded state is higher when compared to the “as-prepared” film surface with  $\sigma_{\text{RMS}} = 0.44 \text{ nm}$  (for comparison see Fig. 5.1.1 (a)). Further, the topographic height variation observed at the film surface decreased to about  $1.5 \text{ nm} - 2 \text{ nm}$ . This is exemplary shown in the linear profile in Fig. 5.1.4 (b) that was measured across the black dotted line added in Fig. 5.1.4 (a). Besides, comparison of height distribution histograms in Fig. 5.1.2 (b) (red and blue curves) also indicates on significant subsidence of the sample surface. Here, surface corrugations clearly visible in the red curve disappeared, when the sample was partly unloaded (blue curve). Only small variation of surface topography, visible in the blue curve in Fig. 5.1.4 (b), indicates some remaining hydrogen-related surface corrugations.

Reverse surface transformation, found in this part of the experiment can be attributed to the process of hydrogen desorption and the dissolution of hydride phase. Further, the observation of the increased topographic surface roughness, as compared to the “as-prepared” film surface state, can be related to two expected contributions, namely to the presence of hydrides itself and to surface corrugations caused by stress release (e.g. remaining glide lines resulting from dislocations formed during the loading process).

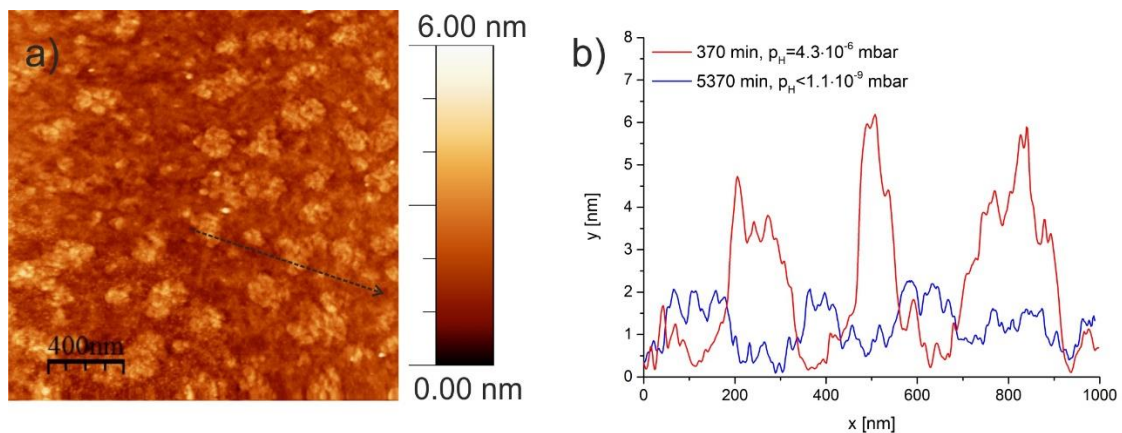


**Fig. 5.1.4 a)** STM surface-image of a 55 nm Nb film measured after long sample unloading for 5370 min (89.5 hrs.) at  $p_H < 1.1 \times 10^{-9} \text{ mbar}$ . Backward surface modifications are clearly visible, as surface corrugations get smaller in comparison to Fig. 5.1.1 (e). The observed topographic roughness  $\sigma_{\text{RMS}} = 0.64 \text{ nm}$  is relatively high if compared with the “as-prepared” film surface state ( $\sigma_{\text{RMS}} = 0.44 \text{ nm}$ ) but small with respect to the loaded sample ( $\sigma_{\text{RMS}} = 1.56 \text{ nm}$ ). (Frame size is  $2000 \times 2000 \text{ nm}^2$ ). **b)** Typical linear profiles measured during the hydrogen loading / unloading experiment: the red curve was measured in Fig. 5.1.1 (e) and blue curve - in Fig. 5.1.4 (a). Significant shrinkage of the film and some residual surface corrugations are detected.

Despite the fact that STM measurements revealed significant reverse surface changes and, hence, essential hydrogen desorption from the sample, the resistance measurement demonstrated a relatively small drop in the curve as compared with the loaded state as shown in Fig. 5.1.5. Because the generation

of new defects caused by hydrogen loading irreversibly changes the microstructure of the sample, the resistance value measured before the hydrogen loading and after the hydrogen loading (in the unloaded state) might be very different. Thus, it can be assumed that the contribution of processes of plastic deformation to the resistance curve in Fig. 5.1.5 is quite big and that it becomes especially visible during the unloading. Besides the resistance curve in Fig. 5.1.5 hints on the relatively slow kinetics of hydrogen desorption from the sample. Thus, according to this qualitative resistance measurement, it can be seen that the kinetics of hydrogen absorption/desorption in Nb-H thin films slows down when the system reaches the two-phase region in the phase diagram and the hydride phase starts to precipitate or decompose.

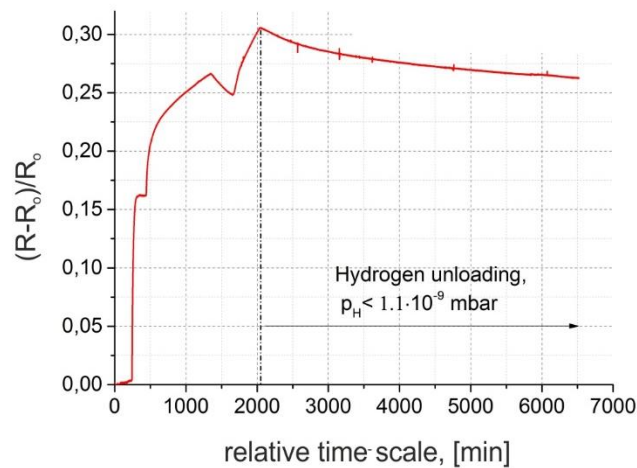


**Fig. 5.1.5** In-situ hydrogen gas loading/unloading resistance measurements of a 55 nm Nb film. As compared to Fig. 5.1.3, the part of resistance curve obtained during the unloading experiment is implemented in the graph. Measured resistance curve point out on the relatively slow kinetics of hydrogen desorption from the sample and significant contribution of process of plastic deformation. As compared to the STM results indicating significant hydrogen desorption from the sample, the resistance curve demonstrates relatively small drop during the unloading of the sample.

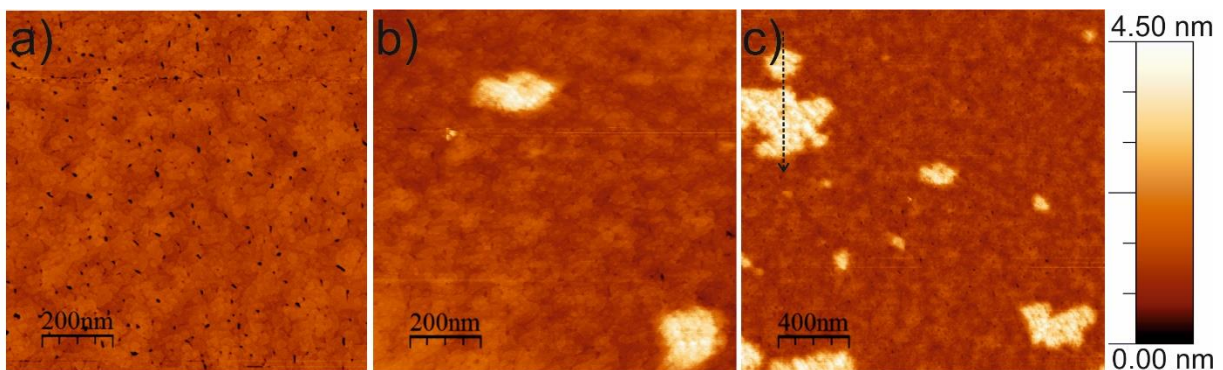
## 5.1.2 40 nm Nb-H film

### 5.1.2.1 Morphology change upon hydrogen loading of a 40 nm Nb-H film

Figure 5.1.6 (a) shows the STM surface-image of a 40 nm Nb film before hydrogen loading. Figure 5.1.6 (b) ( $p_H = 8 \times 10^{-7}$  mbar,  $t_e = 240$  min) and Fig. 5.1.6 (c) ( $p_H = 1.6 \times 10^{-6}$  mbar,  $t_e = 100$  min) demonstrate the surface modification measured during hydrogen loading at different hydrogen pressures  $p_H$  and exposure times  $t_e$ . While the surface topography of the film in Fig. 5.1.6 (a) is relatively flat ( $\sigma_{\text{RMS}} = 0.24$  nm), elevated (bright) regions are detected in Fig. 5.1.6 (b) ( $\sigma_{\text{RMS}} = 0.49$  nm) and in Fig. 5.1.6 (c) ( $\sigma_{\text{RMS}} = 0.67$  nm). Topographic surface changes elevated by about 3 nm – 4 nm from the base film level are visible in the linear profile shown in Fig. 5.1.7 (a). This linear profile was measured across the elevated surface regions appeared on the sample surface during the hydrogen loading, as shown in Fig. 5.1.6 (c). The black

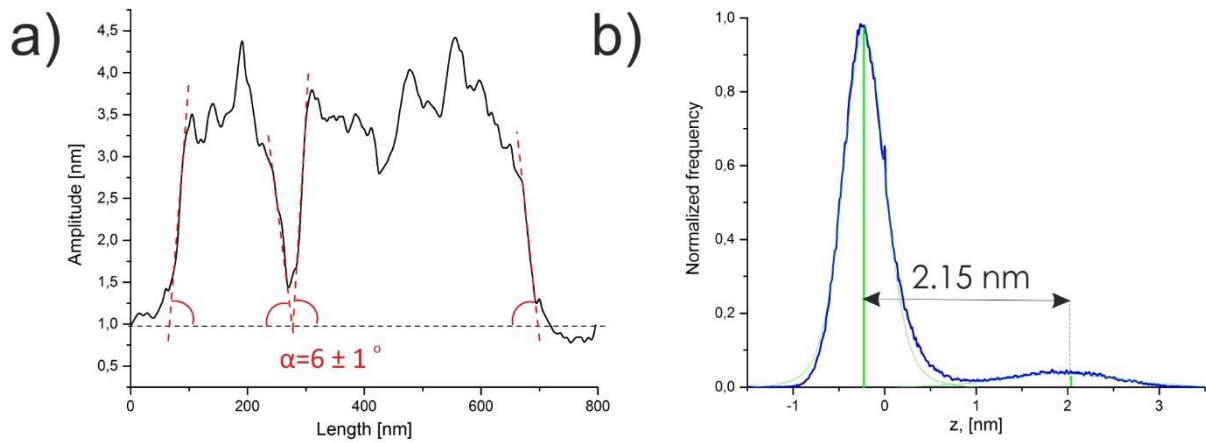
dotted arrow in Fig. 5.1.6 (c) marks the position and the direction of related linear profile. The lateral sizes of the surface corrugations visible in Fig. 5.1.6 (c) vary from 50 nm to about 700 nm. Most of them have irregular shape and steep edges. The slope of the profile in the transition area separating the elevated regions and the surrounding film surface in Fig. 5.1.7 (a) is about  $6(1)^\circ$ . The average distance between the neighboring elevated regions ranges from 500 nm to 750 nm [133].

As discussed in chapter 5.1.1.1, the observed surface corrugations is attributed to the precipitation and growth of the hydride phase in Nb-H films. Thus, elevated (bright) regions in Fig. 5.1.6 correspond to locally formed precipitates of the hydride phase. Hereby, the amplitude of the expected surface corrugations  $\Delta z$  according to the theory of linear elasticity for 40 nm film is estimated about 2.6 nm (see Table 2.1,  $\Delta c \approx 0.47 H/Nb$ ). The experimentally observed surface corrugations shown in Fig. 5.1.7 (a) exceed the theoretically expected value. This hints on additional material transport towards the surface, possibly by the implementation of dislocations.



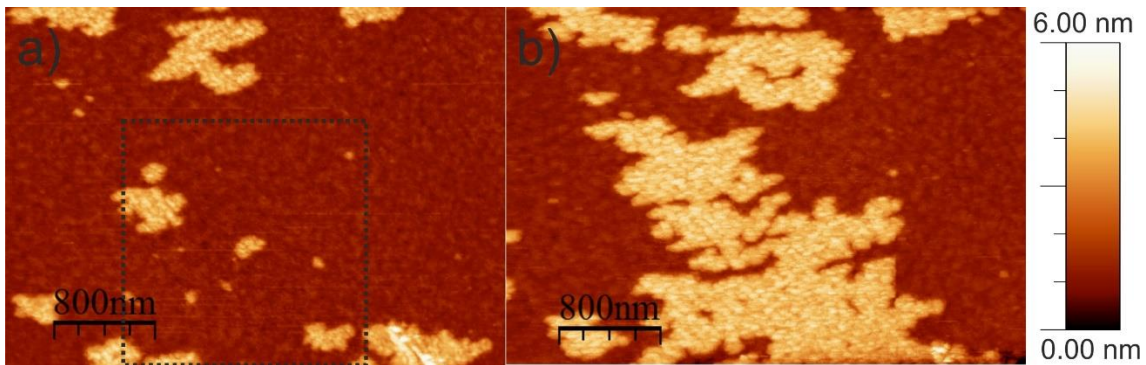
**Fig. 5.1.6** STM surface-image of a 40 nm Nb film **a)** before hydrogen loading ( $p_H < 1 \times 10^{-9}$  mbar), and during hydrogen loading **b)** at  $p_H = 8 \times 10^{-7}$  mbar for  $t_e = 240$  min, and **(c)** at  $p_H = 1.6 \times 10^{-6}$  mbar for a further  $t_e = 100$  min. Only a small number of hydride precipitates is visible. They grow to large lateral sizes up to 700 nm. The average distance between the neighbouring hydrides is about 500 nm – 750 nm [133]. Dotted black arrow indicates the direction and the length of linear profile measured across the hydride precipitate. The related linear profile is given in Fig. 5.1.7 (a). (Frame sizes change from (a)  $500 \times 500$  nm<sup>2</sup>, to (b)  $1000 \times 1000$  nm<sup>2</sup> and (c)  $2000 \times 2000$  nm<sup>2</sup>). Figure created by author from data originally published in Ref. [133].

Figure 5.1.7 (b) gives the height distribution histogram corresponding to the surface topography shown in Fig. 5.1.6 (c). As one can see, two independent peaks corresponding to Nb-H  $\alpha$ -phase (high intensity) and to Nb-H  $\beta$ -phase (low intensity) can be clearly distinguished. These two peaks are separated by about 2.15 nm. This value reflects the average height change detected within the frame size in Fig. 5.1.6 (c). It is lower than the value expected from linear elastic theory.



**Fig. 5.1.7** Details related to the STM surface-image in Fig. 5.1.6 (c): **a)** the linear profile of surface corrugation, whose appearance was detected on the sample surface during hydrogen loading (marked with a black dotted arrow): the height change of about 3 nm - 4 nm and steep edges are clearly visible. The slope of the profile in the transition area between the  $\alpha$ -phase and the  $\beta$ -phase is about  $6(1)^\circ$  (related regions are marked with red dotted lines). **b)** Height distribution histograms: two peaks separated by about 2.15 nm are visible. They represent, respectively, Nb-H  $\alpha$ -phase regions (high intensity) and to Nb-H  $\beta$ -phase regions (low intensity) clearly distinguishable in the STM surface-image in Fig. 5.1.6 (c).

The STM image in Fig. 5.1.8 (a) shows the surface topography change measured after hydrogen loading at  $p_H = 1.6 \times 10^{-6} \text{ mbar}$  for  $t_e = 500 \text{ min}$ . The frame size is  $4500 \times 4500 \text{ nm}^2$ . Here, the surface region marked with a black dotted contour roughly corresponds to the position previously shown in Fig. 5.1.6 (c). According to the STM surface-image in Fig. 5.1.8 (a), at the related loading stage a small number of large hydrides in the micrometer range size grows in the 40 nm Nb-H film. The observed surface topography show that hydrides are irregular in shape.



**Fig. 5.1.8** STM surface-image of a 40 nm Nb film **(a)**  $p_H = 1.6 \times 10^{-6} \text{ mbar}$ ,  $t_e = 500 \text{ min}$ ; the surface region marked with a dotted line roughly corresponds to the position previously shown in Fig. 5.1.6 (c). **(b)**  $p_H = 3 \times 10^{-6} \text{ mbar}$ ,  $t_e = 135 \text{ min}$ . (Frame sizes: (a)  $4500 \times 4500 \text{ nm}^2$  and (b)  $4000 \times 4000 \text{ nm}^2$ ).

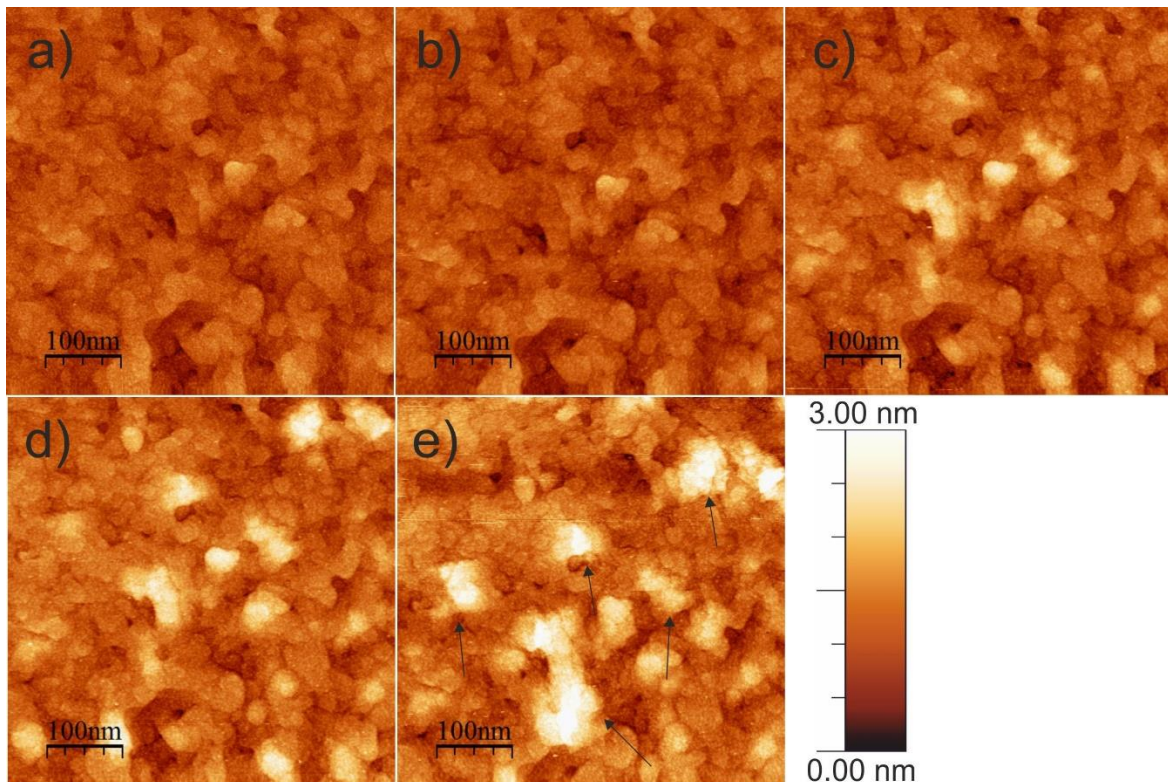
By subsequent pressure change to  $p_H = 3 \times 10^{-6} \text{ mbar}$  the volume fraction of the hydride phase continued to increase, as can be seen in Fig. 5.1.8 (b). Figure 5.1.8 (b) shows the STM image measured after hydrogen loading at  $p_H = 3 \times 10^{-6} \text{ mbar}$  for  $t_e = 135 \text{ min}$ . The volume fraction of hydride phase at this particular loading stage reached about 37%. The position of STM measurements as compared to

Fig. 5.1.8 (a) is the same, but the frame size is slightly rescaled from  $4500 \times 4500 \text{ nm}^2$  (in Fig. 5.1.8 (a)) to  $4000 \times 4000 \text{ nm}^2$  (in Fig. 5.1.8 (b)). At this loading stage it was clearly found that the pre-existing precipitates of hydride phase detected in Fig. 5.1.8 (a) continued to expand after the pressure increase to  $p_H = 3 \times 10^{-6} \text{ mbar}$ . Herewith, they formed massive agglomerates of hydride phase, as shown in Fig. 5.1.8 (b).

### 5.1.3 25 nm Nb-H film

#### 5.1.3.1 Morphology change upon hydrogen loading of a 25 nm Nb-H film

Topography changes observed upon hydrogen loading in a 25 nm Nb-H film are given in Fig. 5.1.9. There are several STM surface-images taken shortly before hydrogen loading (Fig. 5.1.9 (a)) and during hydrogen loading at fixed pressure  $p_H = 7 \times 10^{-7} \text{ mbar}$  (Fig. 5.1.9 (b-e)). The frame size for all the images is  $500 \times 500 \text{ nm}^2$ . Details about exposure times  $t_e$  at given  $p_H$  are given in the figure caption. The initial surface topography is very smooth, as it is shown in Fig. 5.1.9 (a) ( $\sigma_{RMS} = 0.24 \text{ nm}$ ). By hydrogen pressure increase to  $p_H = 7 \times 10^{-7} \text{ mbar}$ , elevated (bright) regions appeared on the sample surface as shown in Fig. 5.1.9 (b-e).



**Fig. 5.1.9** STM surface-image of a 25 nm Nb film [133] **a**) before hydrogen loading ( $p_H < 1 \times 10^{-9} \text{ mbar}$ ) and **(b-e)** during hydrogen loading at  $p_H = 7 \times 10^{-7} \text{ mbar}$  for different exposure times **b**)  $t_e = 220 \text{ min}$ , **(c)**  $t_e = 520 \text{ min}$ , **(d)**  $t_e = 690 \text{ min}$ , **(e)**  $t_e = 1160 \text{ min}$ . New surface corrugation appears upon hydrogen loading. They are visible as elevated (bright) regions and marked with black arrows. (Frame size:  $500 \times 500 \text{ nm}^2$ ).

Similar to the case of the 55 nm and the 40 nm films, the surface topographies are mainly attributed to hydride precipitates in the Nb-film. The height distribution histograms measured at the same position for a fixed pressure  $p_H = 7 \times 10^{-7}$  mbar and different loading times  $t_e$  are given in Fig. 5.1.10.

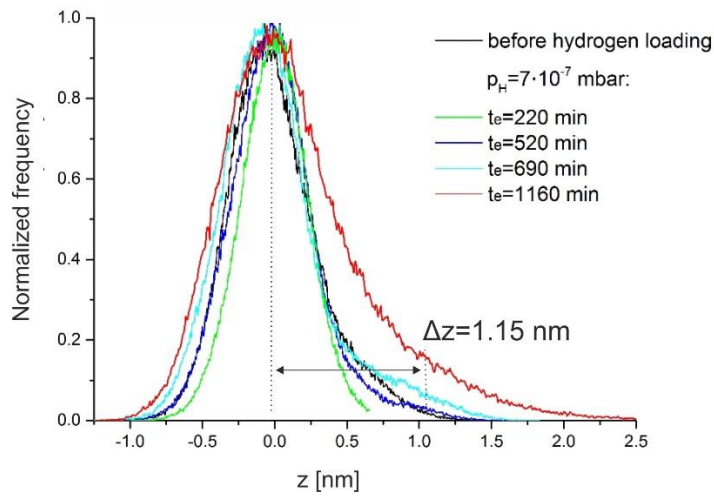


**Fig. 5.1.10** Height distribution histograms of a 25 nm Nb film show the development of the surface topography during hydrogen loading at  $p_H = 7 \times 10^{-7}$  mbar for different  $t_e$ . In average, elevated regions ( $\beta$ -phase) have a height amplitude of about 1.15 nm as measured from the mid-plane corresponding to the  $\alpha$ -phase regions in the STM image.

Here, the main peak corresponds to the mid-plane of the STM surface-image and is related to the  $\alpha$ -phase region. Besides, one can clearly see a small shoulder appearing on the right side of the main peak. This shoulder is attributed to the locally grown hydride phase ( $\beta$ -phase). After fitting the curve with two Gaussian functions, the peak splitting in the height histogram was found to be only  $\Delta z = 1.15$  nm as shown in Fig. 5.1.10.

For the assumed miscibility gap width of 0.3 H/Nb - 0.4 H/Nb the amplitude of surface corrugations  $\Delta z$  according to the theory of linear elasticity for the 25 nm film is expected to be about 1.02 nm – 1.36 nm (see Table 2.1). Thus, experimentally observed average surface corrugations (see Fig. 5.1.10) are close to the theoretically expected value.

As one can see, in the case of the 25 nm film the surface corrugations appearing upon hydrogen loading are relatively small (1 nm - 1.5 nm) and hence, it becomes difficult to define clearly the topography changes related to the hydride phase in the original STM images. Thus, a difference image comparing two intermediate states and highlighting the absolute surface changes was considered, as it is discussed in chapter 3.3.3. Particularly here, in Fig. 5.1.11 (a, b), we can see the difference images of two intermediate states given in Fig. 5.1.9. Figure 5.1.11 (a) shows the result of image subtraction (c) - (a) given in Fig. 5.1.9 ( $t_{diff} = 520$  min). Figure 5.1.11 (b) represents the difference image obtained by subtraction (e) - (a) given in Fig. 5.1.9 ( $t_{diff} = 1160$  min). Surface changes of about 1 nm - 2 nm height are now clearly visible, also in the linear profile exemplary given in Fig. 5.1.11 (c). The slope of the profile in the transition area between

the  $\alpha$ -phase and the  $\beta$ -phase is found to equal about  $2(0.5)^\circ$  as calculated from the linear profile in Fig. 5.1.11 (c). The position and the direction of the linear profile is shown by the black dotted arrow in Fig. 5.1.11 (b).

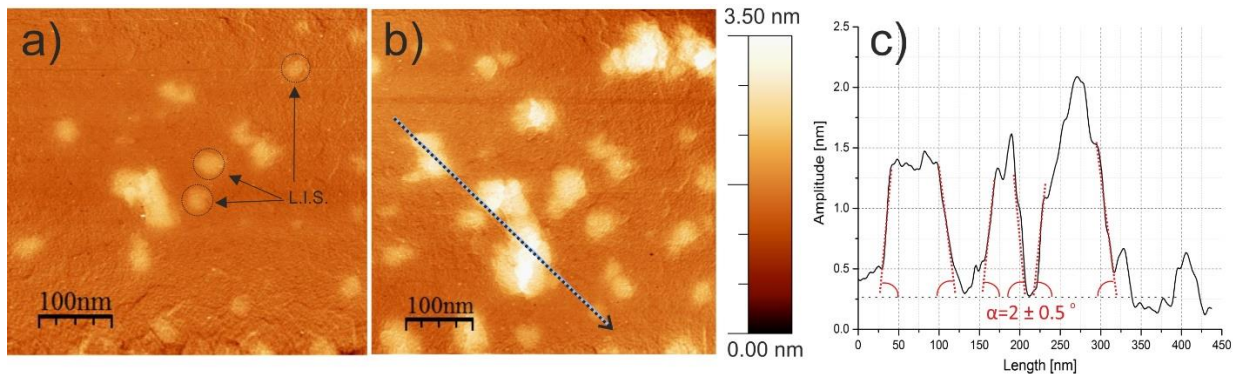


**Fig. 5.1.11 a)** Difference image (Fig. 5.1.9 (c) – Fig. 5.1.9 (a),  $t_{\text{diff}} = 520$  min). First precipitates of hydride phase have a lateral size of about 50 nm. Some hydrides keep their lateral size: their growth appeared very slowly as compared to the total exposure time  $t_e$  [133]. Following the suggestion of Nörthemann et al. [19], [73] this behaviour is labelled as “locked-in size” (L.I.S.) and the related surface elevations are marked by dotted circles. **b)** Difference image (Fig. 5.1.9 (e) – Fig. 5.1.9 (a),  $t_{\text{diff}} = 1160$  min). The number density of hydride precipitates continues to increase. The average distance between the neighbouring hydrides is about 50 nm – 100 nm. Black dashed arrow indicates the direction and the length of linear profile measured across the hydride precipitates. (Frame size:  $500 \times 500$  nm<sup>2</sup>). **c)** Linear profile measured across the hydride precipitates: height changes of about 1 nm - 2 nm are visible. The slope of the profile in the transition area between the  $\alpha$ -phase and the  $\beta$ -phase is about  $2(0.5)^\circ$  (related regions are marked with red dotted lines).

According to the difference images presented above, initially, most of the hydride precipitates reach a lateral size of about 50 nm (see Fig. 5.1.11 (a)) while the average distances between the neighboring hydrides range from 50 nm to 100 nm (see Fig. 5.1.11 (b, c)). In the initial precipitation stage, the hydride precipitates, in a first approximation, have a circular surface shape (Fig. 5.1.11 (a)).

During continuous hydrogen gas loading some precipitates of the hydride phase keep their lateral size: their growth appeared very slowly as compared to the total exposure time  $t_e$ . Following the suggestion of Nörthemann et al. [19], [73] this behaviour is labelled as “locked-in size”. But, at the same time, new surface topographies appear indicating the formation of new hydrides in the film. Thus, by changing the exposure time, the number density of hydride precipitates continues to increase. Thereby, during the phase transformation observed hydrides form a relatively “dense” and “homogeneous” surface topography as shown in Fig. 5.1.11 (b).

Thus, it is suggested, that the phase transformation from  $\alpha$ - to  $\beta$ -phase in the 25 nm film is mainly driven by the formation of new hydride precipitates, and not by growth of the pre-existing ones [133].

The STM surface-images shown in Fig. 5.1.12 (a) and Fig. 5.1.12 (b) were measured directly one after the other during hydrogen loading at  $p_H = 7 \times 10^{-7}$  mbar. The time difference between these two images is only 17 minutes. Besides of small hydrides discussed before, an appearance of few hydrides possessing larger volume, more irregular shape and clearly having facets, visible as straight lines in the

STM-images of the surface, were detected in Fig. 5.1.12 (b). Here, black arrows and dotted lines indicate on sharp facets appearing on the sample surface during the growth of hydride precipitates. Fig. 5.1.12 (c) gives the difference image where these features are clearly detectable.

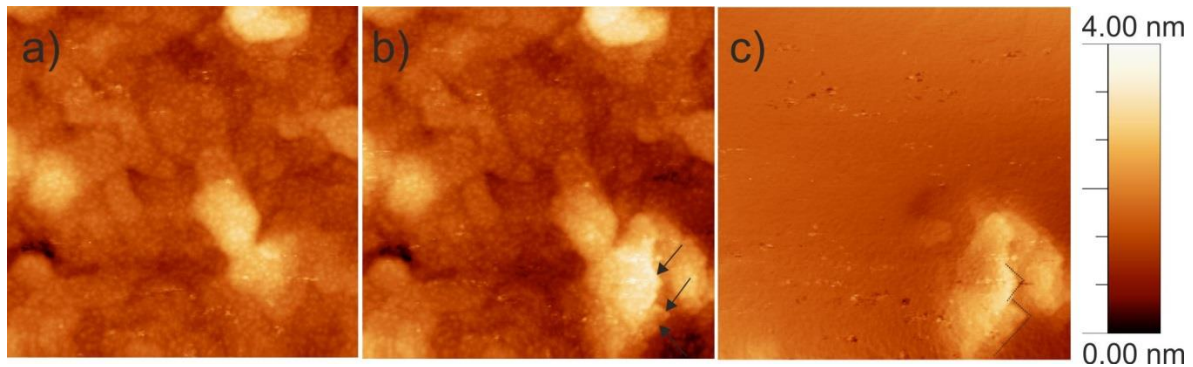


**Fig. 5.1.12** STM surface-images of a 25 nm Nb film showing an appearance of hydride precipitate of an irregular shape: **a)**  $p_H = 7 \times 10^{-7} \text{ mbar}$ ,  $t_e = 501 \text{ min}$  **b)**  $p_H = 7 \times 10^{-7} \text{ mbar}$ ,  $t_e = 518 \text{ min}$  **c)** difference image: hydride of irregular shape with a clearly serving facets, visible as straight lines (marked by black dotted lines) appeared on the sample surface. (Frame size:  $250 \times 250 \text{ nm}^2$ ).

Completed phase transformation was not observed even by increase the hydrogen pressure to  $p_H = 1.6 \times 10^{-6} \text{ mbar}$ . Figure 5.1.13 shows the surface topography measured after about  $t_e = 300 \text{ min}$  at  $p_H = 1.6 \times 10^{-6} \text{ mbar}$ . The frame size is  $1500 \times 1500 \text{ nm}^2$ . The volume fraction of the hydride phase at that loading stage reached about 32 %. Herewith, a large density of small hydrides as compared to thicker films was detected. Thus, the trend that was previously discussed in Fig. 5.1.11 (a, b) was confirmed also for the bigger frame size and higher hydrogen pressure.

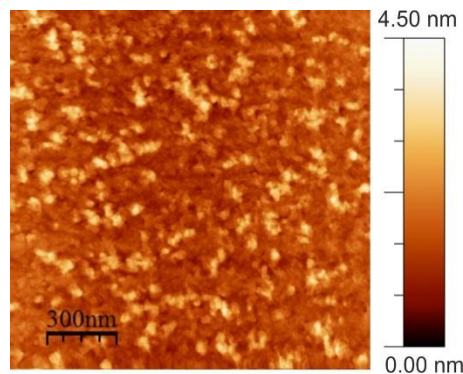


**Fig. 5.1.13** STM surface-image of a 25 nm Nb-H film measured after about  $t_e = 300 \text{ min}$  hydrogen loading at  $p_H = 1.6 \times 10^{-6} \text{ mbar}$ . A large density of small hydrides visibly changes the surface topography as compared to thicker films. (Frame size:  $1500 \times 1500 \text{ nm}^2$ ).

### 5.1.3.2 Morphology change upon hydrogen unloading of a 25 nm Nb-H film

After the hydrogen loading experiment, the hydrogen pressure in the vacuum chamber was reduced from  $p_H = 1.6 \times 10^{-7} \text{ mbar}$  to  $p_H = 8 \times 10^{-9} \text{ mbar}$  to unload the sample. In total, the sample was unloaded for 3800 min (63.3 hrs.). Figure 5.1.14 shows the surface topography changes observed upon

the hydrogen unloading experiment. The frame size is  $250 \times 250 \text{ nm}^2$ . Surface corrugations marked in pink color in Fig. 5.1.14 (a) appeared during the hydrogen loading experiment and, as discussed in chapter 5.1.3.1, result from the local precipitation of hydride phase. Subsequently, during the unloading experiment, partial contraction of the film was found as shown in Fig. 5.1.14 (b). Some hydride precipitates previously visible at the film surface vanished completely as marked by black dotted contours in Fig. 5.1.14 (a, b). The difference image in Fig. 5.1.14 (c, d) clearly shows the absolute difference appeared in the film topography. Here, regions given in pink color correspond to the surface elevations that disappear in Fig. 5.1.14 (b) and, regions given in blue color show the surface regions that stay unchanged. The height change detected in the difference image in Fig. 5.1.14 (c) does not exceed 1.2 nm. The observed surface contraction is attributed to hydrogen desorption from the film interior and a related decomposition of the hydride phase.

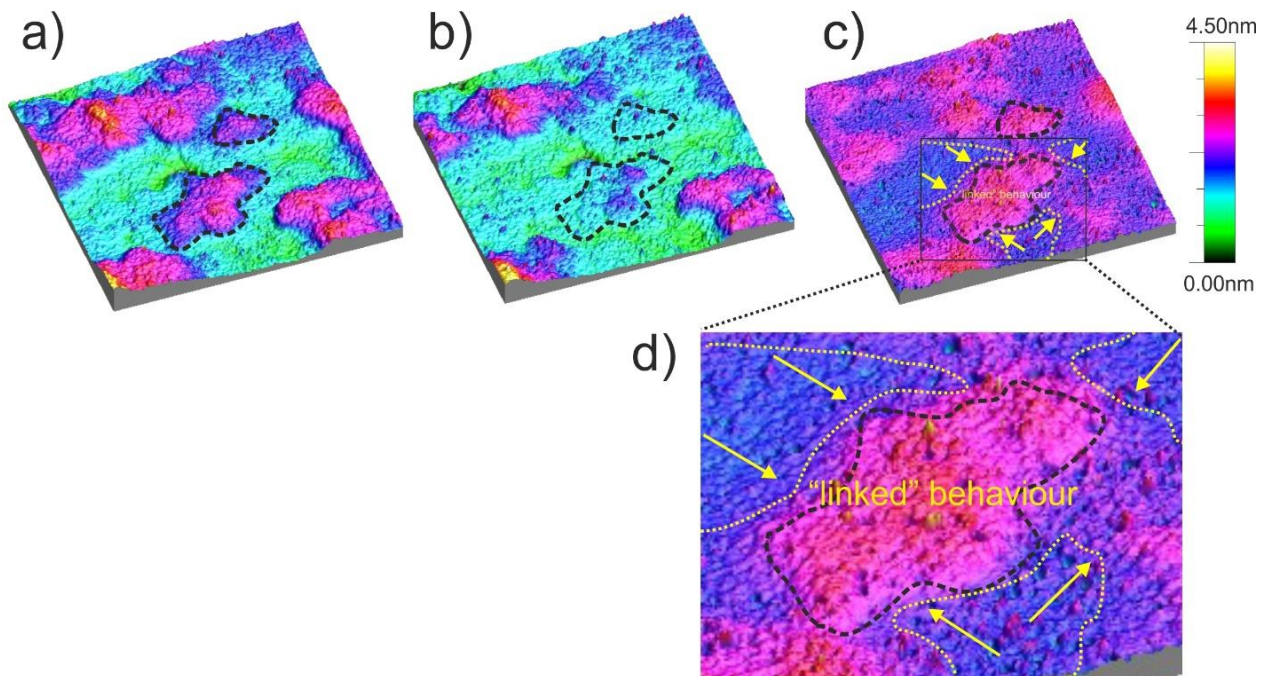


**Fig. 5.1.14** STM surface-images of a 25 nm Nb film: **a)** after hydrogen loading at  $p_H = 1.6 \times 10^{-6} \text{ mbar}$  for  $t_e = 320 \text{ min}$ . Surface regions marked in pink color correspond to the surface change resulting from the precipitation of hydride phase. **b)** After extended hydrogen unloading at  $p_H = 8 \times 10^{-9} \text{ mbar}$  for  $t_{unl} = 3300 \text{ min}$  (55 hrs.) surface topography clearly changed, some elevated region vanished completely (marked by dotted contours), and another only reduced their volume. Surface morphology marked in blue/green colors corresponds to the  $\alpha$ -phase regions. **(c)** Difference image: surface regions marked in pink colour indicate on reverse topography changes occurred during unloading of the sample. **(d)** An enlarged view of a representative part of surface area where a "linked behaviour" can be observed. It is marked by dashed yellow contour lines and highlighted by the arrows. (Frame size:  $250 \times 250 \text{ nm}^2$ ).

By visually comparing the surface area related to hydride precipitates in Fig. 5.1.14 (a) and the areas of reverse topography, changes in the difference image in Fig. 5.1.14 (c, d), a "linked behaviour" can be

observed in the region marked by the dashed yellow contour-lines and the black contour-lines. Here, yellow arrows highlight strong linkage. Therefore, it can be suggested that the surface regions corresponding to the  $\alpha$ -phase shrink together with the hydride phase regions. This observation may support the idea about coherent boundaries between two co-existing phases ( $\alpha/\beta$ ), but it cannot directly approve the wholly coherent nature of the phase transformation in the complete sample volume.

Figure 5.1.15 (a, b, c) presents STM images of surface topography obtained during the unloading experiment, with increasing the measured frame size. The STM surface – image in Fig. 5.1.15 (a) was measured after  $t_{unl} = 3300 \text{ min}$  (55 hrs.) at  $p_H = 8 \times 10^{-9} \text{ mbar}$ . It has a frame size of  $250 \times 250 \text{ nm}^2$  that corresponds to the smallest frame size used in STM measurements. The STM surface-images shown in Fig 5.1.15 (b) ( $p_H = 1.3 \times 10^{-9} \text{ mbar}$ ,  $t_{unl} = 3725 \text{ min}$  (62.1 hrs.)) and Fig. 5.1.15 (c) ( $p_H = 1.3 \times 10^{-9} \text{ mbar}$ ,  $t_{unl} = 3765 \text{ min}$  (62.8 hrs.)) were measured for bigger frame sizes, respectively,  $500 \times 500 \text{ nm}^2$  and  $1000 \times 1000 \text{ nm}^2$ . Elevated (bright) surface regions are detected on all the STM-images given in Fig. 5.1.15. This proves that they are not just a local phenomenon. The observed surface corrugations show that most agglomerations of hydride precipitates present on the sample surface after the hydrogen loading did not vanish during the unloading experiment. The elevated surface topographies visible in Fig. 5.1.15 (c) have a height ranging between 1 nm and 2 nm.

Based on this result and the previously discussed STM results (see chapter 5.1.1.2), it is suggested that residual surface corrugations cannot be completely attributed to the traces of plastic deformation. It is, therefore, possible that the state of complete hydride phase decomposing was not reached in the long-term unloading experiment (see also Fig. 5.1.4 and Fig. 5.1.5).

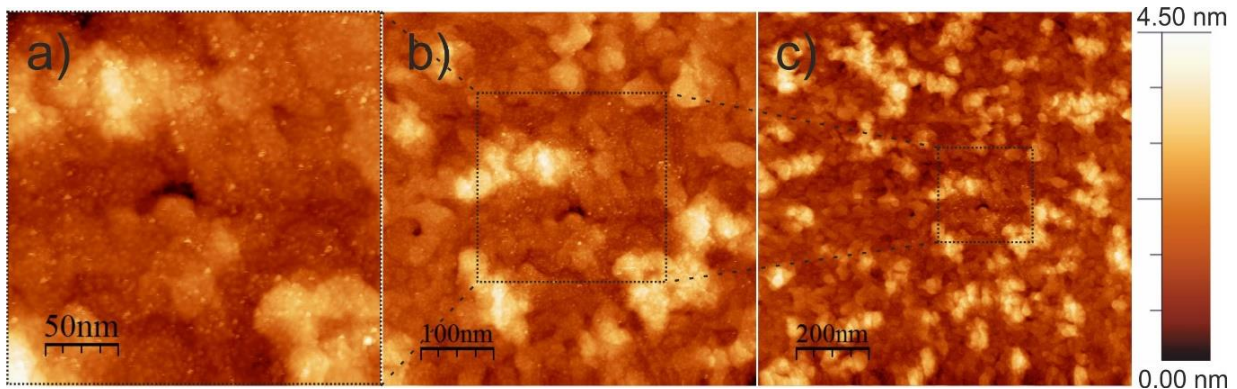


**Fig. 5.1.15** STM surface-images of a 25 nm Nb film after extended hydrogen unloading. **a)** Frame size:  $250 \times 250 \text{ nm}^2$ ,  $p_H = 8 \times 10^{-9} \text{ mbar}$ ,  $t_{unl} = 3300 \text{ min}$  (55 hrs). **b)** Frame size:  $500 \times 500 \text{ nm}^2$ ,  $p_H = 1.3 \times 10^{-9} \text{ mbar}$ ,  $t_{unl} = 3725 \text{ min}$  (62.1 hrs). **c)** Frame size:  $1000 \times 1000 \text{ nm}^2$ ,  $p_H = 1.3 \times 10^{-9} \text{ mbar}$ ,  $t_{unloading} = 3765 \text{ min}$  (62.8 hrs). Surface topographies appeared during the precipitation of the hydride phase (bright regions) stayed present in the STM images even after the unloading experiment. The same areas of interest for differently scaled frame sizes are shown by dotted contours.

## 5.1.4 15 nm Nb-H film

### 5.1.4.1 Morphology change upon hydrogen loading of a 15 nm Nb-H film

A 15 nm Nb film was loaded with hydrogen until the state, in which the sample volume was completely transformed into the hydride phase. In total, the hydrogen pressure was increased four times from  $p_H = 1.3 \times 10^{-9}$  mbar to  $p_H = 3 \times 10^{-6}$  mbar. Figure 5.1.16 (a-l) shows the evolution of surface topography measured upon hydrogen loading at different pressures and exposure times. The frame size used for all the STM surface – images is  $500 \times 500$  nm<sup>2</sup>. Table 5.1.2 contains the information about  $p_H$ ,  $t_e$  and the volume fraction of hydride phase achieved by applying different loading conditions. The evaluation was made based on the related STM images.

**Table 5.1.2** Experimental details on the STM surface-images given in Fig. 5.1.16 ( $p_H$ ,  $t_e$ , Hydride volume fraction).

$p_H$ , [mbar]	$t_e$ , [min]	Hydride volume fraction, [%]
$1.3 \times 10^{-9}$	-	0
$7 \times 10^{-7}$	16	1.4
$7 \times 10^{-7}$	245	4.6
$7 \times 10^{-7}$	782	15.6
$7 \times 10^{-7}$	1068	28.9
$9.2 \times 10^{-7}$	110	36.9
$1.7 \times 10^{-6}$	229	56.6
$3 \times 10^{-6}$	25	63.3
$3 \times 10^{-6}$	530	100

As can be judged from Fig. 5.1.16 (a-l), the sample surface experienced significant changes during the hydrogen loading experiment. New surface corrugations started to appear on the sample surface at  $p_H = 7 \times 10^{-7}$  mbar as shown in Fig. 5.1.16 (b). Subsequently, the surface area of these new elevated regions continued to grow depending on the hydrogen pressure and the related exposure times as shown in Fig. 5.1.16 (c-l).

As previously discussed, these new surface topographies are attributed to the precipitation and growth of the hydride phase in the film. Therefore, according to the STM image in Fig. 5.1.16 (b) first hydrides were detected already after 16 minutes of hydrogen exposure at  $p_H = 7 \times 10^{-7}$  mbar. By subsequent loading at the same pressure, the volume fraction of the hydride phase permanently increases. After hydrogen loading for  $t_e = 1068$  min (17.8 hrs.) no further precipitation or growth of hydride phase was detected. Thus, it can be suggested that further phase transformation is locked. At this

loading stage (see Fig. 5.1.16 (e)) the volume fraction of the hydride phase reached about 28.9 %. Thus, to facilitate further phase transformation, the hydrogen pressure was increased, first to  $p_H = 9.2 \times 10^{-7}$  mbar for  $t_e = 110$  min (Fig. 5.1.16 (f)), then to  $p_H = 1.7 \times 10^{-6}$  mbar for  $t_e = 229$  min (Fig. 5.1.16 (g)) and finally to  $p_H = 3 \times 10^{-6}$  mbar for  $t_e = 530$  min (Fig. 5.1.16 (h-l)). Only at this loading stage, the phase transformation was completed.

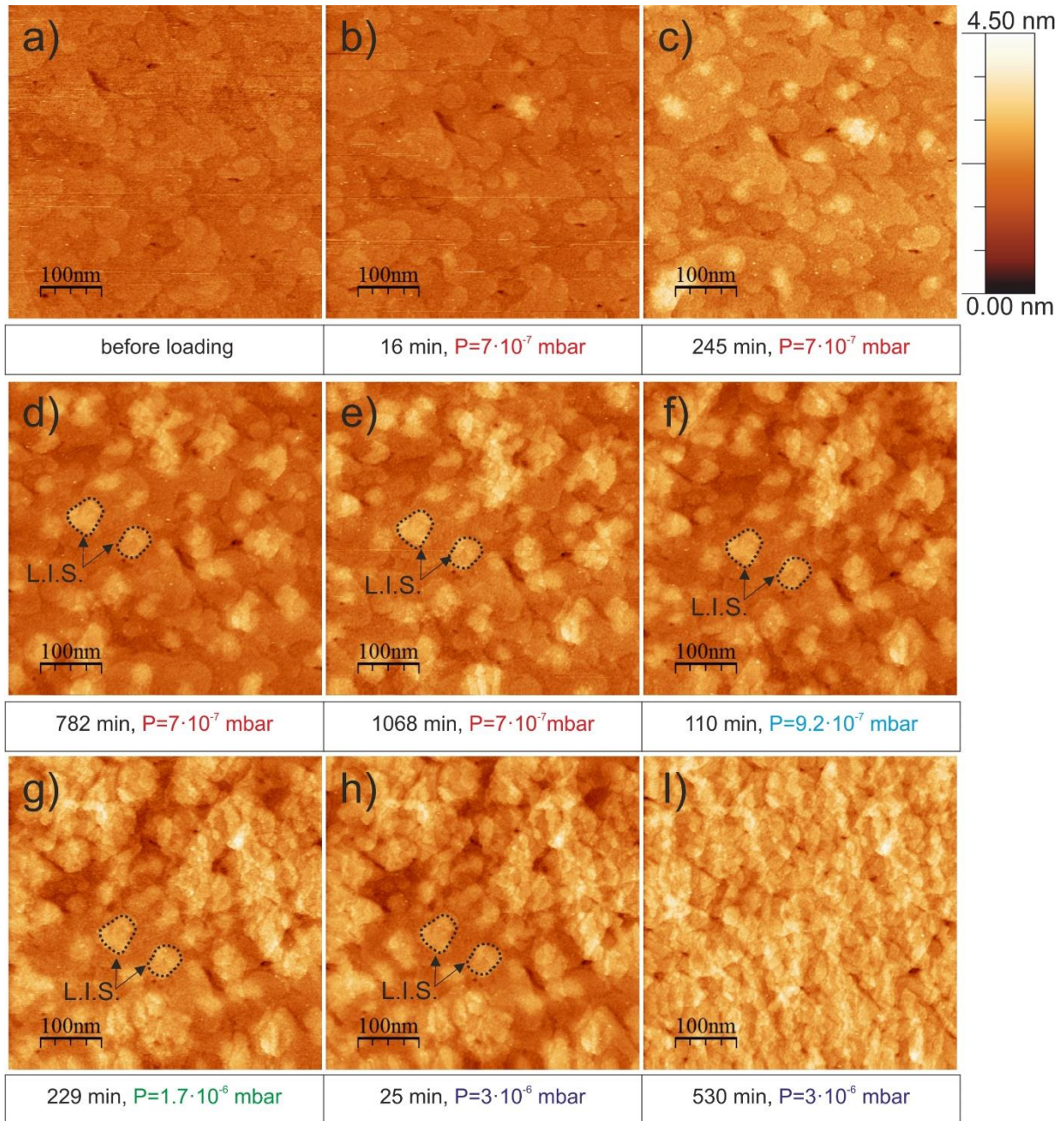


**Fig. 5.1.16** STM surface-images of a 15 nm Nb film shows surface topography change observed upon hydrogen loading at different pressures and exposure times: **a)** before hydrogen loading; **(b-e)**  $p_H = 7 \times 10^{-7}$  mbar; **f)**  $p_H = 9.2 \times 10^{-7}$  mbar; **g)**  $p_H = 1.7 \times 10^{-6}$  mbar; **(h-l)**  $p_H = 3 \times 10^{-6}$  mbar. Two hydrides, that stay “locked-in size” and does not grow by the increase of the hydrogen pressure, are shown by way of example (marked by black dotted contours and labeled as “L.I.S”).

As one can see from Fig. 5.1.16 (a-l), the hydrides form a very “dense” and “homogeneous” surface topography. Thus, it is suggested, that similar to the case of the 25 nm film, phase transformation in the 15 nm films mainly occurs by the formation of new hydride precipitates. Herewith, the hydrides already present in the sample grow very slowly and upon reaching a certain lateral size almost do not change (“locked-in size” or “L.I.S.”). In Fig. 5.1.16 (d-h), two hydrides following this behavior are shown by way of example. They are marked by black dotted contours and labeled as “L.I.S.”. Their average lateral size is fixed by 50 nm and it does not change by the increase of the hydrogen pressure from  $p_H = 7 \times 10^{-7}$  mbar to  $p_H = 3 \times 10^{-6}$  mbar.

Thus, the STM measurements presented in Fig. 5.1.16 (a-l) show that an increase of the mean hydrogen concentration in the sample at RT (and crossing the two-phase region of the Nb-H phase diagram) in the case of thin epitaxial Nb-H films requires a permanent increase of the applied hydrogen pressure within the given time frame. Based on the result, obtained for the first loading step and indicating no further surface topography change ( $p_H = 7 \times 10^{-7}$  mbar,  $t_e = 1068$  min (17.8 hrs.)), it is assumed that there is no fixed plateau pressure corresponding to the phase transformation in the 15 nm Nb-H film. Instead of this, there is a pressure range, in that the phase transformation occurs. Hereby, the lower limit corresponds to initiation of phase transformation and the higher limit to the completion of phase transformation in the sample volume. Very similar trend has also been observed by Nörthemann et al. for thicker films [24], [73].

Figure 5.1.17 gives the height distribution histogram showing the topography change occurring during hydrogen loading at  $p_H = 7 \times 10^{-7}$  mbar and corresponding to the STM images shown in Fig. 5.1.16 (a-e). Again, the main peak corresponds to the mid-plane of the STM image and is attributed to the  $\alpha$ -phase regions. The second peak visible as a shoulder of the main peak corresponds to the hydride ( $\beta$ -phase) regions. Two these peaks are separated by only  $\Delta z = 0.65$  nm. Thus, the average amplitude of surface topography change caused by hydrogen absorption becomes relatively small.

For the assumed miscibility gap of 0.3 H/Nb - 0.4 H/Nb the amplitude of surface corrugations  $\Delta z$  according to the linear elastic theory for the 15 nm film is expected to be about 0.61 nm – 0.82 nm (see Table 2.1). Thus, the average amplitude of surface corrugations corresponds well with the theory. However, at the same time, it can be seen also that the height distribution in Fig. 5.1.17 is quite broad and the height of some hydrides clearly exceeds the theoretically expected change.

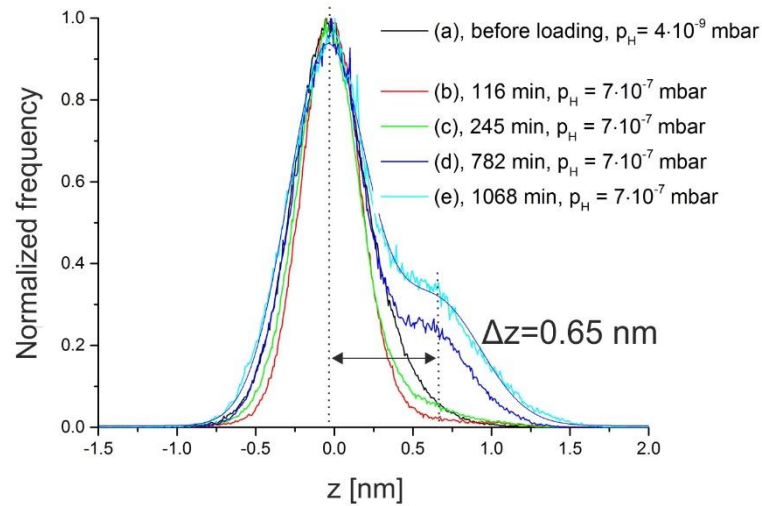


**Fig. 5.1.17** The height distribution histogram shows two close peaks, separated by 0.65 nm and corresponding, respectively, to Nb-H  $\alpha$ -phase regions (high intensity) and Nb-H  $\beta$ -phase regions (a shoulder of the peak).

Because the surface corrugation becomes relatively small, difference images comparing STM images measured at intermediate loading stages will be further considered. The minimum time difference, separating preceding and subsequent images recorded during in-situ STM measurements and used for image subtraction was about 17 minutes. Figure 5.1.18 (a-c) demonstrates first hydride precipitates and the related surface changes detected in the area of interest within first 16 minutes of hydrogen loading at  $p_H = 7 \times 10^{-7}$  mbar. In details, two STM images measured on one after each other (Fig. 5.1.18 (a, b)) and their difference image (Fig. 5.1.18 (c)) are given. According to the difference image in Fig. 5.1.18 (c) and linear profiles measured across hydride precipitates in Fig. 5.1.18 (d, e), in the initial growing stage, hydride precipitates have a shape close to the circle and relatively small lateral dimensions ( $\leq 50$ nm). Furthermore, the absolute height change caused by local precipitation of hydride phase does not exceed 1.2 nm. The lateral sides of hydride precipitates detected in the area of interest are slightly inclined. The slope of the profile in the transition area between the  $\alpha$ -phase and the  $\beta$ -phase lies in a range from  $3^\circ$  to  $4.5^\circ$  as it is shown in Fig. 5.1.18 (d, e).

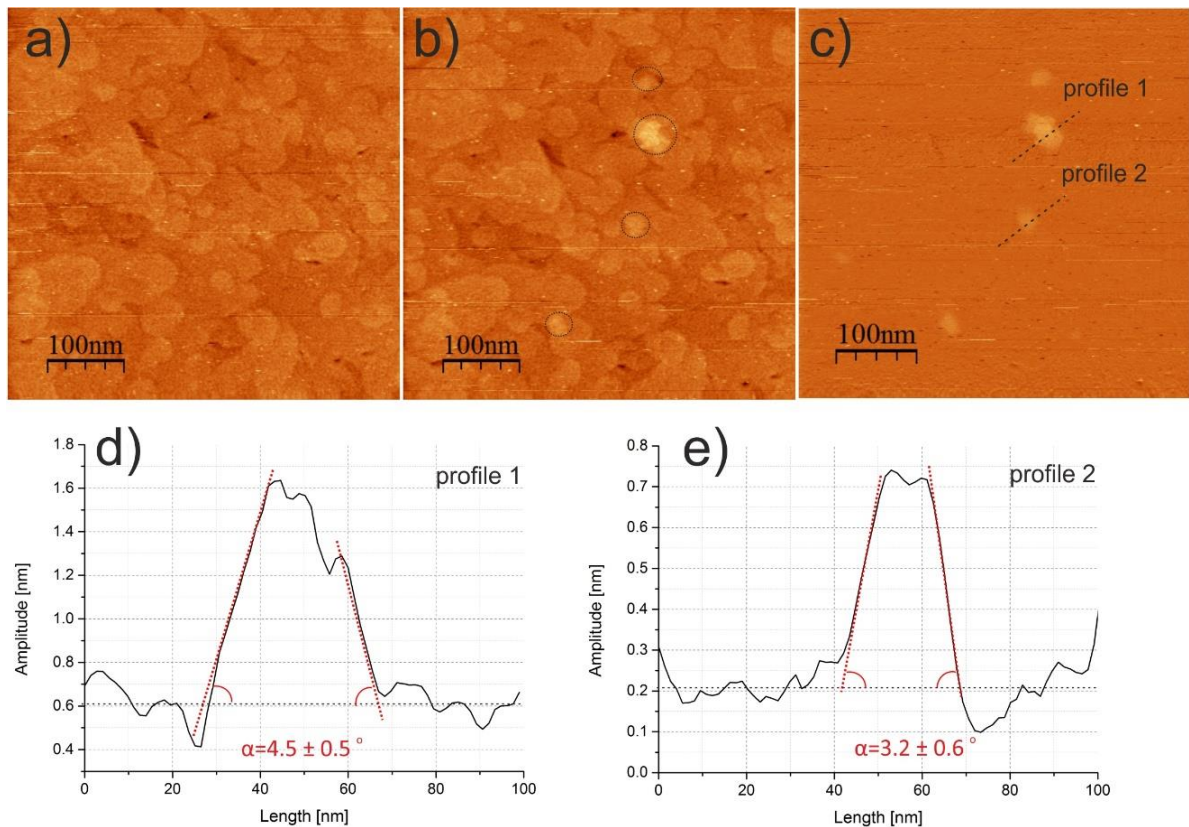


**Fig. 5.1.18** STM surface-images of a 15 nm Nb film: **a)** before hydrogen loading, **b)** early stage of precipitation of hydride phase detected within  $t_e = 16$  min of hydrogen loading at  $p_H = 7 \times 10^{-7}$  mbar. Dotted circles mark the surface regions, where first precipitates of the hydride phase are detected **c)** difference image: elevated (bright) regions of a circular shape are visible. Dashed lines mark the location and length of linear profile measured across the precipitates of hydride phase **d)** linear profile 1 **e)** linear profile 2. The slope of the profile in the transition area between the  $\alpha$ -phase and the  $\beta$ -phase is about  $4.5(0.5)^\circ$  (profile 1) and  $3.2(0.6)^\circ$  (profile 2). Related regions are marked with red dotted lines.

Upon further hydrogen loading at the same hydrogen pressure  $p_H = 7 \times 10^{-7}$  mbar the number and the density of new hydride precipitates continued to increase, and some of them overcome the lateral size of 50 nm as shown Fig. 5.1.19 (a, b). Beside of these larger hydride precipitates, sharp straight edges appeared on the sample surface as shown in the cropped difference image in Fig. 5.1.19 (c). Here, these new surface features are marked with blue lines. The difference image shown in Fig. 5.1.19 (c) was obtained as result of image subtraction and subsequent cropping and zooming. Figure 5.1.19 (d) shows the linear profile measured across one of the sharp, straight edges visible at the surface and marked with a black arrow in Fig. 5.1.19 (c). Other profiles measured in the surface regions marked with the blue lines showed similar curve shapes. The height change measured particularly in the profile in Fig. 5.1.19 (d) as well as in case of four other edges marked with the blue lines, does not exceed 0.3 nm.

It is supposed that the sharp, straight edges appearing on the sample surface are related to the emission of dislocations, visible mainly in the STM difference image. Line profiles measuring this kind of surface corrugation at different positions show a reproducible result: curves have a shape that can be described as an atomic step on the one side and a sloped ramp on the other side of the edge (Fig. 5.1.19

(d)). Similar findings were discussed by Pundt et al. for Gd-H films [18] and were attributed to misfit dislocations formed at the interface between the film and the substrate during hydrogen loading.

Thus, surface changes discovered in Fig. 5.1.19 (c) are attributed to two processes: precipitation of hydride phase (marked with the dotted circle) and formation of misfit dislocations (sharp, straight edges marked with blue lines) visible as the emergence of ramps on the sample surface.

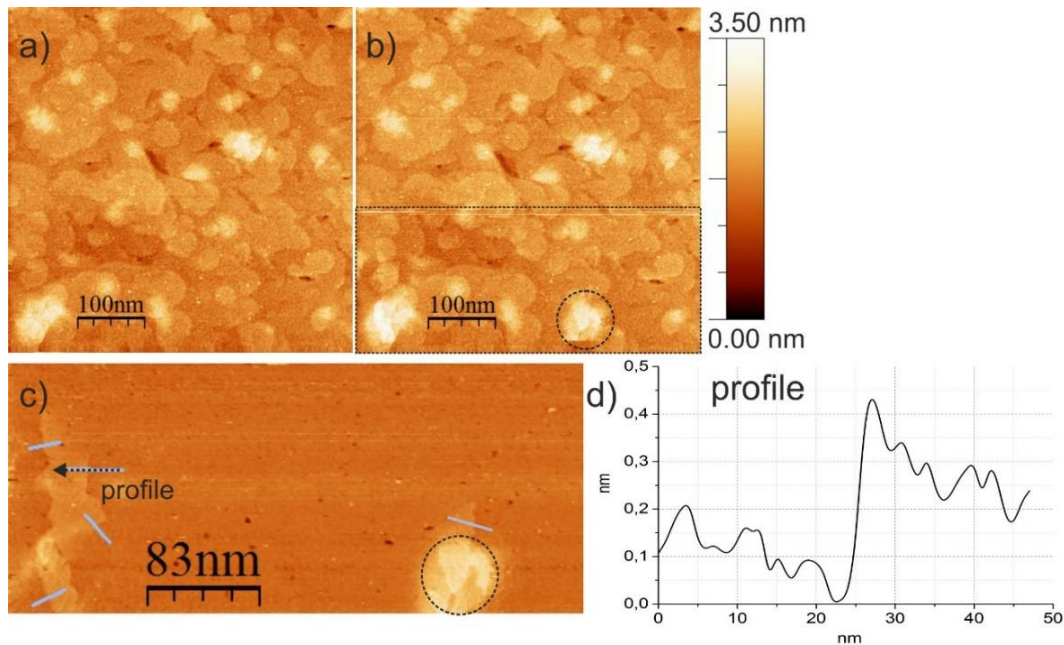


**Fig. 5.1.19** **a)** STM surface – image measured at  $p_H = 7 \times 10^{-7}$  mbar after  $t_e = 135$  min of hydrogen loading. **b)** STM surface – image measured at  $p_H = 7 \times 10^{-7}$  mbar after  $t_e = 152$  min of hydrogen loading. **c)** Cropped and zoomed difference image: two different kinds of surface corrugation are detected. Dotted circle marks the precipitate of hydride phase that appeared within 17 min. Blue lines mark sharp, straight edges that were also detected on the surface. **d)** Linear profile measured across one of the sharp, straight edge visible in the difference image and marked with a black arrow. The height change visible in the profile is lower than 0.3 nm.

Figure 5.1.20 shows massive surface changes that appeared at the late stage of hydrogen loading. STM surface – images shown in Fig. 5.1.20 (a, b) were measured one after the other at  $p_H = 9.2 \times 10^{-7}$  mbar ( $t_e = 212$  min). The STM surface – images in Fig. 5.1.20 (d, e) were as well measured one after the other, but at a higher hydrogen pressure  $p_H = 3 \times 10^{-6}$  mbar ( $t_e = 144$  min). The related difference images are given, correspondingly, in Fig. 5.1.20 (c) and Fig. 5.1.20 (f). The absolute surface changes shown in these difference images, appear within a time interval of about 17 minutes. Some surface features appearing in these difference images looks very similar to those discussed in Fig. 5.1.19 (c, d). In Fig. 5.1.20 (c, f) an appearance of straight, sharp edges of about 0.3 nm in height was detected. The related surface regions in Fig. 5.1.20 (c, f) are marked with the black arrows.

Thus, based on these images, one can suggest the appearance of massive plastic deformation events occurring in the 15 nm Nb-H film. Furthermore, this result seems to be linked with the previously discussed need for subsequently increasing the hydrogen pressure to complete the phase transformation.

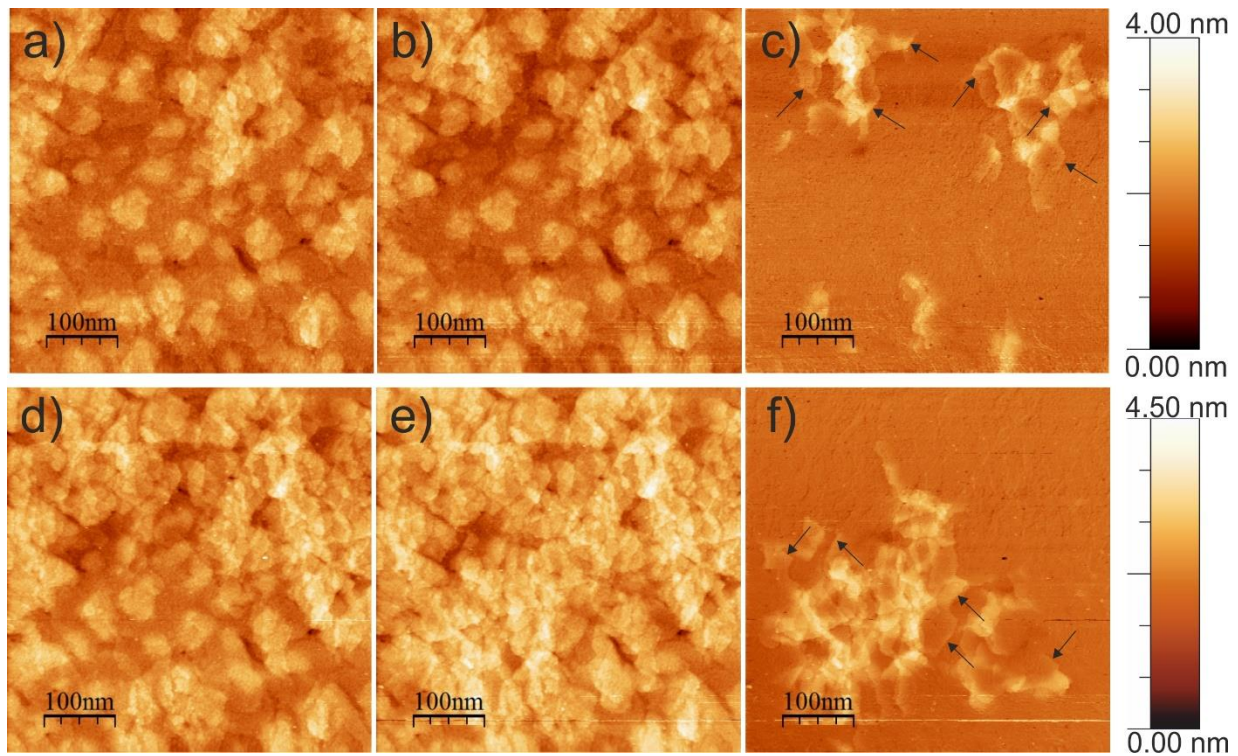


**Fig. 5.1.20** STM surface-images of a 15 nm Nb film showing surface modification appearing at the late stage of sample hydrogenation. **a) - b)** Two following each other STM measurements:  $p_H = 9.2 \times 10^{-7}$  mbar,  $t_e = 212$  min. **c)** Difference image: traces of dislocations are detected on the sample surface in the regions marked with black arrows; steep and sharp edges are clearly visible. **d) - e)** Two following each other STM measurements:  $p_H = 3 \times 10^{-6}$  mbar,  $t_e = 144$  min. **f)** Difference image: massive plastic deformation in the regions transformed into the hydride phase (marked with black arrows) and simultaneous significant increase of hydride volume fraction in the related regions.

In other words, local stress release by the emission of dislocations affects the chemical potential on the local scale [56]. This means that the lattice regions, where the precipitation starts, are mechanically different from others due to the partial stress release occurring in the film. Recently Wagner et al. discussed this concept in detail by the example of film buckling occurring in Nb-H thick films [56]. Here, in the case of Nb-H thin films, the observations of a sloping plateau pressure and partial stress relaxation are attributed to the formation of dislocations at the film / substrate interface. The occurrence of sharp, straight edges and significant increase of volume fraction of hydride phase in related regions visible in Fig. 5.1.20 are linked with each other and, therewith, confirm this concept.

Besides, at late loading stages surface corrugations have a more irregular shape in comparison to the earlier loading stages shown in Fig. 5.1.18. The maximum height change detected in the difference images shown in Fig. 5.1.20 (c, f), reaches up to 1.5 nm. Previously separated regions of hydride phase amalgamate and form a more complex surface topography consisting of agglomerates of hydrides and traces of dislocations. Finally, the hydride phase fills out the complete sample volume.

To summarize, for the 15 nm Nb-H film the presence of phase transformation is clearly proven. It is suggested that similar to the case of the 25 nm film, in the case of the 15 nm film the phase

transformation is governed also by the formation of new hydride precipitates and not by growth of the pre-existing ones. Further, it is suggested that even for this film thickness, events of plastic deformation cannot be completely excluded in intermediate and late stages of hydrogen loading. The observed surface corrugations and their amplitudes for the addressed film thickness hint on remaining stress release. In the present study, this result is related to the formation of dislocations occurring mainly at the film / substrate interface. Further, it is assumed that partial stress release also is the reason for the presence of sloping plateau pressure, as suggested by Wagner et al. [14], [103]. Therefore, the presence of coherent  $\alpha / \beta$  interfaces as suggested by Nörthemann et al. [19] for thin films ( $d \leq 26 \text{ nm}$ ) cannot be unambiguously proven only by using the STM technique, at this stage. Thus, alternative methods are required.

### 5.1.5 8 nm Nb-H film

#### 5.1.5.1 Morphology change upon hydrogen loading of a 8 nm Nb-H film

8 nm Nb-H film is the thinnest film that was analyzed in the frame of this thesis by using in-situ STM. Similar to the case of the 55 nm Nb-H film (chapter 5.1.1), the process of hydrogen loading / unloading was controlled by applying simultaneously two independent techniques: in-situ STM and in-situ electrical resistance measurements.

During hydrogen loading,  $p_H$  was increased from  $p_H = 2.5 \times 10^{-9} \text{ mbar}$  to  $p_H = 4 \times 10^{-5} \text{ mbar}$ . Details about the experimental steps including  $p_H$  and  $t_e$  at given pressures are given in Table 5.1.3.

**Table 5.1.3** Experimental details for a 8 nm Nb film ( $p_H$ ,  $t_e$ )

Experimental step	$p_H$ [mbar]	$t_e$ [min]
	$2.5 \times 10^{-9}$	
I	$2.3 \times 10^{-7}$	60
II	$6 \times 10^{-7}$	50
III	$1.3 \times 10^{-6}$	70
IV	$3 \times 10^{-6}$	70
V	$8 \times 10^{-6}$	905
VI	$4 \times 10^{-5}$	168
VII	$9 \times 10^{-10}$ (unloading)	4725

Figure 5.1.21 (a-f) shows the evolution of surface topography measured at different hydrogen pressures up to  $p_H = 8 \times 10^{-6} \text{ mbar}$ . The frame size for all the present STM images is  $250 \times 250 \text{ nm}^2$ . Overall, STM images measured at different  $p_H$  and  $t_e$  look very similar. Surface roughness ( $\sigma_{\text{RMS}}$ ) for these STM

images ranges from 0.26 nm to 0.28 nm, but visually by eye, no distinguishable new surface features can be specified and localized. The related height distribution histogram is shown in Fig. 5.1.22. As can be seen, it also cannot be used to find signs of topographic changes as it was done for thicker films discussed before.

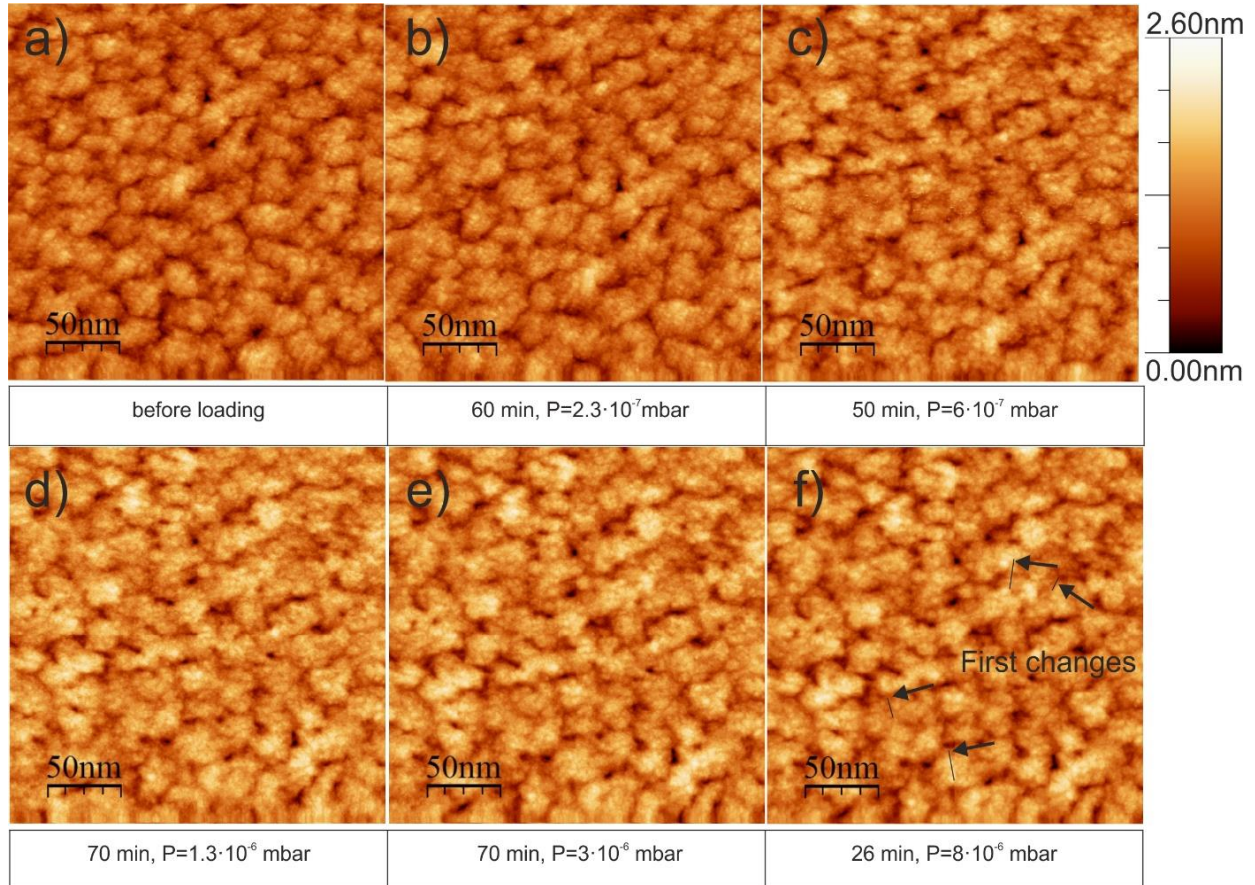


**Fig. 5.1.21** STM surface-images of a 8 nm Nb film demonstrating surface evolution upon hydrogen loading. **(a)** before loading; **(b)**  $p_H = 2.3 \times 10^{-7}$  mbar,  $t_e = 60$  min; **(c)**  $p_H = 6 \times 10^{-7}$  mbar,  $t_e = 50$  min **(d)**  $p_H = 1.3 \times 10^{-6}$  mbar,  $t_e = 70$  min; **(e)**  $p_H = 3 \times 10^{-6}$  mbar,  $t_e = 70$  min; **(f)**  $p_H = 8 \times 10^{-6}$  mbar,  $t_e = 26$  min. First surface change appeared only after increasing the hydrogen pressure to  $p_H = 8 \times 10^{-6}$  mbar. Black arrows mark the related regions.

Thus, because it is quite challenging to recognize the surface modification in the original STM surface – image shown in Fig. 5.1.21, step by step drift correction and image subtraction algorithms were applied to check precisely, if there appears any local topography change between the STM images measured one after the other and at different pressures  $p_H$ . Detailed analysis of the STM surface – images, some of them shown in Fig. 5.1.21 (a-e), reveals that there are no detectable surface topography changes, including any kind of surface corrugation, discussed earlier in this chapter. For the assumed miscibility gap width of 0.4 H/Nb, the amplitude of surface corrugations  $\Delta z$  according to the theory of linear elasticity for the 8 nm film is expected to be about 0.44 nm (see Table 2.1). Further analysis of difference images showed that first surface change during hydrogen loading appeared only after increasing the hydrogen pressure to  $p_H = 8 \times 10^{-6}$  mbar.

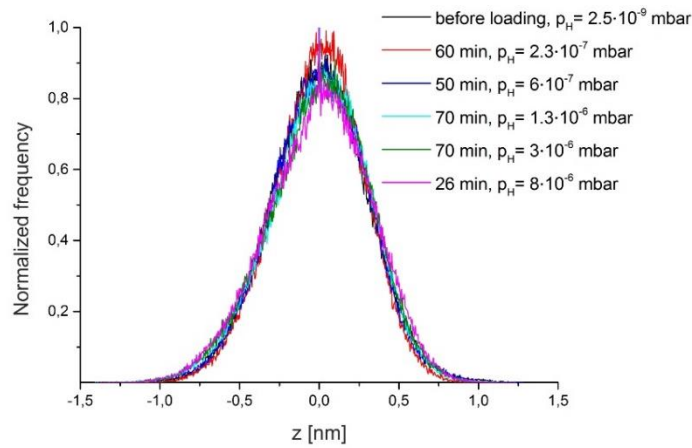


**Fig. 5.1.22** Height distribution histogram describing the STM surface-images shown in Fig. 5.1.21. Additional shoulder in the peak that was observed earlier in case of thick films is not found.

The difference image shown in Fig. 5.1.23 (a) was obtained by subtracting the STM surface-image given in Fig. 5.1.21 (e) from the STM surface-image given Fig. 5.1.21 (f). According to this difference image, some elevated (bright) regions appeared on the film surface. Hence, it can be clearly stated that by pressure increase to  $p_H = 8 \times 10^{-6} \text{ mbar}$  the sample surface experienced notable modification that occurred within 26 minutes after the pressure change. Black arrows in Fig. 5.1.21 (f) mark some surface regions, where according to the difference image in Fig. 5.1.23 (a), first surface changes were detected by in-situ STM measurements.

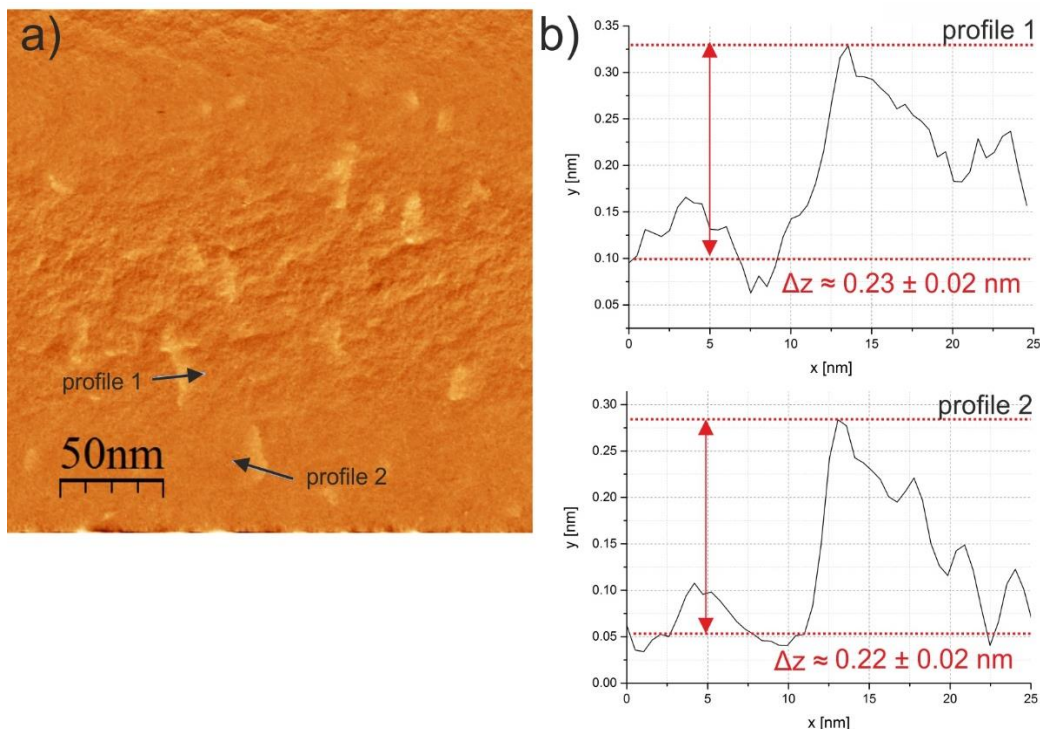


**Fig. 5.1.23** First surface modification was detected in the 8 nm Nb-H film after hydrogen loading for  $t_e = 26 \text{ min}$  at  $p_H = 8 \times 10^{-6} \text{ mbar}$ . **a)** STM difference image: elevated (bright) regions are clearly visible. Black arrows indicate lengths and directions of linear profiles measured across the sharp edges of new surface corrugations. **b)** Two linear profiles: Both curves have a shape of a sloped ramp on one side and an atomic step on other side. ( $\Delta z = 0.22 \text{ nm} - 0.23 \text{ nm}$ ).

At this point, it is important to mention that the applied hydrogen pressure  $p_H = 8 \times 10^{-6}$  mbar related to the first surface changes is 11 times higher in comparison to  $p_H = 7 \times 10^{-7}$  mbar applied to initiate first precipitation of hydride phase in the 15 nm Nb-H films and still 3 times higher than  $p_H = 3 \times 10^{-6}$  mbar applied to complete the phase transformation in the 15 Nb-H film. Furthermore, based on the STM results obtained for thicker samples discussed earlier in the frame of this chapter, it can be stated that local precipitation of hydride phase as well as possible traces of dislocations may cause an occurrence of new surface corrugation in here studied Nb-H thin film system.

Precipitates of hydride phase have a limited volume defined via the closed circular surface contours as it was shown e.g. in Fig. 5.1.18 (c). Similar surface features are not observed, here. Returning to the difference image shown in Fig. 5.1.23 (a), one can see an appearance of atomic steps visible on the film surface. They look like sharp, straight facets. As an example, two linear profiles measured across the new surface corrugations are shown in Fig. 5.1.23 (b). Both curves have a shape of a sloped ramp on one side and an atomic step on other side, as the height of the step is  $\Delta z \approx 0.22 - 0.23$  nm. This kind of surface corrugation was already observed in the case of the 15 nm Nb-H film and, as it was already supposed, might result from the glide-displacement of atomic planes caused by the formation of misfit dislocation at the film / substrate interface.

In principle hydrides could also be very, very large – that was what we expected beforehand. However, this is opposite to what was observed on the 15 and 25 nm films. Therefore, such large hydrides are not very likely and not considered further for interpretation of results in this thickness range.

At this stage, for a better understanding of the sample hydrogenation process, it is suggested to look at the result of resistance measurements that was performed simultaneously on the similar 8 nm Nb-H film. A graph given in Fig. 5.1.24 shows the normalized resistance value (red curve) and logarithmic pressure (blue curve) measured continuously during the hydrogen loading / unloading experiment. On the abscissa axis the relative experiment time is given. On the ordinate axis, on the left side, normalized resistance value and, on the right side, the hydrogen pressure are given. Here one can clearly see a direct correlation between the change of applied hydrogen pressure and the measured resistance curve. Additionally, for combined consideration, Fig. 5.1.25 (a-h) shows the STM difference images representing the absolute change of surface topography detected at different stages of hydrogen loading. The time points corresponding to the related STM images are linked with a relative time scale in the pressure / resistance curve and marked by filled circles (•) in Fig. 5.1.24. The results of this combined experiment are supposed to be considered together.

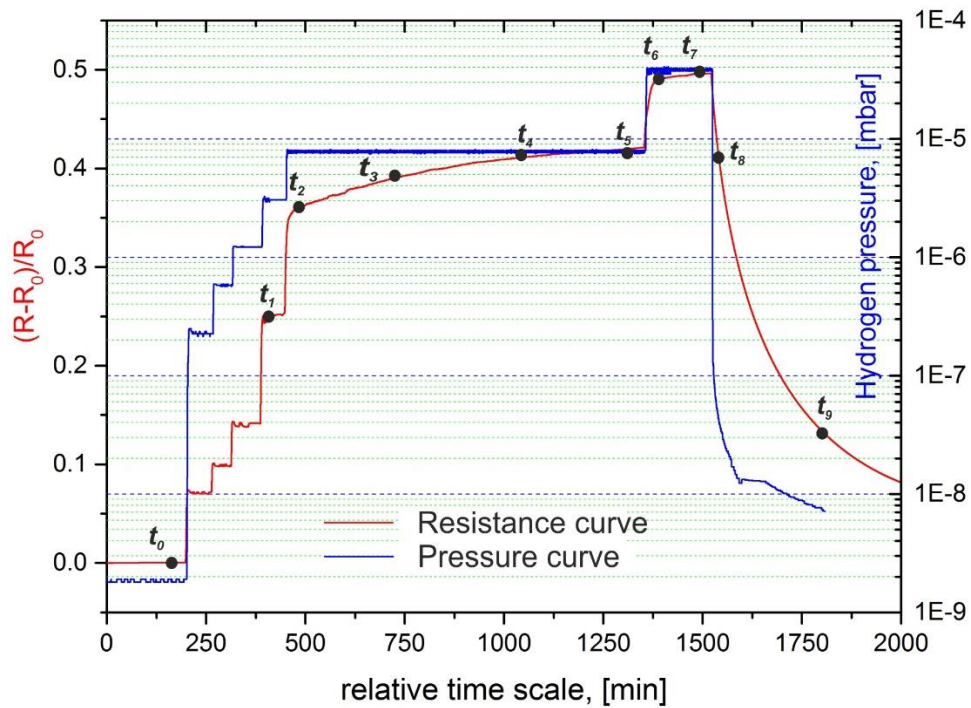


**Fig. 5.1.24** In-situ hydrogen gas loading / unloading resistance measurements of a 8 nm Nb film. On the abscissa axis, the relative time scale is given. On the ordinate axis, on the left side, normalized resistance value and, on the right side, the hydrogen pressure are given. Thus, the blue curve shows the pressure change in the loading chamber and the red curve – the change of normalized resistance value measured during the experiment. The STM images are linked with the relative time scale in the pressure / resistance curve (details see in the text). Therefore, the positions of reference STM images with respect to the relative time scale (•) are implemented. These reference points were used to obtain the difference images given in Fig. 5.1.25.

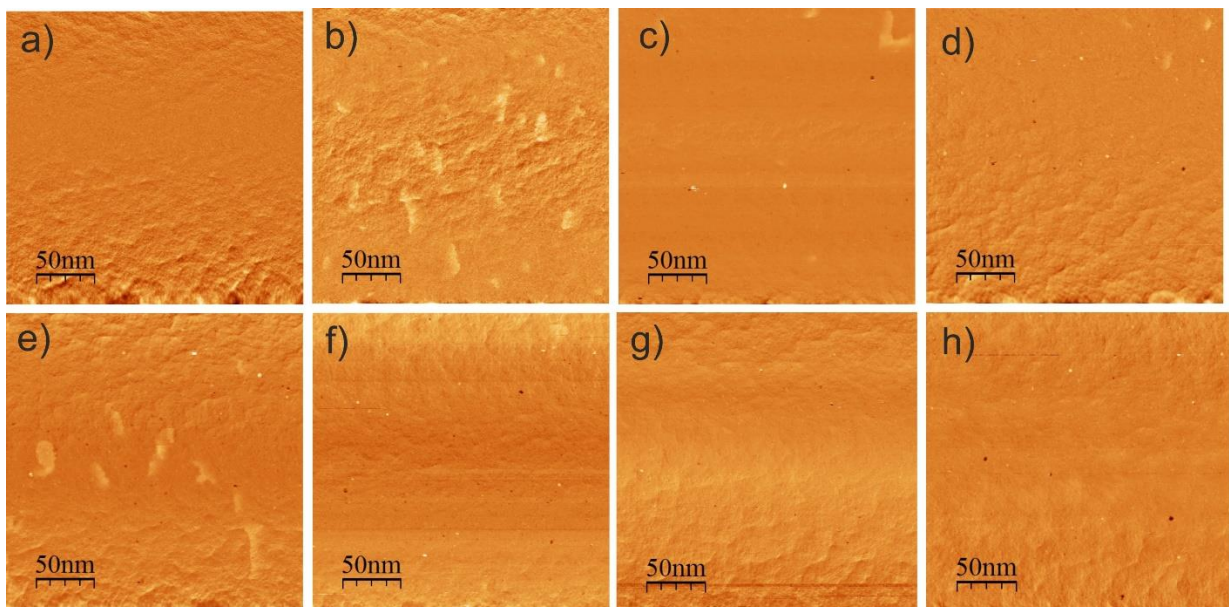


**Fig. 5.1.25** STM difference images represent the absolute change of surface topography detected at different stages of hydrogen loading. The corresponding time points are marked by filled circles (•) in Fig. 5.1.24. The difference images were obtained by subtraction the images measured at different times “*t*” given in Fig. 5.1.24: **a)**  $t_1 - t_0$ ,  $p_H = 3 \times 10^{-6}$  mbar; **b)**  $t_2 - t_1$ ,  $p_H = 8 \times 10^{-6}$  mbar; **c)**  $t_3 - t_2$ ,  $p_H = 8 \times 10^{-6}$  mbar; **d)**  $t_5 - t_4$ ,  $p_H = 8 \times 10^{-6}$  mbar; **e)**  $t_6 - t_5$ ,  $p_H = 4 \times 10^{-5}$  mbar; **f)**  $t_7 - t_6$ ,  $p_H = 4 \times 10^{-5}$  mbar; **g)**  $t_8 - t_7$ ,  $p_H = 4 \times 10^{-8}$  mbar; **h)**  $t_9 - t_7$ ,  $p_H = 4 \times 10^{-9}$  mbar.

First of all, this combined experiment revealed the finding of a relatively fast and strong response of the resistance curve to the change of the hydrogen pressure in the UHV - STM loading chamber. In details, upon every pressure increase up to  $p_H \leq 3 \times 10^{-6}$  mbar, the resistance value increases and within about 7 min - 10 min reaches a new equilibrium value (visible as a plateau region in the red curve in Fig. 5.1.24). At the same time, the STM measurements in this experiment revealed no surface modification, up to  $p_H \leq 3 \times 10^{-6}$  mbar as shown in Fig. 5.1.25 (a). The difference image in Fig. 5.1.25 (a) was obtained by subtraction of the STM image measured at  $p_H = 2.5 \times 10^{-9}$  mbar from the STM image measured at  $p_H = 3 \times 10^{-6}$  mbar. Thus, combination of these results suggests that upon pressure increase hydrogen atoms diffuse relatively fast in the Nb film, and, if there no plastic deformation or precipitation of hydride phase occur, the resistance value jumps and achieves a new equilibrium value corresponding to a certain hydrogen concentration in the sample (solid solution).

By further hydrogen pressure change to  $p_H = 8 \times 10^{-6}$  mbar, the resistance value does not achieve a new equilibrium value even after long hydrogen loading for about  $t_e = 905$  min. Instead of this, the resistance value in the beginning jumps and, then, continues to grow permanently, asymptotically approaching the plateau (equilibrium) value. At the same time, according to the STM difference images, only traces of dislocations appear on the sample surface upon related hydrogen loading step as shown in Fig. 5.1.25 (b). Furthermore, there are no localized circular elevations, similar to those as found for the thicker films. During subsequent hydrogen loading at the same pressure the density of new dislocations becomes smaller as shown in Fig. 5.1.25 (c, d). This trend demonstrates that the major stress release happens relatively fast, soon after the pressure increase. To remind the reader, it is suggested that the observed stress release in the 8 nm Nb-H film is attributed to the formation of misfit dislocation occurring at the film / substrate interface upon H-loading. Besides, a long-time resistance increase hints on further slower plastic deformation still occurring in the system even after long hydrogen exposure times. Careful step-by-step data analysis of difference images obtained at this pressure allows to conclude that hydride precipitates of a circular or any other clearly defined shape were not detected even at the highest applied pressure. Thus, precipitates of the hydride phase were not found.

Alternatively, hydrides of much larger size than the frame size would not be visible as discussed, for example, for coherent hydride precipitates in Pd-H films by Wagner et al. [23]. However, comparison with the previous STM data shows a complete change of the absorption kinetics, for the 8 nm film. This comparison supports the interpretation of the absence of hydrides.

Figure 5.1.25 (d) represents the difference image obtained by subtraction of two STM images, measured after hydrogen exposure at  $p_H = 8 \times 10^{-6}$  mbar for 825 min, and 675 min (see as well Fig. 5.1.24:  $t_5 - t_4$ ). While the STM measurements show very small surface changes appearing at the late stage of extended hydrogen loading at  $p_H = 8 \times 10^{-6}$  mbar (see Fig. 5.1.25 (d)), the related resistance value in Fig. 5.1.24 ( $t = t_5$ ) stays almost constant. Thus, it is suggested that the sloped resistance curve observed in this

measurement can be attributed to the plastic deformation events (the formation of misfit dislocations at the film / substrate interface) appearing in the film at this particular loading pressure. It is regarded to be not related to the phase transformation.

The difference image in Fig. 5.1.25 (e) was obtained by subtraction of the STM surface – image measured at  $p_H = 8 \times 10^{-6} \text{ mbar}$  ( $t_e = 825 \text{ min}$ ) from the STM surface – image measured at  $p_H = 4 \times 10^{-5} \text{ mbar}$  ( $t_e = 60 \text{ min}$ ) (see as well Fig. 5.1.24:  $t_6 - t_5$ ). Thus, one can see that by this further pressure increase to  $p_H = 4 \times 10^{-5} \text{ mbar}$  (Fig. 5.1.25 (e)) new surface corrugations similar to those that were already discussed in Fig. 5.1.23 (a, b) are detected. Again, cylindrical precipitates of hydride phase were not found. All the new surface corrugations visible in Fig. 5.1.25 (e) have a step-like elongated shape and their height does not exceed 0.23 nm. Further analyses of difference images suggest that after two hours of hydrogen loading at  $p_H = 4 \times 10^{-5} \text{ mbar}$  the surface images remain unchanged. Herewith, further surface changes were not detected, as shown Fig. 5.1.25 (f). At the same time, after the pressure increase to  $p_H = 4 \times 10^{-5} \text{ mbar}$ , the resistance shows first a jump and then a sloping curve with a trend to saturation.

Thus, the combined results allow to suggest that for both hydrogen pressures of  $p_H = 8 \times 10^{-6} \text{ mbar}$  and  $p_H = 4 \times 10^{-5} \text{ mbar}$ , only stress release and no precipitation and growth of the hydride phase were observed in the 8 nm Nb-H film. Furthermore, it is clearly visible that stress release is important for equilibration of Nb-H thin film system.

The type of surface corrugations observed by in-situ STM measurements in the case of the 8 nm Nb-H film could be questioned, if only results of the hydrogen loading experiment would be presented. Thus, to strengthen the arguments, suggesting plastic deformation in the film and no precipitation of the hydride phase, further discussion will address the second part of this experiment, namely the hydrogen unloading experiment.

### 5.1.5.2 Morphology change upon hydrogen unloading of a 8 nm Nb-H film

If hydrogen atoms diffuse out of the sample, any extended crystal structure related to the hydride phase (also  $\alpha$ -phase) should shrink and cause reverse surface changes as it was shown in chapter 5.1.3.2. Furthermore, if the hydrogen concentration in the sample becomes low enough, any possible precipitates of hydride phase would completely decompose. Opposite, if the topography change detected during hydrogen loading were caused by events of plastic deformation (at the film / substrate interface) and the related displacement of Nb atoms to the sample surface, surface topography is expected to be not reversible and it should not return to its original state upon sample unloading.

To unload the sample, the hydrogen leak valve was closed, resulting in a fast pressure drop in the vacuum chamber to about  $1 \times 10^{-8} \text{ mbar}$  and, then, subsequent slow exponential pressure decrease up to  $p_H = 9 \times 10^{-10} \text{ mbar}$ , as shown in Fig. 5.1.24.

Figure 5.1.26 shows the complete resistance curve measured during the hydrogen loading / unloading experiment. Here, the abscissa is the relative experimental time and the ordinate is the absolute resistance. According to the resistance curve, before the hydrogen loading experiment, the initial resistance of the film was about  $R = 8.6 \text{ Ohm}$ . Further, during the hydrogen loading experiment, it increased to about  $R = 12.8 \text{ Ohm}$  (48.8 percent of increase as compared to the initial value). Finally, during the unloading experiment, it decreased again up to about  $R = 8.7 \text{ Ohm}$  (2.4 percent of increase as compared to the initial value).

Thus, these measurements clearly reveal a strong drop of the resistance that occurred after decrease of hydrogen pressure. Hereby, the resistance curve doesn't not show completely reversible change. This result might be attributed to two factors: presence of new hydrogen-induced lattice defects (e.g. dislocations [118]) and/or the remaining hydrogen in the sample.

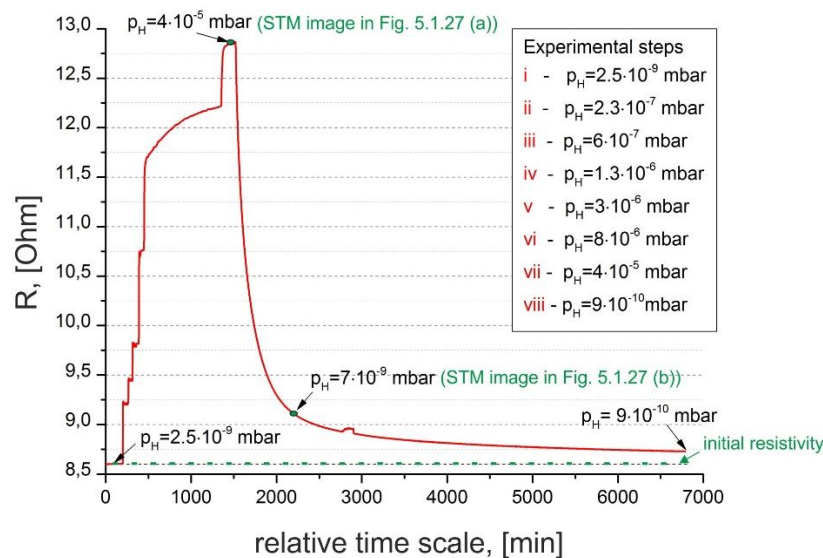


**Fig. 5.1.26** The complete resistance curve including, as compare to Fig. 5.1.24, additionally the data about the unloading of the sample. On the abscissa axis the relative experiment time is given. On the ordinate axis the absolute resistance value is given.

Nevertheless, the observed drastic decrease of the magnitude of resistance confirms the fact that the average hydrogen concentration in the film significantly drops. After about 550 minutes of unloading (9.2 hrs.), the resistance decreased up to about 9.2 Ohm. This result shows that at that particular unloading stage the largest part of the hydrogen atoms already diffused out of the film. Furthermore, for comparison,  $R = 9.2 \text{ Ohm}$  is an equilibrium resistance value reached during the first hydrogen pressure increase to  $p_H = 2.3 \times 10^{-7} \text{ mbar}$ . Therefore, taking into account previous STM results presented in this chapter for thicker films, hydrogen concentration at this pressure should be less than the solubility limit of  $\alpha$ -phase ( $c_H < c_\alpha$ ) in Nb-H thin film system (see chapter 2.4.7). Hence, it means that the mean hydrogen concentration in the 8 nm Nb-H film should be already low enough to decompose any possible precipitates

of the hydride phase, that could be theoretically present in the Nb host matrix after the hydrogen loading experiment with a maximum hydrogen pressure  $p_H = 4 \times 10^{-5} \text{ mbar}$ .

At the same time, STM measurements doesn't not reveal any surface modification during unloading of the sample. Figure 5.1.27 (a) shows the STM surface-image of the 8 nm Nb-film measured at  $p_H = 4 \times 10^{-5} \text{ mbar}$  ( $t_e = 168 \text{ min}$ ). Fig. 5.1.27 (b) presents the same surface region, but measured already during the hydrogen unloading experiment ( $t_{un} = 550 \text{ min}$ , and related to  $R = 9.2 \text{ Ohm}$ ). In Fig. 5.1.24, two STM images correspond to the time-points labeled, respectively, as  $t_7$  and  $t_9$ .

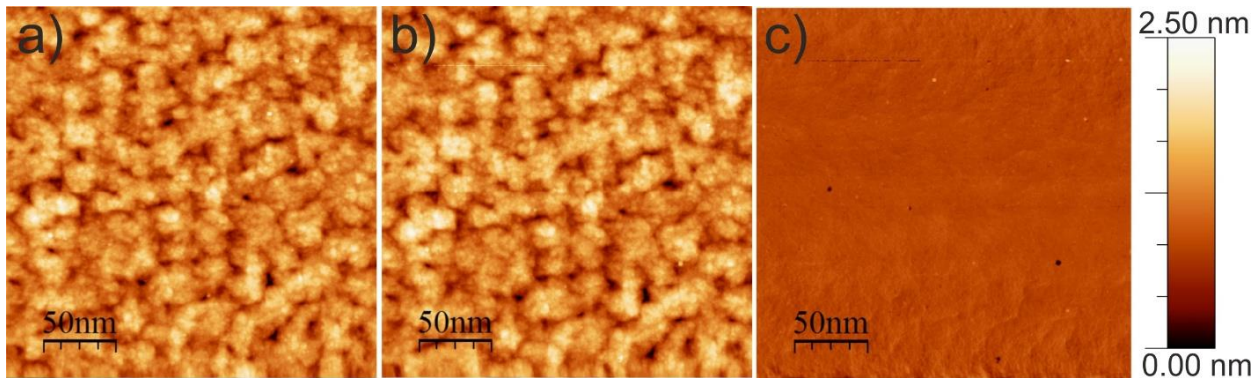


**Fig. 5.1.27** STM surface-images of a 8 nm Nb film **a)** Sample was loaded at  $p_H = 4 \times 10^{-5} \text{ mbar}$  for  $t_e = 168 \text{ min}$  **b)** Sample was unloaded at  $p_H = 4 \times 10^{-9} \text{ mbar}$  for  $t_{unl} = 550 \text{ min}$ . **c)** STM difference image: no reverse surface changes, expected in the case of hydride phase decomposition, are detected. (Frame size:  $250 \times 250 \text{ nm}^2$ ).

Figure 5.1.27 (c) shows the difference image of the two previously taken intermediate images measured in the loaded (Fig. 5.1.27 (a)) and in the unloaded (Fig. 5.1.27 (b)) state. The frame size for all the images is  $250 \times 250 \text{ nm}^2$ . Figure 5.1.27 (c) clearly shows that no new surface modification was detected during the unloading experiment. This means that any surface modifications appearing during the loading experiment remain during the unloading experiment. Taking into account the previously noted drop of the resistance to about  $R = 9.2 \text{ Ohm}$  and the difference image shown in Fig. 5.1.27 (c) it can be clearly stated that all the new surface corrugations measured by STM during sample loading were related to the events of plastic deformation (see Fig. 5.1.23 (a) and Fig. 5.1.25 (b, e)). Beside the difference image given in Fig. 5.1.27 (c), intermediate difference images taken to study the occurrence of local surface changes, as one would expect for local hydride decomposition, show no topographic changes in the chosen frame. In other words, no reverse surface changes appearing during unloading of the sample and indicating on the presence of  $\beta$ -precipitates is found upon the unloading experiment in the STM images. This is also shown in Fig. 5.1.25 (g, h). Here, for subtraction, the STM surface-image measured at  $p_H = 4 \times 10^{-5} \text{ mbar}$  was used as a reference image. The difference images related experimental time-points  $t_7$ ,  $t_8$  and  $t_9$  are given in the graph in Fig. 5.1.24. In general, this result correlates well with the finding during the loading experiment, as shown in Fig. 5.1.23 (a, b, c).

To summarize, the detected irreversible changes of the surface topography stay present on the surface even when the largest amount of hydrogen atoms has left the sample. Any traces of the phase transformation, similar to those that were revealed for thicker films, have not been found. Thus, it is concluded here that the phase transformation in the 8 nm Nb-H film is suppressed. At the same time, traces of dislocations, observed earlier also for thicker films, have been detected. Because the generation of dislocation loops forming around any hydride precipitates can be excluded from the consideration that precipitation does not occur in this film, one can suggest, that only misfit dislocations appearing at the film / substrate interface can release the stress arising in the system during hydrogen loading. Thus, even in the situation when the precipitation of the hydride phase does not occur, a regime of completely elastic and reversible film expansion cannot be realized in the 8 nm film.

### 5.1.6 Summary of STM measurements

In this subchapter, the results of STM measurements performed on five different Nb film thicknesses (55 nm, 40 nm, 25 nm, 15 nm and 8 nm) were presented. The results are summarized here. The hydrogen exposure pressure was varied from  $p_H = 1 \times 10^{-9}$  mbar to  $p_H = 4 \times 10^{-5}$  mbar. Phase transformation was found in the case of 55 nm, 40 nm, 25 nm and 15 nm films. In the case of 8 nm film phase transformation was not detected.

First precipitation of hydride phase for most of the samples was detected at about  $p_H = 7 \times 10^{-7}$  mbar. However, even after long hydrogen loading at these pressure conditions the phase transformation is not completed (Fig. 5.1.9). Further, it is shown that to increase the mean hydrogen concentration in the sample at RT and to cross the two-phase region of the Nb-H phase diagram in the case of thin epitaxial Nb films one needs permanently to increase the applied hydrogen pressure. So, for example, in the case of 15 nm Nb-H film the phase transformation was completed only after  $t_e = 530$  min of hydrogen loading at  $p_H = 3 \times 10^{-6}$  mbar (Fig. 5.1.26). The observed sloping plateau pressure hints on partial stress release that was also observed in the case of Pd-H films [14], [103].

Cyclic hydrogen loading / unloading experiments qualitatively showed that kinetics of hydrogen absorption becomes slow as soon as the phase transformation is initiated (Fig. 5.1.3). Further, it is shown that complete unloading of Nb-H films in vacuum conditions at RT is quite a challenging task, since hydrogen desorption from the sample occurs very slowly (Fig. 5.1.5). Only in the case of 8 nm film the unloading of the sample was possible (Fig. 5.1.26): The main mass of hydrogen released from the sample within about 1000 min (16.7 hrs.). Thus, it can be assumed that the difference in the kinetics of hydrogen desorption is attributed mainly to the increased contribution of mechanical stress (see chapter 2.4.3) and the absence of the hydride phase in the 8 nm film.

Furthermore, STM measurements have shown that depending on the film thickness different regimes of hydride phase precipitation and growth can be found during the phase transformation. Two differing appearances of the hydrides forming for the 40 nm and the 55 nm film and for the 15 nm and the 25 nm film were experimentally revealed. Herewith, typical height of surface corrugations as well as the distribution and lateral sizes of hydrides visibly change.

The 40 nm and the 55 nm films show a small number of large hydrides with a lateral sizes in a range from a few hundred nanometers to a couple of micrometers (Fig. 5.1.1 and Fig. 5.1.8). During hydrogen loading, these hydrides continued to grow forming the surface corrugations of an irregular shape. By repeated hydrogen loading, pre-existing hydrides continued to grow.

In contrast to this, in the case of the 15 nm and the 25 nm film, hydride precipitates demonstrated a much more dense and homogeneous lateral distribution and typically much smaller lateral sizes of about 50 nm – 60 nm (Fig. 5.1.11 and Fig. 5.1.19). According to the FEM simulations of Nörthemann, it is suggested that hydrides in the earlier stage of precipitate growth, in a first approximation, have a cylindrical shape (resulting in a circular surface modification) and grow very slowly as compared to the loading time. Therewith, they preferentially conserve their volume and lateral sizes. Following the suggestion of Nörthemann et al. [19], [73] this behaviour is labelled as “locked-in size”. Upon further hydrogen loading at different  $p_H$ , the number density of hydrides increases.

The difference observed in precipitation and growth of the hydride phase is suggested as a confirmation of an existence of the critical film thickness separating coherent and semi-coherent phase transformation in Nb-H thin films. According to the STM measurements it is assumed to lie in a range between  $d = 25 \text{ nm}$  and  $d = 40 \text{ nm}$ . Furthermore, it is suggested that in the coherent regime ( $d \leq 25 \text{ nm}$ ) the phase transformation is governed mainly by nucleation while in the incoherent regime ( $d \geq 40 \text{ nm}$ ) the transformation is growth-controlled. The related result was recently published in Ref. [133].

Besides, the average height of surface corrugation caused by local volume expansion was found to be scaled down together with the film thickness. While, in the case of the 55 nm Nb film it is about 2.9 nm (5.3 percent from the initial film thickness), in the case of the 15 nm Nb film it decreases to 0.65 nm (4.4 percent from the initial film thickness). Because of this scaling, one cannot draw unambiguous conclusions about the coherency conservation between hydride precipitates and the surrounding  $\alpha$ -matrix only from the local film expansion in STM surface-images. However, during STM measurements performed on the 15 nm and the 25 nm thick samples, some indirect evidences of preferentially coherent phase transformation were revealed. The related results for the thin films of 15 nm and 25 nm thickness, where hydride formation was observed, can be summarized as a following:

- 1) Change of precipitation mode: Preferential appearance of new hydride phase precipitates instead of the further growth of pre-existing ones (Fig. 5.1.11).

- 2) Coupled contraction of co-existing volume fractions of  $\alpha$ - and  $\beta$ -phases in the sample (observed during the hydrogen unloading experiment, Fig. 5.1.14 (d)).
- 3) The finding of the 'locked-in size' precipitates suggests the formation of coherent hydrides for the 15 nm and the 25 nm film (Fig. 5.1.16).
- 4) The decrease of the slope angle revealed in the transition area between the  $\alpha$ -phase and the  $\beta$ -phase region (Fig. 5.1.11 (c) and Fig. 5.1.18 (d, e) vs. Fig. 5.1.7 (a)).

Nevertheless, events of plastic deformation were clearly revealed at the late stage of sample hydrogenation even in the case of 15 nm Nb-H film (Fig. 5.1.19 and Fig. 5.1.20). It was suggested that an appearance of step-like surface corrugations with the sharp, straight edges are related to the emergence of misfit dislocations forming at the film / substrate interface (see chapter 2.4.4).

Finally, combined results of STM and resistance measurements on the 8 nm Nb-H film were provided (chapter 5.1.5). The main result of these simultaneous measurements performed at the same experimental conditions was the finding of suppression of phase transformation in the 8 Nb-H nm film. Despite the fact that at the applied  $p_H = 4 \times 10^{-5}$  mbar the average hydrogen concentration in the sample has to be relatively high to promote the phase transformation process, any precipitation of a hydride phase was not detected. Thus, only Nb-H solid solution phase was present in the film. Furthermore, the combined consideration of the resistance curve (Fig. 5.1.24) and the STM difference images (Fig. 5.1.25) allows to suggest that there are several stages of sample hydrogenation. Up to the pressure  $p_H = 3 \times 10^{-6}$  mbar events of plastic deformation were not detected (Fig. 5.1.25 (a)). This is suggested to directly affect the waiting time required for equilibration the Nb-H system. Directly after the pressure increase to  $p_H = 8 \times 10^{-6}$  mbar and  $p_H = 4 \times 10^{-5}$  mbar, some events of plastic deformation were detected (Fig. 5.1.25 (b, e)). The observed traces of dislocations were related to the stress release occurring at the film / substrate interface. Therewith, sloped resistance curves observed in these combined measurements were attributed to the plastic deformation events appearing in the film at this particular hydrogen loading pressures and not to the phase transformation process. To strengthen this argumentation, the sample was unloaded as shown by resistance measurements (Fig. 5.1.26). Herewith, the related STM measurements did not show any reverse surface modification (Fig. 5.1.27) that would indicate on the decomposition of hydride phase in the film. New surface corrugations stayed present on the surface, even when the major amount of hydrogen atoms was released from the sample.

## 5.2 XRD results upon hydrogen loading

To verify the STM results, namely the finding of the critical film thickness ( $25 \text{ nm} \leq d_c \leq 40 \text{ nm}$ ) and coherent phase transformation for films thicknesses below than  $d_c$ , the second independent experimental technique was required. Therefore, as an alternative method to study the phase transition in Nb-H thin films, in-situ XRD measurements were applied, as presented in chapter 3.5.3. Series of XRD measurements were performed in-situ during hydrogen loading / unloading experiment for different film thicknesses in the range from 5 nm to 105 nm. Changes occurring in the XRD diffraction patterns and their reversibility upon cyclic hydrogen loading have been studied.

### 5.2.1 Different XRD patterns below and above the critical thickness: refinement of the critical value

During the loading experiment the hydrogen gas pressure  $p_H$  was increased from  $p_H = 1 \times 10^{-5} \text{ mbar}$  to  $p_H = 1 \text{ mbar}$ . In-situ XRD measurements show a strong difference in the X-ray patterns of the films with a different thickness above and below the experimentally derived by STM critical film thickness range between 25 nm and 40 nm. First, results of XRD patterns observed for the relatively thick film ( $d > d_{cr}$ ) will be presented in chapter 5.2.1.1. Then, in chapter 5.2.1.2, the results obtained on intermediate films between 37 nm and 15 nm will be given. Finally, the results for films thinner than 15 nm will be presented in chapter 5.2.1.3.

#### 5.2.1.1 Thick Nb film: studies on films with $d > 43 \text{ nm}$

Figure 5.2.1 shows the peak development for different stages of hydrogen loading at  $p_H = 1 \times 10^{-3} \text{ mbar}$  in a 60 nm Nb-H film. The black arrow that is given on the right side in Fig. 5.2.1 shows the time axis of the experiment. In the lowest curve only two peaks are visible, namely the Nb (110) at  $2\theta = 26.35^\circ$  and the Pd (111) at  $2\theta = 27.25^\circ$ . In intermediate curves three peaks, namely the Nb-H ( $\alpha$ -phase), the Nb-H ( $\beta$ -phase) and the Pd (111) peaks are clearly visible. The upper curves show only the Nb-H ( $\beta$ -phase) peak and Pd (111) peak.

Conditionally, changes appearing in XRD patterns during hydrogen absorption are related to three different stages of sample hydrogenation. Gray markers given in Fig. 5.2.1 show the regions corresponding to these three different stages and will be used further in the text for more detailed description of the graph. Hereby, the Pd (111) peak does not change its width and the position is not affected by hydrogen (see also chapter 3.5.3). This can be understood in terms of the solubility ratio between H in Nb and H in Pd at RT for the pressure range used ( $3.33 \times 10^4$  [111]).

During the first stage (i) the Nb crystal lattice undergoes the homogeneous expansion that is visible via the Nb peak shift from  $26.35^\circ$  to  $25.95^\circ$ . At this stage, only the Nb-H ( $\alpha$ -phase) with relatively low hydrogen concentration is present in the sample volume (for details see chapter 2.1.2 and chapter 3.5.3). Observed peak shift corresponds to the lattice expansion of about 1.1 % in the out-of-plane  $\langle 110 \rangle$  crystallographic direction, if compared to the as-prepared state.

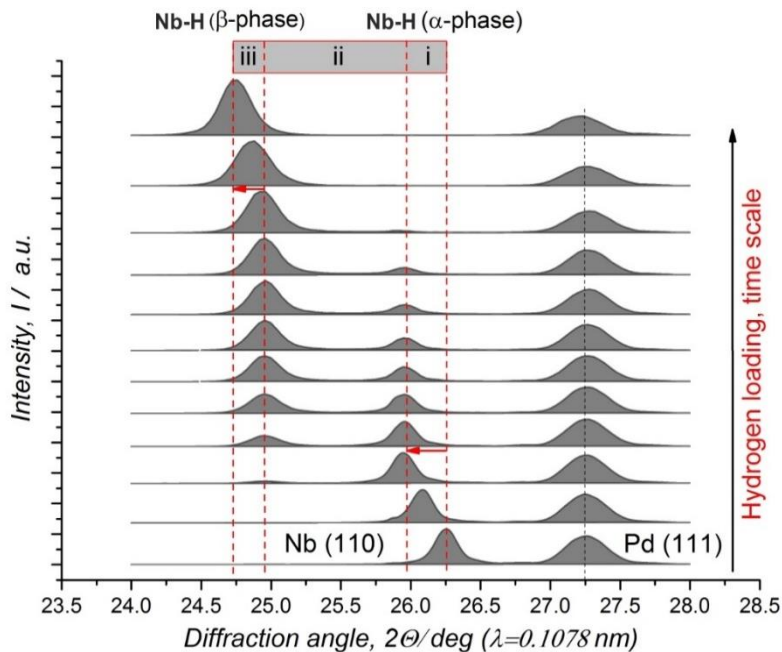


**Fig. 5.2.1** Change of XRD pattern during hydrogen absorption in the 60 nm Nb-H film ( $\lambda = 0.1078 \text{ nm}$ ). The Nb (110) peak shifts to lower angles because of the lattice expansion upon hydrogen absorption. Due to the precipitation of hydride phase in the sample Nb-H ( $\beta$ -phase) peak occurs in the intermediate curves. Thereby, two well-separated peaks corresponding to the Nb-H  $\alpha$  – phase and Nb-H  $\beta$  – phase volume fractions are visible upon phase transformation. Corresponding peak positions are marked with dashed lines. The Pd (111) peak position stays constant. Gray markers conditionally show the regions of three different stages of sample hydrogenation (details see in the text).

The second stage (ii) corresponds to the phase transition from the Nb-H ( $\alpha$ -phase) to the Nb-H ( $\beta$ -phase) occurring continuously in the sample. By continuous hydrogen loading, the Nb-H ( $\beta$ -phase) peak appears and the intensity of the Nb-H ( $\alpha$ -phase) peak lowers. The positions of the Nb-H ( $\alpha$ -phase) peak and the Nb-H ( $\beta$ -phase) peak ( $2\vartheta = 25.95^\circ$  and  $2\vartheta = 24.96^\circ$  respectively) stay constant during the phase transformation. No linkage between the peak positions is visible and the peak positions are independent of each other. Furthermore, the Nb-H ( $\beta$ -phase) peak position at  $2\vartheta = 24.96^\circ$  corresponds to the local lattice expansion of about 5.1 % in the out-of-plane  $\langle 110 \rangle$  crystallographic direction. This result clearly demonstrates the presence of the phase transition and that, in the two-phase field, the two phases behave independently. This is expected for incoherent phases, or large hydrides with negligible interfacial area.

In the third stage (iii) the Nb-H hydride peak shifts from  $2\vartheta = 24.96^\circ$  to  $2\vartheta = 24.75^\circ$ . At this stage,

only the Nb-H ( $\beta$ -phase) with relatively high hydrogen concentration is present in the sample volume. Thus, the Nb-H crystal lattice undergoes a lattice expansion in the hydride single-phase field. The final position of the Nb-H ( $\beta$ -phase) at  $2\vartheta = 24.75^\circ$  corresponds to the lattice expansion of about 6 % in the out-of-plane  $\langle 110 \rangle$  crystallographic direction if compared to the peak position of (110) reflection of the  $\alpha$ -phase, in the as-prepared state.

Thus, in the 60 nm Nb-H film phase transformation is clearly visible via XRD measurements performed in-situ during hydrogen gas loading. Hereby, the Nb-H ( $\alpha$ -phase) and the Nb-H ( $\beta$ -phase) peaks can be well separated. A similar "two peak"- behaviour, besides that demonstrated here for the 60 nm Nb-H film, was found as well in the case of 43 nm, 80 nm and 105 nm thick Nb-H films.

### 5.2.1.2 Intermediate film thickness: studies on 15 nm – 37 nm Nb films

In comparison to XRD patterns obtained for "thick" samples, there was a set of XRD measurements on "intermediate" samples, where XRD patterns showed significant differences despite the use of similar experimental conditions [133]. Studies were performed on 15 nm, 17nm, 25 nm, 30 nm and 37 nm Nb-H films.

The principal differences appearing in the XRD patterns are presented exemplary in Fig. 5.2.2. It shows the peak development for different stages of hydrogen loading at  $p_H = 1 \times 10^{-3}$  mbar for a 17 nm Nb-H film. As previously, the black arrow shows the time axis direction of the experiment. In the bottom curve only two peaks, namely the Nb (110) at  $2\vartheta = 26.22^\circ$  and the Pd (111) at  $2\vartheta = 27.25^\circ$  are visible. The difference appears upon hydrogen loading, namely in the  $2\vartheta$  angle range, where the phase transformation and the "two peaks" – behavior was observed in the case of "thick" films. In detail, only one broad symmetric Nb (110) - peak is now observed in the Fig. 5.2.2. This one broad peak moves towards lower  $2\vartheta$  angles upon hydrogen loading, as shown in Fig 5.2.2. No separated hydride peak appears in the pattern. Due to the lattice expansion caused by hydrogen absorption at  $p_H = 1 \times 10^{-3}$  mbar, the Nb (110) peak shifts from  $26.22^\circ$  to  $24.69^\circ$  that corresponds to about 6.1 % of lattice expansion in the out-of-plane direction  $\langle 110 \rangle$  - crystallographic direction if compared to the peak position of (110) reflection of the  $\alpha$ -phase, in the as-prepared state.

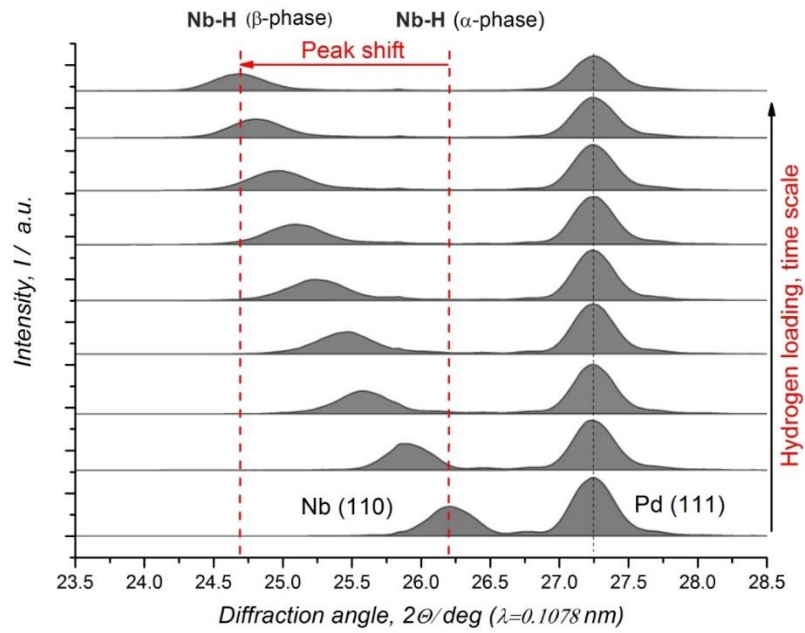


**Fig. 5.2.2** Change of XRD patterns during hydrogen absorption in the 17 nm Nb-H film ( $\lambda = 0.1078 \text{ nm}$ ). The Nb (110) peak shifts to lower angles because of the lattice expansion upon hydrogen absorption. Due to the precipitation of hydride phase in the sample, Nb (110) peak gets broader in the intermediate curves. Thereby, only one broad symmetric peak corresponding to mixture of Nb-H ( $\alpha$ -phase) and Nb-H ( $\beta$ -phase) volume fractions is visible upon phase transformation. Corresponding peak shift is marked with dashed lines. Pd (111) peak position stays constant.

Figure 5.2.2 shows for the peak observed in the marked region (two red vertical lines), a slight drop in intensity and a peak broadening, with respect to the  $\alpha$ -phase reflection. Figure 5.2.3 illustrates the behaviour of the FWHM values of the Nb (110) peak at different  $2\theta$  angles, given in Fig. 5.2.2. The experimental curve clearly shows that the FWHM value changes and reaches a maximum value of  $0.51^\circ$  at a peak position of  $2\theta = 25.25^\circ$  and then starts to decrease. Such a behaviour would not be expected within a single-phase region. Even when defect occurrence could explain the peak broadening upon hydrogen loading, the peak width decrease would be difficult to explain.

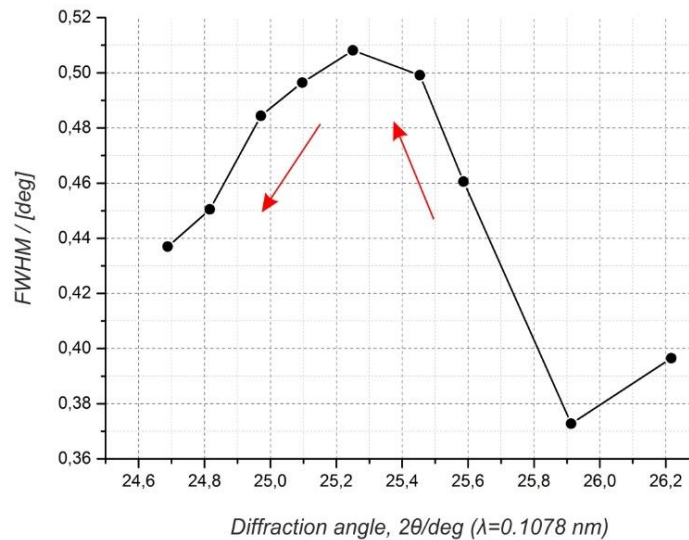


**Fig. 5.2.3** Broadening of Nb (110) peak appearing upon phase transformation. FWHM value is determined from the Gauss fitting applied to Nb (110) peak measured at different intermediate stages of phase transformation in the 17 nm Nb-H film. Measured experimental curve shows that the FWHM value in the beginning increases and reaches its maximum value equal  $0.51^\circ$  under  $2\theta = 25.25^\circ$  and then starts to decrease.

At this point it should be reminded that the fact of phase transformation was explicitly found with STM measurements for similar thicknesses of films (see chapter 5.1.4.1). Thus, even though there is just one peak, phase transition is known to appear. Thus, the finding of peak broadening, intensity drop and strong shift must be related to the phase transition. It can be understood in the frame of a coherent matching between the two coexisting Nb-H ( $\alpha$ -phase) and Nb-H ( $\beta$  – phase) volume fractions in the sample. The detailed explanation and argumentation how two coexisting phases can build one peak will be given later in chapter 6.1.

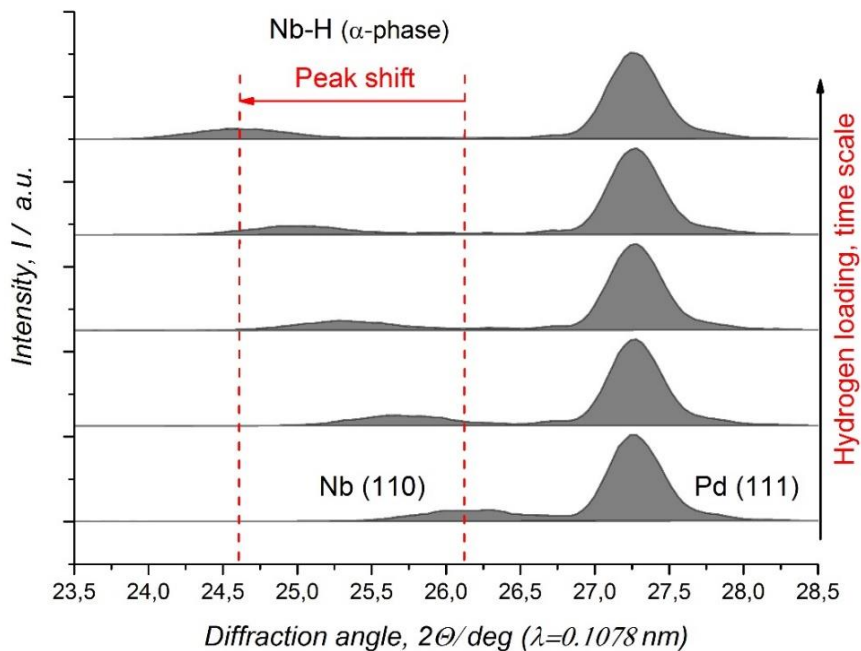
The peak position at  $2\theta = 25.25^\circ$  should roughly correspond to the transformation stage, where the coexisting Nb-H ( $\alpha$ -phase) and Nb-H ( $\beta$ -phase) occupy roughly equal volume fractions. The corresponding average lattice expansion in the out-of-plane  $\langle 110 \rangle$  - crystallographic direction at this stage reaches about 3.8 % if compared to the peak position of (110) reflection of the  $\alpha$ -phase, in the as-prepared state.

In the frame of this study, a similar "one peak" - behaviour, as demonstrated for the 17 nm Nb-H film, was found as well for the 15 nm, 25 nm, 30 nm and 37 nm thick Nb-H films. Therewith, in XRD-pattern, for these films only the broadening of the Nb (110) peak and the drop of its intensity suggest the presence of the phase transformation, in this intermediate film thickness range.

In common, these results show that phase transformation can become nearly invisible for XRD measurements. Hence, the phase transformation can be easily missed or the XRD result can be misinterpreted as the absence of phase separation.

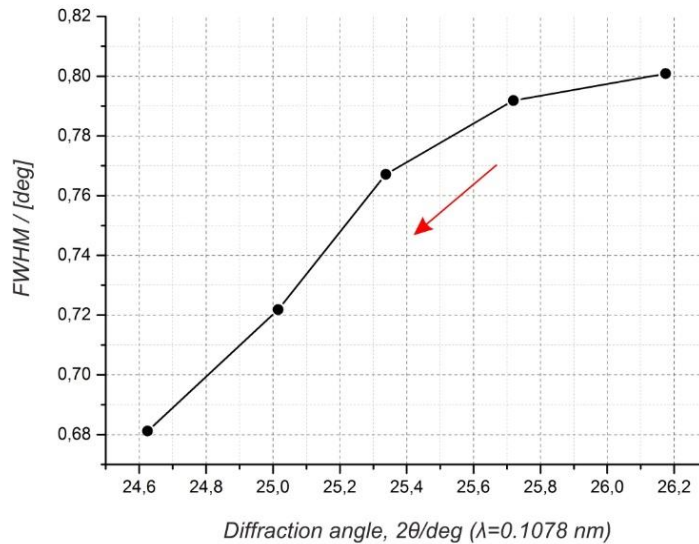
### 5.2.1.3 Thin films: studies on films with $d < 15$ nm

Figure 5.2.4 shows XRD patterns measured during hydrogen absorption in a 8 nm Nb-H film. Hydrogen pressure during this loading experiment was increased from  $p_H = 5 \times 10^{-5}$  mbar to  $p_H = 1 \times 10^{-1}$  mbar. First notable peak shift was detected at  $p_H = 1 \times 10^{-3}$  mbar within about 10 min. To facilitate further hydrogen absorption,  $p_H$  was several times increased and after all applied steps it reached  $p_H = 1 \times 10^{-1}$  mbar. At this stage, the system came into an equilibrium state that was proven by accompanying electrical resistance measurements and fixed final position of the Nb (110) peak. Total exposure time of the sample to hydrogen atmosphere was about  $t_e = 280$  min. XRD patterns shown in Fig. 5.2.4 demonstrate strong peak shift, as marked with a red arrow.



**Fig. 5.2.4** Change of XRD patterns during hydrogen absorption in the 8 nm Nb-H film ( $\lambda = 0.1078$  nm). The Nb (110) peak shifts to lower angles because of the lattice expansion upon hydrogen absorption (marked with a red arrow).

This peak shift appeared within about 195 minutes and was confirmed by set of 22 XRD scans measured after each other. The maximum intensity of Nb (110) peak stayed constant during hydrogen absorption. The FWHM value of the peak continuously decreased simultaneously with the peak shift. Due to the lattice expansion caused by hydrogen absorption, the Nb (110) peak shifts from  $26.17^\circ$  to  $24.62^\circ$  that corresponds to about 6.1% of lattice expansion in the out-of-plane  $\langle 110 \rangle$  - crystallographic direction if compared to the peak position of (110) reflection of the  $\alpha$ -phase, in the as-prepared state. Figure 5.2.5 clearly demonstrates the shrinking of the Nb (110) peak width from  $0.8^\circ$  to  $0.68^\circ$  that occurred during hydrogen absorption and lattice expansion. Hereby, intermediate peak broadening, as discussed previously for intermediate film thicknesses (see Fig. 5.2.3), was not found. Similar results were obtained for the 5 nm Nb-H film.



**Fig. 5.2.5** Shift and shrinking of Nb (110) peak width appearing upon hydrogen loading. FWHM value is determined from the Gauss fitting applied to Nb (110) peak measured at different intermediate stages of hydrogen loading in the 8 nm Nb-H film. Observed experimental dependency shows that the FWHM value decrease from  $0.8^\circ$  to  $0.68^\circ$ . Peak broadening is not found.

Thus, it is suggested that for this film thickness range, phase separation does not appear. This interpretation correlates with the STM results on the 8 nm Nb-H film, as previously presented in chapter 5.1.5. Hydrogen absorption in the sample without any phase separation causes a homogeneous lattice expansion that is visible in XRD patterns as only a shift of the Nb (110) peak. Thereby, XRD patterns might look very similar to “one peak” behavior that was found before for thicker samples (15 nm, 17 nm, 25 nm, 30 nm, 37 nm). However, there, the peak also broadened upon hydrogen absorption – for films of 8 nm and 5 nm, the peak width continuously decreases upon hydrogen absorption. The possible explanation why this happens will be given later in chapter 5.2.3.

The series of in-situ hydrogen gas loading XRD experiments performed for different film thicknesses in the range from 5 nm to 105 nm allowed to find experimentally the thickness range, where the shape of XRD patterns switches between three different types, as shown exemplary for 60 nm (“two peak” behaviour), 17 nm (“one peak” behaviour) and 8 nm (“one broad peak” behaviour) Nb-H films. Table 5.2.1 summarizes the information about different types of XRD patterns and the peak broadening measured for different film thicknesses. All the samples were exposed to hydrogen pressures not exceeding  $p_H = 1 \text{ mbar}$ . According to the Table 5.2.1, switching between different XRD patterns occurs first in the thickness range between 37 nm - 43 nm and then between 8 nm - 15 nm.

**Table 5.2.1** Different behavior of the Nb-H related peaks in the XRD pattern in dependence on the film thickness. Three different regimes (marked by different colours) are revealed: “two peak” behaviour, “one peak” behaviour and “one broad peak” behaviour.

Nb film thickness, [nm]	Peak separation, [yes / no]	Peak broadening, [- / yes / no]
105	Yes	-
80	Yes	-
60	Yes	-
43	Yes	-
37	No	Yes
30	No	Yes
25	No	Yes
17	No	Yes
15	No	Yes
8	No	No
5	No	No

## 5.2.2 Cyclic hydrogen loading: reversibility test

In the case of coherent phase transformation, reversible lattice changes are expected to be found during cyclic hydrogen loading / unloading experiments. Thereby, in the frame of this study, this type of experiment was performed for several film thicknesses. Possible peak broadening and irreversible shift of the Nb (110) peak in the unloaded sample state were addressed with respect to the initial peak state before the hydrogen loading experiment.

To facilitate hydrogen desorption from Nb-H film, the samples were exposed to atmospheric environment (by breaking the vacuum conditions in the chamber) or, sometimes, by use of bottled oxygen gas, as described in chapter 3.5.3.

Figure 5.2.6 demonstrates the change of XRD patterns observed during hydrogen desorption from the 17 nm Nb-H film (intermediate thickness range) that was previously loaded with hydrogen. Exposing the sample to atmospheric conditions shifts the Nb (110) peak from  $2\theta = 24.733^\circ$  in the loaded state to about  $2\theta = 26.194^\circ$  in the unloaded state. The reverse peak shift is attributed to the contraction of interplanar distances in the measured  $\langle 110 \rangle$  - crystallographic direction. Thus, the cyclic hydrogen loading / unloading experiment was successfully carried out.

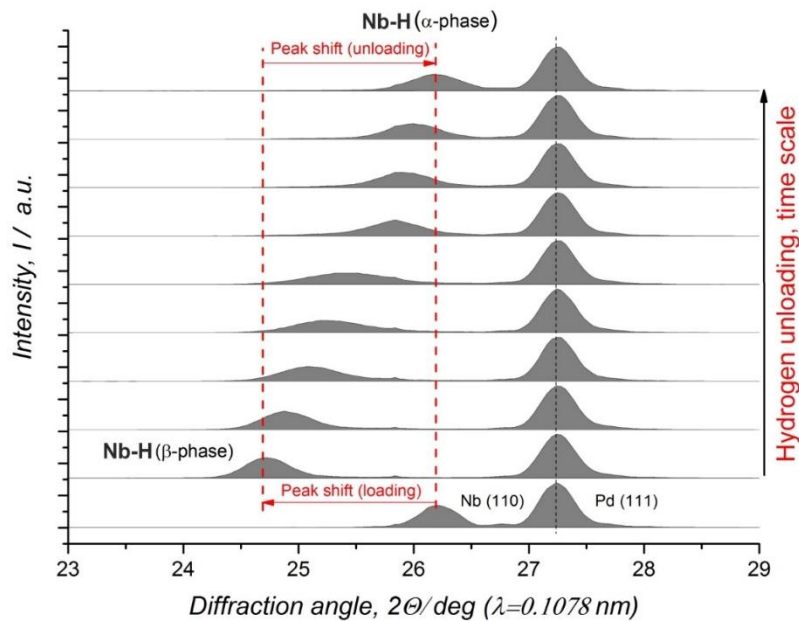


**Fig. 5.2.6** Change of XRD patterns observed during hydrogen desorption from the 17 nm Nb-H film ( $\lambda = 0.1078 \text{ nm}$ ). Reverse hydride phase decomposition is visible in the XRD patterns as a single broad peak that shifts forward to the higher angles. Therewith Nb (110) peak shifts from  $2\theta = 24.733^\circ$  (in the loaded state) to about  $2\theta = 26.194^\circ$  (in the unloaded state).

Figure 5.2.7 shows the FWHM values of Nb (110) peaks measured at different  $2\theta$  angles for different stages of reverse phase transformation given in Fig. 5.2.6. Similar to the result obtained upon hydrogen loading, significant broadening of Nb (110) peak was found. However, the broadening of the Nb (110) - peak appearing upon reverse phase decomposing becomes much stronger in comparison to the first loading experiment discussed in chapter 5.2.1. The measured experimental curve shows that the FWHM value reached its maximum value equal  $0.84^\circ$  under  $2\theta = 25.45^\circ$  and then started to decrease. Again, this is attributed to crossing the concentration range related to a miscibility gap of the Nb-H film system and the reverse transformation from the  $\beta$ -phase into the  $\alpha$ -phase. Thus, the intermediate peak broadening and the peak shift confirm the presence of two coexisting phases in the 17 nm Nb-H film.

Furthermore, as compared to the FWHM value of initial Nb (110) peak in the as-prepared sample state ( $FWHM = 0.396^\circ$ ), a peak broadening of about  $0.554^\circ$  remains in the unloaded state at  $2\theta = 26.194^\circ$  (see Fig. 5.2.7: the related area of interest is marked with a red dashed ellipse). Even by the assumption that some residual hydrogen atoms may be present in the sample, and that the hydrogen concentration in the film is not equal to zero, the hydride phase should be clearly decomposed at this unloaded state. Thereby, the detected significant peak broadening indicates on some irreversible lattice distortions that appeared in the sample during cyclic hydrogen loading / unloading experiment.

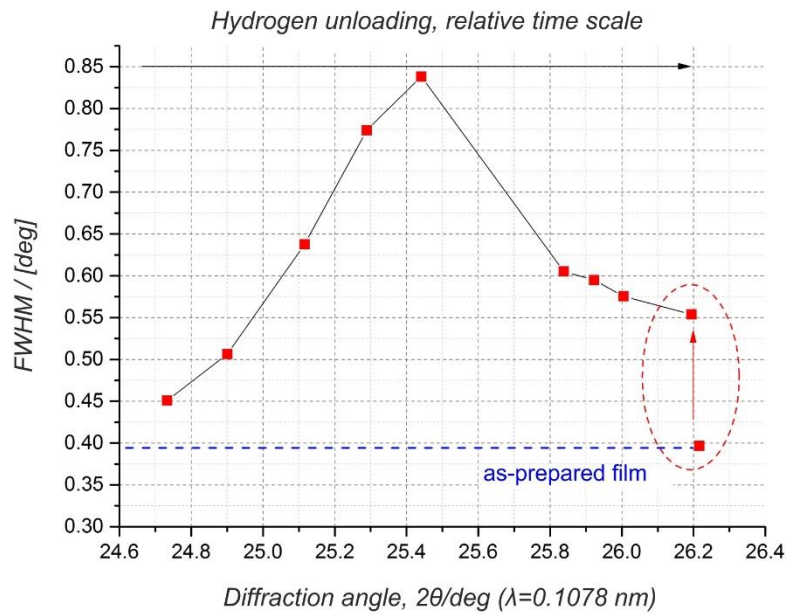


**Fig. 5.2.7** FWHM value determined from the Gauss fitting applied to Nb (110) peak measured at different intermediate stages of reverse decomposition of hydride phase in the 17 nm Nb-H film. Measured experimental curve shows that the FWHM value in the beginning increases and reaches its maximum value equal  $0.84^\circ$  under  $2\theta = 25.45^\circ$  and then starts to decrease. As compared to the FWHM value of initial Nb (110) peak in the as-prepared sample state ( $FWHM = 0.396^\circ$ ), significant peak broadening of about  $0.554^\circ$  was measured in the unloaded state at  $2\theta = 26.194^\circ$  (marked with a red dashed ellipse).

### 5.2.3 Suppression of phase transformation in the 8 nm thin film

As presented above, hydrogen absorption in the thinnest films leads to peak width reduction. This result can be explained by the film expansion upon hydrogen absorption. To prove it, Scherrer's formula was applied as a first approximation (see chapter 3.5.1). Thereby, the two Nb (110) peaks corresponding to the initial and to the final stage of hydrogen loading were considered, as given in Fig. 5.2.4.

By calculating the theoretically expected FWHM ( $B_{theor}$ ) by using Eq. (3.4), the domain size  $D$  was assumed to equal to the film thickness (8 nm and 8.47 nm, respectively, as determined by XRR measurements), and by taking  $\lambda = 0.1078$  nm. The calculation results are presented in Table 5.2.2.

**Table 5.2.2** The calculation of peak width reduction due to the film expansion according to the Scherrer's formula.

Loading stage	$2\theta$ [degrees]	$D$ [nm]	$B_{theor}$ [radians]	$B_{teor}$ [degrees]	$B_{exp}$ [degrees]	$\Delta B$ [degrees]
as-prepared	26.174	8.00	0.012451	0.7134	0.8008	0.087
loaded sample	24.625	8.47	0.011738	0.6716	0.68116	0.009

According to the calculation results, one can see that the film expansion upon hydrogen absorption in the thinnest films can indeed result in a visible decrease of the peak width. The decrease of the calculated  $B_{theor}$  related to the FWHM from  $0.71^\circ$  to  $0.67^\circ$  stays in good agreement with the experimental observation of a FWHM reduction from  $0.80^\circ$  to  $0.68^\circ$ , resulting from the reverse dependency on the film thickness. The theoretically possible value of peak broadening ( $0.67^\circ$ ) related to the film expansion caused by hydrogen absorption is very close to the experimentally measured FWHM value ( $0.68^\circ$ ). It is important to note that the  $B_{exp}$  includes as well the instrumental line broadening that might make this value higher as compared to the calculated one.

Thus, the change of the peak shape (constant intensity and decreasing FWHM) can be mainly attributed to the lattice expansion detected in homogeneous high concentration solid solution phase. To strengthen this point, it should be reminded that any intermediate peak broadening (during H-loading) that could appear in the XRD patterns due to the presence of micro-stresses and coherency strain [134] related to the precipitation of the hydride phase in the case of 8 nm Nb-H film was not observed (see Fig. 5.2.5).

The unloading of the sample shows that the Nb (110) peak again shifts backwards to higher angles in the unloaded sample state. It shifts from  $2\vartheta = 26.174^\circ$  (as-prepared state) to about  $2\vartheta = 26.407^\circ$  (unloaded state). The corresponding graph is given in Fig. 5.2.8. Besides, the FWHM value increases from  $0.80^\circ$  (as-prepared state) to  $0.86^\circ$  (unloaded state). Thus, the Nb (110) peak of the unloaded film is wider than that of the initial hydrogen-free film.

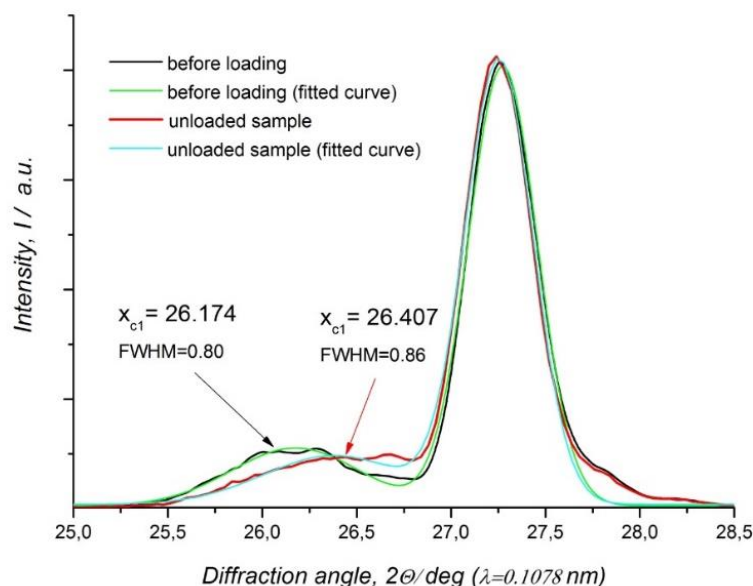


**Fig. 5.2.8** Change of XRD patterns observed after the hydrogen loading / unloading experiment on the 8 nm Nb-H film ( $\lambda = 0.1078 \text{ nm}$ ). Due to irreversible hydrogen-induced microstructural changes, Nb (110) peak shifts as compare to the as-prepared sample state ( $2\vartheta = 26.174^\circ$ ) to higher angle ( $2\vartheta = 26.407^\circ$ ), while the FWHM value increases from  $0.80^\circ$  (as-prepared state) to  $0.86^\circ$  (unloaded state).

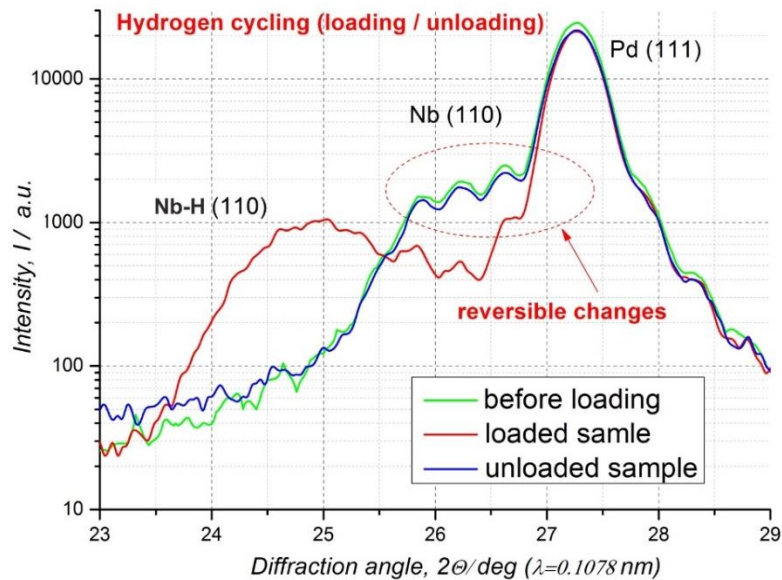
Two these observations indicate irreversible microstructural changes occurring in the sample during the hydrogen loading / unloading experiment. If tensile stress results from dislocation emission upon hydrogen loading of this film, the finally unloaded film might also be thinner than the initial film via transverse contraction.

To summarize, the phase transformation in the 8 nm Nb-H film does not occur: only Nb-H solid solution phase is presented during the hydrogen loading/unloading experiment in the film. Nevertheless, stress release was clearly detected by XRD. Hence, since the absence of precipitation of the hydride is suggested, only the formation of dislocation occurring at the film / substrate interface may explain the irreversible changes detected in the sample.

#### 5.2.4 Reversible changes in the 5nm Nb-H film

During a hydrogen loading / unloading experiment performed on the 5 nm Nb-H film, XRD patterns and XRR curves were measured at different intermediate loading / unloading stages. On top of this, in combination with the XRD technique, resistance measurements were carried out. During the loading experiment hydrogen pressure was increased from  $p_H = 5 \times 10^{-5} \text{ mbar}$  to  $p_H = 6 \times 10^{-3} \text{ mbar}$ . A first notable peak shift of Nb (110) was detected at  $p_H = 5 \times 10^{-4} \text{ mbar}$ . The total exposure time of the sample to hydrogen atmosphere was about  $t_e = 220 \text{ min}$ . To facilitate hydrogen desorption and to unload the sample, the sample was exposed to atmospheric conditions for about  $t_e = 120 \text{ min}$ .

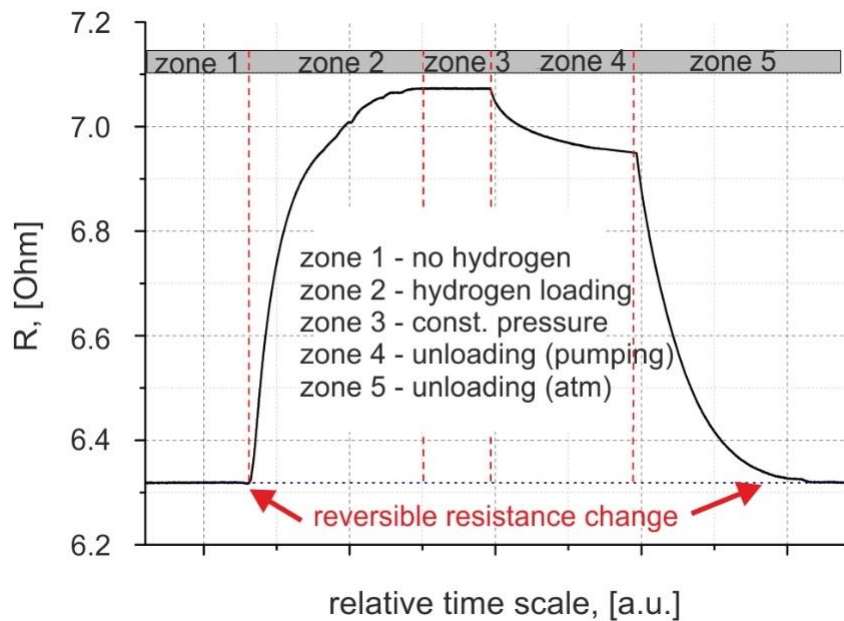
Figure 5.2.9 shows XRD patterns obtained during the hydrogen loading / unloading experiment for the 5 nm Nb-H film. Because the intensity of the related Nb (110) peak was relatively low, the intensity-axis is here given in logarithmic scale. Only the three most important curves are shown in the graph. The green curve corresponds to the reference state before the hydrogen loading; the red one was measured after  $t_e = 220 \text{ min}$  of hydrogen loading; and the blue one was measured after  $t_e = 120 \text{ min}$  of hydrogen unloading. The intermediate curves are not shown in the graph. Similar to the case of 8 nm Nb film, at the intermediate stages, only one broad XRD peak, shifting depending on the experimental direction, was observed. Furthermore, during hydrogen loading the decrease of the peak width was again observed in the XRD patterns.



**Fig. 5.2.9** Change of XRD patterns during hydrogen loading / unloading experiment in the 5 nm Nb-H film ( $\lambda = 0.1078$  nm). The green curve corresponds to the reference state before hydrogen loading; the red curve was measured after  $t_e = 220$  min of hydrogen loading; the blue curve was measured after  $t_e = 120$  min of hydrogen unloading. During hydrogen loading, Nb (110) peak shifts from  $2\vartheta = 26.60^\circ$  to  $2\vartheta = 25.09^\circ$  that corresponds to the lattice expansion of about 5.9%. During hydrogen unloading, Nb (110) peak shifts backwards to the initial position and shows completely reversible change including interference fringes (marked with a dashed red ellipse).

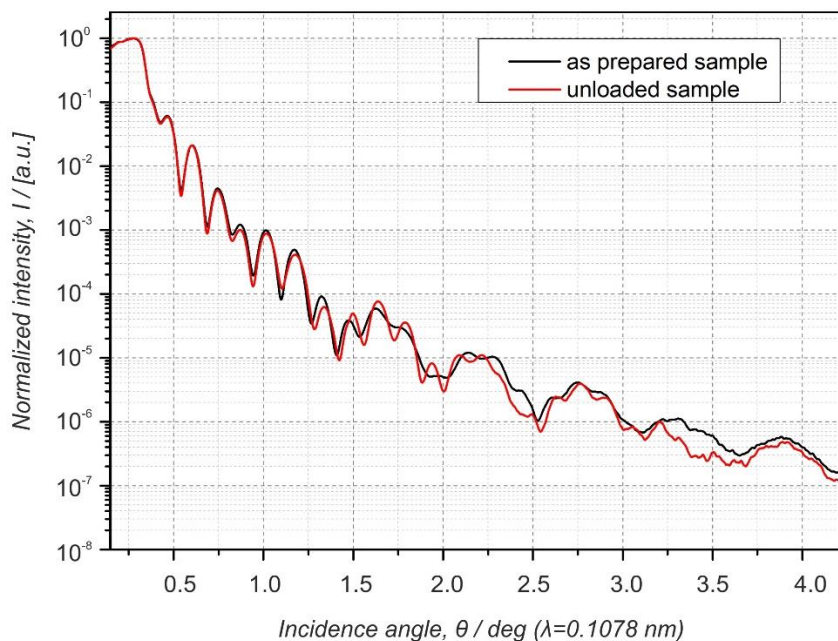
The XRD pattern corresponding to the as-prepared sample state in Fig. 5.2.9 (green curve) exhibits thickness fringes resulting from the strong interference of photons reflected at different interfaces (Pd, Pd/Nb and Nb/ $\text{Al}_2\text{O}_3$ ) that can be expected in thin films with smooth interfaces [23], [135]. The XRD patterns in Fig. 5.2.9 show that during hydrogen loading (red curve), the Nb (110) peak shifts from  $2\vartheta = 26.60^\circ$  to  $2\vartheta = 25.09^\circ$ , indicating the Nb lattice expansion of about 5.9% with respect to the as-prepared film state (green curve). After hydrogen unloading (blue curve), the 5 nm Nb-H film possesses fully reversible XRD patterns. All the peak features observed for Nb (110) reflection in the as-prepared sample state (green curve) fully reappear after hydrogen unloading (the area of interest is marked with a dashed red ellipse in Fig. 5.2.9).

Figure 5.2.10 gives the resistance curve measured together with XRD also for all intermediate experimental stages. There are five vertical dashed lines specifying five intermediate experimental stages: 1<sup>st</sup> zone – no hydrogen, 2<sup>nd</sup> zone - hydrogen loading, 3<sup>rd</sup> zone – an equilibrium state at the fixed hydrogen pressure of  $p_H = 6 \times 10^{-3}$  mbar, 4<sup>th</sup> zone – unloading via the use of pumps and 5<sup>th</sup> zone - unloading via the use of atmospheric conditions. This resistance curve shows that the main amount of hydrogen diffuses out of the sample during the unloading (5<sup>th</sup> zone in Fig. 5.2.10). It reveals fully reversible resistance changes appearing during the loading / unloading experiment, as demonstrated by the complete match between the initial and the final resistance value. The reference value measured before hydrogen loading and the final value measured in the unloaded state were found to be the same and equal  $R = 6.32$  Ohm.



**Fig. 5.2.10** Resistance curve measured in-situ during hydrogen loading / unloading experiment performed on the 5 nm Nb-H film. There are five vertical dashed lines specifying five intermediate experimental stages: 1<sup>st</sup> zone – no hydrogen, 2<sup>nd</sup> zone - hydrogen loading, 3<sup>rd</sup> zone – an equilibrium state at  $p_H = 6 \times 10^{-3}$  mbar, 4<sup>th</sup> zone – unloading via the use of pumps and 5<sup>th</sup> zone - unloading via the use of atmospheric conditions.

To check the correlation between the sample volume change and the measured out-of-plane lattice expansion of the 5 nm Nb-H film, reflectivity curves (XRR) were measured at three different experimental stages: 1) before hydrogen loading, 2) in the equilibrium loaded state at  $p_H = 6 \times 10^{-3}$  mbar, and 3) in the equilibrium unloaded state. Figure 5.2.11 shows, as an example, the combined result of two XRR curves measured 1) before hydrogen loading (black curve) and 2) in the unloaded state (red curve). According to this graph, it can be seen that the reflectivity curve mainly restored its shape in the unloaded state. As it was discussed in chapter 3.5.2, via the physical modeling, by choosing the best correlation between the simulated and experimentally measured curves, parameters of the Nb and the Pd layers, namely their thicknesses, roughness at different interfaces and densities, were determined. An example of fitting of the experimental curve is given in Fig. 5.2.12. This particular fitting was done for the XRR curve measured shortly before hydrogen loading. The red curve in Fig. 5.2.12 represents the experimentally measured reflectivity curve, while the green one corresponds to the simulated XRR curve.



**Fig. 5.2.11** XRR curves measured for the 5 nm Nb-H film at different experimental stages: 1) before hydrogen loading (black curve) and 2) in the unloaded state (red curve).

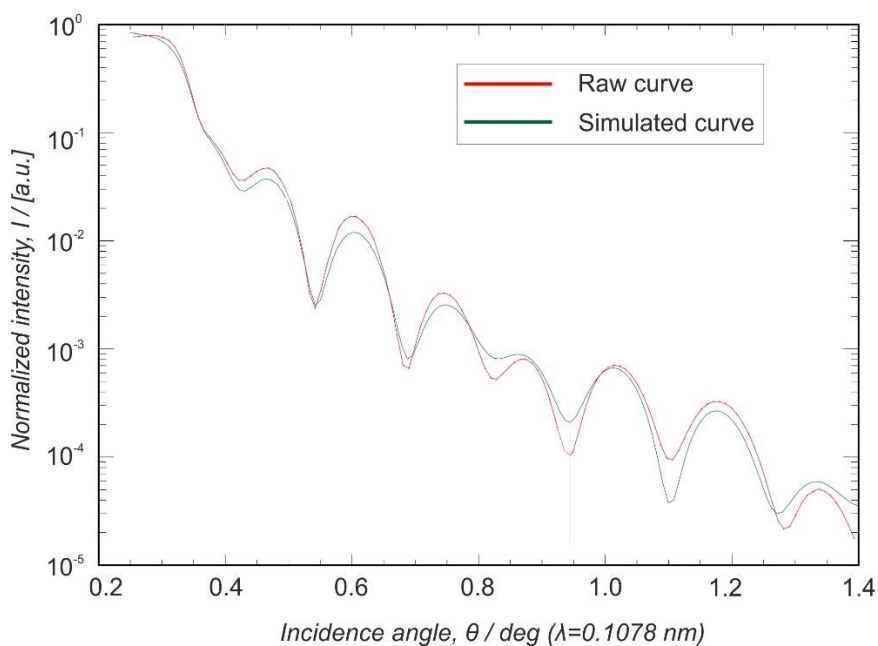


**Fig. 5.2.12** Red curve represents the XRR curve that was measured for the 5 nm Nb-H films shortly before hydrogen loading. Green curve shows the simulated curve that was fitted. Details regarding the physical model are given in Table 5.2.3. (Fitting: IMD software [136])

The result of the physical modeling obtained for this particular XRR curve as well as the results for two subsequent XRR curves measured in 2) loaded and in 3) unloaded states including all the required details regarding the physical model are given in Table 5.2.3.

**Table 5.2.3** Results of the physical modeling based on three XRR curves measured: 1) - shortly before hydrogen loading, 2) - in the loaded state and 3) - in the unloaded state. The estimated absolute error for the film thickness determination by this method does not exceed 0.1 nm.

Experimental stage	Z (Pd), [nm]	Z (Nb), [nm]	$\sigma_r$ (Pd), [nm]	$\sigma_r$ (Pd/Nb), [nm]	$\sigma_r$ (Nb / Al <sub>2</sub> O <sub>3</sub> ), [nm]	$\rho$ (Pd), [kg/cm <sup>3</sup> ]	$\rho$ (Nb), [g/cm <sup>3</sup> ]	$\rho$ (Al <sub>2</sub> O <sub>3</sub> ), [g/cm <sup>3</sup> ]
(1)	14.95	5.45	0.19	0.45	0.21	11.55	8.64	3.97
(2)	14.95	5.77	0.3	0.39	0.23	11.66	8.58	3.97
(3)	14.90	5.43	0.35	0.31	0.19	11.68	8.66	3.97

According to the Table 5.2.3 one can see that during hydrogen loading the thickness of Nb layer increases from 5.45 nm to 5.77 nm. This expansion corresponds to the thickness change (in fact the volume change) of about 5.9%. At the same time, during the loading experiment, the thickness of Pd capping layer doesn't not change. This correlates well with the XRD results shown earlier in Fig. 5.2.9. Besides, the evaluation of the sample parameters after the XRR curve (3) obtained in the unloaded sample state shows that because of hydrogen desorption from the sample, the thickness of Nb layer decreased from 5.77 nm to 5.43 nm. Thereby, within the experimental error ( $\approx 0.1$  nm), the sample thickness doesn't not change if compared to the as-prepared sample state (5.45 nm). For this film thickness an absence of dislocations is therefore, suggested. Thus, this film should behave as predicted by the linear elastic theory. This interpretation will be further strengthened in chapter 6.4.

The mean hydrogen content in the samples can now be calculated: By determining the film expansion ( $\frac{\Delta d}{d}$ ) measured via XRR and the lattice expansion ( $\frac{\Delta a_{110}}{a_{110}}$ ) measured via XRD in the out-of-plane <110> - crystallographic direction it is found, in good agreement, that:

$$\frac{\Delta d}{d} = 0.059 \quad \text{and} \quad \frac{\Delta a_{110}}{a_{110}} = 0.059,$$

If an ideal one-dimensional expansion is assumed, as described in chapter 2.4.1, the average hydrogen concentration in the Nb-H film, as given by Eq. (2.22) with  $\frac{\Delta z}{d_0} = 0.136 \cdot c_H$ , is approximately equal to 0.43 H/Nb. Despite the simplicity of this approach, the calculated concentration value is supposed to be very close to the true hydrogen concentration in the Nb-H film. This conclusion based on the results in Fig. 5.2.9 and Fig. 5.2.10. They confirm reversible behaviour of XRD patterns and resistance curve, and, thus, fully elastic regime which is required for applying linear elastic theory.

### 5.2.5 Summary of XRD measurements

The results of XRD measurements performed in-situ during the hydrogen loading / unloading experiment on films of different thicknesses in the range from 5 nm to 105 nm are presented. During the loading experiment, the hydrogen pressure  $p_H$  was increased from  $p_H = 1 \times 10^{-5} \text{ mbar}$  to  $p_H = 1 \text{ mbar}$ . During unloading experiments, the samples were exposed to atmospheric conditions.

In-situ XRD measurements shows a strong difference in the XRD patterns of the films with a thickness  $d \leq 37 \text{ nm}$ . This value is higher than the calculated critical film thickness of  $d_c = 26 \text{ nm}$  [19]. Further, It is found that in the case of relatively thick samples ( $d \geq 43 \text{ nm}$ ) the  $\alpha$ -phase and the hydride  $\beta$ -phase related peaks can be well separated. Therewith, positions of the  $\alpha$ -phase peak and the hydride  $\beta$ -phase peak stay constant and only corresponding peak intensities change during the phase transformation. This kind of change observed in the XRD patterns during the phase transformation is conditionally called "two peak"- behaviour. Opposite to this, for the intermediate film thickness ( $15 \text{ nm} \leq d \leq 37 \text{ nm}$ ) only one symmetric peak moving towards lower  $2\theta$  angles during the phase transformation is observed. In other words, no additional hydride peak appears in XRD patterns. This kind of change observed in XRD patterns is conditionally called "one peak"- behaviour. Similar experiments performed on a variety of samples shows that the switchover between different XRD patterns occurs in the thickness range between  $37 \text{ nm} - 43 \text{ nm}$ . Besides, for ultrathin films ( $d < 15 \text{ nm}$ ) it is defined "one broad peak" - behaviour in that as it is suggested, the phase separation does not appear.

Besides, it is shown that the peak broadening and the change of maximum intensity are the signs of phase transformation and coherent matching of the phases, in the case when "one peak" - behaviour is observed in XRD patterns during the hydrogen loading experiment. Peak broadening during the phase transformation is revealed for film thicknesses in the range from  $15 \text{ nm}$  to  $37 \text{ nm}$ . Furthermore, during unloading of these samples, XRD patterns demonstrate a significant peak broadening and a peak shift towards higher angles. This indicates irreversible microstructural changes that appear in the sample during the hydrogen loading / unloading experiment.

In the case of 8 nm film peak broadening and intensity drop are not found, but on the contrary, the shrinking of Nb (110) peak and a constant peak intensity are observed in XRD patterns during hydrogen loading. The inverse dependency of FWHM on the film thickness suggested by Scherrer's formula stays in a good agreement with the experimentally measured decrease of FWHM values. Similar to XRD patterns measured in the case of thicker films, the peak shape and its position after the unloading experiment indicate irreversible hydrogen-induced microstructural changes that appear in the sample.

In the case of the 5 nm Nb-H film completely reversible changes in XRD patterns are observed during the hydrogen loading / unloading experiment. Besides that, to verify full unloading of the sample, the result of resistance measurements are presented. The resistance curve also shows reversible changes, if one compares the resistance measured in the as-prepared and in the unloaded sample states. Thus, based on the combined results it is suggested that stress relaxation doesn't appear at applied loading conditions in the 5 nm Nb-H film. On top of this to check the correlation between the sample volume change and the measured out-of-plane lattice expansion, XRR measurements are performed at three different experimental stages: 1) before hydrogen loading 2) in the equilibrium loaded state, and 3) in the equilibrium unloaded state. By comparing the film expansion ( $\frac{\Delta d}{d}$ ) measured via XRR and the lattice expansion ( $\frac{\Delta a_{110}}{a_{110}}$ ) measured via XRD in the out-of-plane  $\langle 110 \rangle$  - crystallographic direction, it is found that they are both equal to 0.059. Finally, by use the theory of linear elasticity and related linear dependency between the film thickness and the average hydrogen concentration, the hydrogen concentration reached in the 5 nm Nb-H film upon hydrogen loading is estimated. Thus, hydrogen concentration that could cause the observed film expansion is about 0.43 H/Nb.

### 5.3 Mechanical stress measurements upon hydrogen loading

In this chapter stress measurements results on Nb-film thicknesses ranging from 5 nm to 40 nm will be shown. They are required to prove the suggested occurrence of ultrahigh stresses and the suggested presence of pure elastic behavior for films below critical sizes. By doing this experiment, several hydrogen loading and unloading cycles were performed while the mechanical stress and the EMF were determined, as described in chapter 3.6.1 and chapter 3.6.2. Herewith, hydrogen was introduced into the films by electrochemical loading. Both, stepwise electrochemical loading and continuous electrochemical loading with a constant current were applied depending on the addressed film thickness (details will be given in the text).

In the case of ultrathin films (5 nm, 7 nm and 10 nm) the data were obtained by Magnus Hamm, during his Master thesis [74]. Combined results were recently published in Ref. [75]. The content of sub-chapters will be organized based on certain generalized aspects that were found in the experiments when the film thickness is reduced from 40 nm to 5 nm.

#### 5.3.1 Stress-strain curve for the 40 nm thick film

Figure 5.3.1 gives the stress curves measured for the 40 nm Nb-H film. In details, besides the first loading curve (1. red), the unloading (1. black) and second loading (2. blue) curves are shown. During the first loading (1. red), compressive in-plane stress initially increases linearly with about  $\sigma = - (11.45 \pm 0.25)$  GPa/ $c_H$ , up to an inflection point. Hereby, the first inflection point in the stress curve corresponds to the deviation from the linear elastic behavior caused by stress release, as it was discussed in chapter 2.4.4. In the 40 nm Nb-H film, first stress release is detected at  $c_H = 0.11$  H/Nb and at a mechanical stress of about  $\sigma = - 1.2$  GPa. Here, plastic deformation via dislocation formation is assumed. Thus, this experimental point will be associated with the critical yield stress and the critical hydrogen concentration in the sample (see chapter 2.4.3 and chapter 2.4.4). Because Nb films deposited on Al<sub>2</sub>O<sub>3</sub> sapphire substrate are known for their strong adhesion, film delamination from the stabilizer as a side mechanism for stress release can be excluded for this film thickness (see chapter 2.4.4). In addition, film delamination is typically visible by eye, and in this study, it was not detected. Besides, the second inflection point is visible at about 0.57 H/Nb. In Fig. 5.3.1 these two experimental points are marked by x. Finally, the stress curve terminates at a total stress  $\sigma = - 3.8$  GPa at a concentration of  $c_H = 1$  H/Nb. Based on the stress measurements shown in Fig. 5.3.1 one can state that the maximum relative mechanical stress lies below the theoretically expected from the pure elastic response, calculated in chapter 2.4.1 ( $\langle \sigma' \rangle_{teor} = -9.6 \cdot c_H$ ). The stress was reduced by plastic deformation as demonstrated by the shape of the stress curve (1. Red, see also chapter 2.4.4). Besides, stress release was also proven during the unloading experiment. The obtained stress curve

(1. black) shows that hydrogen release results in tensile stress of  $\sigma = 0.8$  GPa after unloading. During the second loading (2. blue), in the presence of dislocations formed in the first cycle, the stress increase demonstrates a slightly convex curve. However, no clear point of inflection can be detected.

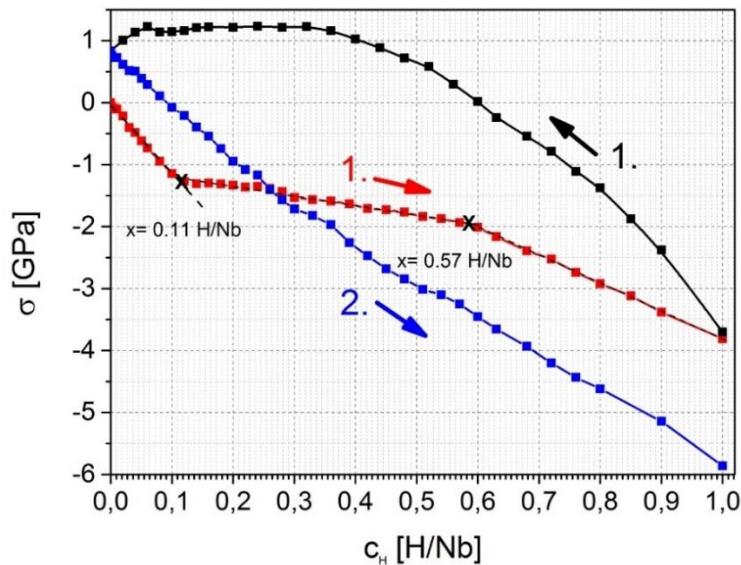


**Fig. 5.3.1** Stress curve of the 40 nm Nb-H film. The first (1. red) and the second loading curve (2. blue) of the 40 nm differ strongly. Plastic deformation (onset marked with x) reduces the stress increase at 0.11 H/Nb and at 0.57 H/Nb, during the first loading run. Unloading results in 0.8 GPa tensile stress (1. black). During the second loading run (2. blue), no clear point of inflection is detected.

Simultaneously with stress measurements, the EMF curve was obtained. Figure 5.3.2 shows the EMF curve measured during the first hydrogen loading of the 40 nm Nb-H film. Here, two concentration values marked with ● confine the plateau region in the EMF curve as discussed in chapter 2.4.8. Besides, the black dotted line representing the linear dependency predicted by Sieverts' law [16] is given as a reference. In a bulk Me-H systems the deviation from this linear dependency defines the onset of the two-phase region that seems to work as well in Nb-H films for  $d \geq 40$  nm. Gray regions in Fig. 5.3.2 define three segments in the EMF curve named:  $\alpha$  ( $\alpha$  - phase),  $\alpha+\beta$  (two coexisting phases in the presence of new generated lattice defects) and  $\beta$  ( $\beta$  - phase in the presence of new generated lattice defects).

By combined consideration of two curves given in Fig. 5.3.1 and Fig. 5.3.2, it is found that the second inflection point in the stress curve ( $c_H = 0.57$  H/Nb) corresponds to the hydrogen concentration at which phase transformation was mainly completed. Further, the deviation from the predicted linear elastic behavior is detected at  $c_H$  corresponding to the beginning of plateau region in the EMF curve. In details, first stress release is visible at  $c_H = 0.11$  H/Nb (see Fig. 5.3.1), while phase transformation is supposed to be initiated at  $c_H = 0.1$  H/Nb (see Fig. 5.3.2). Thus, measured stress curve proves the fact that stress release occurs in the very beginning of phase transformation process. Besides, the flat plateau, observed in Fig. 5.3.2 is more typical for the bulk systems (chapter 2.4.8). This result indicates strong stress release.

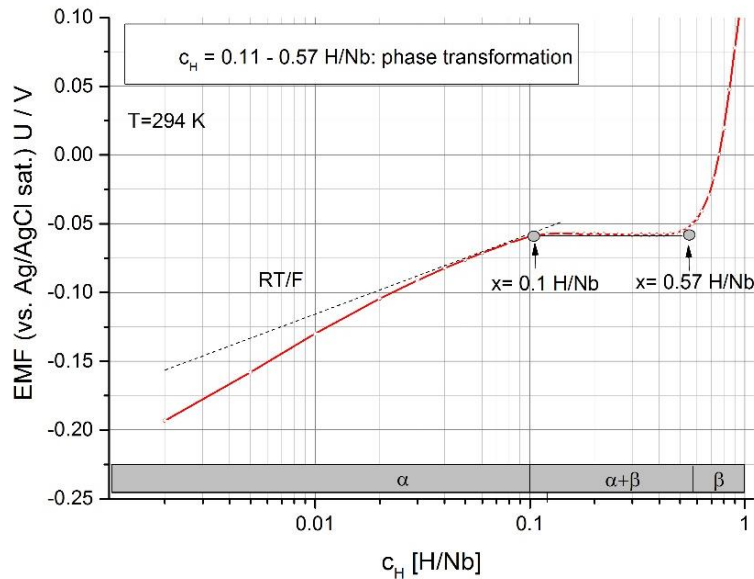


**Fig. 5.3.2** EMF curve measured simultaneously with a stress curve during first hydrogen loading of the 40 nm Nb-H film. The black dashed line represents the linear dependency predicted by Sieverts' law [16]. Additionally, there two concentration values marked with ● given in the graph. They confine the plateau region in the EMF curve, at that the phase transformation occurs.

### 5.3.2 Stress-strain curve for the 25 nm thick film

In Fig. 5.3.3 the stress curves measured for the 25 nm Nb-H film are given. As before, besides the first loading curve (1. red), the unloading (1. black) and second loading (2. blue) curves are shown. During the first loading (1. red), the compressive stress initially increases linearly with about  $\sigma = - (11.57 \pm 0.19)$  GPa/ $c_H$ . Further, one can see that at the stress of - 2.9 GPa (marked by x) and hydrogen concentration of  $c_H = 0.26$  H/Nb, an inflection point appears and further stress increase is diminished. Stress release is very effective and the stress curve even slightly turns upwards. The second inflection point is visible at about 0.49 H/Nb. Finally, the stress curve terminates at  $\sigma = - 4.6$  GPa at a concentration of  $c_H = 0.72$  H/Nb. Similar to the result on the 40 nm Nb-H film, the deviation from the linear elastic behavior (dashed black line) at the inflection point indicates stress release, most probably via dislocation formation. The unloading experiment (1. black) results in tensile stress of  $\sigma = + 2.8$  GPa appearing in the sample. This finding also proves irreversible microstructural changes occurring in the 25 nm Nb-H film upon hydrogen loading / unloading experiment. During the second loading (2. blue), in the presence of dislocations formed in the first cycle, the stress increases linearly up to a concentration of 0.72 H/Nb and no point of inflection is detected anymore. The film follows a linear elastic stress dependency and reflects the stress expected for purely elastic film expansion. As the film only shows this behavior after the first loading cycle, it will be called as 'quasi-elastic' behavior, as suggested in Ref. [75]. Herewith, hydrogen-induced stress change of  $\Delta\sigma = - (7.4 \pm 0.7)$  GPa for  $\Delta c_H = 0.7$  H/Nb, and a final stress of  $\sigma = - (4.6 \pm 0.5)$  GPa builds up in this film, at  $c_H = 0.72$  H/Nb.

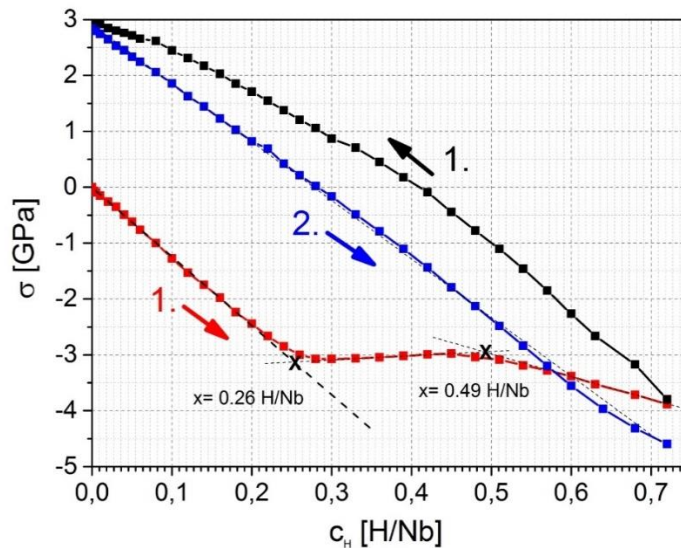


**Fig. 5.3.3** Stress curve of the 25 nm Nb-H film. The first (1. red) and the second loading curve (2. blue) of the 25 nm differ strongly. Plastic deformation (onset marked with x) reduces the stress increase at 0.26 H/Nb and at 0.49 H/Nb, during the first loading run. Unloading results in 2.8 GPa tensile stress (1. black). During the second loading run (2. blue), no further plastic deformation is detected.

Figure 5.3.4 shows the EMF curve measured during the first hydrogen loading of the 25 nm Nb-H film. As it can be seen, there are three concentration values marked with (●) in the graph. The first one of about  $c_H = 0.1$  H/Nb indicates the point of deflection where the deviation from the Sievert's law (black dashed line) appears. The second one ( $c_H = 0.2$  H/Nb) and the third one ( $c_H = 0.49$  H/Nb) confine the plateau-like region in the EMF curve.

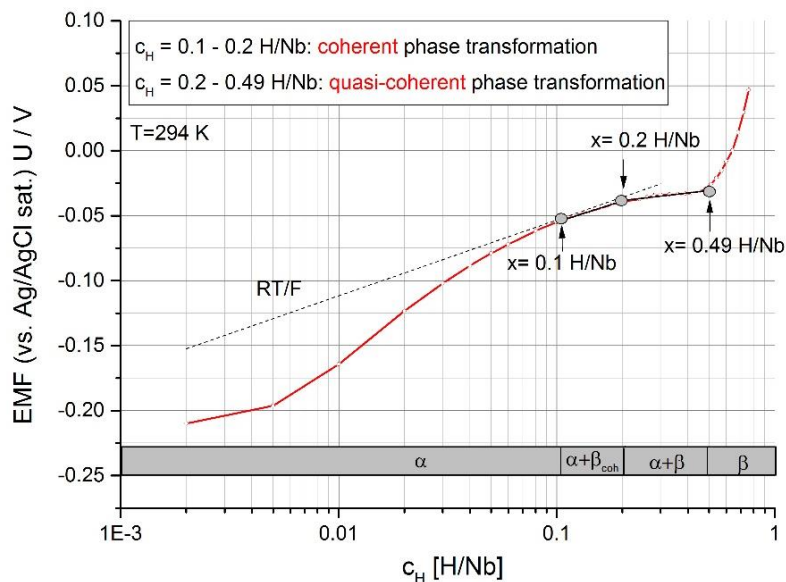


**Fig. 5.3.4** EMF curve measured simultaneously with a stress curve during first hydrogen loading of the 25 nm Nb-H film. The black dashed line represent the linear dependency predicted by Sieverts' law [16]. Additionally, there three concentration values marked with (●) given in the graph (details see in the text).

By combined consideration of the two curves given in Fig. 5.3.3 and Fig. 5.3.4, it can be seen that the third inflection point in the stress curve ( $c_H = 0.49$  H/Nb) corresponds to the hydrogen concentration at which the phase transformation is completed. Further, the deviation from the predicted linear elastic behavior occurs in the concentration range of phase transition, as visible in Fig. 5.3.3. Moreover, first stress release is detected at  $c_H = 0.26$  H/Nb (see Fig. 5.3.3). In this figure, phase transformation would be expected to occur close to  $c_H = 0.20$  H/Nb. However, it will be shown later on, that the phase transformation is initiated already at  $c_H = 0.1$  H/Nb (for details see chapter 6.6). Thus, the measured stress curve shows that events of plastic deformation take place at the intermediate stage of phase transformation. Gray regions in Fig. 5.3.4 define four segments in the EMF curve named:  $\alpha$  ( $\alpha$  - phase),  $\alpha+\beta_{\text{coherent}}$  (two coherently coexisting phases),  $\alpha+\beta$  (two coexisting phases in the presence of new generated lattice defects) and  $\beta$  ( $\beta$  - phase in the presence of new generated lattice defects).

### 5.3.3 Combined stress-strain curves for films of different thickness

In chapter 5.3.1 and chapter 5.3.2, the stress curves measured in the case of 40 nm and 25 nm films were addressed. Similar analysis of stress curves has been performed as well, in the case of 5 nm, 7 nm, 10 nm and 15 nm films. Figure 5.3.5 (a) summarizes the mechanical stress resulting from hydrogen uptake for films of different thicknesses, ranging from 5 nm to 40 nm, for the first loading run [75]. Except the 5 nm film, all the given stress measurements were performed in stepwise loading mode. For Nb films above 5 nm film thickness (red curves), the compressive stress first increases linearly up to a certain hydrogen concentration, that is defined by the film thickness. These yield hydrogen concentrations are marked by  $\times$  for each curve in Fig. 5.3.5 (a). According to the graph in Fig. 5.3.5 (a), it has a trend to increase by decreasing the film thickness. The details on the stress developments are summarized in Table 5.3.1. According to these data, all the slopes lie in the theoretically predicted range. In details, in the case of the 40 nm thick film, first stress relaxation occurs at relatively low  $c_H = 0.11$  H/Nb. Herewith, relative mechanical stress of about  $\sigma = -1.2$  GPa is reached on that loading stage. In the case of 25 nm and 15 nm thick, first stress release is detected significantly later at  $c_H = 0.22 - 0.26$  H/Nb. Herewith, relative mechanical stress caused by hydrogen absorption in the film reaches a magnitude of about  $\sigma = -2.8$  GPa. Furthermore, additional bending points can be found in the stress curve in the case of 40 nm, 25 nm and 15 nm thick films (see Table 5.3.1). For 10 nm and 7 nm thick films, a first deviation from the linear dependency is observed at  $c_H \geq 0.5$  H/Nb. The measured mechanical stress in the moment of stress relaxation reaches, respectively,  $\sigma = -5.0$  GPa and  $\sigma = -5.8$  GPa. Finally, in the case of the 5 nm thin film (blue curve), the compressive stress always increases linearly up to the final concentration of  $c_H = 1$  H/Nb. No inflection points are detected. This finding is a strong indication for the absence of plastic deformation. Thus, it is suggested that dislocations cannot be formed for films of less than 5 nm thickness [75].

Using the observed thickness dependency of the yield stresses measured for thicker films, a theoretical thickness, below which plastic deformation is expected to be absent [75], can be calculated (chapter 2.4.3, Eq. (2.26)). As shown in Fig. 5.3.5 (b), theory predicts an absence of dislocations for a film thickness of 3.4 nm, using  $c_{pl} = (C_1/d) \cdot \ln(C_2 \cdot d)$  [68], with  $C_1 = 1.2$  and  $C_2 = 5$  as fitted to the obtained values (x in Fig. 5.3.5 (a)) [75]. Thus, the theoretically predicted critical film thickness is close to the experimentally observed one shown in Fig. 5.3.5 (a).

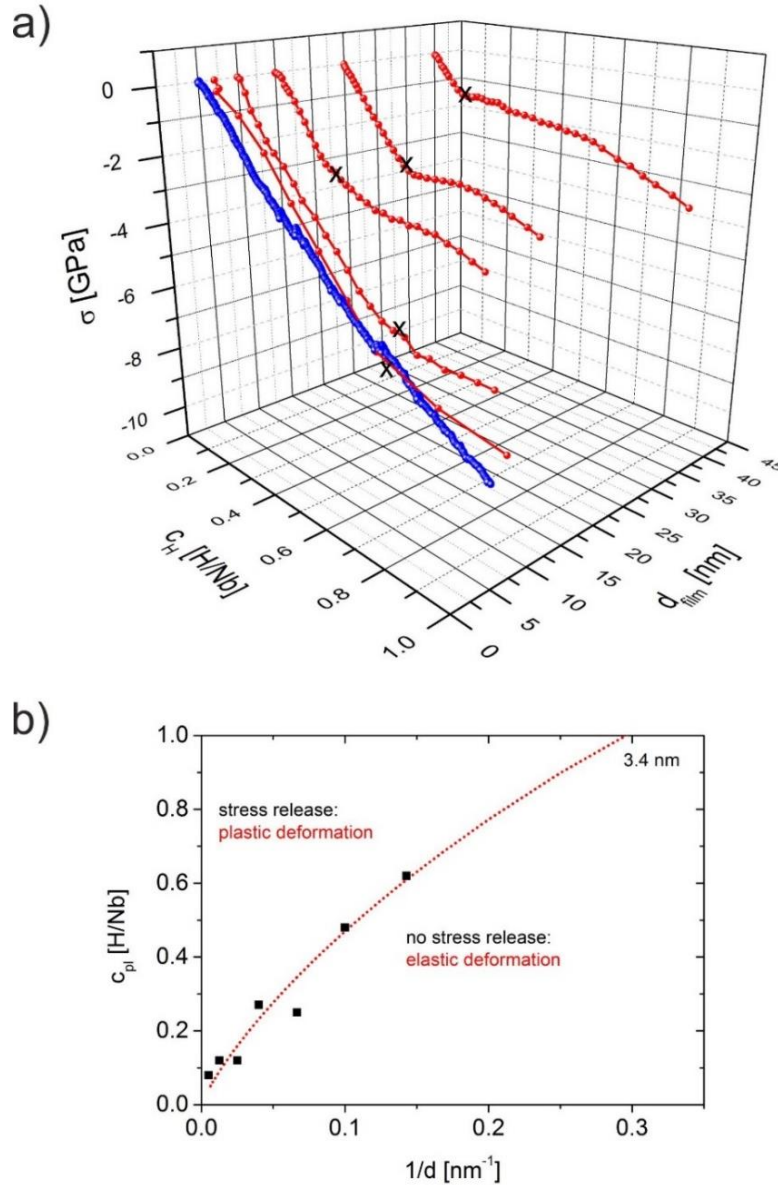


**Fig. 5.3.5 a)** Hydrogen induced stress arising during first loading of Nb films of different thickness  $d$  between 5 nm and 40 nm. Films above 6 nm film thickness (red curves) deform plastically that reduces the final stress. Films below 6 nm film thickness (blue curve) show a linear dependency between the concentration of hydrogen atoms and stress measured in the film. They stay in the elastic regime and reach an ultrahigh stress state [75]. **b)** Theoretical model [68] suggesting  $c_{pl} = (C_1/d) \cdot \ln(C_2 \cdot d)$  with  $C_1 = 1.2$  and  $C_2 = 5$  as fitted to the experimental values predicts an absence of dislocations for  $d = 3.4$  nm. This value is relatively close to the experimental one. [75] Figure created by author from data originally published in Ref. [75].

**Table 5.3.1** Slope of stress / composition curves and conditions of stress relaxation (upon stepwise loading). In the case of 5 nm Nb-H film (\*) - continuous hydrogen loading mode was applied (for details see chapter 3.6.1).

d [nm]	Initial curve slope k [GPa/c <sub>H</sub> ]	c <sub>H</sub> <sup>1</sup> (1 <sup>st</sup> inflection point / stress relaxation)	σ (c <sub>H</sub> <sup>1</sup> ) [GPa]	c <sub>H</sub> <sup>2</sup> (2 <sup>nd</sup> inflection point)
40	-11.45 ± 0.25	0.11	-1.2	0.57
25	-11.57 ± 0.19	0.26	-2.9	0.49
15	-11.58 ± 0.44	0.22	-2.7	0.44
10	-10.55 ± 0.18	0.5	-5.0	-
7	-10.63 ± 0.15	0.55	-5.8	-
5	-10.73 ± 0.53	-	-	-
5 (*)	-8.01 ± 2.00	-	-	-

### 5.3.4 Reaching the elastic limit in stress-strain curves: elastic and quasi-elastic behavior

To further study the suppression of plastic deformation in ultra-thin films, the stress build-up in successive hydrogen loading cycles is investigated [74], [75]. Figure 5.3.6 shows the mechanical stress data of the 5 nm (Fig. 5.3.6 (a)) and the 10 nm film (Fig. 5.3.6 (b)) including subsequent loading data [75]. In Fig. 5.3.6 (a) the stress  $\sigma$  is given with respect to the stress measured before each loading sequence. Thereby, intrinsic stress, presented in the film before hydrogen loading is not shown. According to this graph the compressive stress increases quasi-linearly with the hydrogen concentration over the whole hydrogen concentration range [75] and reaches a maximum stress of  $- (8 \pm 2)$  GPa at  $c_H = 1$  H/Nb. Thus, this result reflects the value expected for linear - elastic regime. Besides, the first (1. red) and the second (2. blue) loading curves closely reproduce each other. Herewith, inflection points similar to the observed ones in Fig. 5.3.5 (a) are not detected in any of the loading runs. Thus, for the 5 nm Nb-H film plastic deformation can be excluded [75].

Fig. 5.3.6 (b) shows the result of stress measurements on the 10 nm film. Here, the first loading (1. red) and unloading curve (1. black) and the second loading (2. blue) curves are presented [75]. As one can see, during the first loading (1., red), the compressive stress initially increases linearly with about  $- 11$  GPa/c<sub>H</sub>. However, at a relative yield stress of about  $- 5$  GPa (marked by  $\times$ ) and a concentration of  $c_H = 0.5$  H/Nb, an inflection point appears and, hence, subsequent increase of hydrogen-induced mechanical stress becomes less steep. The highest relative stress of  $\sigma = - 7$  GPa is measured at a concentration of  $c_H = 1$  H/Nb [75].

Further, unloading (1., black) results in relative tensile stress of  $+ 1.8$  GPa. During the second loading (2., blue), in the presence of dislocations formed in the first cycle, the stress increased linearly up to an concentration of  $1$  H/Nb and no point of inflection is detected. Thus, the film follows the linear

elastic dependency and therefore behaves quasi-elastically. An ultrahigh hydrogen induced stress difference of  $\Delta\sigma = -(11.8 \pm 1.2)$  GPa and a final stress of  $\sigma = -(10 \pm 1)$  GPa built up in this film, at  $c_H = 1$  H/Nb. In subsequent cycles, this reversible behavior was maintained [74], [75]. In total for 10 nm thin films, this result indicates on the complete absence of further plastic deformation and dislocation formation after first loading.

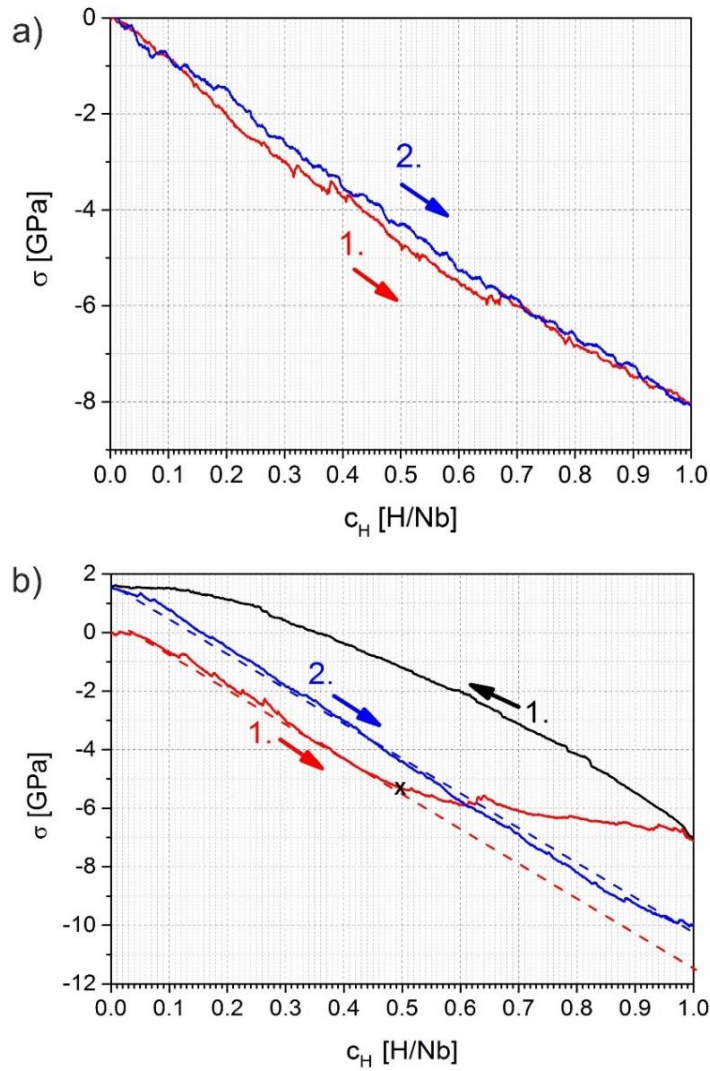


**Fig. 5.3.6** Elastic and quasi-elastic behavior in ultra-thin Nb-H films. **a)** The 5 nm Nb film shows similar behavior for the first (1. red) and the second loading (2. blue). Here, plastic deformation is not detected and the stress curves nearly reproduce each other. **b)** The first (1. red) and the second loading curve (2. blue) of the 10 nm differ strongly [75]. During the first loading, plastic deformation reduces the stress increase at 0.5 H/Nb (marked with x). Besides, unloading results in 1.8 GPa tensile stress. Opposite, during the second loading (2. blue), plastic deformation is not detected. The stress-composition curve behaves quasi-elastically. Figure created by author from data originally published in Ref. [75].

### 5.3.5 Change of phase boundaries

Figure 5.3.7 shows the EMF curves measured for different film thicknesses ranging from 5 nm to 40 nm during first hydrogen loading (stepwise loading). The information about the bending points in the EMF curves is summarized in Table 5.3.2. According to these data, there is a slight shift of the solubility limits (low  $c_H$  and high  $c_H$ ) and a decrease of the width of the miscibility gap occurring for the addressed film thicknesses. With the decrease of the film thickness, the plateau region shrinks, while the slope of the EMF curve in the related concentration ranges becomes steeper (marked with black dashed vertical lines). In the case of the 5 nm film the EMF curve demonstrates a very steep permanent slope in the whole hydrogen concentration range. Thereby, only one bending point at about  $c_H \approx 0.47$  H/Nb is visible in the graph.

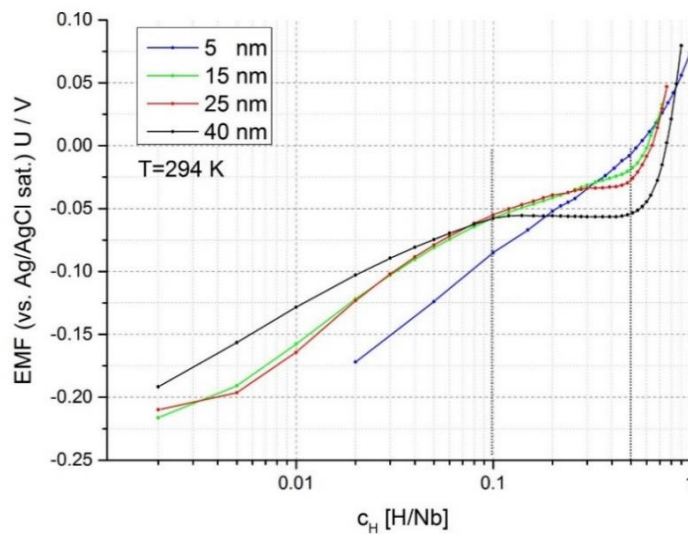


**Fig. 5.3.7** EMF curves measured for different film thicknesses from 5 nm to 40 nm. By reducing the film thickness the plateau region shrinks, while the slope of the EMF curve in the related concentration range becomes steeper (marked with black dashed vertical lines).

**Table 5.3.2** Bending points in the EMF curve in Fig. 5.3.7. The estimated absolute error for the given bending points is about 0.05 [H/Nb].

Film thickness $d$ [nm]	Bending points in the EMF curve [H/Nb]	
	Low $c_H$	High $c_H$
40	0.1	0.5
25	0.1 - 0.2	0.48
15	0.1 - 0.25	0.47
5	-	0.45

By repeated hydrogen loading of films with a thickness exceeding  $d \geq 7$  nm the EMF curves obtained during the first (red curve) and the second (blue curve) hydrogen loading experiment

demonstrate a shift with respect to each other as it is exemplary shown in Fig. 5.3.8 (a) for the 15 nm Nb-H film. Opposite to this result EMF curves obtained during the first (red curve) and the second (blue curve) hydrogen loading of the 5 nm Nb-H film nearly reproduce each other as it is shown in Fig. 5.3.8 (b). Only at relatively high  $c_H > 0.55$  H/Nb some slight deviation is visible.

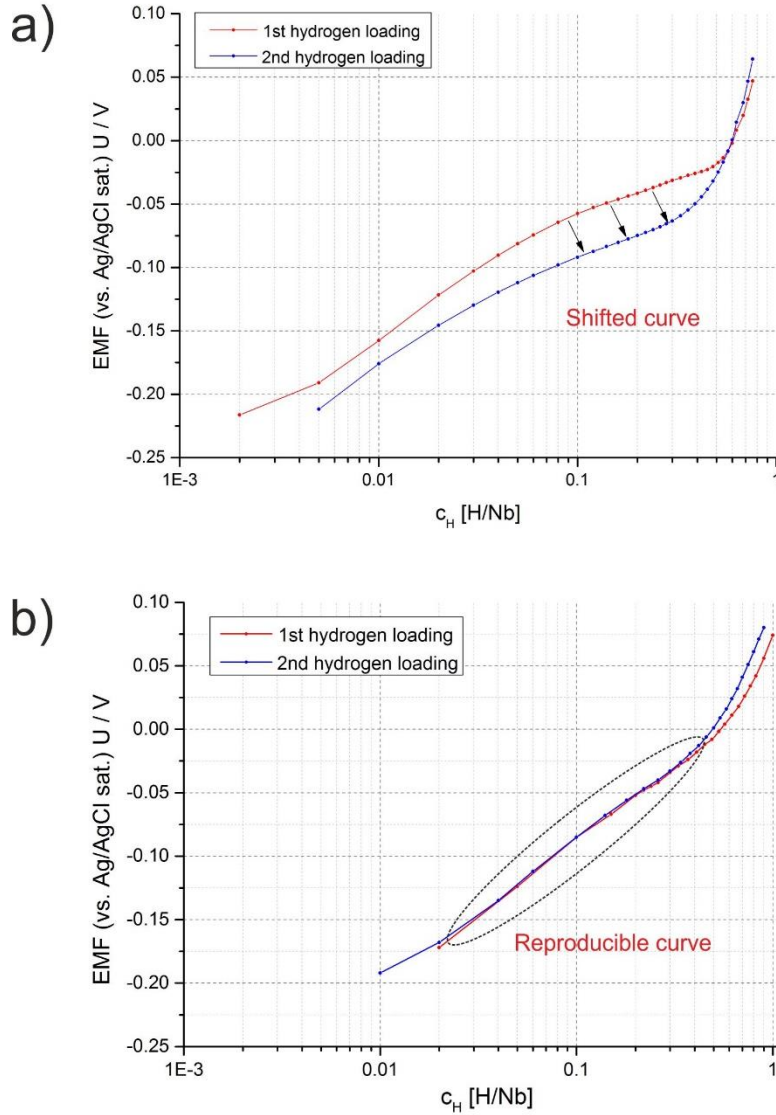


**Fig. 5.3.8** EMF curves measured during the first and the second hydrogen loading for **a)** 15 nm Nb-H film and **b)** 5 nm Nb-H film. While in the case of the 15 nm film EMF curves are shifted with respect to each other, in the case of the 5 nm film EMF curves nearly reproduce each other.

### 5.3.6 Summary of stress measurements

The actual stress measurements results show that the linear elastic regime of ultrahigh stress can be reached in a controlled way for Nb-H thin film system below a critical size [75]. In the elastic range of very thin films ( $d \leq 5$  nm), ultrahigh stress can be achieved already during the first hydrogen loading ( $\sigma = -8 \pm 2$  GPa).

It is shown that the 5 nm film demonstrates reversible behavior by repeated loading / unloading cycles. The compressive stress always increases linearly up to the hydrogen concentration of  $c_H = 1 \text{ H/Nb}$ . Herewith, no inflection point is detected in the stress-composition curve. This result is a strong indication for the absence of plastic deformation.

It is suggested that for the quasi-elastic behavior of slightly thicker films ( $d > 5 \text{ nm}$ ), dislocation formation is allowed during the first hydrogen loading. Herewith, stress release turns the sample into tensile stress during unloading that leads to complete absence of further plastic deformation and dislocation formation after the first loading [75]. All the films exceeding this thickness ( $d = 5 \text{ nm}$ ) deviate from the linear dependency predicted by the theory of linear elasticity.

Further, it is revealed that the initial stress development (slope of the stress / composition curve) for all the samples lies in the theoretically predicted range. The experimentally found trend shows that this deviation associated with the plastic deformation, occurs at higher hydrogen concentrations when the film thickness is decreased.

The EMF measurements show that the width of the plateau region slightly decreases by reducing the film thickness and that a plateau region cannot be determined for  $d \leq 10 \text{ nm}$ . Combined consideration of stress and EMF curves suggests that the visibility of plateau-like region in the EMF curve should be mainly attributed to stress release appearing by reaching a critical yield stress and a certain critical hydrogen concentration in the sample. It is argued that these critical values are mainly controlled by the film thickness. In the case of 25 nm and 15 nm films first stress release occurs only at intermediate stages of sample hydrogenation, respectively, at  $c_H = 0.26 \text{ H/Nb}$  and  $c_H = 0.22 \text{ H/Nb}$ . This is in contrast to results on the 40 nm thick film which shows a clearly visible plateau in the EMF curve, whose beginning at  $c_H = 0.1 \text{ H/Nb}$  matches with an activation of stress release, detected already at  $c_H = 0.11 \text{ H/Nb}$ . Thus, this relatively early stress release allows seeing a plateau region in the EMF curve, as typical for bulk-like samples. Accordingly, the thicker samples exhibit the same properties. Therefore, one can suggest that in the two-phase region, before the first stress release appears in the system, one deals with the coherent phase transformation, while for the later stages of the phase transformation one can only assume coherent phase transformation and thereby conditionally call it quasi-coherent.

Additionally, EMF measurements performed for different samples show that at repeated hydrogen loading for films with a thickness  $d \geq 7 \text{ nm}$  the EMF curves obtained during the first and the second loading experiment are shifted with respect to each other. This change might be attributed to the stress release and the related plastic deformation occurring in the film during the first hydrogen loading. In contrast, in the case of the 5 nm film, EMF curves obtained during the first and the second hydrogen loading experiment reproduce each other. Thus, the obtained result correlates well with an elastic behavior confirmed also by stress measurements.

## 6 Global discussion

In this central chapter, the results obtained via different measurement techniques for similar Nb-H film thicknesses (in-situ STM, in-situ XRD, stress and EMF measurements) are combined and discussed. Hereby, the details on the phase transformation upon hydrogen loading, namely different precipitation and growth modes, critical thicknesses influencing coherent or incoherent pathways of phase transitions and (ir)reversible changes occurring in the samples will be addressed. Additionally, the influence of the mechanical stress on the suppression of phase transformation in ultrathin Nb-H films will be considered. Besides, the invisibility of phase transformation via in-situ XRD measurements will be discussed.

Finally, the applicability of the theoretical model suggested by Nörthemann et al. (see chapter 2.4.6) will be discussed with respect to the experimental results obtained in this study.

### 6.1 Precipitation and growth of hydride phase: different modes (based on STM and XRD results)

STM measurements have shown (see chapter 5.1.2.1 and chapter 5.1.3.1) that, depending on the film thickness, different regimes of hydride phase precipitation and growth can be found during the phase transformation in Nb-H films. Therewith, typical height change, distribution and lateral sizes of hydride precipitates were found to be very different [133].

The different appearances of the hydrides forming in the 25 nm films and in the 40 nm films are compared exemplary in Fig. 6.1 (a, b). The appearance of hydrides for films below 25 nm resembles that of the 25 nm film, and the appearance of hydrides for films above 40 nm resembles that of the 40 nm film. The hydrogen pressure for both STM images is about  $p_H = 1.6 \times 10^{-6}$  mbar. They both were obtained after extensive loading. The height difference in the topography of the two films is illustrated in the height histograms, added in an inset for each STM image (see Fig. 6.1 (a, b)).

For the 25 nm film, shown in Fig. 6.1 (a), and the films below this thickness, a large number of small surface elevations related to hydride precipitates is found. Thus, it is suggested that for the addressed film thickness the phase transformation is governed mainly by nucleation [133] that is linked to a “locked-in size” behaviour (for details see chapter 5.1.3.1).

The term “locked in-size” was employed here because of the relatively slow enlargement of the lateral size of precipitates (as compared to the experimental loading time scale) of a certain size, and, their related limited lateral size (as compare to the measured frame size). This finding of the “locked-in size” can be interpreted by the arising elastic strain energy that, in a first approach, in the elastic regime depends on the particular volume of a single precipitate.

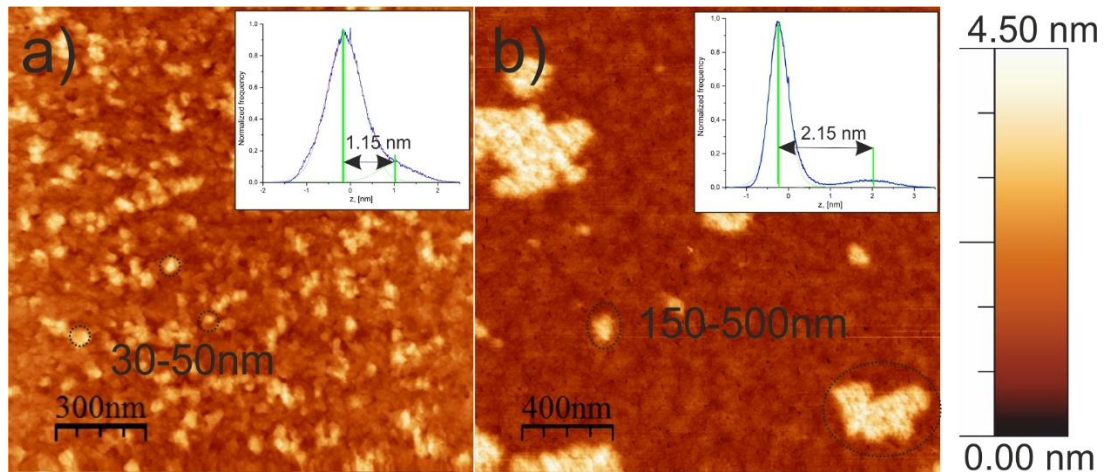


**Fig. 6.1 a)** STM surface-image of the 25 nm Nb-H film after extended hydrogen loading at  $p_H = 1.6 \times 10^{-6}$  mbar. A large number density of small hydrides (30 nm - 50 nm in lateral size) is found (see chapter 5.1.3.1). Inset: The height histogram shows two close peaks, separated by 1.15 nm [133]. **b)** STM surface-image of the 40 nm Nb-H film after extended hydrogen loading at  $p_H = 1.6 \times 10^{-6}$  mbar. A small number of large hydrides with sizes of up to 500 nm in lateral size is visible (see chapter 5.1.2.1). Inset: The height histogram shows two peaks separated by 2.15 nm [133]. (Frame size: a)  $1500 \times 1500$  nm<sup>2</sup> and b)  $2000 \times 2000$  nm<sup>2</sup>). Figure created by author from data originally published in Ref. [133].

The finding of “locked in-size” precipitates correlates well with Nörthemann’s results, who invented this name [24]. Nörthemann found them for thicker films, for the kind of hydrides that were called *T1* and suggested to be fully coherent (see chapter 2.4.5, [19], [24]). However, for the films studied by Nörthemann, all hydrides became incoherent and *T2-type* upon loading [24], [73]. This is different for the films below 25 nm presented in this study.

For the assumed miscibility gap width of  $\Delta c_H = 0.3$  H/Nb - 0.4 H/Nb (see chapter 5.3.2) the amplitude of surface corrugations  $\Delta z$  according to the theory of linear elasticity for 25 nm film is expected to be about 1.02 nm - 1.36 nm (see Table 2.1). In our case, the experimentally found surface corrugations have height amplitudes  $\Delta z$  ranging from 1 nm to 1.5 nm (see Fig. 5.1.11 (c)). Thus, the observed surface corrugations are close to the theoretically expected values. Besides, the amplitude of surface corrugations  $\Delta z$  found here corresponds to the values reported by Nörthemann et al. [24], [73] for coherent hydride precipitates of *T1-type*. The slope of the profile in the transition area between the  $\alpha$ -phase and the  $\beta$ -phase was always found to be about  $2.2(0.5)^\circ$  (see Fig. 5.1.11 (c)). In total, these findings hint on the absence of any dislocation loop formation around the observed hydride precipitates in the 25 nm film (for details see chapter 2.4.5 and Fig. 2.14). Hence, exclusively coherent phase transformation in the 25 nm film is suggested.

Additionally, it is found that some of these small hydrides coalesce together at a late stage of hydrogen loading. It allows the increase of their total volume and, apparently, facilitates the accompanying increase of local topography change up to 2 nm (see Fig. 5.1.11 (c)) in height. Since this

magnitude already significantly exceeds the theoretically expected one (see Table 2.1), this can be interpreted by material transport towards the precipitate surface, which demonstrates that some stress release in the 25 nm for this bigger precipitates cannot be excluded.

In contrast to this, the 40 nm film in Fig. 6.1 (b) (and the films above this thickness) shows a small number of large hydrides with lateral sizes in the range from a few hundred nanometres up to almost micrometre size [133] (see also Fig. 5.1.8). During further hydrogen loading, these hydrides continue to grow and form surface corrugations of irregular shapes (for details see chapter 5.1.2.1)

According to Nörthemann's results on films of similar thicknesses, this kind of hydrides is assumed to be incoherently linked with a surrounding  $\alpha$ -matrix and conditionally called T2 (see chapter 2.4.5, [19], [24]). For the miscibility gap width of  $\Delta c_H = 0.47$  H/Nb (see chapter 5.3.1) the amplitude of surface corrugations  $\Delta z$  according to the theory of linear elasticity for the 40 nm film is expected to be about  $\Delta z = 2.6$  nm (see Table 2.1). However, the experimentally found surface corrugations for this film thickness have a height amplitude  $\Delta z$  ranging from 2.5 nm to 3.5 nm (Fig. 5.1.7 (a)) that mainly exceeds the theoretical value. Thus, there is a deviation from the linear elastic approach. This can be attributed to significant plastic deformation occurring in the 40 nm film. The slope of the profile in the transition area between the  $\alpha$ -phase and the  $\beta$ -phase was found to be about  $6(1)^\circ$  (see Fig. 5.1.7 (a)), which is clearly larger as compared to the 25 nm film. This finding hints on the formation of dislocation loops around hydride precipitates in the 40 nm film as given by Nörthemann (for details see chapter 2.4.5 and Fig. 2.14). Hence, incoherent phase transformation in the 40 nm film is suggested.

By repeated hydrogen loading upon pressure increase, the pre-existing hydrides continue to grow as shown in Fig. 5.1.8 (a, b). Thus, it can be assumed that possible stress release at the  $\alpha/\beta$  interface facilitates the lateral growth of the pre-existing hydrides. It might happen because hydrogen absorption in pre-expanded lattice regions is energetically more favourable [16]. Moreover, the new generated dislocations located around the hydrides themselves are energetically favourable sites for further hydrogen accommodation due to the locally reduced chemical potential of hydrogen [9], [56], [137], [138]. In total, it can be suggested that for the addressed film thickness the transformation is growth-controlled [133].

To explain the finding of different modes of hydride precipitation and growth, there is a number of possibly influencing factors that are supposed to be considered. First of all, it should be noted that the samples were prepared at similar experimental conditions by use of the same sputter rates and relatively close deposition temperatures. As discussed in chapter 4, the temperature decrease (see Fig. 4.3) from 800 °C (40 nm film) to about 740 °C (25 nm film) improves the surface conditions and, at the same time, still allows producing epitaxial films of good structural quality confirmed by XRD measurements (see Fig. 4.4). Thus, the tiny optimization of the deposition temperature applied in this study to get the desired

“smooth” and “closed” surface topographies (see chapter 4), is suggested here to not affect the mechanisms of hydride precipitation and growth. Further, the Pd islands added on the Nb film to facilitate the hydrogen absorption are very small and are always distributed homogeneously over the Nb surface (see Fig. 4.6). Their distribution is always the same, for all film thicknesses. This allows excluding this factor from the consideration as also concluded in earlier studies by Nörthemann [73]. Further, the hydrogen pressures that were applied for loading of different film thicknesses were changed in a quite broad range, but for qualitative comparison the STM images obtained at similar experimental pressures are used (e.g. in Fig. 6.1:  $p_H = 1.6 \times 10^{-6} \text{ mbar}$ ). Another factor is the number of pre-existing defects in the as-prepared film state (dislocations, vacancies, impurity atoms, grain boundaries, interfaces and surfaces). In the present study, it is assumed that for all regarded samples, this parameter does not change significantly (also due to the similarity of preparation conditions of our samples) and, hence, their impact is neglected. This is also in accordance with earlier studies [14], [127].

Therefore, the differences observed in the two different regimes of hydride phase precipitation and growth detected in thin epitaxial Nb films, may be mainly attributed to the “degree of ideality” of the coherency state (coherent or semi-coherent) at the  $\alpha/\beta$ -interface that increases by reducing the film thickness. This value cannot be directly measured, but is implemented in the discussion to qualitatively explain the obtained results.

Further, at this point of the discussion, to support the result of STM measurements hinting on the coherent phase transformation in the 25 nm film (chapter 5.1.3.1) and the 15 nm film (chapter 5.1.4.1), the results of XRD measurements have to be considered. To remind the reader, in-situ XRD measurements shown in chapter 5.2.1 reveal the phase transformation down to 15 nm film thickness. This result stays in a good agreement with the STM measurements that unambiguously reveal local precipitates of hydride phase in these films.

A strong difference in the XRD patterns of the films with a different thickness is clearly found. Conditionally called “two peak” - behaviour ( $d \geq 43 \text{ nm}$ ) and “one peak” - behaviour ( $15 \text{ nm} \leq d \leq 37 \text{ nm}$ ) are observed experimentally (for details see chapter 5.2.1). Two typical examples of different XRD patterns demonstrating the change in the peak behaviour, measured under the same experimental conditions, but for different film thicknesses (60 nm and 17 nm) are given in Fig. 6.2.

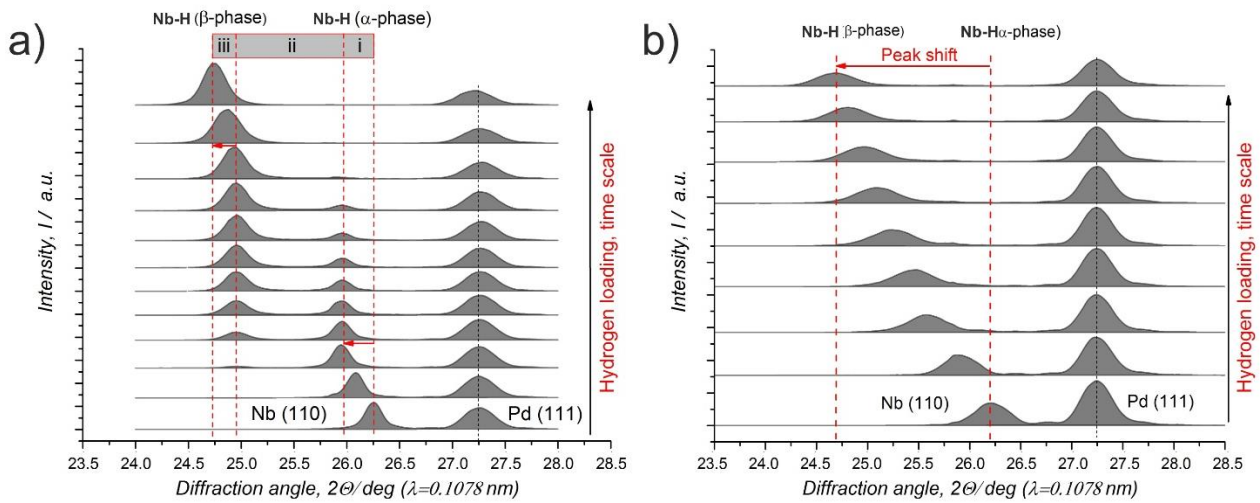


**Fig. 6.2** Change of XRD patterns upon hydrogen loading of Nb-H films, of **a)** 60 nm and **b)** 17 nm film thickness ( $\lambda = 0.1078$  nm). For both films, the Nb (110) peak shifts to lower angles because of the hydrogen-induced lattice expansion. Differences appear in the two-phase region: **a)** Two well-separated peaks corresponding to the  $\alpha$ - and the  $\beta$ - phases are visible at the intermediate loading stages. Their positions are marked with dashed lines. **b)** Only one broadened peak is detected at the intermediate loading stages, its intensity changes. The phase separation becomes nearly XRD-invisible [133].

There is a number of reasons that, as it is suggested, facilitate an appearance of the “one peak” – behaviour in the XRD patterns measured for the “intermediate” film thickness range in Nb-H films. Figure 6.3 demonstrates roughly the sketch of XRD measurements performed in the  $\vartheta$ - $2\vartheta$  geometry. It can be assumed that, for the coherent hydride formation, the  $\alpha$ -phase is strained by the presence of the  $\beta$ - phase (hydride) precipitates and the hydrides are compressed by the surrounding  $\alpha$ -matrix. Thereby, the contribution of coherent micro-strain in the diffracted beam becomes significant. It leads to an additional diffuse photon scattering on (110) crystal planes oriented parallel to the sample surface. By this, the (110)-interplanar spacing changes gradually in the vertical direction.

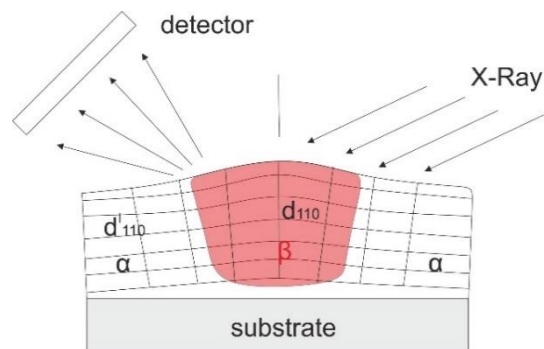


**Fig. 6.3** The sketch of XRD measurements performed in the  $\vartheta$ - $2\vartheta$  geometry. Coherent micro-strain appearing at the interface between the  $\alpha$ - and  $\beta$ -phase volumes fractions cause an additional diffuse scattering visible via the peak broadening.

Furthermore, the local hydrogen concentration change within the sample becomes smaller, when the film thickness is reduced. This happens, because the width of miscibility gap shrinks with a decrease of the film thickness, (see chapter 5.3.5 and Ref. [14]).

Two final important factors are the high density and typically small lateral size of hydride precipitates in case of “intermediate” films as compared to the “thick” ones (see Fig. 6.1 (a, b)). At this stage of the discussion, it is important to note that the surface area irradiated by the X-ray beam is very large ( $\approx 5 \times 10^{-1} \text{ mm}^2$ ) as compared to the lateral size of individual hydride precipitates (e.g. in the 25 nm thick film:  $\approx 1 \times 10^{-8} \text{ mm}^2$ ). Thus, the coherent phase transformation governed by nucleation [133] as revealed by STM measurements (see Fig. 6.1 (a)) in the presence of a relatively small modulation of hydrogen concentration (not mix up with a spinodal decomposition) becomes nearly invisible via XRD measurements. In total, it is suggested that during the hydrogen absorption in Nb-H thin films all the previously discussed contributions become visible via the peak broadening by crossing the two-phase region and continuous peak shift, whose position seems to depend on the average hydrogen concentration in the sample (for details see chapter 5.2.1).

A similar behaviour was reported in literature in the past, for coherently decomposed systems [139], [140], [141]. C. Gente et al. [139] and R. Busch et al. [140] observed in their studies on Cu-Co alloys only one XRD peak while the sample consisted of phase-separated (fcc) Cu- and (fcc) Co-rich regions. The separated regions were found to be coherently linked and small in size [139], [140]. A single broad XRD reflection was also reported by Michaelsen et al. for coherent Cu-Co multi-layers, below a layer thickness of 8 nm [141]. According to Michaelsen et al, different layers become XRD-invisible because of the lattice coherency.

Another finding also supports the suggested coherent match between the phases: If the phases were matched incoherently, the XRD peak profile would change asymmetrically upon hydrogen loading in the two-phase region. This is not observed in Fig. 6.2 (b). For thicker films ( $d \geq 43 \text{ nm}$ ), incoherency and significantly larger hydride lateral dimensions (see Fig. 6.1 (b)) make two XRD peaks related to different phases well distinguishable in the XRD pattern.

Thus, based on our XRD results, on the related literature data and on the STM results, the discussed “one peak” behaviour observed during in-situ XRD measurements on Nb-H thin films in the range of  $15 \text{ nm} \leq d \leq 37 \text{ nm}$  can be attributed to the coherency state. In more details, this result can be explained by the coherent lattice matching between the  $\alpha$ -phase and the hydride phase in combination with a high number density of small precipitates, distributed homogeneously in the  $\alpha$ -matrix (see Fig. 6.1 (a)). To summarize this sub-chapter, combined consideration of STM and XRD data suggests coherent phase transformation for an “intermediate” thickness range in the Nb-H thin film system ( $15 \text{ nm} \leq d \leq 37 \text{ nm}$ ).

## 6.2 Irreversible changes in thin Nb-H films (based on STM, XRD and stress measurements results)

For all the film thicknesses above  $d \geq 8 \text{ nm}$  according to the actual STM, XRD and stress measurements results, the presence of irreversible microstructural changes occurring in the Nb-H epitaxial films upon the hydrogen loading / unloading experiments was clearly proven. To remind the reader, it is supposed that in our samples dislocation formation is the dominant mechanism of stress release (see chapter 2.4.4).

As discussed in chapter 2.4.4, dislocation formation can occur at the hydride/ $\alpha$ -matrix interface [9], [19], [22] as well as at the hydride/substrate interface [18], [20], [21], [23], [35]. Concerning the theoretical prediction made by Nörthemann, the steep height increase at the interface between  $\alpha$ -phase and hydride phase as detected by STM for film thickness  $d \geq 40 \text{ nm}$ , suggests the formation of dislocation loops (see chapter 2.4.6) forming around the hydride precipitates. For the 25 nm film and films below this thickness coherent phase transformation occurs, as revealed by STM and XRD measurements (see chapter 6.1). Further, it is suggested that an appearance of ramps with sharp straight edges detected by STM (see chapter 5.1.4.1 and chapter 5.1.5.1) can be attributed to the emergence of misfit dislocations forming mainly at the film / substrate interface (see chapter 2.4.3). This was directly proven by STM measurements on the 8 nm film, where local precipitation of hydride phase does not appear. One of the related STM difference images is given in Fig. 6.4 (a). Here, only the traces of dislocations are detected, as previously discussed in chapter 5.1.5.

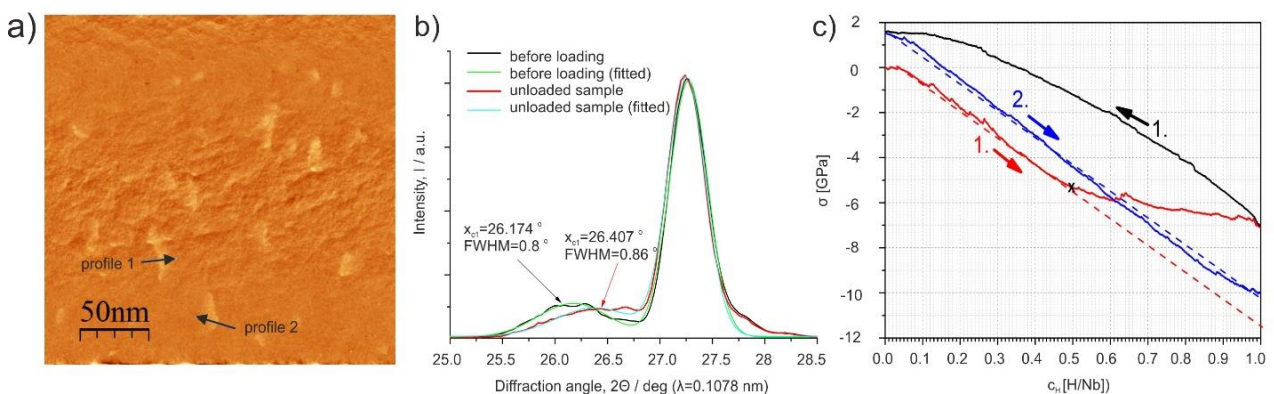


**Fig. 6.4** Combination of STM, XRD and stress measurements results that proves the presence of stress release in Nb-H films for  $d = 8 \text{ nm} - 10 \text{ nm}$ . **a)** STM difference image: traces of dislocations visible as elevated (bright) regions are detected **b)** Irreversible microstructural change in the 8 nm Nb-H film: as compared to the as-prepared sample state, Nb (110) peak is shifted and became broader in the unloaded state. **c)** The deviation from the linear elastic behavior (red curve) and the residual tensile stress observed in the unloaded sample state (black curve) are clearly visible [75].

Furthermore, stress release was confirmed explicitly by two additional independent techniques, namely by in-situ XRD and in-situ stress measurements. To remind the reader, the related XRD patterns demonstrates significant peak broadening and peak shift forward to the higher angles measured in the unloaded sample state for film thickness  $d \geq 8 \text{ nm}$  (see chapter 5.2.2 and chapter 5.2.3). One of the related XRD measurements, performed particularly on the 8 nm film is given in Fig. 6.4 (b). Here, the irreversible microstructural changes are visible via the different Nb (110) peak positions measured, in the as-prepared (black curve, peak at  $2\theta = 26.174^\circ$ ) and the unloaded (red curve peak at  $2\theta = 26.407^\circ$ ) sample states, respectively. The observed lattice contraction in the out-of-plane direction related to the peak shift from  $26.174^\circ$  to  $26.407^\circ$  indicates in-plane lattice stretching resulting from the Poisson effect. It is not expected in the elastic regime with one-dimensional film expansion predicted by the theory of linear elasticity (see chapter 2.4.1). Besides, peak broadening itself can be attributed to both factors: increased density of defects and, at the same time, increased mosaicity of the film (disorientation or imperfections of crystal structure) resulting from the dislocation formation and their movement. The instrumental peak broadening related to the method itself is expected to be negligible, since the relative sample / detector geometry and the parameters of the primary X-Ray beam were not changed.

The next important point is that XRD measurements stay in a good agreement with the stress measurements performed for similar film thickness range. For all the measured film thicknesses above  $d \geq 7 \text{ nm}$  a deviation from the linear - elastic behaviour was clearly observed (see Table 5.3.1). This, again, indicates plastic deformation occurring in the films as discussed in chapter 2.4.4. One of the related stress-composition curves measured, particularly, for the 10 nm is given in Fig. 6.4 (c) [75]. Here, the deviation from the linear elastic behavior (solid red curve deviating from the dashed red curve) and the residual tensile stress observed in the unloaded sample state (black curve value of  $\sigma_H = + 1.8 \text{ GPa}$  at  $c_H = 0 \text{ H/Nb}$  deviating from the initial value of the red curve, set to  $\sigma_H = 0 \text{ GPa}$  at  $c_H = 0 \text{ H/Nb}$ ) are clearly visible.

Huge mechanical in-plane stress in the GPa range measured in our samples upon hydrogen loading (see chapter 5.3) is suggested to arise mainly due to the strong adhesion between the film and the substrate [17], [30]. Although the average stress contains the contributing stress from the complete sample and includes coherency stress arising at the  $\alpha/\beta$  interfaces, in this work it is argued that the film / substrate interface and the nearby regions mainly react on the hydrogen-induced stress and, hence, have to be considered as the main origin of hydrogen-induced dislocations.

### 6.3 Quasi-elastic behavior detected by using stress measurements

As discussed in chapter 5.3.4, for films of  $d \geq 7 \text{ nm}$ , the unloading of the sample results in tensile stress arising in the film. Exemplary it was shown for the 10 nm film, where the stress in the unloaded

sample state achieved about + 1.8 GPa (see Fig. 6.4 (c)). The interesting finding is that during the second loading, in the presence of dislocations formed in the first cycle, the stress increases linearly up to a concentration of 1 H/Nb and no point of inflection was detected. An ultrahigh hydrogen-induced stress difference of  $\Delta\sigma = -(11.8 \pm 1.2)$  GPa and a final stress of  $\sigma = -(10 \pm 1)$  GPa built up in the 10 nm film, at  $c_H = 1$  H/Nb [75]. Thus, by second hydrogen loading the system followed the linear elastic dependency and reflected the stress expected for the pure elastic response ( $\langle\sigma'\rangle = -9.6 \cdot c_H$ , see chapter 2.4.1). Because the film shows this behavior only after the first loading cycle, we conditionally named it as 'quasi-elastic' [75]. This finding indicates on the complete absence of further plastic deformation and dislocation formation after the first loading. Thus, hydrogen assisted hardening of epitaxial Nb-H films occurring in the presence of residual tensile stress is found [75].

It is supposed that dislocations generated upon the first loading at the film / substrate interface significantly change the Nb layer. This modified sample volume contains a dislocation network that results in material strengthening due to the work hardening [142]. In total, one may assume that the interaction between the dislocations prohibits the mobility of pre-existing dislocation and suppress the generation of the new defects [75]. Thus, the nucleation barrier for dislocation formation is increased that causes an appearance of significantly higher mechanical stresses accumulated in the system. Hereby, the amount of force required to start plastic deformation is larger than it was for the original film.

#### **6.4 Evidence of pure elastic one-dimensional film expansion: reversibility test based on XRD, resistance, EMF, stress and XRR measurements**

For the 5 nm film according to our XRD, resistance, stress and EMF measurements, reversible changes occurring in the 5 nm Nb-H film during the hydrogen loading / unloading experiment were clearly proven. Related data for the film thickness  $d = 5$  nm are summarized in Fig. 6.5. As discussed in chapter 5.2.4, the XRD patterns for the unloaded sample reappeared in their original shape. This reflects reversibility (elastic behavior) of the microstructural changes occurred in the film. Here, it is once again shown in Fig. 6.5 (a), where the green curve corresponds to the XRD pattern measured in the as-prepared sample state, and the blue one – to the unloaded sample state. The resistance curve shown in Fig. 6.5 (b) also indicates completely reversible behavior during the loading / unloading experiment, as discussed in chapter 5.2.4. Two these results are in full accordance with the stress curve shown in Fig. 6.5 (c) showing no deviation from the linear elastic behavior (see chapter 2.4.1). For this film thickness the compressive stress increased quasi-linearly with the hydrogen concentration over the whole hydrogen concentration range and reached a maximum stress of  $-(8 \pm 2)$  GPa at  $c_H = 1$  H/Nb [75]. Tensile stress, detected for thicker films in the unloaded sample state after the first loading cycle (see Fig. 6.4 (c)) for the 5 nm film was not found.

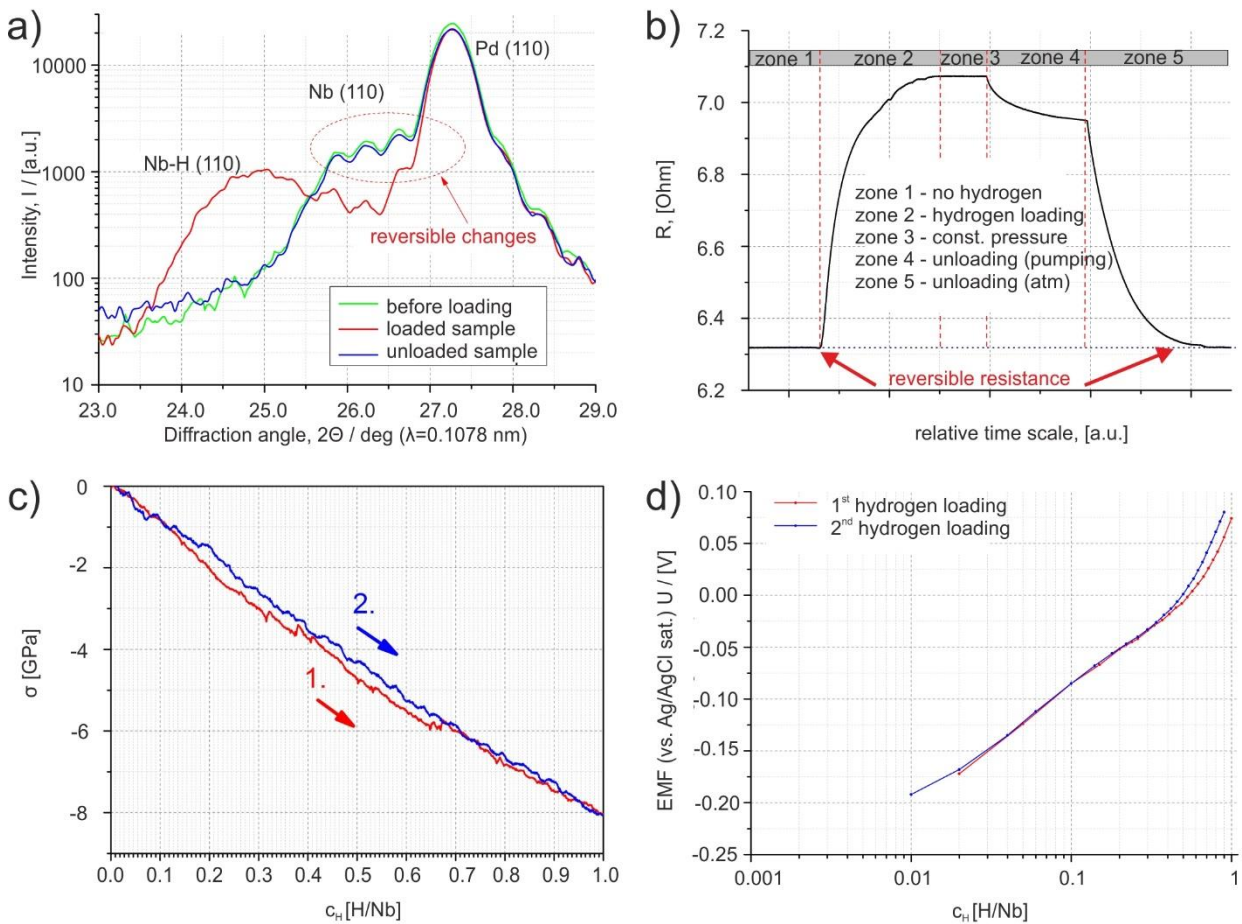


**Fig. 6.5** Combination of XRD, resistance, stress, and EMF measurements results that proves the fact of reversible (elastic) behavior in Nb-H films for  $d = 5$  nm. **a)** Change of XRD patterns during hydrogen loading / unloading experiment: The green curve corresponds to the reference stage before hydrogen loading and the blue one – to the unloaded sample state. Two these curves mainly reproduce each other. **b)** Resistance curve measured in-situ during hydrogen loading / unloading experiment: the resistance value measured in “zone 1” (as-prepared sample state) and in “zone 5” (unloaded sample state) are equal to each other **c)** Stress-composition curves show similar behavior for the first (1. red) and the second loading (2. blue). No plastic deformation is detected. The stress curves match each other [75]. **d)** EMF curves measured during the first (in red color) and the second (in blue color) loading experiments nearly reproduce each other.

Further, as compare to the thicker films (see chapter 5.3.5), the EMF curve measured for the 5 nm film did not reveal any differences between the first and the second loading curves as shown in Fig. 6.5 (d). This behavior is also expected for a reversible process.

Finally, by comparing the film expansion ( $\frac{\Delta d}{d}$ ) measured via XRR and the lattice expansion ( $\frac{\Delta a_{110}}{a_{110}}$ ) measured via XRD in the out-of-plane  $\langle 110 \rangle$  - crystallographic direction it is shown in chapter 5.2.4 that corresponding values are equal to each other. Considering all the previously reviewed data for the 5 nm film, this result indicates the realization of the ideal one-dimensional expansion model described in chapter 2.4.1. Thus, it is suggested here that for the 5 nm epitaxial Nb-H film, any stress release is suppressed and the system follows the pure elastic behavior, predicted by the linear elastic theory (see chapter 2.4.1).

## 6.5 Suppression of phase transformation in ultrathin films

As discussed in chapter 5.1.5, the STM measurements performed on the 8 nm Nb-H film showed that the phase transformation from  $\alpha$ - to  $\beta$ -phase does not occur. In other words, by reducing the film thickness  $d \leq 8 \text{ nm}$  our model system transforms continuously into the high concentration solid solution phase without any phase separation (see chapter 2.1.2). Thus, if, upon increase of hydrogen concentration, phase separation in the Nb-H film is suppressed, “one peak” behavior discussed in chapter 6.1 should not appear in XRD patterns: The related XRD measurements performed on the 8 nm film supports this interpretation and shows only a “one broad peak” behavior without any intermediate peak broadening (see chapter 5.2.1).

The suppression of phase transformation can be attributed to the increasing impact of mechanical stress on the thermodynamics of Nb-H thin film system. The impact of mechanical stress was recently implemented in a theoretical model by Wagner et. al. [56], [103]. This theory was shortly introduced in chapters 2.4.8 and chapter 2.4.9 and will be applied here. The  $E_{HH}$  and  $T_c$  values were estimated from the EMF curves measured for different film thicknesses, taking the measured in-plane stresses of the films during H-loading into account. This presented exemplarily in Fig. 6.6 (a, b, c). By using Eq. 2.27 and assuming that  $E_{HH}$  stays mainly constant in the whole hydrogen concentration range, measured EMF curves were fitted by use Eq. 2.27. Hereby, the measured electromotive force (EMF)  $U$  of a hydrogen - loaded film was linked to the chemical potential  $\mu_H$  via Eq. 3.10.  $E_{HH}$ ,  $T_c$  and  $E_o$  were considered as fitting parameters.

The experimental (“black”) and fitted (“red”) EMF-curves films are given in Fig. 6.6 (a, b, c) for 40 nm, 25 nm and 5 nm thick films, respectively. As previously, the abscissa gives the hydrogen concentration and the ordinate the EMF value  $U$ . The fitted curves match the experimental curves well in the important, intermediate concentration range (see Fig. 6.6 (a, b, c)). The fitted curve in Fig. 6.6 (a, b) surrounds the measured curve in a Maxwell-type shape, as expected in the two-phase region [14]. However, in the low concentration range ( $c_H \leq 0.05 \text{ H / Nb}$  for 40 nm and 25 nm and  $c_H \leq 0.10 \text{ H / Nb}$  for 5 nm film) clear deviations occur. This can be explained in terms of limitation of the model that not includes the influence of defects on the shape of the EMF-curve [14], [103]. For thin films, this contribution typically becomes stronger [9]. Besides, for the 5 nm film, additional deviations are observed at  $c_H > 0.5 \text{ H / Nb}$ . The apparent reasons for this phenomenon are not clear. Table 6.1 contains the parameters ( $E_{HH}$ ,  $r$ ,  $E_o$ ) derived from the fitted curves given in Fig. 6.6 (a, b, c) and the data of Song et al. [32] and Edelmann [33] as well as a bulk value [16] for references.

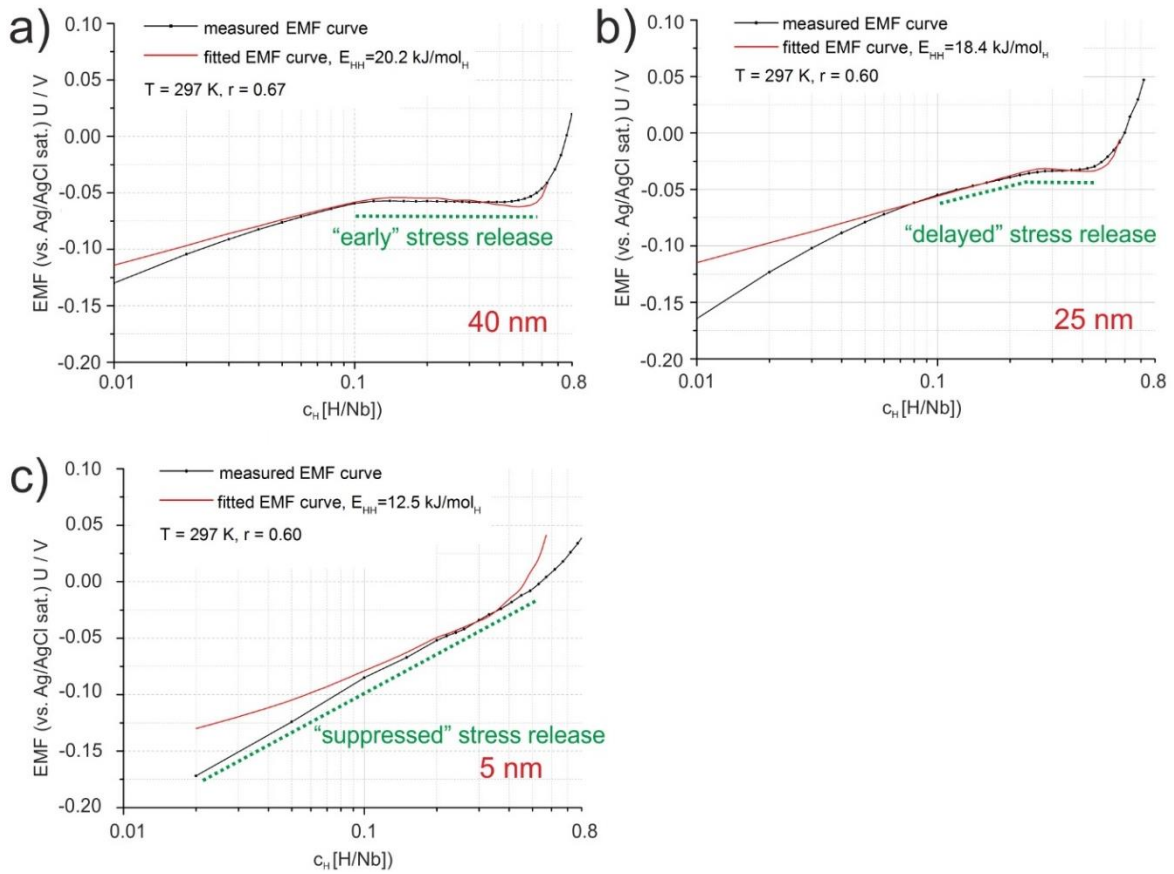


**Fig. 6.6** Experimental (given in black color) and fitted (given in red color) EMF curves. In the presence of compressive stress the slope and the shape of the chemical potential depends on the particular stress development (details see in the text). **a)** 40 nm: “early” stress release results in an appearance of plateau region **b)** 25 nm: “delayed” stress release results in the change of the slope inside the two-phase region **c)** 5nm: “suppression” of stress release results in a permanently sloped EMF curve. The shape of the EMF curve can be also partly related to the absence of phase separation.

**Table 6.1** Fitted parameters derived from the shape of the EMF curves given in Fig. 6.6 (a, b, c). Here, the hydrogen-hydrogen interaction energy ( $E_{HH}$ ), the number of available interstitial sites per metal atom ( $r$ ), the site energy ( $E_0$ ) and the calculated critical temperature ( $T_c$ ) are summarized for different film thicknesses ( $d$ ).

$d$ , [nm]	$E_{HH}$ , [kJ/mol <sub>H</sub> ]	$r$	$E_0$ , [kJ/mol <sub>H</sub> ]	$T_c$ , [K] (Eq. 2.32)
40	22.2	0.67	-15.2	366
25	18.4	0.6	-15.6	324
5	12.5	0.6	-18.8	243
23 [33]	12.4	-	-	-
32 [32]	7.7	-	-	254 - 275
Bulk [16]	25.1	0.62	-	444

All the calculated parameters lie in the expected range if compared with the “bulk” system. According to Table 6.1, performed model calculation shows, that  $E_{HH}$  for thin films is expected to lie below the  $E_{HH}$  reported for the “bulk” samples [16].

At the same time, the calculated values are 2 - 2.5 times higher as compared to the value reported by Edelmann [33] and Song [32], for comparable film thicknesses (see Table 6.1). This difference can be explained by the fact that in the related works the authors did not consider any stress contribution to the strain-pressure isotherms used for the calculation of  $E_{HH}$  [14]. In opposite, this work supports the results of Wagner et al. [14], [103] that the stress contribution modifies the EMF curve significantly (more details will be given in chapter 6.6). The fit of the EMF curve with different parameters shows that in the absence of the measured stress term in the fitting equation, the calculated  $E_{HH}$  becomes smaller - that might explain the difference to the literature data of Edelmann or Song et al. [32], [33]. Thus, the obtained result strongly depends on the particular physical model chosen for the fitting.

Further, the calculations show that by decreasing the film thickness the H-H interaction energy  $E_{HH}$  visibly decreases. In the case of 5 nm film, that demonstrates no stress release (see chapter 6.4) and the highest stress state (see chapter 5.3.3), the calculated  $E_{HH}$  drops by a factor of two if compared to the value known for the “bulk” samples (see Table 6.1). Hence, since the stress contribution in “bulk” samples is negligible (for details see chapter 2.3.1 and chapter 2.4.1), this result on thin Nb-H films indicates that the compressive stress reduces  $E_{HH}$ .

The drop of  $E_{HH}$  yields a destabilization of the hydride phase and subsequent decrease of  $T_c$ , as visible in the last column of Table 6.1. Here, the critical temperatures ( $T_c$ ) of hydride formation were calculated according to Wagner’s model and, particularly, by using Eq. 2.32. According to the model calculations, performed for the 40 nm and the 25 nm film,  $T_c$  for these samples lies well below “bulk” value  $T_c^{bulk} = 444 K$ , but still above RT ( $T_{RT} = 294 K$ ). Thus, phase transformation should occur upon the hydrogen gas loading performed at RT. The related STM and XRD experiments clearly proved the presence of phase transformation for this film thickness range occurring by hydrogen gas loading at RT. Further,  $T_c$  tends to decrease with a decrease of the film thickness from 40 nm to 5 nm. Moreover,  $T_c = 243 K$  calculated for the 5 nm film lies significantly below  $T_{RT} = 294 K$ . This is in good accordance with the finding that the 5 nm (and also the 8 nm) film does not show traces of phase transition at  $T_{RT} = 294 K$ . The exact value of  $T_c$  cannot be proven experimentally in frame of this study, since all the measurements were performed at RT. Nevertheless, the use of the methodological approach describing the measured EMF shows that for this film thickness range, the phase separation is not expected. Thus, these calculations directly support STM (chapter 5.1.5) and XRD (chapter 5.2.1) data indicating on the suppression of phase separation in the considered Nb-H model system for the film thickness below  $d = 8 nm$ . Furthermore, the stress measurements results (chapter 5.3.3) confirm the assumption of a dominant role of the mechanical stress arising in the system on the destabilization of the hydride phase.

Finally, one has to note that by the presence of compressive stress, the slope and the shape of the chemical potential (EMF curve in Fig. 6.6 (a, b, c)) strongly depends on the particular stress

development. Hereby, based on the result obtained in this work, one can distinguish three different shapes of EMF curves (see also chapter 5.3.2). “Early” stress release occurring at low hydrogen concentrations ( $c_H \leq c_{\alpha,lim}$ ) results in the appearance of a horizontal plateau region in the EMF curve. It corresponds to the phase transformation occurring within the system (see Fig. 6.6 (a)). “Delayed” stress release occurs already during the phase transformation at intermediate hydrogen concentrations ( $c_{\alpha,lim} \leq c_H \leq c_{\beta,lim}$ ). The argumentation will be given in chapter 6.6. It results in the appearance of two different slopes present in the EMF curve in the two-phase region (see Fig. 6.6 (b)). For films, in which stress release appears at high hydrogen concentrations or even stress release does not happen at all, the EMF curves possess a permanent slope and no inflection point (see Fig. 6.6 (c)). This behavior is supposed to be related to the significant stress contribution and already shows the suppression of the phase transformation.

## 6.6 Stress contribution and change of solubility limits visible in EMF curves

As discussed at the end of the previous chapter, mechanical stress arising in the system significantly affects the EMF curve. In this chapter, this topic is discussed in more details. The EMF curve obtained for a 40 nm film (see Fig. 6.7 (a)) has a clearly visible plateau region ( $0.1 \text{ H/Nb} \leq c_H \leq 0.57 \text{ H/Nb}$ ) corresponding to the miscibility gap where the phase transformation occurs. This result is conventional for the bulk-like systems [67]. Hereby, the beginning of the plateau region correlates with the initiation of stress release ( $c_H = 0.11 \text{ H/Nb}$ ) detected in the film (see Table 5.3.1). Therefore, this result allows concluding that an appearance of bulk-like plateau region in the EMF curve is directly linked with a relatively early stress release occurring in the system, when the hydrides start to precipitate.

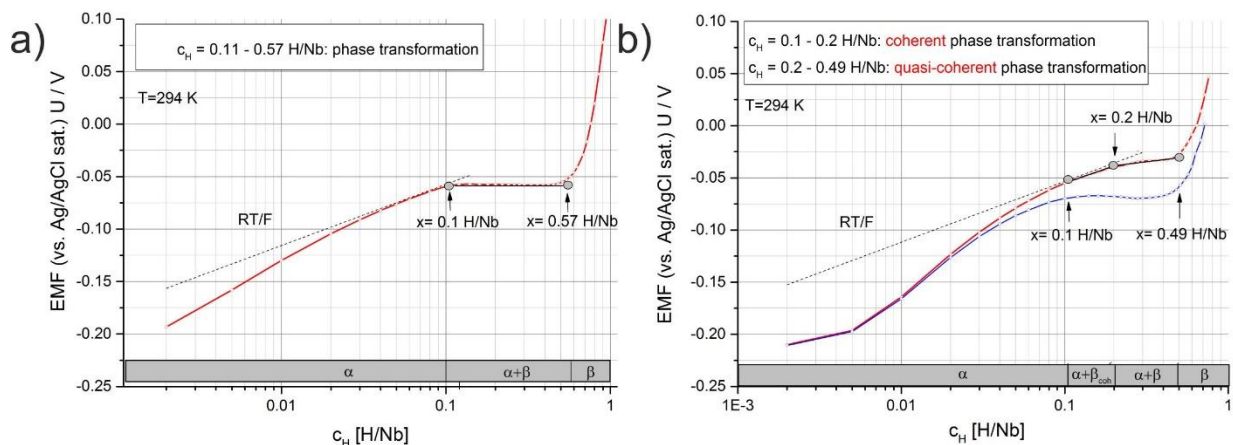


**Fig. 6.7** The difference occurring in the EMF curve due to the stress contribution: **a)** 40 nm film: a clearly detectable plateau region is visible at  $0.1 \text{ H/Nb} \leq c_H \leq 0.57 \text{ H/Nb}$ , **b)** 25 nm film: red curve corresponds to the original EMF including the stress contribution and the blue one – obtained by subtracting of the stress contribution (details see in the text).

Opposite to this result, the EMF curve obtained for the 25 nm film in the two-phase region is curved (see Fig. 6.7 (b)). When applying the model suggested by Wagner et al. for description of the EMF curve (Eq. (2.27)) and subtraction the stress contribution term ( $\Delta\mu_H(\sigma) = -1.124 \cdot \sigma \frac{kJ}{mol_H}$ , [56]) from the measured EMF curve, the plateau region (Maxwell-shape) gets visible for a range of  $0.1 \text{ H/Nb} \leq c_H \leq 0.49 \text{ H/Nb}$  as given by the blue curve in Fig. 6.7 (b). Its start at  $c_H = 0.1 \text{ H/Nb}$  corresponds to the beginning of the two-phase region in the 40 nm film (Fig. 6.7 (a)). At the same time, stress measurements performed on the 25 nm film shows that first stress release was detected at  $c_H = 0.26 \text{ H/Nb}$  (see Table 5.3.1). Therefore, it is concluded that stress release occurring at higher hydrogen concentrations directly affects the EMF curve and makes it problematic to identify clearly the boundaries and the width of the miscibility gap. Further, it is suggested that the bending point roughly estimated at  $c_H = 0.2 \text{ H/Nb}$  is most probably related to the stress release occurring in the sample, while the lower boundary of the solubility gap lies below this value ( $0.1 \text{ H/Nb} \leq c_{\alpha,lim} \leq 0.2 \text{ H/Nb}$ ).

A more accurate determination of this low limit is challenging, but its value is obviously below what is reported for Nb-film of comparable thickness by Dornheim et al. ( $c_{\alpha,lim} = 0.26 \text{ nm}$  [35]). The observed deviation might be attributed to many factors including the differences in the conditions of the film preparation as well as in the experimental conditions. Nevertheless, the two EMF curves given in Fig. 6.7 (b) clearly show that the contribution of mechanical stress to the shape of the EMF curve should be always regarded, when the solubility limits and the width of the miscibility gap are of interest.

## 6.7 Critical film thickness for coherent phase transformation: model validation (STM, XRD, EMF and stress measurements)

According to the STM results (chapter 5.1), the critical film thickness separating coherent and semi-coherent phase transformation lies in the thickness range between 25 nm and 40 nm. A more precise determination was not possible due to the limited number of the experimental data. At the same time, XRD results (chapter 5.2) performed for a similar film thickness range showed that the critical film thickness lies in the thickness range between 37 nm and 43 nm. Thus, the XRD and STM data supports each other, since experimentally derived two ranges overlap. Hereby, XRD data give a more precise value because of the bigger number of the experimental data. Thus, based on this combined result of STM and XRD measurements, the critical film thickness corresponding to preferable coherent phase transformation is supposed to lie in the thickness range from 37 nm to 40 nm. While for the 43 nm film the measurements of XRD patterns demonstrated two overlapping, but still distinguishable  $\alpha$ -phase and hydride phase related peaks, the measurements on the 37 nm film showed already “one peak” behaviour (see Table 5.2.1). According to the results of chapter 6.1, this “one peak” behaviour was related to the coherent

match between the  $\alpha$ - and the hydride phase. Thus, according to the experimental data, the critical film thickness is higher than the theoretical one ( $d_c = 26 \text{ nm}$ , predicted by Nörthemann [19]). Our empirical model explaining different appearance of XRD patterns proposed in chapter 6.1 is supported by the STM results showing significant changes occurring in the regime of hydride phase precipitation and growth in the film thickness range from 25 nm to 40 nm (see Fig. 6.1).

Returning to the starting point, namely to the result of finite element modeling [19], related theoretical prediction was done for the fully coherent phase transformation that is a kind of an extreme case. To remind the reader, the simulation is based on a simplified physical model, in which only one hydride precipitate of cylindrical shape is considered (see chapter 2.4.6). Furthermore, the interaction between the neighboring precipitates and as a result, the superposition of their stress fields that might affect the critical film thickness is not implemented in the model. Another critical point is the presence of the imperfect interfaces between the film and the substrate. In Nörthemann's simulation, its possible impact to the coherency conservation was not regarded at all, despite the fact that huge mechanical stresses arising at this interface may cause dislocation formation and irreversible lattice distortion as it was shown in this PhD work. These contributions may lead to an underestimation of the film thickness separating the coherent and the incoherent phase transition  $d_c$ .

Thus, the actual experimental results show that the effect of coherent interfaces in the phase transformation becomes visible at higher film thickness  $d_c = 37 \text{ nm} - 40 \text{ nm}$ , but the "degree of ideality" of the coherency state still can be increased by reducing the film thickness. Based on the related experimental result we define this value as the critical film thickness separating coherent and semi-coherent phase transformation. Hereby, even in case of dominant coherent phase transformation, stress release may occur, since new defects still can be generated e.g. at the film / substrate interface [23]. STM measurements revealed that for the film thickness  $15 \text{ nm} \leq d \leq 25 \text{ nm}$  hydrides in the initial stage of precipitating have a circular shape and a relatively small slope of the profile in the transition area between the  $\alpha$ -phase and the  $\beta$ -phase (for details see chapter 5.1.3 and chapter 5.1.4). These topographic changes are attributed to the coherency state (see chapter 2.4.5) that actually correlate well with Nörthemann's theory [19], [73]. Nevertheless, some irreversible change of interfaces and sample volume appears during the hydride phase precipitation and grow at the late stages of sample hydrogenation, as revealed by STM, XRD and stress measurements. Thus, in total the validation of the suggested theoretical model shows that the achievement of pure coherent phase transformation without any stress release is not possible for the Nb/Al<sub>2</sub>O<sub>3</sub> system at ambient temperature. Stress release was clearly detected even below theoretically predicted critical film thickness of the 26 nm film (see chapter 6.2). To summarize the data, it is suggested to specify the "degree of ideality" in dependence on the film thickness. Hereby, three different regimes of "full plasticity", "partial plasticity" and "elastic behavior" are defined. The details are given in Table 6.2.

Further, it is supposed that the hydrogen-induced dislocations formed mainly in the region nearby the film / substrate interface (see chapter 6.2). These dislocations appear, because the system needs to accommodate huge mechanical stresses occurring by the presence of the related interface and due to the increasing lattice mismatch in the presence of hydrogen.

By further reduction of the film thickness, the stress contribution increases (see chapter 5.3.3). This results in the suppression of the phase transformation (see chapter 6.5). The "second critical film thickness" where this change occurs, lies in the range between 8 nm and 15 nm. Here, the phase transition is suppressed (see chapter 6.5). Finally, by reducing the film thickness down to 5 nm, the regime of pure elastic and reversible sample change predicted by the linear elastic theory can be realized (see chapter 6.4). Herewith, the regime of linear elastic expansion and ultrahigh mechanical stress can be reproducibly achieved (chapter 5.3.4).

**Table 6.2** "Degree of ideality" and different regimes of stress release experimentally derived for the model Nb-H thin film system.

Film thickness	Degree of ideality	$\alpha/\beta$ phase boundary	Film/ substrate interface
$d \geq 43 \text{ nm}$	full plasticity	incoherent	dislocations
$37 \text{ nm} < d < 40 \text{ nm}$	↓		dislocations
$15 \text{ nm} \leq d \leq 37 \text{ nm}$	partial plasticity	coherent	dislocations
$8 \text{ nm} < d < 15 \text{ nm}$	↓		dislocations
$d \leq 5 \text{ nm}$	elastic behavior	no phase transformation	no dislocations

## 7 Summary and outlook

For nanoscale systems such as Nb-H thin films, changes of physical properties have been suggested to appear below certain critical sizes. The presence of these critical sizes and the related changes of thermodynamical and mechanical properties are the central topics of this thesis, using the model system of Nb-H thin films. This includes the suggested appearance of coherent phase transformation, the suggested drop of  $T_c$  to less than  $T_{RT} = 294\text{ K}$ , the suggested occurrence of ultrahigh stresses and the suggested presence of pure linear elasticity for films below critical sizes.

Recently, Nörthemann et al. ([19], chapter 2.4.6) suggested the presence of a coherent phase transformation for Nb-H thin films of thickness  $d$  of less than  $d_c \leq 26\text{ nm}$ . The film thickness range regarded in this thesis varies from above this value to far below this value, to see the differences occurring in the system more clearly. Since all the effects and, especially, the efficiency of stress release depends on the film thickness ( $d$ ),  $d$  was considered in this PhD study as a tunable size parameter that was varied from 105 nm to 5 nm. To avoid the influence of grain boundaries on the hydrogen absorption and the phase transformation and to minimize the number of pre-existing defects in the model Nb-H/ $\text{Al}_2\text{O}_3$  thin film / substrate system, epitaxially grown Nb films with flat surfaces were addressed.

In this thesis, the critical film thickness for coherent phase transformation ( $d_c$ ) was derived experimentally as based on the STM and the XRD methods. Besides, a systematic study on the stress development and stress release within the Nb-H films upon hydrogen loading depending on the film thickness was performed. Hereby, a regime of the pure elastic one-dimensional film expansion and high stress state predicted by the linear elastic theory was realized for film thicknesses below  $d = 5\text{ nm}$ . Furthermore, changes occurring in the regime of hydride phase precipitation and growth in the coherent and the semi-coherent phase transformation were studied. Finally, a large effect of high mechanical stress on the drop of  $T_c$  in thin epitaxial Nb-H films was proven.

The topic was investigated by studying different aspects of hydrogen-induced changes occurring in the sample during the hydrogen loading / unloading experiments for different film thicknesses. Therefore, the results obtained for similar film thicknesses by using different in-situ techniques including STM (chapter 5.1), XRD (chapter 5.2), electrical resistance (chapter 5.1 and chapter 5.2) in the vacuum conditions, and in-situ EMF and substrate curvature measurements (chapter 5.3) under ambient conditions, were considered and discussed with respect to each other. This kind of combined approach provides the most complete picture of the physical processes occurring in the system during the hydrogen absorption and desorption in/from the sample.

The presented in-situ STM measurements have shown that, depending on the film thickness, two different regimes of hydride phase precipitation and growth can be distinguished. It is qualitatively shown

in chapter 6.1 where typical lateral dimensions and the densities of hydride precipitates are compared for the cases of the 25 nm and the 40 nm films under similar loading conditions. It was suggested that related differences are attributed mainly to the “degree of the ideality of the coherency state” at the  $\alpha/\beta$ -interface that increases by reducing the film thickness. Hereby, it is concluded that for the 25 nm film, the phase transformation is governed mainly by nucleation (preferential nucleation of new precipitates instead of their lateral expansion). On the other hand, for the 40 nm film the phase transformation is hydride growth-dominated (preferential growth of precipitates). These results were published in Ref. [133]. They are in line with results of Kürschner et al. for Pd-H thin films [143].

In-situ XRD measurements surprisingly revealed also a strong difference occurring in the XRD patterns measured for the films of different thickness above and below the calculated critical value ( $d_c = 26 \text{ nm}$ ). Conditionally called “two peak”-behaviour ( $d \geq 43 \text{ nm}$ ) and “one peak” – behaviour ( $15 \text{ nm} \leq d \leq 37 \text{ nm}$ ) were observed experimentally. With respect to the STM results, a model was proposed, in which coherent lattice matching between the  $\alpha$ -phase and the hydride phase in combination with a high number density of small precipitates, distributed homogeneously in the  $\alpha$ -matrix makes the “one peak” – behaviour observable (see chapter 6.1). It is shown as well that intermediate peak broadening in some cases can be considered as a sign of phase transformation that in the presence of coherent phase boundaries becomes nearly XRD-invisible (see chapter 5.2.1). Thus, it was pointed out that in some cases an independent technique is required to identify the phase separation.

Further, by use of in-situ stress measurements, hydrogen-induced mechanical stresses were measured and analysed for deviations from the linear elastic behaviour that results from stress release. Herewith, the maximum mechanical stress achieved is about -10 GPa (chapter 5.3.4). It should be noted that this huge value was never measured before on any similar systems. Besides, it was clearly shown that the inflection point in the stress-composition curve permanently shifts to higher hydrogen concentrations with decreasing the film thickness. On top of this, a quasi-elastic sample behaviour, in which the stress curve follows a linear elastic behaviour in the second and subsequent loading cycles (see chapter 6.3), was found for the film thickness range between 7 nm and 25 nm. This finding was attributed to work hardening, occurring due to the interaction between the dislocations formed during the first loading cycle. These results were published in Ref. [75].

A large influence of mechanical stresses on the thermodynamics of the system was directly addressed in the EMF measurements that possess a sloping plateau region corresponding to the phase transformation and the shift of solubility limits (chapter 6.5 and chapter 6.6). Hereby it is found that, in the presence of compressive stress, the slope and the shape of the chemical potential (EMF curve) depend on the particular stress development. It is assumed that partial stress release also is the reason for the presence of sloping plateau pressure, as suggested by Wagner et al. [103]. Using the thermodynamic

description recently suggested by Wagner et al. [14], [103] that bases on the theoretical description of EMF curves (chapter 2.4.9) it was revealed that by decreasing the film thickness the H-H interaction energy  $E_{HH}$  visibly decreases. This result is supposed to be directly linked with the increasing contribution of mechanical stress, destabilizing the hydride phase. It is suggested further that in ultrathin Nb-H films the stress arising in the system can even suppress the formation of the hydride phase at room temperature, by subsequently dropping of  $T_c$  down to  $T_c < T_{RT} = 294$  K. This was confirmed by STM and XRD results. The film thickness, at which this change occurs, lies in the range between 8 nm and 15 nm. The calculation based on the theoretical model describing the EMF curve [14], [103] performed for the 5 nm film supports the related experimental results.

For all film thicknesses above  $d \geq 8$  nm, irreversible microstructural changes occur in Nb-H epitaxial films upon the hydrogen loading / unloading. These changes were related to misfit dislocations and it was suggested that hydrogen-induced dislocations mainly appear in the region near to the film / substrate interface.

Finally, it was established that by decreasing the film thickness down to 5 nm, and likely below that value, stress release can be completely suppressed (chapter 6.4). Here, the requirements of the linear elastic model are fully satisfied and, hence, the regime of pure elastic and reversible sample change is achieved even upon cyclic hydrogen loading. It is important to note that in Nb-H thin films loaded at RT this regime was realized in the case when no phase transformation was found in the system.

In general, the validation of the suggested theoretical model shows that the achievement of pure coherent phase transformation is a challenging task, since the stress release was clearly detected down to 5 nm film thickness. However, in this research, the corresponding result is mainly attributed to the dislocation formation occurring at the film / substrate interface due to the high mechanical stress arising in the system. The interfaces between the hydride and the  $\alpha$ -phase are regarded as being coherent and coherent thermodynamics should hold. However, the critical film thickness suggested by Nörthemann et al. ([19], chapter 2.4.6) is underestimated because of remaining path of stress release. Thus, in this thesis, it is proposed to regard only “the degree of ideality” and the related regimes of stress release that according to our results visibly changes with a decrease of the film thickness (some characteristic film thicknesses are summarized in Table 6.2). The STM and the XRD data obtained for different film thicknesses clearly support the influence of coherency state at the  $\alpha / \beta$  interface on the results obtained for different film thicknesses above and below the suggested here critical film thickness range  $37 \text{ nm} \leq d_c \leq 40 \text{ nm}$ . “Locked-in size” behaviour, different modes of hydride phase precipitation and growth, small steepness of hydride precipitates and typical XRD patterns (“one peak” behaviour) hint on a dominant coherent phase transformation occurring in Nb-H thin films for the film thickness range between 15 nm and 37 nm.

To summarize, three important film thickness ranges can be experimentally derived for the model Nb-H/Al<sub>2</sub>O<sub>3</sub> thin film/substrate system:

- 1)  $d_1 \approx 37 \text{ nm} - 40 \text{ nm}$ : thickness range that separates the coherent and the incoherent phase transformation; irreversible microstructural changes occur in the sample.
- 2)  $d_2 \approx 8 \text{ nm} - 15 \text{ nm}$ : thickness range of coherent phase transition, in which  $T_c$  drops below to RT (suppression of phase separation), but film/substrate dislocations release stress; irreversible microstructural changes occur in the sample during the first loading cycle.
- 3)  $d_3 \leq 5 \text{ nm}$ : No precipitation of hydride phase occurs in the film at room temperature; reversible microstructural changes occur in the sample during first and subsequent loading cycles.

Because of the model character, these results give fundamental insights into the physics of decomposition in thin alloy films when crossing the predicted  $d_c$ - values. They will be transferable to other nano-sized systems fixed to stabilizers offering the possibility to tune the stress state and to affect the stabilities of phases by crossing critical system sizes. The realization of pure elastic or quasi-elastic regimes for ultrathin films might be interesting from the application point of view for materials interacting with hydrogen (e.g. for protective layers), since complete reversibility upon cyclic hydrogen loading and film properties independent of the sample history are needed.

## Bibliography

1. A. Züttel, A. Remhof, A. Borgschulte, O. Friedrichs, *Hydrogen: the future energy carrier*, *Phil. Trans. R. Soc. A* 368 (2010) 3329.
2. M. Latroche, *Structural and thermodynamic properties of metallic hybrids used for energy*, *Phys.Chem. Solids* 65 (2004) 517.
3. E. Akiba, *Hydrogen-absorbing alloys*, *Curr. Opin. Solid State Mater. Sci.* 4 (1999) 267.
4. R. Wiswall, *Hydrogen storage in metals*, in *Hydrogen in Metals II* (G. Alefeld, J. Völkl, eds.), *Topics in Applied Physics Vol. 29*, Springer-Verlag Berlin Heidelberg New York, (1978).
5. L. Schlapbach, A. Züttel, *Hydrogen-storage materials for mobile applications*, *Nature* 414 (2001) 353.
6. M. Conte, P. P. Prosini, S. Passerini, *Overview of energy/hydrogen storage: state-of-the-art of the technologies and prospects for nanomaterials*, *Mater. Sci. Eng. B* 108 (2004) 2.
7. A. Züttel (Editor), A. Borgschulte (Editor), L. Schlapbach (Editor), *Hydrogen as a Future Energy Carrier*, WILEY-VCH Verlag GmbH & Co, Weinheim, (2008).
8. V. A. Blagojević, D. G. Minić, J. G. Novaković, D. M. Minić (ed), *Hydrogen Economy: Modern Concepts*, (2012).
9. A. Pundt, R. Kirchheim, *Hydrogen in Metals: Microstructural Aspects*, *Annual Review Materials Research* 36 (2006) 555.
10. A. Pundt, *Metal-hydrogen-systems: what happens when systems go to the nano-scale? in Materials Challenges in Alternative and Renewable Energy II* Wiley & Sons -Th (2013) 181.
11. A. Züttel, P. Wenger, P. Sudan, P. Mauron, S-I Orimo, *Hydrogen density in nanostructured carbon, metals and complex materials*, *Mater. Sci. Eng. B* 108 (2004) 9.
12. M. Hirscher, M. Becher, M. Haluska, U. Dettlaff-Weglikowska, A. Quintel, G.S. Duesberg, Y.-M. Choi, P. Downes, M. Hulman, S. Roth, I. Stepanek, P. Bernier, *Hydrogen storage in sonicated carbon materials*, *Appl. Phys. A* 72 (2001) 129.
13. U. Laudahn, A. Pundt, M. Bicker, U. v. Hülsen, U. Geyer, T. Wagner, R. Kirchheim, *Hydrogen induced stresses in Nb single layers*, *J. Alloys. Comp.* 293-295 (1999) 490.
14. S. Wagner, *Dünne Palladium-Wasserstoff-Schichten als Modellsystem: Thermodynamik struktureller Phasenübergänge unter elastischen und mikrostrukturellen Zwangsbedingungen*. Dissertation, Universität Göttingen, (2014).
15. M. Hirscher, K. Hirose, *Handbook of Hydrogen Storage: New Materials for Future Energy Storage*, Wiley-VCH, (2008).
16. Y. Fukai, *The Metal-Hydrogen system*, *Springer Series in Material Science 21*, Springer-Verlag, Berlin, Heidelberg, (2005).
17. E. Nikitin, *Controlled delamination of metal films by hydrogen loading*. Dissertation. Universität Göttingen, (2008).

## Bibliography

---

18. A. Pundt, M. Getzlaff, M. Bode, R. Kirchheim, R. Wiesendanger, Nano scale surface modifications during hydrogen absorption in Gd thin films, *Phys. Rev. B* 61 (2000) 9964.
19. K. Nörthemann, A. Pundt, Coherent-to-semi-coherent transition of precipitates in niobium hydrogen thin films, *Phys. Rev. B* 78 (2008) 014105.
20. P. M. Reimer, H. Zabel, C.P. Flynn, J.A. Dura, K. Ritley, Hydrogen Annealing: Effect of hydrogen on the coherence of epitaxial Nb films on sapphire substrates, *Z. Phys. Chem.* 181 (1993) 375.
21. H. Zabel, A. Weidinger, Hydrogen in thin metal films and superlattices, *Comments Condens. Matter* 17 (1995) 239.
22. A. Pundt, U. Laudahn, U.v. Hülsen, U. Geyer, T. Wagner, M. Getzlaff, M. Bode, R. Wiesendanger, R. Kirchheim, Hydrogen induced plastic deformation of thin films, *Mater. Res. Soc. Symp. Proc.* 594 (2000) 75.
23. S. Wagner, H. Uchida, V. Burlaka, M. Vlach, M. Vlcek, F. Lukac, J. Cizek, C. Baehtz, A. Bell, A. Pundt, Achieving coherent phase transition in palladium–hydrogen thin films, *Scripta Mater.* 64 (2011) 978.
24. K. Nörthemann, A. Pundt, Double-locked nucleation and growth kinetics in Nb-H thin films, *Phys. Rev. B* 83 (2011) 155420.
25. U. Laudahn, Spannungen und Dehnungen von mit Wasserstoff beladenen Nb-Einfach und Pd-Nb-Vielfachschichten. Dissertation. Universität Göttingen, (1998).
26. S. Wagner, A. Pundt, Conduction mechanisms during the growth of Pd thin films: Experiment and model, *Phys. Rev. B* 78 (2008) 155131.
27. G. Gutekunst, J. Mayer, V. Vitek, M. Rühle, Atomic structure of epitaxial Nb-Al<sub>2</sub>O<sub>3</sub> interfaces II. Misfit dislocations, *Philos. Mag. A* 75 (1997) 1357.
28. A. R. Wildes, K. Mayer, K. Theis-Bröhl, The growth and structure of epitaxial niobium on sapphire, *Thin Solid Films* 401 (2001) 7.
29. G. Gutekunst, J. Mayer, M. Rühle, Atomic structure of epitaxial Nb-Al<sub>2</sub>O<sub>3</sub> interfaces I. Coherent regions, *Philos. Mag. A* 75 (1997) 1329.
30. G. Song, A. Remhof, K. Theis-Bröhl, H. Zabel, Extraordinary Adhesion of Niobium on Sapphire Substrates, *Phys. Rev. Lett.* 79 (1997) 5062.
31. K. Nörthemann, R. Kirchheim, A. Pundt, Surface modifications of Nb-films during hydrogen loading, *J. Alloys. Comp.* 356-357 (2003) 541.
32. G. Song, M. Geitz, A. Abromeit, H. Zabel, Solubility isotherms of hydrogen in epitaxial Nb(110) films, *Phys. Rev. B* 54 (1996) 14093.
33. T. Edelmann. Löslichkeitsisothermen und Strukturänderungen von wasserstoffbeladenen epitaktischen Niobschichten. Dissertation, LMU München, (1999).
34. S. Schmid, Strukturänderungen und Defektstrukturen in wasserstoffbeladenen epitaktisch gewachsenen Niobschichten. Dissertation, LMU München, (1999).
35. M. Dornheim. Spannungen, Dehnungen und Lage der Phasengrenzen in dünnen Nb- und Y-Schichten bei Wasserstoffbe- und -entladung. Dissertation. Universität Göttingen, (2002).

## Bibliography

---

36. A. Pundt, K. Nörthemann, S. Schmidt, *Hydrogen-related Surface Modifications of 20 nm thin Straight-sided Niobium Nano-Wires and Niobium Meander-Films*, *J. Alloys. Comp.* 446-447 (2007) 549.
37. G.L. Zhou, C.P. Flynn, *Fingered morphology of niobium (110) grown by molecular-beam epitaxy*, *Phys. Rev. B* 59 (1999) 7860.
38. T. Schober, H. Wenzl: *In Hydrogen in Metals II*, ed. by G. Alefeld, J. Völkl, *Topics Appl. Phys.*, Vol. 29, Springer, (1978).
39. H. Zabel, J. Peisl, *The incoherent phase transitions of hydrogen and deuterium in niobium*, *J. Phys. F* 9 (1979) 1461.
40. J. A. Pryde, C. G. Titcomb, *Solution of Hydrogen in Niobium*, *Trans. Faraday Soc.* 65 (1969) 2758.
41. T. Kuji, T.B. Flanagan, *The effect of isotopic substitution on the critical temperature of the niobium-hydrogen system*, *J. Phys. F* 15 (1985) L59.
42. H. Wenzl, J.-M. Welter, *Properties and Preparation of Nb-H Interstitial Alloys*, in : *Current Topics in Materials Science*, Vol. 1, ed. by E. Kaldis (North-Holland Publ. Comp., Amsterdam) 1977.
43. H. Zabel, H. Peisl, *Coherent  $\alpha$ - $\alpha'$  phase transition of hydrogen in niobium*, *Acta. Met.* 28 (1980) 589.
44. H. Peisl, *Wasserstoff in Metallen*, *Phys. B1.* 37 (1981) 209.
45. H. Wenzl, *Ordered and disordered hydrogen interstitials in Niobium, Tantalum and Vanadium crystals: Structures and Phase diagrams*, *J. Phys. Colloques* 38 (1977) C7-221.
46. C. Julien (editor), J. P. Peteira-Ramos (editor) and A. Momchilov (editor). *New Trends in Intercalation Compounds for Energy Storage*, Springer-Science+Business Media, B.V., (2001).
47. H. Peisl: *In Hydrogen in Metals I*, ed. by G. Alefeld, J. Völkl, *Basic properties*, Vol. 28, Springer, (1978).
48. H. Pfeiffer, H. Peisl, *Lattice expansion of niobium and tantalum due to dissolved hydrogen and deuterium*, *Phys. Lett. A* 60 (1977) 363.
49. E. Grier, M. Jenkins, A. Petford-Long, R. C. C. Ward, M. R. Wells, *Misfit dislocations of epitaxial (110) niobium || (11-20) sapphire interfaces grown by molecular beam epitaxy*, *Thin Solid Films*, 358 (2000) 94.
50. P. F. Miceli, H. Zabel, J. A. Dura, C. P. Flynn, *Anomalous lattice expansion of metal-hydrogen thin films*, *J. Mater. Res.* 6 (1991) 964.
51. Q.M. Yang, G. Schmitz, S. Fähler, H. U. Krebs, R. Kirchheim, *Hydrogen in Pd/Nb multilayers*, *Phys. Rev. B* 54 (1996) 9131.
52. R. Kirchheim, *Interaction of hydrogen with external stress fields*, *Acta Metall.* 34 (1986) 37.
53. S. C. Jain, A. H. Harker, R. A. Cowley, *Misfit strain and misfit dislocations in lattice mismatched epitaxial layers and other systems*, *Philos. Mag. A* 75 (1997) 1461.
54. J. Weissmüller, *Thermodynamics of nanocrystalline solids*, in: *Nanocrystalline Metals and Oxides: Selected Properties and Applications*, Kluwer Acad. Publ., Boston, (2001).

## Bibliography

---

55. J. Weissmüller, C. Lemier, *On the size dependence of the critical point of nanoscale interstitial solid solutions*, *Philos. Mag. Lett.* 80 (2000) 411.
56. S. Wagner, M. Moser, C. Greupel, K. Peeper, P. Reichart, A. Pundt, G. Dollinger, *Hydrogen microscopy – Distribution of hydrogen in buckled niobium hydrogen thin films*, *Int. J. Hydrogen Energy* 38 (2013) 13822.
57. G. Andersson, B. Hjörvarsson, P. Isberg, *Influence of compressive biaxial strain on the hydrogen uptake of ultrathin single-crystal vanadium layers*, *Phys. Rev. B* 55 (1997) 1774.
58. B. Hjörvarsson, G. Andersson, E. Karlsson, *Metallic superlattices: quasi two-dimensional playground for hydrogen*, *J. Alloys Comp.* 253–254 (1997) 51.
59. S. Wagner, A. Pundt, *Mechanical stress impact on thin Pd<sub>1-x</sub>Fex film thermodynamic properties*, *Appl. Phys. Lett.* 92 (2008) 051914.
60. R. Koch, *The intrinsic stress of polycrystalline and epitaxial thin metal films*, *J. Phys. Condens. Matter* 6 (1994) 9519.
61. M. F. Doerner, W. D. Nix, *Stresses and deformation processes in thin films on substrates*, *Critical Reviews in Solid State and Materials Sciences* 14 (1988) 225.
62. J.A. Thornton, J. Tabock, D.W. Hoffman, *Internal stresses in metallic films deposited by cylindrical magnetron sputtering*, *Thin Solid Films* 64 (1979) 111.
63. M. Pletea, W. Brückner, H. Wendrock, R. Kaltofen, *Stress evolution during and after sputter deposition of Cu thin films onto Si (100) substrates under various sputtering pressures*, *J. Appl. Phys.* 97 (2005) 054908.
64. T. Scharf, J. Faupel, K. Sturm, H.U. Krebs, *Pulsed laser deposition of metals in various inert gas atmospheres*, *Appl. Phys. A* 79 (2004) 1587.
65. T. Scharf, J. Faupel, K. Sturm, H.U. Krebs, *Intrinsic stress evolution in laser deposited thin films*, *J. Appl. Phys.* 94 (2003) 4273.
66. H. Windischmann, *Intrinsic stress in sputter-deposited thin films*, *Critical Reviews in Solid State and Materials Sciences* 17 (1992) 547.
67. R. Kirchheim, A. Pundt, *Hydrogen in Metals*, *Physical Metallurgy*, D. E. Laughlin, K. Hono, (Eds.), Elsevier, Oxford (2014) 2597.
68. A. Pundt, *Nanoskalige Metall-Wasserstoff-Systeme, Habilitation, Universität Göttingen, (2005).*
69. L. D. Landau, E. M. Lifschitz, *Theory of Elasticity, Course of Theoretical Physics, vol.7, Third English Edition (1986).*
70. J. F. Nye, *Physical Properties of Crystals*. Clarendon Press, Oxford. (1985).
71. D. Sander, *The correlation between mechanical stress and magnetic anisotropy in ultrathin films*. In: *Reports on Progress in Physics* 62 (1999) 809.
72. K. H. Hellweg, O. Madelung, *Zahlenwerte und Funktionen aus Naturwissenschaft und Technik*. In: *Landolt Beornstein, volume 18(III)*. Springer, Berlin (1984).
73. K. Nörthemann, *Wasserstoffabsorption in epitaktischen Niobschichten: Eine STM-Studie, Dissertation, Universität Göttingen, (2006).*

## Bibliography

---

74. M. Hamm, *Ultra-hohe Spannungen in wasserstoffbeladenen Niob Schichten unterhalb der kritischen Schichtdicke. Masterarbeit, Universität Göttingen, (2013).*
75. M. Hamm, V. Burlaka, S. Wagner, A. Pundt, *Achieving reversibility of ultra-high mechanical stress by hydrogen loading of thin films, Appl. Phys. Lett. 106 (2015) 243108.*
76. J.W. Matthews, *Defects associated with the accomodation of misfit between crystals, J. Vac. Sci. Technol. 12 (1975) 126.*
77. J.W. Matthews, A.E. Blakeslee, *Defects in epitaxial multilayers: I. Misfit dislocations, J. Cryst. Growth 27 (1974) 118.*
78. J.W. Matthews, A.E. Blakeslee, *Defects in epitaxial multilayers: II. Dislocation pile-ups, threading dislocations, slip lines and cracks, J. Cryst. Growth 29 (1975) 273.*
79. J.H. Van der Merwe, *Crystal Interfaces. Part I. Semi-Infinite Crystals, J. Appl. Phys. 34 (1963) 117.*
80. J.H. Van der Merwe, *Crystal Interfaces. Part II. Finite Overgrowths, J. Appl. Phys. 34 (1963) 123.*
81. W. D. Nix, *Mechanical Properties of Thin Films, Met. Trans. 20A (1989) 2217.*
82. E. Fromm, E. Gebhardt, *Gase und Kohlenstoff in Metallen, Springer, Berlin, (1976).*
83. U. Laudahn, S. Fähler, H. U. Krebs, A. Pundt, M. Bicker, U. v. Hülsen, U. Geyer, R. Kirchheim, *Determination of elastic constants in thin films using hydrogen loading, Appl. Phys. Lett. 74 (1999) 647.*
84. A. Pundt, *Hydrogen in nano-sized metals, Adv. Eng. Mater. 6 (2004) 11.*
85. W. Nix, H. Gao, *Indentation size effects in crystalline materials: a law for strain gradient plasticity, J. Mech Phys. Solids 46 (1998) 411.*
86. M. A. Meyers, A. Mishra, D. J. Benson, *Mechanical properties of nanocrystalline materials, Progress in Materials Science 51 (2006) 427.*
87. M. Dornheim, A. Pundt, R. S. Kirchheim, S. J. v. d. Molen, E. S. Kooij, J. Keersemaekers, R. Griessen, H. Harms, U. Geyer, *Stress development in thin yttrium films on hard substrates during hydrogen loading, J. Appl. Phys. 93 (2003) 8958.*
88. E. J. Grier, O. Kolosov, A. K. Petford-Long, R.C.C. Ward, M. R. Wells, B. Hjörvarsson, *Structural changes to epitaxial (0001) holmium layers during hydrogen loading, J. Phys. D.: Appl. Phys. 33 (2000) 894.*
89. J. W. J. Kerssemakers, S. J. van der Molen, N. J. Koeman, R. Günther, R. Griessen, *Pixel switching of epitaxial Pd/YHx/CaF2 switchable mirrors, Nature 406 (2000) 489.*
90. J. W. J. Kerssemakers, S. J. van der Molen, R. Günther, B. Dam, R. Griessen, *In situ monitoring of optical and structural switching in epitaxial YHx switchable mirrors, J. Alloys Comp., 330-332 (2002) 342.*
91. <https://www.comsol.com/comsol-multiphysics>
92. C. Borchers, U. Laudahn, A. Pundt, S. Fähler, H.-U. Krebs, R. Kirchheim, *Influence of hydrogen loading on the microstructure of niobium-palladium multilayers, Philos. Mag. A 80 (2000) 543.*
93. F. Kroupa, *Circular edge dislocation loop, Czech. J. Phys., Sect. B 10 (1960) 284.*

## Bibliography

---

94. A. Kumar, M. Gautam, A. Subramaniam, *Critical sizes for the stabilization of coherent precipitates*, *J. Appl. Phys.* 115 (2014) 193509.
95. G. Song, *Hydrogen in thin niobium films*, Dissertation, Ruhr-Universität Bochum, (2000).
96. R. Kirchheim, *Solid solutions of hydrogen in complex materials*, In *Solid State Physics*, eds. H. Ehrenreich and F. Spaepen, Elsevier, Amsterdam, (2004), 59, 203.
97. E. Tal-Gutelmacher, A. Pundt, R. Kirchheim, *The Effect of Residual Hydrogen on Hydrogenation Behaviour of Titanium Thin Films*, *Scr. Mater.* 62 (2010) 709.
98. A. Baldi, V. Palmisano, M. Gonzalez-Silveira, Y. Pivak, M. Slaman, H. Schreuders, B. Dam, R. Griessen, *Quasifree Mg–H thin films*, *Appl. Phys. Lett.* 95 (2009) 071903.
99. A. Baldi, M. Gonzalez-Silveira, V. Palmisano, B. Dam, R. Griessen, *Destabilization of the Mg-H system through elastic constraints*, *PRL* 102 (2009) 226102.
100. R. Gremaud, M. Gonzalez-Silveira, Y. Pivak, S. de Man, M. Slaman, H. Schreuders, B. Dam, R. Griessen, *Hydrogenography of PdH<sub>x</sub> thin films: Influence of H-induced stress relaxation processes*, *Acta Mater.* 57 (2009) 1209.
101. A. Baldi, B. Dam, *Thin film metal hydrides for hydrogen storage applications*, *J. Mater. Chem.* 21 (2011) 4021.
102. E. M. Salomons, R. Feenstra, D. G. de Groot, J. H. Rector, R. Griessen, *Pressure-composition isotherms of thin PdH<sub>c</sub> films*, *J. Less Common Met.* 130 (1987) 415.
103. S. Wagner, A. Pundt, *Quasi-thermodynamic model on hydride formation in palladium–hydrogen thin films: Impact of elastic and microstructural constraints*, *Int. J. Hydrogen Energy* 41 (2016) 2727.
104. F. Larché, J. Cahn, *A linear theory of thermochemical equilibrium of solids under stress*, *Acta Metall.* 21 (1973) 1051.
105. F. Larché, J. Cahn, *The interactions of composition and stress in crystalline solids*, *Acta Metall.* 33 (1985) 331.
106. H. Wagner: *In Hydrogen in Metals I*, ed. by G. Alefeld, J. Völkl, *Basic Properties.*, Vol. 28, Springer, (1978).
107. F. Stillesjoe, S. Olafsson, P. Isberg, B. Hjoervarsson, *Thermodynamic properties of hydrogen in quasi-two-dimensional vanadium lattices*, *J. Phys. Condens. Matter* 7 (1995) 8139.
108. G. Song, A. Remhof, D. Labergerie, C. Sutter, H. Zabel, *Hydrogen in thin epitaxial Nb films*, *J. Alloys Comp.* 293–295 (1999) 476.
109. M. N. Barber, *in Phase Transitions and Critical Phenomena*, edited by C. Domb and J. L. Lebowitz, Vol. 8, Academic Press, London, (1983).
110. C. Domb, *The Critical Point: A Historical Introduction to the Modern Theory of Critical Phenomena*, Taylor & Francis Ltd, (1996).
111. P. Kesten, *Hochauflösende Untersuchung der lokalen Wasserstoffverteilung in metallischen Multischichten mit Hilfe der tomographischen Atomsonde und der Sekundärionenmassenspektrometrie*. Dissertation. Universität Göttingen, (2000).

## Bibliography

---

112. R. Wiesendanger, *Scanning Probe Microscopy and Spectroscopy: Methods and Applications*, Cambridge University Press, (1994).
113. C. Julian Chen, *Introduction to Scanning Tunneling Microscopy*, Oxford University Press, New York, (2007).
114. S. Woedtke, *Dissertation, Inst. f. Exp. u. Ang. Phys. der CAU Kiel*, (2002).
115. I. Horcas, R. Fernandez, J.M. Gomez-Rodriguez, J. Colchero, J. Gomez-Herrero, A. M. Baro, *Rev. Sci. Instrum.* 78 (2007) 013705 (WSxM solutions website "[www.wsxmsolutions.com](http://www.wsxmsolutions.com)").
116. <http://gwyddion.net>
117. L. J. van der Pauw, *A method of measuring specific resistivity and Hall Effect of discs of arbitrary shape*, *Philips Research Reports* 13 (1958) 1.
118. S. Wagner, A. Pundt, *Combined impact of microstructure and mechanical stress in PdHc thin films electrical resistivity*, *Acta Mater.* 59 (2011) 1862.
119. C. Hammond, *The basics of crystallography and diffraction*, 3rd Ed, Oxford University Press, USA, (2009).
120. B. D. Cullity, S. R. Stock, *Elements of X-Ray Diffraction*, 3rd Ed., Prentice-Hall Inc., (2001).
121. M. Yasaka, *The Rigaku Journal*, *X-ray thin-film measurement techniques V. X-ray reflectivity measurement*, 26 (2010) 1.
122. W. E. Wallace, W. L. Wu, *A novel method for determining thin film density by energy-dispersive x-ray reflectivity*, *Appl. Phys. Lett.* 67 (1995) 1203.
123. <https://www.bruker.com/products/x-ray-diffraction-and-elemental-analysis/x-ray-diffraction/xrd-software/overview/leptos.html>.
124. <http://www.rxollc.com/idl>
125. R. Kirchheim, R. B. McLellan, *Electrochemical Methods for Measuring Diffusivities of Hydrogen in Palladium and Palladium Alloys*, *J. Electrochem. Soc.* 127 (1980) 2419.
126. P. W. Atkins, M. J. Clugston, *Principles of physical chemistry*, Pitman, London (1982).
127. R. Gemma, *Hydrogen in V-Fe thin films and Fe/V-Fe multi-layered thin films. Dissertation*, Universität Göttingen, (2011).
128. R. Kirchheim, *Hydrogen solubility and diffusivity in defective and amorphous metals*, *Prog. Mater. Sci.* 32 (1988) 262.
129. A. Pundt, E. Nikitin, R. Kirchheim, P. Pekarski, *Adhesion energy between metal films and polymers obtained by studying buckling induced by hydrogen*, *Acta Mater.* 52 (2004) 1579.
130. C. G. Stoney, *The Tension of Metallic Films Deposited by Electrolysis*. In: *Proceedings of the Royal Society of London. Series A*, 82 (553) (1909) 172.
131. E. Tal-Gutelmacher, A. Pundt, R. Kirchheim, *The influence of films thickness on hydrogenation behavior of titanium thin films*, *J. Mater. Sci.* 45 (2010) 6389.
132. <http://www.webelements.com>

## Bibliography

---

133. V. Burlaka, S. Wagner, A. Pundt, *In-situ STM and XRD studies on Nb–H films: Coherent and incoherent phase transitions*, *J. Alloy Comp.* 645 Suppl. 1 (2015) 388.
134. A. K. Singh, *Advanced X-ray Techniques in Research and Industry (Stand Alone)*, IOS Press, (2005).
135. P. F. Fewster, *X-ray analysis of thin films and multilayers*, *Rep. Prog. Phys.* 59 (1996) 1339.
136. D. Windt, *IMD—Software for modeling the optical properties of multilayer*, *COMPUTERS IN PHYSICS* 12 (1998) 360.
137. M. Maxelon, A. Pundt, W.P. Hintzen, R. Kirchheim, *Small angle neutron scattering of hydrogen segregation at dislocations in palladium*, *Scripta Mater.* 44 (2001) 817.
138. M. Maxelon, A. Pundt, W. P. Hintzen, J. Barker, R. Kirchheim, *Interaction of hydrogen and deuterium with dislocations in palladium as observed by small angle neutron scattering*, *Acta Mat.* 49 (2001) 2625.
139. C. Gente, M. Oehring, R. Bormann, *Formation of thermodynamically unstable solid solutions in the Cu-Co system by mechanical alloying* *Phys. Rev. B* 48 (1993) 13244.
140. R. Busch, F. Gärtner, C. Borchers, P. Haasen, R. Bormann, *Microstructure development during rapid solidification of highly supersaturated Cu-Co alloys*, *Acta. Metall. Mater.* 43 (1995) 3467.
141. C. Michaelsen, *On the structure and homogeneity of solid solutions: The limits of conventional X-ray diffraction*, *Phil. Mag.* 72 (1995) 813.
142. B. A. Kolachev, *Hydrogen embrittlement of non-ferrous metals*, Translated from Russian, Israel Program for scientific translations, (1968).
143. J. Kürschner, S. Wagner, A. Pundt, *Delamination-supported growth of hydrides in Pd thin films studied by electrochemical hydrogenography*, *J. Alloy Comp.* 593 (2014) 87.

## Acknowledgments

I am using this opportunity to express my sincere appreciation to everyone who supported me throughout the course of this PhD project. First of all, I am immensely grateful to Prof. Dr. Astrid Pundt for giving me the opportunity to write my PhD thesis under her supervision. Without her continuous support and guidance throughout my PhD studies, this work would not have been possible. Furthermore, I would like to thank her for her valuable and constructive suggestions and fruitful discussions on this research work. Her feedback given on this thesis is very much appreciated.

Besides my supervisor, I would especially like to thank Prof. Dr. Hans Christian Hofsäss for co-reviewing this thesis. I wish to thank the members of my thesis committee for their time and patience: Prof. Dr. Hans-Ulrich Krebs, Prof. Dr. Michael Seibt, Prof. Dr. Vasily Moshnyaga and PD Dr.-Ing. Helmut Klein.

I would also like to thank Dr. Stefan Wagner for his support throughout my work in the research group, and especially at the beginning of my PhD studies, when he had found time to share his experience with me and introduced me to the topic of Me-H systems. Besides, I am very grateful him for the feedback he provided on this thesis.

It gives me great pleasure in acknowledging the support and help of Dr. Kai Nörthemann, who has introduced me to the In-situ STM methods during a six week crash course and taught me how to evaluate related data and to use his computer scripts developed to automate the process of STM data evaluation. This helped me to get started on my experiments and to properly handle the STM data.

I owe my deep gratitude to Dr. Helmut Uchida for providing me with some theoretical insights and helping to search for hydrogen-related literature. Without his great database, the search for literature would have been much more difficult. I also thank him for his support during XRD measurements and his user guide, which I have always found helpful during my stays at the synchrotron beamlines in Grenoble and in Hamburg.

I wish to acknowledge the organizational help provided by Dr. Ryota Gemma and Dr. Chika Izawa back in the days when I just arrived in Göttingen to start my PhD.

My deep appreciation goes to Magnus Hamm for great results obtained on Nb-H ultrathin films. Those results have made important contribution to chapter 5.3.

Special thanks should be given to Dr. May L. Martin for her comments on some of the chapters.

I express my warm thanks to Marian Bongers for helping me with the XRR and XRD measurements conducted in-house as well as at the synchrotron facility in Grenoble. Besides, I would like to thank him for sharing his experience with bureaucratic regulations in Germany.

I thank Marc Waninger, Jara Kürschner, Martin Deutges, Anshu Tyagi and Mari Tiegel for the great time we spent together at different conferences.

I would like to thank all the members of "H in metals" group and "Defactants" group once again for the productive joint work, interesting conversations and the great times spent together.

I would like to express my very great appreciation to Tobias Schulz, Matthias Hahn, Karin Ahlborn, Michael Malchow, Frank Köhler, Dr. Vladimir Roddatis, Dieter Plischke, Michael Tetzlaff, Denny Wagner and Kerstin Born for their valuable support in dealing with technical issues.

My special thanks are also extended to Dr. Carsten Baetz (ESRF), Dr. Anthony Bell (HASYLAB) and Dr. Oliver Seeck (HASYLAB) for their comprehensive technical support during my experiments performed at the synchrotron beam facilities in Grenoble and in Hamburg.

I would like to offer my heartfelt thanks to Christina Kuba and Karin Haake for their help with administrative matters.

I sincerely thank my friends from Göttingen for their companionship and the great time together, all the laugh and fun we had. I will always associate this period of my life with those people.

Finally, I am particularly grateful to my mother Olga A. Burlaka, my father Igor A. Burlaka and my wife Dr. Victoria Burlaka for their faith, encouragement and constant emotional support. I would like to express my highest appreciation to my love Victoria, who believed in me and supported me in every possible way. Words cannot express how grateful I am to her for this!

I also want to thank the Deutsche Forschungsgemeinschaft for their financial support (DFG; Project PU131/12--1).

## Curriculum vitae

### Personal data

Name: Vladimir Burlaka  
Date and place of birth: December 20, 1986, Saint Petersburg, Russia  
Citizenship: Russian  
Family status: married, one child

### Education

09.1994 – 06.2001 Middle school “Shemetovo”, Sergiev Posad, Moscow region, Russia

09.2001 – 06.2004 Physics and Mathematics Lyceum, Sergiev Posad, Moscow region, Russia

09.2004 – 02.2010 National Research Nuclear University MEPhI (Moscow Engineering Physics Institute), Faculty of Experimental and Theoretical Physics, Moscow, Russia

Diploma in Physics, Department of Plasma Physics, Supervisor – Prof. Dr. Alexander A. Pisarev  
“Deuterium trapping and surface modification of graphite MPG-8 during Deuterium ion bombardment in the stationary magnetron discharge”

10.2010 – present PhD student in the research group of Prof. Dr. Astrid Pundt, Institut für Materialphysik , Georg-August University, Göttingen, Germany

### Professional employment

03.2010 – 09.2010 Engineer in the research group of Prof. Dr. Alexander A. Pisarev, National Research Nuclear University MEPhI (Moscow Engineering Physics Institute), Faculty of Experimental and Theoretical Physics, Plasma Physics Department, Moscow, Russia

10.2010 – present Research associate in the research group of Prof. Dr. Astrid Pundt, Institut für Materialphysik , Georg-August University, Göttingen, Germany

## Publications related to this work

- *V. Burlaka, S. Wagner, A. Pundt, In-situ STM and XRD studies on Nb–H films: Coherent and incoherent phase transitions, Journal of Alloys and Compounds 645 (2015) 388-391.*
- *M. Hamm, V. Burlaka, S. Wagner, A. Pundt, Achieving reversibility of ultra-high mechanical stress by hydrogen loading of thin films, Applied Physics Letters 106 (2015) 243108.*
- *S. Wagner, H.T.Uchida, V. Burlaka, M. Vlach, M. Vlcek, F. Lukac, J. Cizek, C. Baetz, A. Bell, A. Pundt, Achieving coherent phase transition in palladium–hydrogen thin films, Scripta Materialia 64 (2011) 978-981.*

## Submitted

- *V. Burlaka, S. Wagner, M. Hamm, A. Pundt, Suppression of phase transformation in Nb-H thin films below switchover-thickness*

## Other publications

- *K. A. Moshkunov, I. V. Vizgalov, V. I. Burlaka, Yu. M. Gasparyan, A. A. Pisarev, Deuterium Release from Lithium Irradiated by Deuterium Plasma, Bulletin of the Russian Academy of Sciences. Physics, 76 (2012) 716-720.*
- *V. I. Burlaka, Yu. M. Gasparyan, A. A. Pisarev, I. V. Visgalov, A. A. Rusinov, S. A. Krat, Deuterium trapping in graphite MPG-8 and carbon films growing under irradiation by deuterium plasma, Problems of Atomic Science & Engineering (PASE), Ser. "Thermonuclear Fusion", 2 (2010) 33-38. (In Russian).*
- *A. A. Pisarev, V. I. Burlaka, G. V. Krashevskaya, A. A. Rusinov, G. V. Khodachenko, L. V. Misozhnikov, I. N. Yurkevich, Diagnostics of properties of capacitor foil with extended nanostructured surface, Bulletin of the Lebedev Physics Institute, 37 (2010) 26-28.*